A gamma-ray backscattering technique for in vivo body composition studies

Morgan, Helen M.

Award date:
2001

Awarding institution:
University of Bath

A GAMMA-RAY BACKSCATTERING TECHNIQUE FOR *IN VIVO* BODY COMPOSITION STUDIES

submitted by Helen M Morgan
for the degree of PhD
of the University of Bath
2001

ProQuest LLC
789 East Eisenhower Parkway
P.O. Box 1346
Ann Arbor, MI 48106-1346

Abstract

A method of measuring fat fraction and bone mineral content using a gamma-ray backscattering technique has been investigated in order to explore the potential of the technique as a clinical diagnostic tool. Simple tissue substitute materials have been used: ethanol to represent fat, distilled water to represent lean (muscle) tissue and potassium hydrogen phosphate (K_2HPO_4) to represent bone. For the bone mineral investigations phantoms to represent different anatomical sites have been used to determine the feasibility of a clinical technique.

The backscattered spectrum from the 59.54 keV gamma ray of americium-241 has been measured with a hyperpure germanium detector. Different approaches to analysing the spectra have been examined. These approaches were measurement of the coherent to Compton scattering ratios, Compton profile width and Compton profile ratios.

For the fat fraction investigations none of the methods studied had a clear advantage over any other. The coherent to Compton scattering ratio had large uncertainties due to counting statistics but gave greatest discrimination between fat and muscle substitutes. It was also the method least sensitive to positioning uncertainties. In a clinical setting it should enable a fat fraction determination with an uncertainty of 0.1 (standard deviation).

For the bone mineral density investigations phantoms representing three anatomical sites have been studied: lumbar spine, heel bone and jawbone. None of the methods of analysis investigated were suitable for measurements of bone mineral density in the lumbar spine, which typically lies at a depth of 85 mm below the skin surface. For the sites of the heel and jaw where the bone is more superficial, the coherent to Compton ratio measurement would achieve the necessary precision of one per cent on a bone density determination.

For a clinical investigation the effective radiation dose from this technique has been determined to be 2 μSv.

Acknowledgements

I would like to acknowledge the help and encouragement of my supervisor Professor Stephen Lillicrap, my colleague Dr John Shakeshaft for his computing expertise and discussions on various issues, and my two supervisors Dr Richard Sullivan and Professor John Davies.

For financial support I would like to thank the Wessex Regional Medical Physics Service, Royal United Hospital, Bath.

Table of Contents

Chapter 1 Introduction 1

1.1 Soft tissue 2

1.1.1 Fat fraction 2

1.2 Bone 3

1.2.1 Bone structure 4

1.2.2 Osteoporosis 6

1.3 Objectives 7

Chapter 2 Theory 8

2.1 Photon scattering processes 8

2.1.1 Photoelectric effect 8

2.1.2 Coherent scattering 9

2.1.3 Compton scattering 10

2.2 Analysis of data 11

2.2.1 Coherent to Compton scattering ratio 11

2.2.2 Compton profile 14

2.2.3 Compton profile ratios 18

2.3 Summary 20

Chapter 3 Experimental details 22

3.1 Radionuclide source 22

3.2 Detector and electronics 23

3.2.1 Detector efficiency 25

3.2.2 Detector energy resolution 26

3.2.3 Calibration and linearity of the detection system 28

3.3 Collimation of source and detector 29

3.4 Substitutes for biological tissues 31

3.4.1 Substitutes for fat and lean tissue 32

3.4.2 Substitute for bone 34

Chapter 4 Target Volume Determination 36

4.1 Introduction 36

4.2 Experimental method 37

4.3 Results 38

4.4 Discussion 42

Chapter 5 Studies on Water and Ethanol 44

5.1 Coherent to Compton scattering ratio 45

5.2 Compton profile shapes 51

5.3 Compton profile ratios 60

5.4 Ethanol as fat substitute 62

5.5 Small diameter phantom studies 64

5.6 Estimation of uncertainties for fat fraction measurements 66

5.7 Reproducibility of measurements 69

5.8 Fat fraction determination 73

5.9 Summary of Investigations 74

Chapter 6 Investigations of Bone Mineral Composition 76

6.1 Introduction 76

6.2 Description of the lumbar spine 77

6.3 Experimental arrangement 79

6.4 Coherent to Compton scattering ratios 82

6.5 Compton profiles 87

6.6 Compton profile ratios 89

6.7 Comparison with the results of other workers 94

6.8 Conclusions 97

Chapter 7 Studies on Heel Phantom 100

7.1 Introduction 100

7.2 Description of the calcaneum (heel bone) 102

7.3 Experimental arrangement 103

7.4 Feasibility study and comparison of results with other workers 105

7.5 Coherent to Compton scattering ratio 109

7.6 Compton profile ratios 117
7.7 Compton profile width 120
7.8 Effect of phantom position 122
7.9 Uncertainties in density determinations 123
7.10 Conclusions 124

Chapter 8 Studies on Jaw Phantom 127
8.1 Introduction 127
8.2 Description of the jawbone 128
8.3 Experimental arrangement 129
8.4 Coherent to Compton scattering ratio 131
8.5 Compton profile ratios 136
8.6 Uncertainties in density determination 142
8.7 Discussion 145
8.8 Summary and conclusions 150

Chapter 9 Dosimetry 152
9.1 Measured surface dose rates 152
9.2 Calculated surface dose rates 153
9.3 Discussion 154

Chapter 10 Conclusions 156
10.1 Summary of work to date 156
10.1.1 Fat fraction investigations 156
10.1.2 Bone mineral composition investigations 158
10.2 Proposal for a clinical system 160

List of references 162

Appendix 169
Published work 169

Chapter 1 Introduction

X-ray and gamma-ray sources have been used in medical diagnostic applications both to image and analyse various tissues of the body. The main applications have been transmission imaging with x-ray sources and organ imaging with gamma-ray emitting radiopharmaceuticals in nuclear medicine studies. Both of these applications are based on the measurement of the residual unscattered x-ray or gamma-ray photons. Steps are taken during these measurements to suppress interference by scattered photons.

Many workers (reviewed by Holt *et al* 1984) have investigated the possibility of using Compton scattered x-rays and gamma-rays for both imaging and densitometry. Coherent scatter in x-ray diffraction studies is well established. More recently, low angle x-ray scattering using broad spectrum x-ray sources has been used for tissue characterisation (Harding *et al* 1990, Royle and Speller 1991).

A number of workers (Kerr *et al* 1980, Puumalainen *et al* 1982, Webster and Lillicrap 1985, Gigante and Sciuti 1985) have proposed or used the measurement of coherent to Compton scattered photons from irradiated bone and other tissues to determine information on the composition of the tissue. Since the probability of coherent scatter reduces rapidly with increasing angle of scatter, much of the work has been performed using scattering angles of 90° or less. However, Holt *et al* (1983) used a scattering angle approaching 180° to analyse small biological specimens and detected clear coherent scatter peaks in the scatter spectrum. They also demonstrated differences in the Compton scatter profile due to changes in the chemical composition of the scatterer. A backscattering measurement geometry, in which the scattering angle is large (approaching 180°), has the advantage of a simpler measurement set-up and positioning in a clinical setting.

Knowledge of the composition of the human body is of interest in diagnosing disease and also monitoring the efficacy of treatments. Body composition studies deal primarily with the measurement of components of soft tissue (fat and water) and bone. The purpose of this work is to examine the potential of using a gamma-ray backscattering technique to assess regional body composition *in vivo* at selected sites. Particular areas of interest are the relative amounts of fat and muscle in a block of tissue, and the bone mineral density. Measurement of bone mineral density is used widely for screening and monitoring of

osteoporosis. At present fat content is not measured but inferred from measurements of lean body mass. There is no absolute method for the measurement of fat content, and different methods of analysis give different results.

The aim of this project is to explore the feasibility of a practical measurement system suitable for clinical applications. In developing this technique the objectives are that any clinical investigation should not take more than 30 minutes and that the radiation dose to the patient should be sufficiently low that the patient receives a net benefit from the investigation.

1.1 Soft tissue

The soft tissues of particular interest in the work reported here are fat and muscle. Fat is an oily material, which is widely present in the body. It also forms a distinct tissue; adipose. Adipose tissue is areolar tissue (a type of connective tissue) which has fat cells enmeshed in it.

Muscle consists of a number of bundles of fibres placed side by side, all running in the same direction and bound together by a thin membrane of connective tissue. It consists of 75 per cent water and 25 per cent solids, of which the most important (20 per cent) is a protein known as myosin. Only two per cent of muscle is fat.

1.1.1 Fat fraction

There are many methods of measuring fat from relatively low technology anthropomorphic measurements of skin-fold thickness and determination of body density by underwater weighing through to the high technology methods of dual energy x-ray absorptiometry (DEXA), magnetic resonance imaging (MRI), computerised tomography (CT) and neutron activation analysis. To quote Tothill *et al* (1998), "The assessment of fat proportion has received more attention and generated more different techniques than any other aspect of body composition indicating its importance in nutrition studies, but also its difficulties. The assessment of accuracy is difficult as the nearest to a reference technique is post mortem dissection and chemical analysis." Each method has its assumptions and limitations and no single method can be regarded as a reference technique. There have

been several studies comparing different techniques and further comparisons are still needed in order to improve each technique (Fowler *et al* 1992, Pierson *et al* 1995, Tothill *et al* 1994, 1998 and Ryde *et al* 1998).

Chapter 5 examines the possibility of using a gamma-ray backscattering technique to measure fat fraction. The measurement of fat and fat free mass is important in monitoring patients with advanced liver disease who suffer muscle wasting, and following liver transplant. In these patients the weight gain should be in lean body mass but is frequently due to increase in fat (Hussaini *et al* 1998, Soo *et al* 1998). The measurement of body fat content is also important when monitoring growth hormone deficient adults (Areberg *et al* 1998), patients undergoing dialysis (Johansson *et al* 1998), and children with cystic fibrosis who gain extra lower body fat, to determine the efficacy of treatments (Allen *et al* 1998). Monitoring obese patients on different hypocaloric diets to determine their effectiveness is another area of investigation (Westmacott *et al* 1998).

Puumalainen *et al* (1977) reported that " evaluation of the fat content of liver tissue would be of great clinical significance in the differential diagnosis of diffuse liver diseases. The present methods rely on subjective histological analysis of liver needle biopsies. However a biopsy specimen is not always representative e.g. when liver contains locally distributed disease processes."

Boyd *et al* (1995) have investigated the relative amounts of fat and connective and epithelial tissue in the breast by studying mammographic x-ray films and found that decreases in fat content are associated with increases in risk for breast cancer.

1.2 Bone

Chapters 6, 7 and 8 examine the possibility of using a gamma-ray backscattering technique to measure bone density. The measurement of bone mineral content is well recognised as a means of diagnosing osteoporosis. The usual site for monitoring change in bone mineral content is the lumbar region of the spine. The work described in Chapter 6 examines the use of this technique for measurements of bone density in the lumbar spine. The calcaneum (heel) is the measurement site for ultrasound determination of bone mineral content and this might be a suitable area for the technique described in this report. In addition, Horner *et al* (1996) demonstrated that mandibular (jaw) bone mineral density,

assessed from dental x-ray films, could be used to detect osteoporosis. The mandibular bone is also superficial and is another site to be investigated with the proposed technique. This section describes the structure of bone and the conditions for which a bone density measurement may be useful.

1.2.1 Bone structure

There are two types of bone structure. About 70 per cent of the bone is cortical, compact or dense bone and the remainder is trabecular, cancellous or spongy bone (ICRP 23, 1974). Both types of bone are different arrangements of the same histologic elements. In general cortical bone is on the exterior of the skeleton and trabecular bone is on the interior. Trabecular bone has a honeycomb structure and the interstitial spaces are filled with fatty or haematogenous marrow. Trabecular bone hence has a larger surface area than cortical bone and more cells on it per unit volume. This leads to the relatively greater metabolic activity of trabecular bone relative to cortical bone.

Bone is the hardest of the connective tissues; its hardness results from the deposition of bone mineral within a supporting lattice of organic matrix. Bone mineral consists essentially of mineral salts, mainly calcium hydroxyapatite ($Ca_{10}(PO_4)_6(OH)_2$) and calcium phosphate. The calcium phosphate has no mechanical function.

There are four types of bones:

1. Long bones – These make up the limbs, arms, forearms, thighs and legs. They consist of an elongated shaft with two extremities. The shaft consists of a cylinder of cortical bone containing yellow bone marrow. A thin outer layer of cortical bone with an interior of trabecular bone containing red marrow forms the extremities.

2. Short bones – These have no shaft but consist of smaller masses of trabecular bone surrounded by a shell of cortical bone. They are roughly cuboid in shape; examples are the small bones in the wrist and ankle.

3. Flat bones – These consist of two layers of cortical bone with a layer of cancellous bone in between. The bones of the skull and the scapula are examples of flat bones.

4. Irregular bones – These bones do not fit into the previous categories and include the vertebrae, most of the bones in the face, and heel bones.

Bone is composed of myriads of tiny crystals of calcium hydroxyapatite which impregnate an infrastructure of collagen fibres. These crystals are only about 7 nm in length when first attached between collagen building blocks but grow up to around 60 nm in length in mature bone. The whole is embedded in a structureless mucopolysaccharide ground substance. The structurally supportive tissue is in a continuous state of reappraisal or bone turnover, which is mediated by two types of cell: osteoblasts, which are descended from connective tissue stem cells, and osteoclasts, which are multinucleated tissue macrophages descended from marrow stem cells.

Osteoblasts are responsible for synthesising the organic constituents of bone and the calcification of the osteoid matrix. Osteoclasts are responsible for the resorption of bone. It is thought that the mineral phase of bone is liberated first, causing a temporary increase in the flux of calcium and phosphorous into the extracellular fluid space. The organic constituents of the bone are then digested away and then excreted in the urine.

Bone turnover is the combination of bone formation and bone resorption. This process is related to both the body's requirements to maintain a physiological concentration of ionised calcium in the body fluids and to maintain the structural integrity of the skeleton. Bone turnover is relatively rapid in trabecular bone and slow in cortical bone. This is probably due to the greater surface available for metabolic activity in trabecular bone.

New bone formation cannot proceed until the osteoclasts have digested an amount of bone substance to make calcium available. Similarly if an increase in the calcium level in the plasma is required to maintain the correct physiological concentration, bone resorption is first required.

The resorptive phase of bone turnover at a particular site is fairly rapid and usually takes place within a few weeks. However, the formation of new bone at the same site is relatively slow and may take several months. If there is a strong stimulus for bone resorption, trabecular bone may be severely weakened since it is most active. This in turn could lead to structural failures in trabecular bone.

There is about 1 kg of calcium and 440 g of phosphorus in the skeleton of an average 70 kg man. Almost 99 per cent of this calcium in the skeleton is in the form of calcium hydroxyapatite.

Calcium is lost from the body fluids into the urine, faeces, sweat and milk, and to the skeleton of the developing foetus *in utero*, whether or not there is calcium in the diet. To maintain the equilibrium in the body fluids calcium must be absorbed from the gut or reabsorbed from the skeleton. The intestinal absorption of calcium from the gut is usually sufficient but this is dependent on vitamin D, which promotes the absorption of calcium from the gut. In man vitamin D is mainly obtained by synthesis of cholecalciferol (vitamin D_3) in the skin after exposure to ultra-violet light.

The skeletal bone mass reaches a maximum value in the adult between the ages of 20 and 40 years. Thereafter the bone mass decreases with age at all body sites. However, the change in bone mass depends on the proportions of cortical and trabecular bone at each site. As a consequence the vertebral bodies appear to lose bone mass more rapidly in the post early middle life period and then the rate of bone loss reduces.

Both men and women reach peak bone mass between the ages of 20 and 40 years, but in women the rate of bone loss is three times greater than in men. On average a woman will loose 30 per cent of her bone mass between the ages of 50 and 80 years whilst a man will loose only 10 per cent over the same period.

1.2.2 Osteoporosis

Osteoporosis is usually defined as a quantitative deficiency of bone substance, which is sufficient to make the affected part(s) of the skeleton susceptible to mechanical failure. The probability of fracture or structural failure in any part of the skeleton will increase as the bone mass per unit volume or whole bone density at that site reduces. Unfortunately there is no threshold level of bone mass below which there is a risk of fracture from minor trauma. Two definitions of osteoporosis are currently in use. The first (Christianson 1993) describes the disease as being characterised by low bone mass and microarchitectural deterioration of bone tissue with a consequent increase in bone fragility and susceptibility to fracture. The second definition developed by the World Health Organisation (1994) is more commonly used. It describes osteoporosis as a bone mineral density that is

2.5 standard deviations below the peak bone mass expected in a normal healthy young woman. Both of these definitions have a role to play. It has been postulated that bone density is attributable for 70 to 75 per cent of the fracture risk whilst the remaining 20 to 25 per cent is dependent on additional factors. These include the microstructure and architecture of bone and the state of bone re-modelling (Kleerekoper *et al* 1985).

Osteoporosis is recognised as a significant public health risk. In the United Kingdom, the Department of Health (1995) estimated that one in three women and one in twelve men were likely to suffer from osteoporosis with a cost to the National Health Service of around £750 million per year. Calman (1995) recognised that osteoporosis is a growing problem due partly to the increase in the number of elderly people in the population. The European Commission (1998) predicted that the incidence of hip fractures in the European Union would more than double over the next fifty years to reach 972,000 incidents per year. This will have a significant impact on health services. Consequently there is now more interest in developing the understanding of osteoporosis to improve the treatment of the disease or even prevent it.

1.3 Objectives

One object of the reported work in this thesis was to determine whether or not a backscattering technique could be used for *in vivo* analysis of body composition. A backscattering technique has been employed in preference to forward scattering since the geometry would be more compact to use in a clinical setting and would also be more reproducible. It gives good resolution between the coherent and Compton peaks, but has the disadvantage that the signal from the coherent photons is small compared with the signal from the Compton photons. This report examines the possibilities of using the coherent to Compton scattering ratio, the Compton profile width and the ratio of counts in the high energy region of the Compton profile to the counts in the whole of the Compton profile, as methods of analysing body compositions.

The long-term aim of the project is to develop a practical system for clinical use to measure the fat content of tissue and to measure bone mineral density.

Chapter 2 Theory

2.1 Photon scattering processes

There are five major types of interaction between a photon beam and an absorbing material. These processes are photoelectric effect, coherent scattering, the Compton effect, pair production and photodisintegration. Photodisintegration is an interaction between the photon and the nucleus in which a neutron or proton is ejected from the nucleus. It only occurs for incident photon energies above 10 MeV. Pair production is an interaction between the photon and the field around the nucleus in which the whole of the energy of the photon is converted to the mass and kinetic energy of an electron and a positron. It only occurs for incident photon energies greater than 1.02 MeV (twice the rest mass of the electron). Diagnostic investigations involve much lower energies of incident photons and so the processes of photodisintegration and pair production will not be considered further. The other three processes are important for the range of energies and atomic numbers encountered in diagnostic imaging: photoelectric effect, coherent scattering and Compton effect all involve interactions between the incident photon and the atomic electrons.

2.1.1 Photoelectric effect

In this process the incident photon interacts with an atom and ejects one of the orbiting electrons. The entire energy of the photon $h\nu$ is transferred to the atomic electron. The kinetic energy of the ejected electron (the photoelectron) is equal to $h\nu$-E_B where E_B is the binding energy of the electron. Interactions may take place with electrons from the K, L, M or N shells.

After the electron has been ejected, the atom is left in an excited state due to the vacancy created in the shell. The vacancy may be filled by an outer orbital electron with the emission of characteristic x-rays. Since the K-shell binding energy of soft tissue is of the order of 0.5 keV the energy of any characteristic x-rays is very low and so for clinical purposes can be considered to be absorbed locally. For practical purposes, in a photoelectric collision in tissue, one electron is produced of equal energy to the incident photon. Photoelectrons tend to be ejected in a direction at right angles to the incident

photons for low energy photons. The photoelectrons are emitted in a more forward direction as the incident photon energy increases.

The probability of photoelectric absorption depends on the photon energy as $1/E^3$. It also depends strongly on the atomic number Z of the absorbing material, being approximately proportional to Z^3. It is this dependence on atomic number that forms the basis of many applications in diagnostic radiology. The difference in atomic number between bone, muscle and fat amplifies the difference in x-ray absorption, provided the photoelectric effect is the main interaction process.

2.1.2 Coherent scattering

Coherent scattering is also known as Classical, Rayleigh or elastic scattering. It may be visualised by considering the wave nature of electromagnetic radiation. As the electromagnetic wave passes near the electron it sets the electron into oscillation with the same frequency as the wave. The oscillating electron radiates the energy at the same frequency as the incident wave. No energy is changed into electronic motion and no energy is absorbed in the medium. The probability of coherent scattering is proportional to the square of atomic number (Z^2). The effect is greatest at small scattering angles and decreases with increasing scattering angle. Using classical reasoning, Thomson showed that the fraction of incident energy scattered at angle θ into unit solid angle was given by:

$$\frac{d\sigma_T}{d\Omega} = \frac{e^4}{2m_e{}^2c^4}\left(1+\cos^2\theta\right) \qquad \textbf{Equation 2.1}$$

where $d\sigma_T/d\Omega$ is the Thomson differential scattering cross section,
e is the electronic charge,
m_e is the mass of the electron, and
c is the velocity of light.

This equation assumes that the binding energy of the electron is much less than the incident photon energy, and the Thomson differential scattering cross section has the same value for all photon energies.

2.1.3 Compton scattering

In the Compton process the photon interacts with an atomic electron which behaves as though it were a "free" electron. The electron is considered "free" since its binding energy is much less than the energy of the incident photon. In this process the electron receives some energy from the photon and is emitted at an angle ϕ. The photon with reduced energy is scattered through an angle θ. When the recoil of the electron is taken into account, the number of photons scattered into unit solid angle at angle θ is given by the Klein-Nishina formula:

$$\frac{d\sigma_e}{d\Omega} = \frac{e^4}{2m_e^2 c^4}\left(1+\cos^2\theta\right)\left\{\frac{1}{1+\alpha(1-\cos\theta)}\right\}^2\left\{1+\frac{\alpha^2(1-\cos\theta)^2}{(1+\alpha(1-\cos\theta))(1+\cos^2\theta)}\right\}$$

Equation 2.2

where α is the ratio $h\nu/m_e c^2$, the ratio of the incident energy of the photon to the rest energy of the electron (511 keV).

The Klein-Nishina formula applies only for a single free electron. The first factor in this formula is the same as that obtained by Thomson. When α is small i.e. the incident photon energy is small compared with the rest energy of the electron, the expression reduces to Equation 2.1.

The energy of the Compton peak is determined by the angle through which the radiation has been scattered and is given by the expression below:

$$E = \frac{E_0}{(1+E_0(1-\cos\theta)/m_e c^2)}$$

Equation 2.3

where E is the Compton peak energy,

E_0 is the incident energy,

$m_e c^2$ is the rest energy of the electron, and

θ is the angle through which the photon has been scattered.

As the angle of scatter increases, the Compton peak energy decreases. So the greater the angle of scatter, the greater the difference in energy between the coherent and Compton

peaks in the energy spectrum. However, the intensity of the coherent peak decreases as the scattering angle increases.

2.2 Analysis of data

The investigations reported here examine radiation scattered by the coherent and Compton processes. An energy spectrum of scattered radiation obtained for 59.54 keV photons incident on a water target is shown in Figure 2.1, which demonstrates the Compton and coherent peaks. Three methods of analysing the spectral data obtained have been examined. They are the coherent to Compton scattering ratio, the Compton profile shape and the Compton profile ratios.

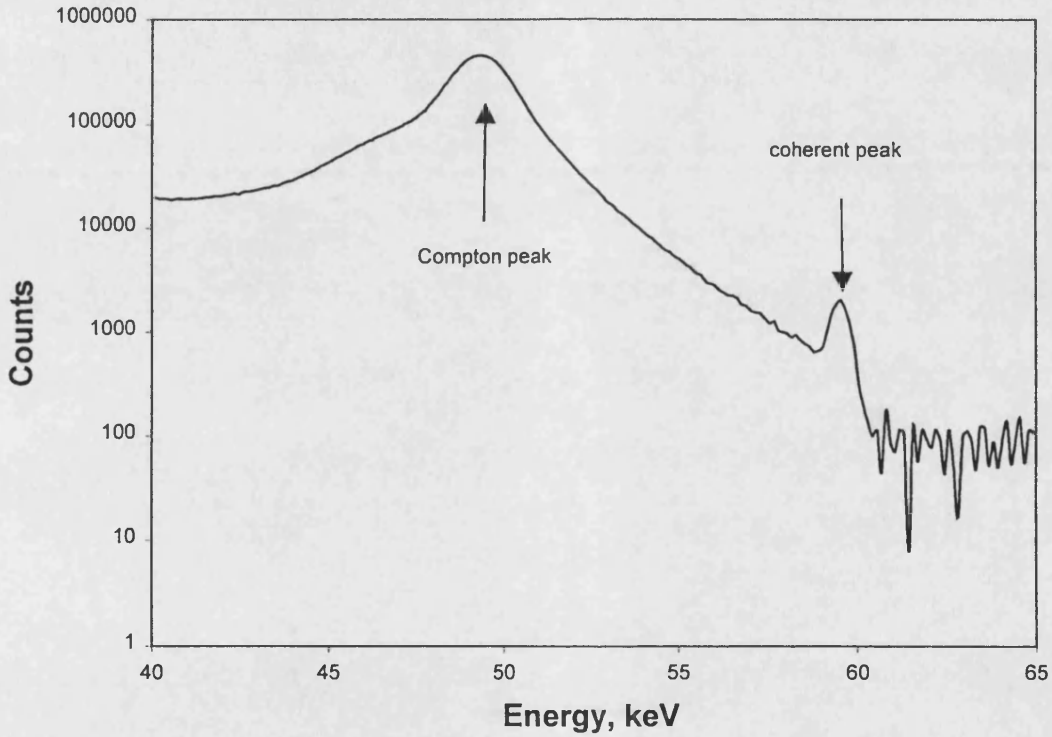

Figure 2.1 Energy spectrum of radiation scattered through 150° from 59.54 keV incident photons on water target.

2.2.1 Coherent to Compton scattering ratio

When a target material is subjected to a beam of radiation, the radiation is scattered. Scattered photons will have a range of energies. The energy of the scattered radiation may

be the same as the incident radiation (elastic or coherent scatter) or a lower energy from inelastic or Compton scatter. The energy spectrum of the scattered photons shows a peak from each of these mechanisms (see Figure 2.1).

The coherent to Compton scattering ratio R is the ratio of the differential atomic cross-sections for coherent and Compton scattering per unit solid angle per atom, and is a function of photon energy, atomic number and scattering angle:

$$R = \frac{d\sigma_{coh}}{d\Omega} \Big/ \frac{d\sigma_{Com}}{d\Omega} \qquad \textbf{Equation 2.4}$$

The differential coherent scattering cross-section per atom is given by:

$$\frac{d\sigma_{coh}(\theta)}{d\Omega} = \frac{d\sigma_T(\theta)}{d\Omega}[F(x,Z)]^2 \qquad \textbf{Equation 2.5}$$

where $d\sigma_T(\theta)/d\Omega$ is the Thomson differential scattering cross section per electron,

θ is the angular change in direction between the incident and scattered photons, and

$F(x,Z)$ is the atomic form factor which represents the ratio of the amplitude of the coherent scattering by an entire atom to that by a single free electron (Evans 1958), and is a function of the change in momentum x, of the scattered photon and the atomic number Z of the scattering medium.

The differential Compton scattering cross section per atom is similarly given by

$$\frac{d\sigma_{Com}(\theta)}{d\Omega} = \frac{d\sigma_e(\theta)}{d\Omega} S(x,Z) \qquad \textbf{Equation 2.6}$$

where $d\sigma_e(\theta)/d\Omega$ is the Klein-Nishina differential collision cross section per free electron, and

$S(x,Z)$ is the incoherent scattering function.

Tightly bound electrons may not participate in an incoherent scattering event if their binding energy is greater than the free electron recoil energy. The function $S(x,Z)$ is the

product of the number of electrons per atom and the probability that an atomic electron will undergo some transition as a result of receiving a momentum transfer x (Evans 1958).

The expected ratio R may be expressed as:

$$R = P(k,\theta) \times \frac{F^2(x,Z)}{S(x,Z)} \qquad \textbf{Equation 2.7}$$

where $$P(k,\theta) = \frac{[1+k(1-\cos\theta)]^2(1+\cos^2\theta)}{1+\cos^2\theta + \frac{[k^2(1-\cos\theta)^2]}{[1+k(1-\cos\theta)]}} \qquad \textbf{Equation 2.8}$$

$F(x,Z)$ is the atomic form factor which allows for the whole atom to be acting as a scatterer,

$S(x,Z)$ is the incoherent scattering function to allow for electron binding effects,

k is the incident energy in units of electron rest mass, and

x is the momentum transfer, given by $x = \sin(\theta/2)/\lambda$ (Å).

The ratio R applies to narrow beam geometry and a well-defined scatter angle. The atomic form factor and incoherent scattering functions have been calculated and tabulated by Hubbell *et al* (1975).

Equation 2.7 may be used to determine the coherent to Compton scattering ratio for pure elements. For a compound of known composition, a modified version of Equation 2.7 is required which averages the coherent to Compton scattering contributions from the component elements, weighted for fractional atomic abundance:

$$R = P(k,\theta) \frac{\sum_i (F_{Z_i}(x,Z_i))^2 a_i}{\sum_i S_{Z_i}(x,Z_i) a_i} \qquad \textbf{Equation 2.9}$$

where a_i is the atomic fraction of element i in the compound.

The ratio R will vary with incident energy and scattering angle for a particular compound. However, for a fixed scattering geometry and incident photon energy the ratio R could be used to give an indication of the composition of the material under investigation. In particular it may be used to indicate the proportion of fat to muscle and the bone mineral density. The advantage of using a ratio is that systematic error in the measurement due to changes in the scattering volume and absorption along the incident and scattered beam

profiles will be minimised (Holt *et al* 1983). This is of particular importance for *in vivo* studies.

A plot of calculated values of coherent to Compton scattering ratio against scattering angle for 59.54 keV incident photons for the biological materials of interest in this work is shown in Figure 2.2. The figure demonstrates that the coherent to Compton scattering ratio distinguishes well between cortical bone, spongiosa bone and muscle (soft tissue) but less well between muscle and adipose tissues where the coherent signal is smaller.

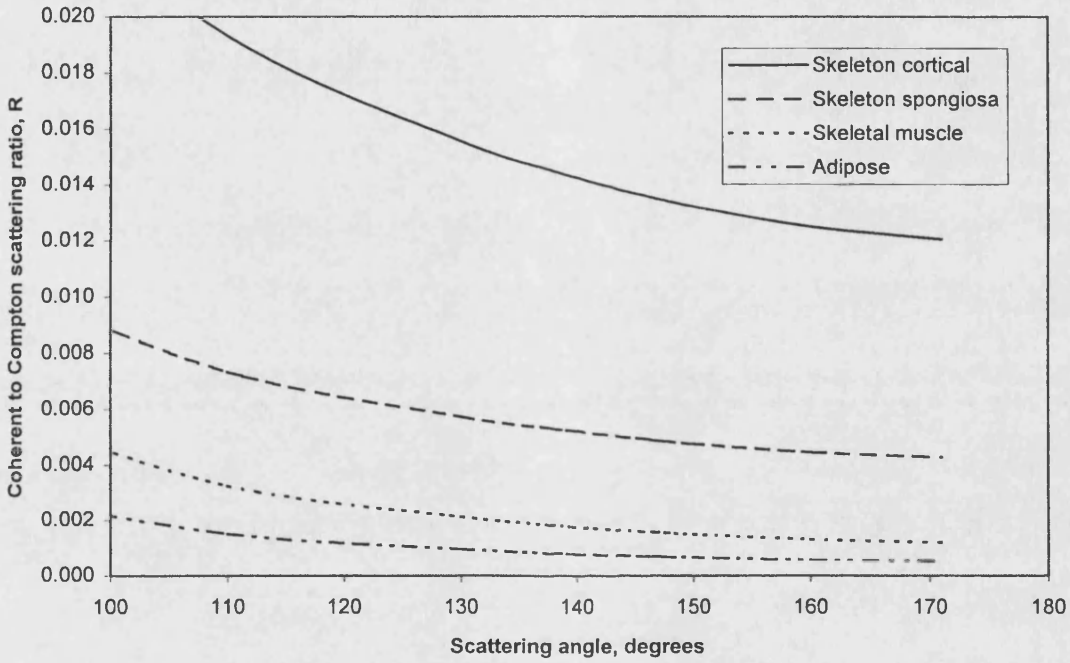

Figure 2.2 Variation of coherent to Compton scattering ratios with scattering angle for 59.54 keV photons incident on different biological tissues

2.2.2 Compton profile

Biological materials are composed mainly of low atomic number materials and the values of coherent cross-section reduce drastically at large scattering angles which means that long acquisition times or high dose rates are required to obtain sufficient counts in the coherent peak of the spectrum for sufficient accuracy. The count rate is not such a problem in the Compton region. The Compton profile shape is sensitive to the chemical composition of the scatterer and is already used in molecular and solid state physics to

determine the electron density of the scatterer (Williams 1977). The incoherently scattered gamma radiation is effectively Doppler broadened because of the momentum of the target electrons. The resulting Compton profile shape represents a momentum distribution of the electrons which is independent of the atomic number of the scatterer or target.

Holt *et al* (1983) investigated the use of the profile shape for *in vitro* analysis. Using a Compton spectrometer they made measurements on small volumes (1.3 ml and 0.5 ml) of saline solutions of varying concentration, breast cyst fluid and rat livers. Compton scattering of americium-241 gamma rays through a fixed angle of 171° was measured. At this angle the energy transfer to the target electrons is around 12 keV so the Compton and coherent peaks are well separated, which facilitated the Compton profile analysis. The Compton profile shape obtained for each material was normalised to equal area under the curve and a difference of seven per cent was then found between the height of the profiles obtained from breast cyst fluid and saline (the characteristic line shape of the breast cyst fluid was narrower). Similarly the profiles obtained from samples of rat livers demonstrated a difference of six per cent compared with saline. A difference of three per cent in the Compton peak value was found between rat liver treated with phenobarbitone and untreated liver samples once the spectra had been normalised to equal area.

This report presents the result of an investigation into the measurement of the Compton profile width as a means of determining fat content or bone mineral composition. The full widths at half maximum (FWHM) of the Compton peaks have been determined as a measure of profile shape. Tartari (1996) has suggested that the full width third maximum (FW1/3M) or full width quarter maximum (FW1/4M) may be better measurement methods. In the region close to the Compton peak the magnitude and shape of the distribution is mainly due to the interaction between the incident photons and the outermost atomic electrons (see Section 2.1.3). Williams (1977) postulated that the momentum distribution of the outermost atomic electrons might be affected by chemical bonds. The Compton distribution in the high and low energy regions (each side of the Compton peak) corresponds to high values of momentum transfer and is not influenced by the chemical environment. Tartari *et al* (1992) demonstrated that these outer regions represent the atomic binding energy of the core electrons and thus the atomic number of the material under investigation. Consequently, the FW1/3M or the FW1/4M may be more sensitive to composition than the FWHM.

The energy broadening of Compton scattered photons was first investigated thoroughly by Dumond (1933). He reported that the effect of an atomic electron's motion on the Compton scattering process could be described as a Doppler broadening mechanism. The precise analogy pursued by Dumond was that of the reflection of light from a moving mirror. Although later quantum mechanical calculations became more accurate an approximate indication of likely differences in Compton profile width may be extrapolated from Dumond's 1933 paper.

If light is reflected from a mirror moving towards an observer with velocity υ the wavelength change $\Delta\lambda/\lambda$ is $(2\upsilon/c)\cos\theta$, provided that $\Delta\lambda/\lambda << 1$. ($c$ is the velocity of light and θ is the angle between the incident and reflected light.) Then for a backscatter situation $\Delta\lambda/\lambda = 2\upsilon/c$. In Dumond's analogy the moving electron is the moving mirror. In the extreme the electron may move either toward or away from the observer (detector) and the maximum width of a backscattered Compton line is $4\upsilon\lambda/c$.

In the same paper Dumond reported spectrographic measurements on carbon (graphite) using molybdenum K_α radiation as the source. From the profile of the broadened Compton line he derived the momentum distribution in units of υ/c (see Figure 2.3). In his results the peak of the momentum distribution corresponds approximately to the half height of the Compton profile. This peak is at a value of υ/c = 0.0082, which is somewhat higher than the calculated momentum distribution maximum, which occurs at υ/c= 0.005. The momentum of the electrons in the L shell orbits dominates the calculated value. The distribution of the higher momentum K shell electrons has a much lower maximum than for the L shell electrons. These higher momentum electrons are responsible for broadening the tail of the Compton profile.

To ascertain whether or not it is worth exploring the broadening of the Compton profile to distinguish between different tissues such as muscle and fat, an indication of the differences in momentum distributions for different tissues would be useful. An approximate approach is to look at information regarding carbon and oxygen. Muscle consists of about 70 per cent oxygen and fat about 60 per cent carbon. In Bohr's atomic theory the kinetic energy of an electron in orbit is numerically equal to its binding energy (Richtmyer *et al* 1955). For carbon the L shell electrons contribute most to the broadening of the Compton profile at full width half maximum. The binding energy of the L shell electrons of carbon is reported as 5 eV (Kaye and Laby 1978) which corresponds to a value

of υ/c = 0.0044. Dumond theoretically computed a momentum distribution for carbon atoms with a maximum value for υ/c = 0.005 and measured it in graphite to be 0.0082.

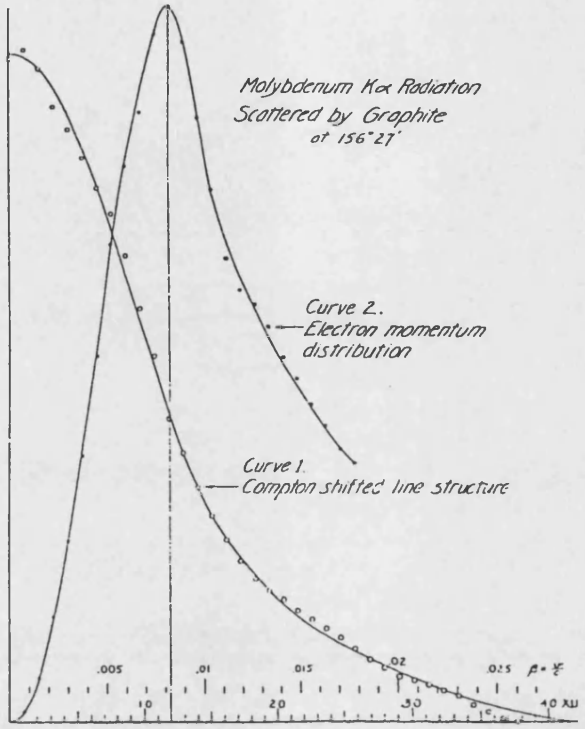

Figure 2.3 Half profile of a typical modified line structure after application of all corrections and the resulting derived electron momentum distribution. On the abscissa the units for the line structure are in xu (=10^{-13} m) and for the momentum distribution are in $\beta = \upsilon/c$. The momentum is $p = m\beta c$ (Dumond 1933).

Oxygen has two more L shell electrons than carbon and may be expected to behave similarly to carbon with respect to incident high-energy photons. The binding energy of the L shell electrons is a little higher at 8 eV, which corresponds to a value of υ/c = 0.0056. Using this approximation oxygen would appear to have a momentum distribution with its maximum about 30 per cent higher than carbon. If Dumond's measured maximum value of υ/c for carbon of 0.0082 is taken, then the maximum value for oxygen would be about 0.0104.

Using these values the relative widths of the Compton profiles for carbon and oxygen may be estimated. For an americium-241 gamma source of energy 59.54 keV and 150° backscatter the Compton peak occurs at 48.9 keV (λ=25.4 pm). For carbon the width of

the Compton line $(4\lambda\upsilon/c)$ would be $4\times25.4\times0.0082=0.833$ pm. At 48.9 keV this is equivalent to a Compton profile width of 1.60 keV. Similarly, using the estimated maximum value of the momentum distribution for oxygen (υ/c = 0.0104), the width of the line would be $4\times25.4\times0.0104=1.06$ pm. For a Compton peak of 48.9 keV this is equivalent to 2.03 keV. The estimated difference in the maxima of the electron momentum distributions suggests that a difference of 430 eV in line width could be expected. The two tissues muscle and fat, which have high oxygen and carbon contents respectively, would be expected to have a smaller difference in the width of their Compton lines at this energy. However, the result of this approximation is an encouragement to investigate the Compton profile width further as an indicator of tissue composition.

The above considerations are based solely on the Doppler broadening of the Compton line (by electrons in motion). The other effect on the Compton profile in a real situation is multiple scatter in the volume of the tissue irradiated for the measurement. This aspect is considered next.

2.2.3 Compton profile ratios

Dumond (1933) examined the shape of the Compton profile, and found that multiple scatter distorted the shape of the profile. Hence an accurate determination of the electron momentum distribution requires the use of very thin targets. Other workers (MacKenzie 1990 and Tartari *et al* 1992) have suggested the use of a different ratio employing the high energy tail of the Compton profile. They suggest this would overcome the problems of small count rates in the coherent region and also the multiple scattered information. MacKenzie (1990) found that when this technique was used with thick targets the Compton profile was distorted, but that the distortion was confined almost entirely to the low energy side of the profile. The analysis is similar to the coherent to Compton scattering ratio analysis but is not restricted by the coherent scattering process being very weak for low atomic number (biological) materials. He has demonstrated that the ratio of counts from thick and thin aluminium targets (20 mm and 3 mm) is close to unity on each side of the Compton peak. However, for thick targets of different low atomic number materials the ratio is close to unity on the low energy side but deviates far from unity on the high energy side. This demonstrates that multiple scattering masks the difference in profile shape on the low energy side but the profile shape differences are retained on the

high energy side. MacKenzie (1990) suggested the term Dumond spectroscopy for this type of analysis.

Based on this work, using americium-241 as the photon source, MacKenzie suggested the use of a ratio HP to characterise the Compton profile shape by the high momentum fraction i.e. the ratio of the counts in the high energy tail to those in the whole Compton profile:

$$HP = \sum_{\varepsilon=52}^{58} n(\varepsilon) \Big/ \sum_{\varepsilon=40}^{58} n(\varepsilon) \qquad \textbf{Equation 2.10}$$

where ε is the photon energy in keV.

Tartari *et al* (1991) used Monte Carlo procedures to calculate the multiple scatter and single scatter components of the Compton distribution. These calculations demonstrated that comparing the multiple scatter intensity for a small scattering angle with a backscattering geometry, the multiple scatter tends to concentrate itself under the single scatter peak distribution which shifts towards lower energies as the scatter angle increases. These calculations also demonstrated that single scattering dominates in the energy region just below the coherent peak, especially for incident energies less than 100 keV and scattering angles of 120° or greater.

Williams (1977) attributed the shape of the Compton profile in the region close to the peak maximum to be due mainly to the interaction of the incident photons with the outermost atomic electrons, whose momentum may be affected by chemical bonds. Tartari *et al* (1992) suggested that the high and low energy regions of the Compton profile correspond to high values of momentum transfer and are not influenced by the chemical environment. The Compton distribution in these regions will therefore represent the atomic binding energy of the core electrons and thus the element atomic number. Further use of the Monte Carlo code (Tartari *et al* 1992) for large water cylinders (100 mm diameter and length) demonstrated that the double scatter component peaked close to the maximum of the single scattered Compton photons. The triple and high order scattering were of less intensity and broadened toward the low energy region.

The free electron model gives a sharply bounded distribution between the energy interval E_1 and E_2 defined below for incident energy E_0 and scattering angle θ:

$$E_1 = \left[\frac{1}{E_0} + 2(1+\cos(\theta/2))/m_e c^2 \right]^{-1} \qquad \textbf{Equation 2.11}$$

$$E_2 = \left[\frac{1}{E_0} + 2(1-\cos(\theta/2))/m_e c^2 \right]^{-1} \qquad \textbf{Equation 2.12}$$

The second scattering is affected by the electron bonds so the edges of the doubly scattered distribution are rounded off. The high energy side of the doubly scattered distribution falls below the singly scattered one so the shape is still representative of the target atomic number. The total distribution between E_2 and the coherent peak will be the sum of the singly scattered Compton component with part of the doubly scattered component but the third and higher order scattering will be negligible (Tartari *et al* 1991). Since the high energy side of the Compton profile is unaffected by multiple scatter it could be used to characterise the fat, soft tissue or bone mineral content of the target material.

On the basis of the above work Tartari *et al* (1992) examined the effectiveness of the ratio of the area between different limits of the high energy tail and the area in the energy region of the singly scattered Compton distribution. They concluded that there was only an advantage in using the high-energy tail in determining a ratio as a means of characterisation when the coherent peak is not easily measurable. If the fat content of the target is high the large amount of low atomic number materials gives poor counting statistics in the coherent region. For this situation Tartari *et al* (1992) proposed a ratio:

$$R_k = \sum_{\varepsilon=\delta\varepsilon} n(\varepsilon) \Big/ \sum_{\varepsilon=40}^{56} n(\varepsilon) \qquad \textbf{Equation 2.13}$$

where $\delta\varepsilon$ is the energy interval in the high energy Compton profile.

2.3 Summary

In this chapter the theoretical background to the measurable parameters of a photon backscattering technique using americium-241 has been examined. It has been shown that the coherent to Compton scattering ratio distinguishes well between cortical bone, trabecular bone and soft tissue, but less well between adipose and muscle tissue, where also the coherent signal will be small.

From an approximate classical review of Doppler broadening of the Compton line which might be expected from the motion of outer shell electrons, there would appear to be significant differences between the expected broadening due to oxygen and carbon. This difference in broadening might make this a useful technique to distinguish between adipose and muscle tissue.

Finally the reasons suggested by MacKenzie (1990) and Tartari *et al* (1992) in advocating using a ratio of the high energy part of the Compton profile to the total Compton profile have been reviewed. Their reasoning is that the high energy part of the Compton profile is less influenced than the lower energies by the presence of multiple scatter.

In the following chapters all three techniques are explored for their potential to obtain useful information about fat fraction and bone density.

Chapter 3 Experimental details

An experimental arrangement is required to investigate both coherent and Compton scattering as a means of distinguishing between fat and muscle and to measure bone mineral density in an *in vivo* application. The aim is to obtain a measurement with diagnostic precision whilst delivering the minimum possible radiation dose to the patient.

The essential items required for scattering experiments are a source of photons, beam collimation and a suitable photon detector with associated electronics. To improve the ease of set-up in a clinical application a backscattering technique has been investigated. This has the advantage that the coherent and Compton peaks are well resolved at the expense of a low coherent count rate. Different sample materials have been used as substitutes for the biological tissues of interest.

3.1 Radionuclide source

In order to have a measurable coherent scattering signal from biological materials it is necessary to limit the photon energy to less than or equal to 100 keV as the coherent signal decreases markedly above this energy. To give adequate penetration in tissue there is a lower energy limit of 20 to 30 keV. For a clinical application it would be necessary to have a photon flux sufficiently high to keep the measurement time to 15 minutes or less. A long half-life would be beneficial in maintaining a high photon flux with time and eliminating the need to replace the source on a regular basis, which would also keep the cost down. A monoenergetic source of appropriate energy would mean that maximum benefit was obtained from the radiation dose to the patient.

Americium-241 has been widely used in coherent to Compton scattering experiments to investigate bone mineral density (Stalp and Mazess 1980, Ling *et al* 1982, Karellas *et al* 1983, Gigante and Sciuti 1985, Shukla *et al* 1986, Ndlovu *et al* 1991, Tartari *et al* 1992, 1994, Singh *et al* 1997). Karellas *et al* (1983) increased the photon flux by using six 7.4 GBq sources in a line to give an approximate photon output of 3.3×10^8 photons per second per steradian. This enabled clinical trials to be performed with a measurement time of about 15 minutes (Shukla *et al* 1985, 1986). Gigante and Sciuti (1985) used a source of 7.4 GBq and made data collections in 400 seconds.

The radionuclide source used for the investigations reported here is 7.4 GBq americium-241 incorporated in a ceramic bead sealed in a welded stainless steel capsule (Amersham AMC 26). A 7.4 GBq source is the highest activity that is available commercially as a single source. The main photon emission is at 59.54 keV with a line efficiency of 35.7%. The other photons emitted are of low energy (and therefore largely absorbed in the bead or capsule) or have a low line efficiency, making americium-241 effectively a monoenergetic photon source. It also has a long half-life (432.2 years) and is readily available.

The slow decay rate and high degree of self-absorption within the americium-241 itself due to its high atomic number (Z=95) limit the available photon flux. The manufacturer's specification of flux for the americium-241 source used here is 5.5×10^7 photons per second per steradian.

For a clinical set-up it is proposed that four 7.4 GBq americium-241 sources would be used, arranged in a ring around the detector. This would enable similar precision to be achieved as with a single source but with a reduction in acquisition time by a factor of four.

3.2 Detector and electronics

A high-resolution detector is necessary to discriminate between the coherent and Compton peaks in the scattered photon spectrum. The energy difference between the coherent and Compton peaks for an incident photon energy of 60 keV at a scattering angle of 150° is 10.6 keV. The best resolution achievable with a NaI (Tl) scintillation detector is around seven per cent at 662 keV gamma-ray from caesium-137, which corresponds to a resolution of around 15 keV for an incident photon energy of 60 keV. The energy resolution is dependent on the number of information carriers produced by a radiation interaction. Scintillation detectors are very inefficient in converting the incident radiation into light and then to an electrical signal and the statistical fluctuations in the small number of carriers limit the energy resolution that can be achieved. This resolution would not be sufficient for resolving the coherent and Compton peaks, or allow investigation of the Compton profile.

A better energy resolution is achieved by using semiconductor materials as radiation detectors, which give the largest number of information carriers per pulse for a given

incident radiation event. The information carriers are electron-hole pairs, which are created along the path taken by the charged particle through the detector. The motion of the electron hole pair in an applied electric field generates the basic electrical signal from the detector.

The detector used for these investigations is a high purity germanium detector (HPGe) (EG&G Ortec, Model GLP-32355/100-P-S) with a detection volume of 32 mm diameter and 10 mm thick. It is fitted with a thin (0.254 mm) beryllium front window, which allows photons with energies down to 3 keV to enter the active volume. Its upper limit of operation is 300 keV. The energy resolution is quoted as 355 eV full width half maximum (FWHM) at 5.9 keV and 580 eV FWHM at 122 keV.

The detector crystal is predominantly P-type HPGe with a front face of Li diffused N^+ contact with an ion-implanted contact on the rear face. It is operated with a bias voltage of -1500 volts applied between the N^+ contact and the ion implanted (P^+) contact. This ensures that the detector is fully depleted and the active volume of the detector extends from one contact to the other. The detector is operated at liquid nitrogen temperature. This is to reduce the thermal generation of electron-hole pairs within the depletion region since in germanium there is only a small energy gap (less than 1 eV) between the valence and conduction bands.

When the detector is in operation photons incident on the crystal will interact within the depletion region and create electron-hole pairs. The number of electron-hole pairs created will depend on the energy deposited by the incident photons. Under the influence of the applied voltage the electron-hole pairs will move toward the end contacts and then to a charge sensitive preamplifier. The "front end" of the preamplifier is cryogenically cooled to achieve the lowest electronic noise and optimum energy resolution. The "front end" includes an input field effect transistor and the feedback element of the charge sensitive preamplifier. The preamplifier converts the signal received into a voltage pulse. The pulse height is proportional to energy.

The associated electronics for the detector are shown in Figure 3.1. The bias voltage to the detector was supplied by an Ortec 459 bias supply. The signal from the preamplifier was fed to an amplifier (Ortec 572) and then to an analogue to digital converter (ND582 ADC). The output from the ADC was fed to an EG&G Ortec multi-channel analyser for pulse

processing. The output was displayed in real time on a personal computer. The data acquired were converted into ASCII format and then further analysed using Microsoft Excel software.

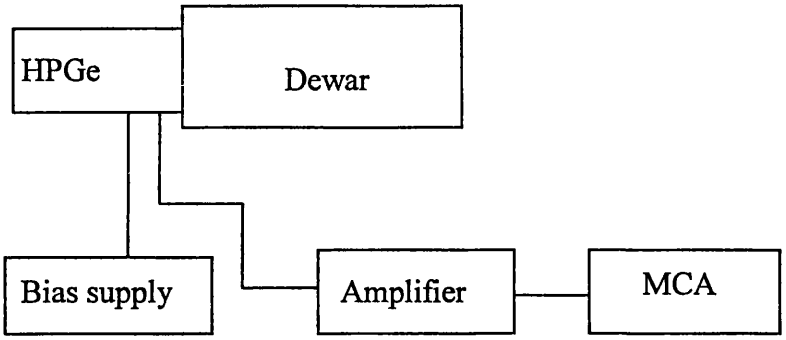

Figure 3.1 Schematic representation of detector and electronics

3.2.1 Detector efficiency

The intrinsic (full-energy) efficiency of the detector is the probability that a photon of a given energy incident on the front contact of the detector element will be completely absorbed by the detector element itself. The published efficiency for the detector used in these measurements is reproduced in Figure 3.2. It demonstrates that for the 10 mm thick detector element used for the investigations reported here, the intrinsic full-energy efficiency is 100 per cent for photon energies between 30 and 70 keV. For these investigations using an americium-241 source, only a narrow range of energies are of interest. The energy range extends from 40 keV to the coherent peak at 59.54 keV, which is well within the 100 per cent efficiency limit of the detector.

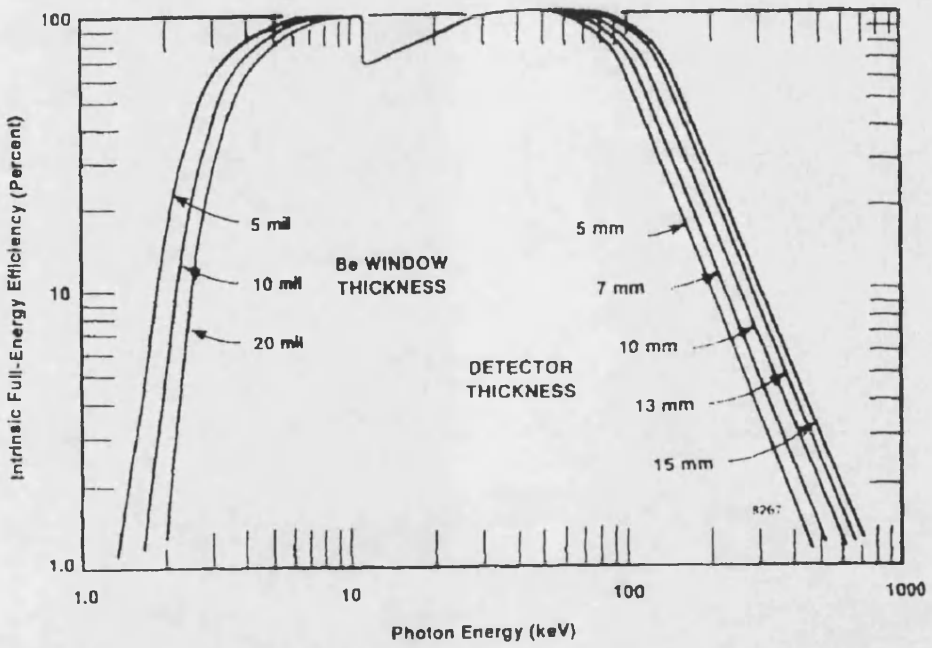

Figure 3.2 **Variation of intrinsic full-energy efficiency with energy for GLP detector as a function of Be window thickness and detector thickness (EG&G Ortec catalogue)**

3.2.2 Detector energy resolution

The quoted energy resolution for the detector is 355 eV full width half maximum (FWHM) at 5.9 keV and 580 eV FWHM at 122 keV for a pulse shaping time τ of 6 μs. The pulse shaping time is chosen to avoid pulse pile-up and tail pile-up. These effects occur when the count rate is sufficiently high that incoming pulses overlap. Tail pile-up occurs when there is superposition of a pulse on the tail of a preceding pulse. The effect on the measurement is to worsen the resolution by adding wings to the recorded peaks in the pulse height spectra. Pulse pile-up occurs when two closely spaced signal pulses combine to form one distorted pulse. This type of pile-up causes distortions in the recorded spectrum and interferes with measurements based on determining the area under full-energy peaks. Knoll (1979) recommends using a duty cycle of less than 10^{-3} to minimise these effects, which are related to count rate. The duty cycle is the product of the pulse shaping time τ and the count rate. For a count rate of 1000 counts per second, the pulse shaping time would need to be 1 μs to meet this criterion.

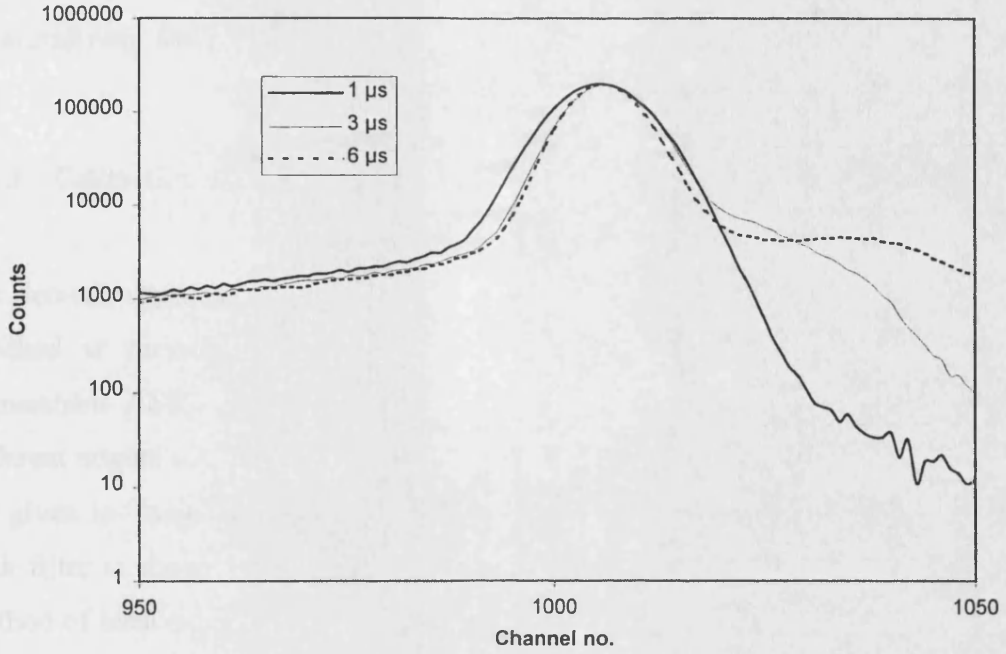

Figure 3.3 Semi-log plot of americium-241 peak to demonstrate effect of pulse shaping time for count rate of 850 counts per second

Figure 3.3 shows the effect of the pulse shaping time on the coherent peak of an americium-241 source for a count rate of 850 counts per second. A logarithmic scale has been used on the ordinate to demonstrate the effect of the pulse shaping time on resolution and tail pile-up more clearly. The energy resolution given by the FWHMs for the three different pulse shaping times τ at 59.54 keV are 709 eV for 1 µs, 606 eV for 3 µs and 548 eV for 6 µs. For the 1 µs pulse shaping time the energy resolution is not as good as the resolution for the longer times examined but the effect of tail pile-up is minimised. In the investigations reported here the main area of interest is the Compton profile and the count rate in the Compton peak will be much greater than that in the coherent peak. The investigations will examine the high-energy tail of the Compton peak and it will be important to minimise the effect of tail pile-up, which could otherwise distort the Compton profile shape at the high-energy end. Since a scattering angle of 150° is used there is good separation of the coherent and Compton peaks so the increased width of the coherent peak with the shorter pulse shaping time should not present a problem. At higher count rates the effect of tail pile-up would be more marked. A pulse shaping time of 1 µs was used for all the investigations described in this report. The measured resolution of the system for a pulse shaping time of 1 µs is 709 eV FWHM at 59.54 keV for an americium-241 source (i.e. 1.2%). The peak shape is defined as the ratio of full width tenth maximum (FWTM)

to the FWHM. The theoretical Gaussian peak has a FWTM/FWHM ratio of 1.83; the measured ratio for the americium-241 peak was quite close to this value at 1.87.

3.2.3 Calibration and linearity of the detection system

The detection system was calibrated against an americium-241 source and the linearity was checked at periodic intervals using an americium-241 variable energy x-ray source (Amersham AMC 2084). This employed an americium-241 source in front of which different targets could be positioned to generate different energy spectral lines. The details are given in Table 3.1. A plot of channel number in which the peak count occurred for each filter is shown in Figure 3.4. A straight line has been fitted to the data using the method of least squares, giving the offset and slope for the calibration of the system. The coefficient of determination R^2 was also calculated. This coefficient is derived from

$$R^2 = 1 - \frac{SSE}{SST} \qquad \textbf{Equation 3.1}$$

where *SSE* is the squared difference between the actual and estimated y value, the residual sum of squares, and

SST is the sum of the squared difference between actual y values and average of y values, the total sum of squares.

The smaller the residual sum of squares is compared with the total sum of squares the larger the value of the coefficient of determination which indicates how well the equation resulting from the regression analysis fits the data. The coefficient of determination R^2 was 0.9999.

Table 3.1 Targets and energies of characteristic x-ray emissions from americium-241 variable energy x-ray source (Amersham)

Target	Energy, keV	
	K_α	K_β
copper	8.04	8.91
rubidium	13.37	14.97
molybdenum	17.44	19.63
silver	22.10	24.99
barium	32.06	36.55
terbium	44.23	50.65

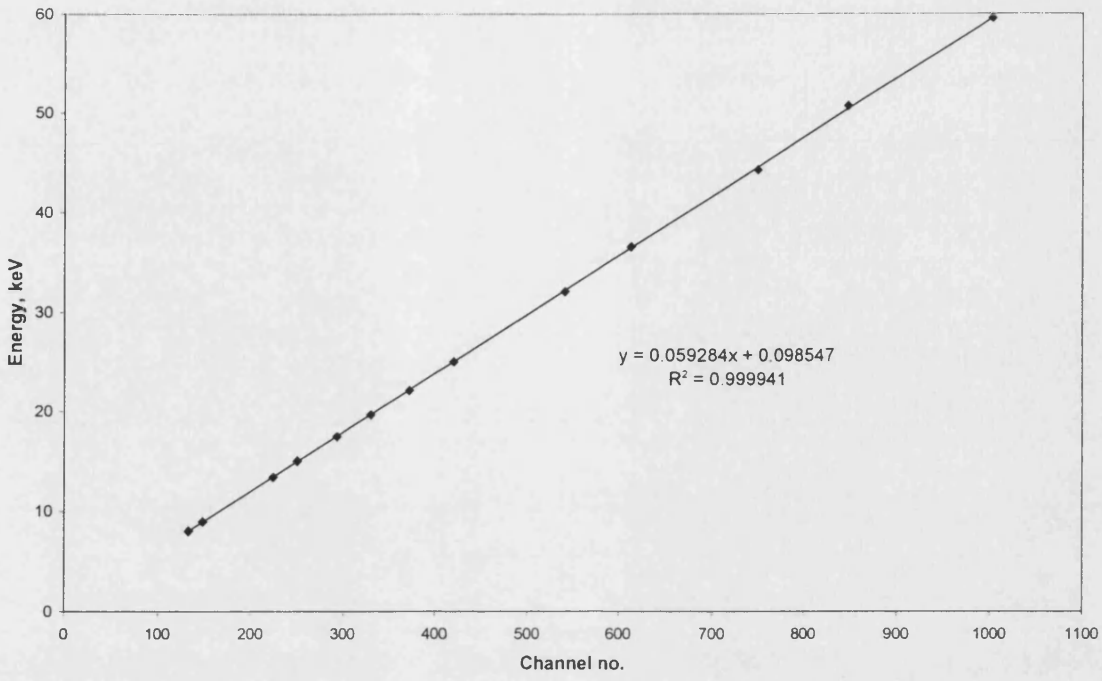

Figure 3.1 Linearity of detection system measured with variable energy americium-241 x-ray source

3.3 Collimation of source and detector

The source is housed in a lead sheath with a collimator of 5 mm diameter aperture and 55 mm in length. This gives an irradiation cone with a radius of 6 mm at the source-detector focus, i.e. the intersection of the source and detector axes (see Figure 3.5).

A steel sleeve with an aperture of 5 mm, 10 mm or 40 mm diameter surrounds the detector head. The thickness of the steel was 10 mm around the sides of the detector and 20 mm over the front face. The 5 mm and 10 mm diameter apertures were parallel sided whilst the largest aperture converged to the rear face of the active element of the detector. These apertures correspond to acceptance angles for the scattered radiation arriving at the detector of 8°, 16° and 56° respectively.

The source in its sheath is positioned at an angle of 30° to the detector by means of a machined lead housing. The backscatter geometry necessitates that the source is alongside the detector and the physical size of the detector limits the proximity of the source-detector focus. For this experimental set-up the source-detector focus is at 120 mm from the front

face of the detector collimator. The machined lead housing was necessary to prevent radiation from the americium-241 source reaching the detector directly.

The dimensions of the apertures in the source and detector collimators determine the volume of the sample from which information is obtained. At the focus the diameter of the sample irradiated by the collimated americium-241 source was around 12 mm ignoring penumbra. The apertures in the detector collimator were chosen to limit the diameter of the sample from which information was collected. The 5 mm diameter aperture gave an acceptance cone of 21 mm diameter and the 10 mm diameter gave an acceptance cone of 42 mm diameter at the focus. The 40 mm diameter only served to shield the sides of the detector element and allowed the whole of the front face of the crystal to be used, an acceptance cone of around 76 mm diameter at the focus.

The volume of interest has been approximated to a cylinder, where the radius of the cylinder is the radius of the radiation beam at the focus and the cylinder height is determined from the diameter of the detector cone of acceptance at the focus. This is shown schematically in Figure 3.5 and the volumes are tabulated in Table 3.2.

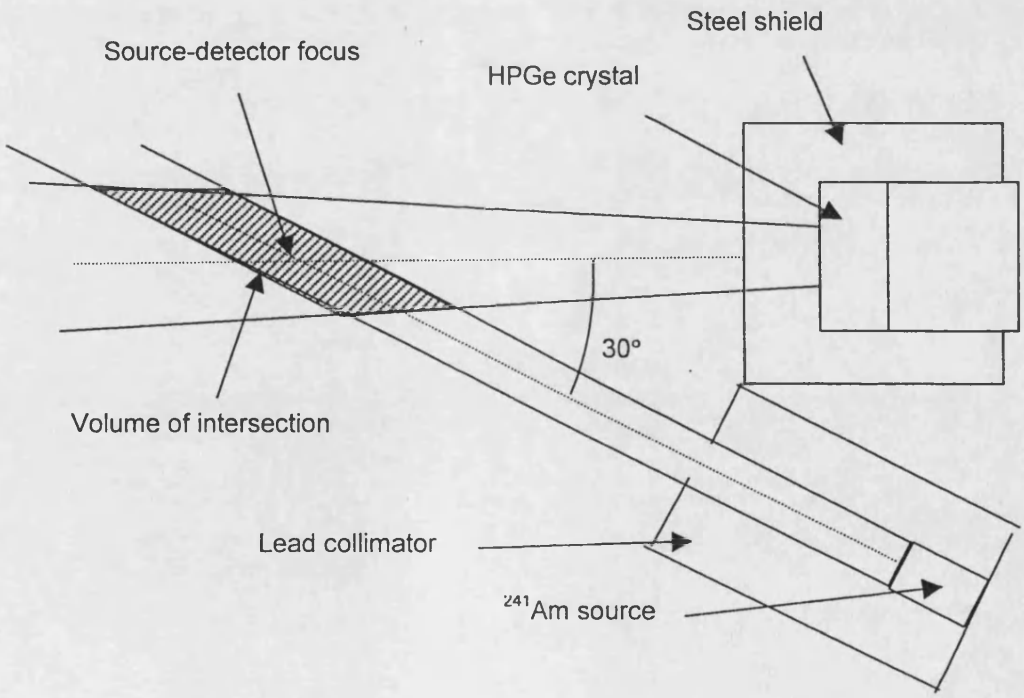

Figure 3.5 Schematic representation of volume of interest

For phantoms with a diameter less than the diameter of the detector acceptance cone at the focus the cylinder height will be defined by the diameter of the phantom. The resulting volumes for these circumstances are given in Table 3.3.

Table 3.2 Volume of interest for different detector apertures

Detector aperture dia. mm	Diameter at focus, mm	Volume of interest, mm^3
5	21	4800
10	42	9600
40	76	17100

Table 3.3 Volume of interest for different phantom diameters

Detector aperture dia., mm	Phantom diameter, mm	Volume of interest, mm^3
40	38	4000
40	55	5800
40	75	7900

3.4 Substitutes for biological tissues

Both solids and liquids have been used as substitutes for biological tissues, depending on the investigation. For the target volume investigations described in the next chapter slabs of epoxy resin material were used so that the depth of sample could be easily varied. For the fat and lean tissue (muscle) investigations liquids were used so that they could be mixed to produce different concentrations. Similarly liquids of different concentrations were used for the bone mineral investigations to represent different bone mineral densities. The compositions of the biological tissues are given in Table 3.4.

Table 3.4 Recommended elemental composition and density of selected body tissues (ICRU Report 44 1989)

Tissue	Elemental composition (percentage by mass)					Density, kg m^{-3}
	H	C	N	O	Others	
Adipose tissue	11.4	59.8	0.7	27.8	0.1Na, 0.1 S, 0.3 Cl, 0.2 K, 0.1 Fe	950
Muscle (skeletal)	10.2	14.3	3.4	71.0	0.1 Na, 0.2 P, 0.3 S,0.1 CL, 0.4 K	1050
Skeleton cortical bone	3.4	15.5	4.2	43.5	0.1 Na, 0.2 Mg, 10.3 P, 0.3 S, 22.5 Ca	1920
Skeleton spongiosa	8.5	40.4	2.8	36.7	0.1 Na, 0.1 Mg, 3.4 P, 0.2 S, 0.2 Cl, 0.1 K, 7.4 Ca, 0.1 Fe,	1180

3.4.1 Substitutes for fat and lean tissue

Adipose tissue and skeletal muscle have been taken as the standards for fat and lean tissue. Various materials have been used as substitutes in phantoms. Shypailo *et al* (1998) made whole body phantoms with anthropomorphic shaped skeletons to evaluate DEXA measurements. The phantoms utilised a 0.6% solution of NaCl in water to represent lean tissue and polyethylene overlays to substitute excess body fat. Nord and Payne (1990) proposed the use of stearic acid for 100 per cent fat and pure water for fat free material in an effort to standardise DEXA measurements. Kelly *et al* (1998) found that water appears slightly fatty to x-rays having an apparent fat content of 8.6% but used these two standards to develop a calibration step phantom out of acrylic and acrylic/aluminium combinations where the acrylic represented 68 per cent fat. Nord (1998) used a combination of acrylic and PVC sheets to simulate soft tissue compositions of up to 46 per cent fat. Oldroyd *et al* (1998) designed a total body phantom for DEXA, which utilised aluminium to represent the skeleton, and polythene containers 0.6 cm thick filled with distilled water, to represent fat and lean tissue respectively.

The target volume investigations described in the next chapter used slabs of epoxy resin water substitute phantom (SXR) which had been formulated specially for radiotherapy

dosimetry for energies up to 150 keV (Putney 1996) based on work by White *et al* (1977). The elemental composition (per cent by mass) is:

H: 8.32%, C: 68.1%, N: 2.38%, O: 19.11%, Cl: 0.14%, Ca: 1.92%

This composition is similar to that for adipose tissue but the presence of calcium and chlorine produce a higher effective atomic number than for fat.

For the fat fraction studies reported here distilled water has been used to represent lean tissue as for the DEXA studies mentioned above and ethanol has been used to represent fat. Two liquids were chosen so that they could be mixed together to produce solutions of different fat fraction if required. Some experiments were performed with a block of lard in order to validate the ethanol measurements. The elemental compositions (percentage by mass) of water and ethanol are:

Water (H_2O) : 11.1% H, 88.9% O

Ethanol (C_2H_5OH) : 13.0% H, 52.2% C, and 34.8% O

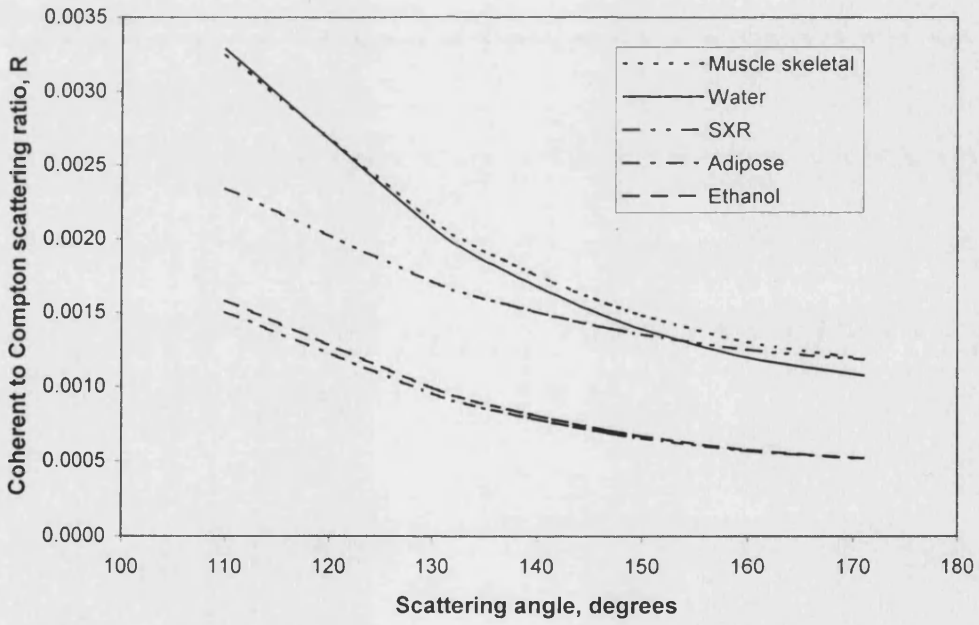

Figure 3.1 Calculated coherent to Compton scattering ratios for adipose tissue (fat), skeletal muscle (lean) and substitutes for incident energy 59.54 keV

The values of atomic form factor and incoherent scattering function were derived from data published by Hubbell *et al* (1975) in order to compute the coherent to Compton scattering ratios for a range of scattering angles for comparison with those expected from

adipose and skeletal muscle. As can be seen from Figure 3.6, the epoxy resin (SXR) is similar to water over the range of 140° to 170° scattering angle, and the ethanol and water have very similar curves to adipose and skeletal muscle respectively.

3.4.2 Substitute for bone

Most workers investigating the effect of the coherent to Compton scattering ratio from trabecular bone have used phantoms containing aqueous solutions of potassium hydrogen phosphate (K_2HPO_4). Ling *et al* (1982) and Karellas *et al* (1983) used aqueous solutions of K_2HPO_4 of varying concentration to simulate trabecular bone as did Leichter *et al* (1984), Tartari *et al* (1994) and Singh *et al* (1997). Leichter *et al* (1985) also used calibration phantoms of bone ash suspended in white petrolatum in varying concentrations and found these to be more representative of trabecular bone. Gigante and Sciuti (1985) used suspensions of calcium phosphate ($Ca_3(PO_4)_2$) in glycerine as well as aqueous solutions of K_2HPO_4, and simulated soft tissue effects with 5 mm thick plexiglass sheet.

For these investigations solutions of K_2HPO_4 were made with distilled water, of varying concentration in the density range 1000 kg m^{-3} to 1500 kg m^{-3}, which includes the density of normal trabecular bone. These solutions are easy to make as K_2HPO_4 dissolves easily in water. The coherent to Compton scattering ratios have been determined for the different concentration solutions. They have been derived from the atomic form factor for coherent scattering and the incoherent scattering function as tabulated by Hubbell *et al* (1975) for an incident energy of 59.54 keV and also for spongiosa bone and cortical bone using the compositions recommended in ICRU 44 (1989). These values are shown graphically in Figure 3.7. The curves demonstrate the suitability of using different concentrations of K_2HPO_4 solution as substitutes for different bone densities.

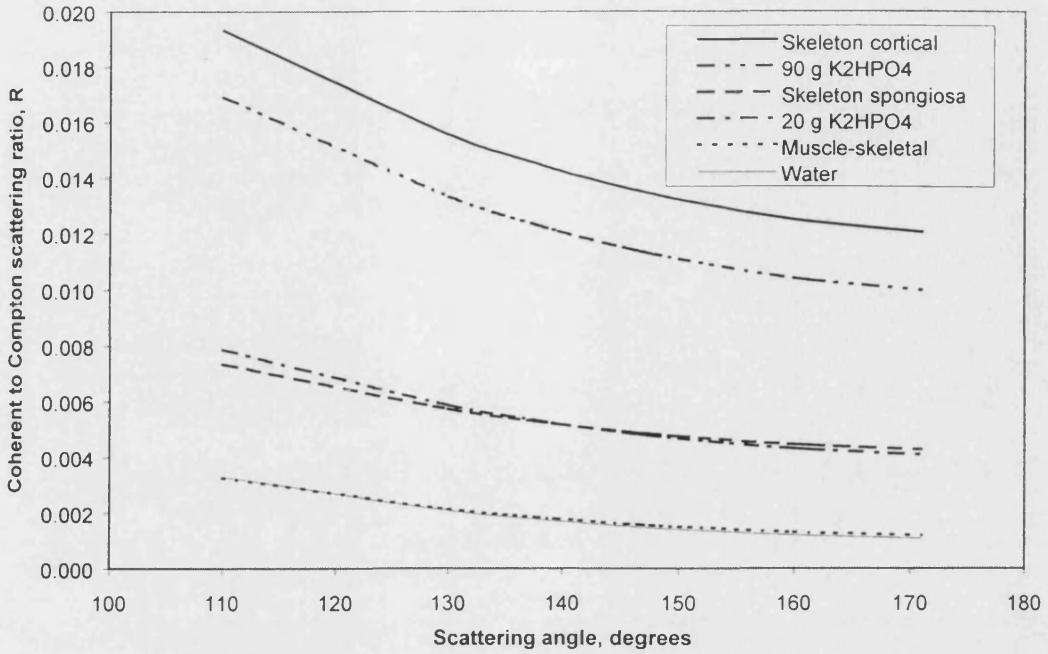

Figure 3.7 **Calculated coherent to Compton scattering ratios for bone, muscle and different concentration substitutes for 59.54 keV incident photons. (90 g and 20 g are the weights of K_2HPO_4 per 100 ml of water).**

Chapter 4 Target Volume Determination

4.1 Introduction

With the experimental set-up described in Chapter 3 and with extended tissue volumes it is necessary to know the origin of the scattered radiation. The intersection of the radiation beam cone from the 7.4 GBq americium-241 bead source and the acceptance angle of the detector will define a nominal target volume. For the investigations reported in this chapter the source collimator had an aperture of 5 mm diameter and the detector collimator aperture was 10 mm. The single scattered radiation detected will not all have been scattered through 150°, but from a range of backscattered angles between 130° and approaching 180°. Multiple scattered radiation will arise from a much wider range of angles. The material under investigation will attenuate some of the backscattered radiation.

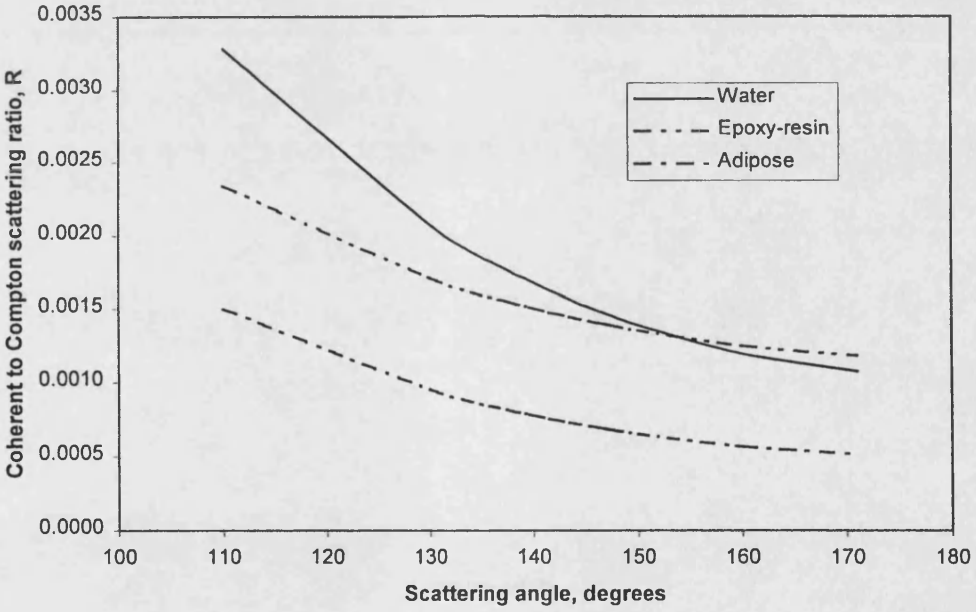

Figure 4.1 Variation of coherent to Compton scattering ratio R with scattering angle for water, adipose and epoxy-resin

An experiment was performed using slabs of the epoxy-resin water substitute phantom material (SXR) described in Chapter 3, Section 3.4.1. The composition is similar to that for adipose tissue but the presence of calcium and chlorine produce a higher effective atomic number than for fat. Figure 4.1 shows the variation of the calculated values of the

coherent to Compton scattering ratio with scattering angle in the range of interest for water, adipose and epoxy-resin. The values have been calculated using Equation 2.9 (Chapter 2) and tabulated values of the atomic form factor and the incoherent scattering function (Hubbell *et al* 1975). The figure demonstrates that the calculated coherent to Compton scattering ratio for the epoxy-resin phantom material is close to that for water for scattering angles between 140° and 170°.

4.2 Experimental method

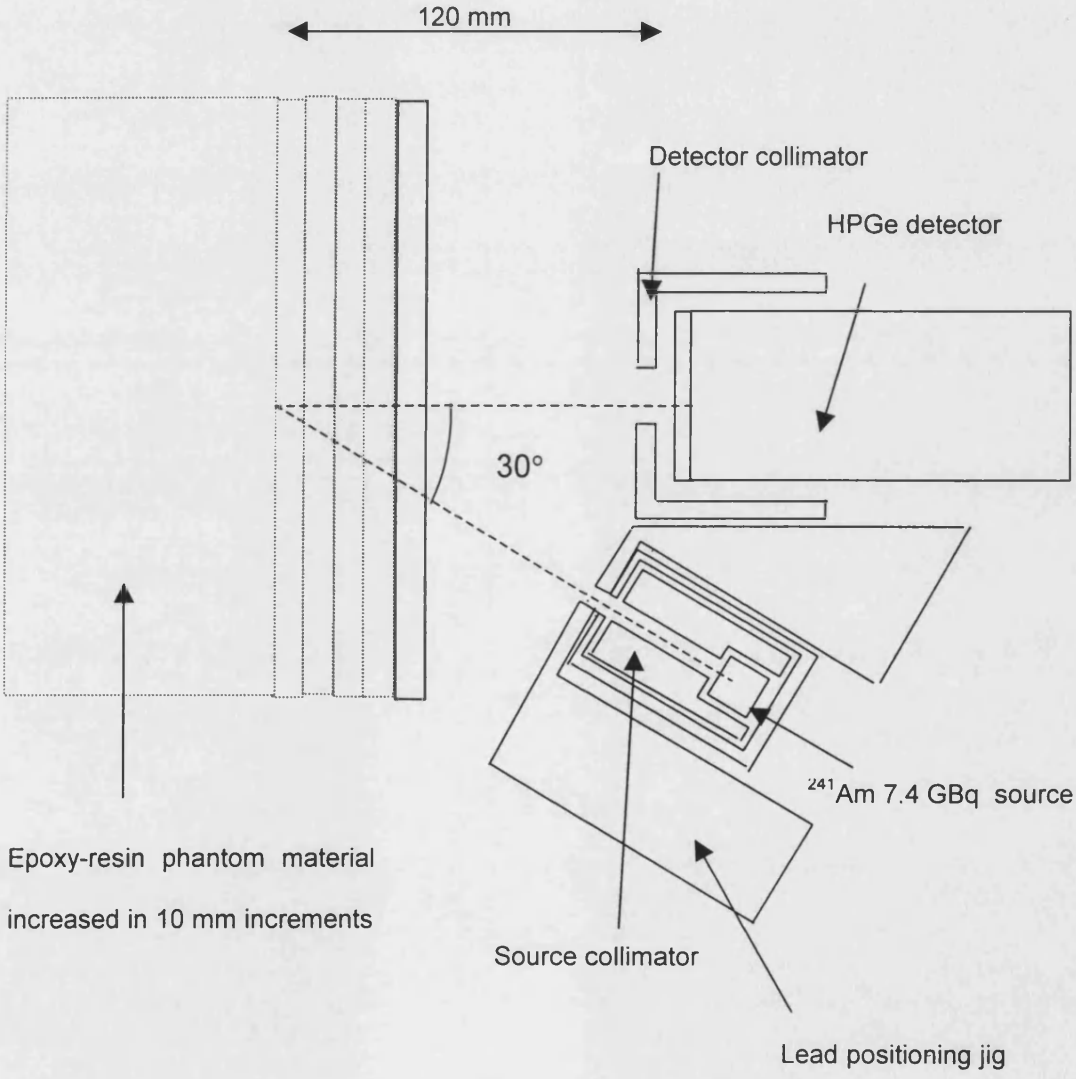

Figure 4.2 Experimental arrangement for target volume investigations

Using the equipment described in Chapter 3, the experiment was set up as shown in Figure 4.2. The epoxy-resin material was formed in slabs 300 mm × 300 mm square and 10 mm and 20 mm in thickness. Initially a 10 mm slab was positioned 50 mm in front of

the focus (intersection of central axes of radiation beam and detector). The thickness of the phantom was increased from 10 mm up to 110 mm in 10 mm steps and data were acquired for 24 hours for each step. Subsequently the experiment was repeated with the first 10 mm thick slab only 20 mm in front of the focus. A further data acquisition for 24 hours with no epoxy-resin slabs present was made to measure the background.

4.3 Results

After background subtraction the data from each acquisition were summed between 44 keV and 56 keV to give the total counts in the Compton region, and between 59 keV and 60 keV to give the total counts in the coherent region.

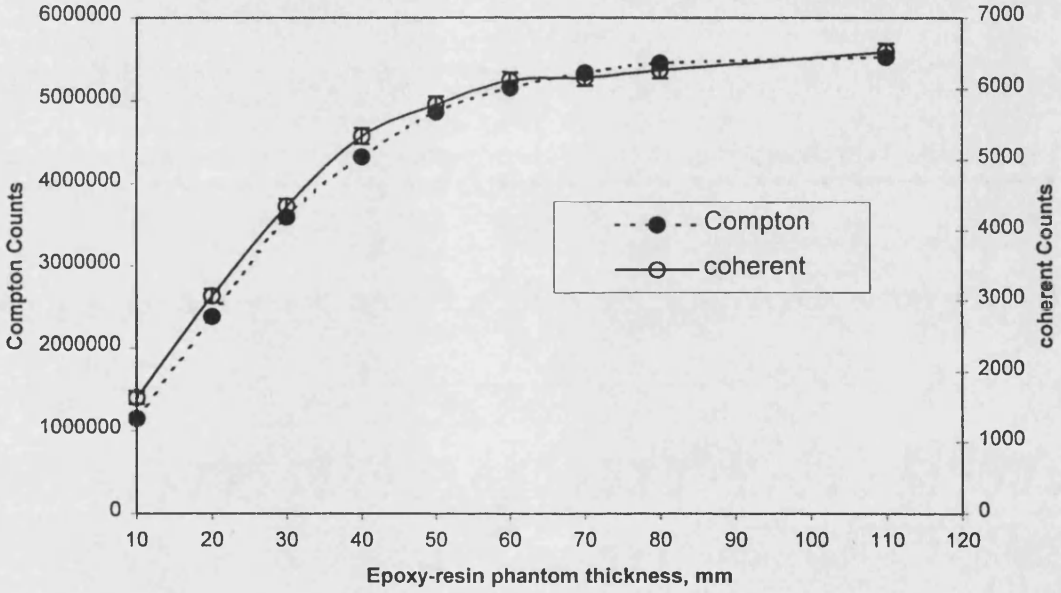

Figure 4.3 Compton and coherent counts for increasing phantom thickness (background subtracted)

Figure 4.3 shows the variation of the integrated count rates in both the Compton and coherent scatter peaks with phantom thickness, with the front surface of the phantom material at 50 mm in front of the focus. The uncertainty on the coherent count for the 10 mm thickness was ± 5 per cent due to counting statistics, but this improved to ± 2 per cent as the thickness of the phantom increased due to the increase in count rate. The uncertainty on the Compton count due to counting statistics was better than 0.05 per cent

for all phantom thicknesses investigated. The counts in both the Compton and coherent regions increased as the phantom thickness was increased up to 50 mm with a fairly uniform contribution from each of the first four 10 mm layers. There was little additional contribution beyond 60 mm of phantom thickness. Thus providing that the tissue is at least 50 mm in depth, over 90 per cent of both Compton and coherent scatter counts arise from the first 50 mm depth with the experimental geometry shown in Figure 4.2. For depths greater than 50 mm the count rate in both regions did not increase significantly.

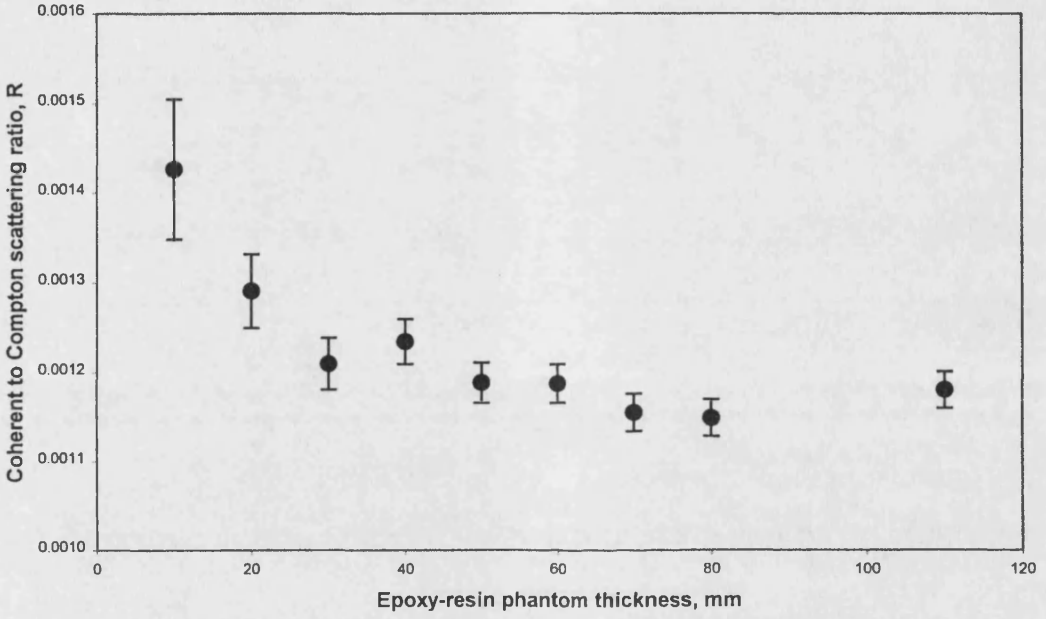

Figure 4.4 Variation of coherent to Compton scattering ratio R with thickness of phantom

The same integration ranges for the Compton and coherent counts with background subtracted were used to determine the coherent to Compton scattering ratios for the different depths of epoxy-resin material. These results are shown in Figure 4.4. The coherent to Compton scattering ratio decreases, showing that the equivalent scattering angle increases, with increasing phantom depth. The coherent to Compton scattering ratio reaches a constant value for a phantom depth of 50 mm or greater. This is as expected from the results of Figure 4.3, which shows that 90 per cent of the scattered counts arise from the first 50 mm depth. The higher values of coherent to Compton scattering ratio for depths of 10 mm and 20 mm result from the smaller angle of scatter at these depths of phantom. This is due to the coherent scatter rate decreasing more rapidly than the Compton scatter rate as the scattering angle increases. The measured values of coherent to

Compton scattering ratio for depths of 50 mm or greater represent an approximate average of the ratios in the first 50 mm depth of tissue.

The variation in the peak energy of the Compton profile with increasing phantom depth was also investigated. The results are shown in Figure 4.5. For a phantom depth of 10 mm the Compton peak occurred at 49.8 keV which equates to a backscatter angle of 133° (from Equation 2.3, Chapter 2). The Compton peak energy shifted to 49.5 keV for a phantom of 50 mm depth which equates to a backscatter angle of 138°. For greater depths the change in Compton peak energy was not so great; at 110 mm depth of phantom the Compton peak only shifted by a further 0.2 keV to 49.3 keV corresponding to a backscatter angle of 141.5°.

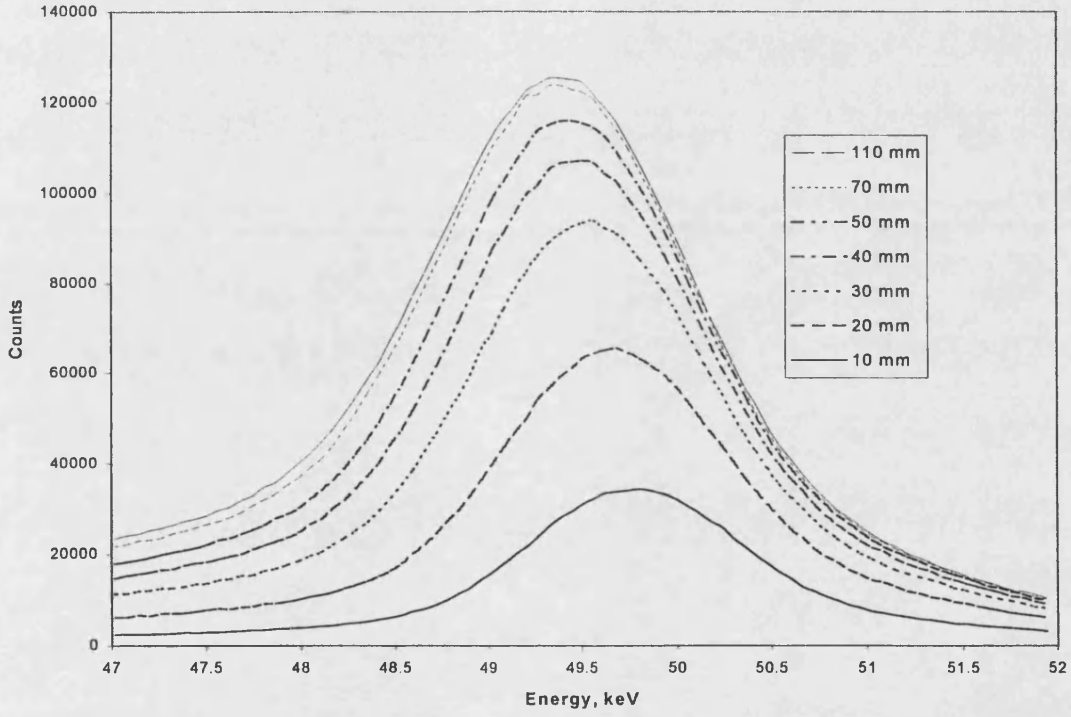

Figure 4.5 Compton profiles for increasing thickness of phantom to demonstrate shift in Compton peak energy

Although the geometry of the system is designed to detect scattered radiation at 150°, in the epoxy-resin phantom the energy of the Compton peak for depths of 50 mm or greater indicates that the equivalent backscatter angle is around 140°. This is due to the large size of the phantom and the large acceptance angle of the detector.

The effect of phantom depth on the Compton profile shape was also examined, by the measurement of the full width half maximum (FWHM) of the Compton profile. The results are shown in Figure 4.6 and demonstrate that the value of the FWHM increases with phantom depth up to a depth of 50 mm. Beyond 50 mm depth the FWHM increases only slowly up to 70 mm depth and then remains constant within experimental uncertainties.

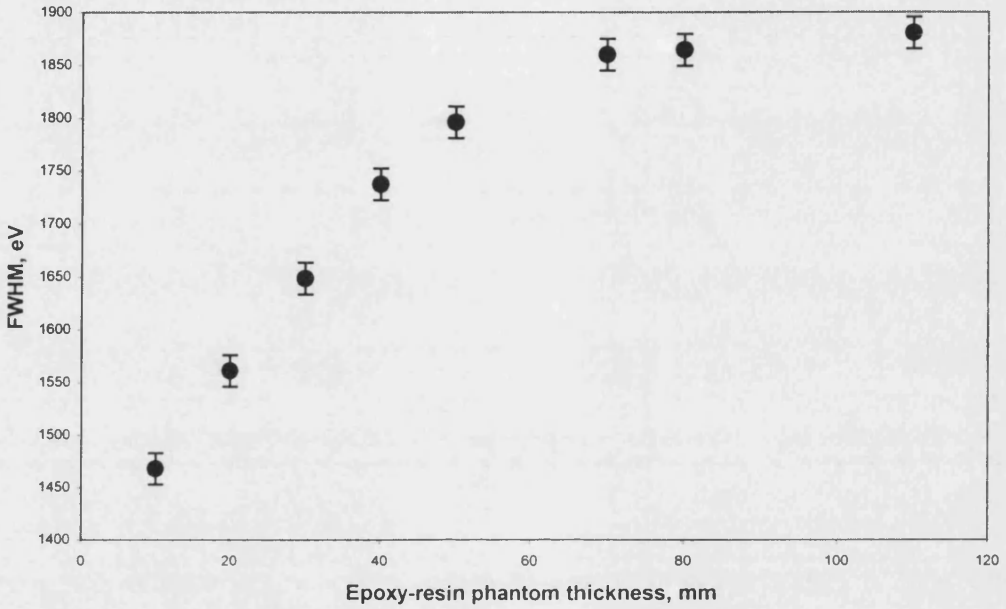

Figure 4.6 Variation in FWHM with increasing phantom thickness

A similar experiment was performed with the front surface of the phantom material at 20 mm in front of the focus instead of the previous 50 mm. This was to determine whether the depth of the focus within the phantom influences the depth at which the measured parameters tend to a constant value. Integrating the counts in the Compton and coherent regions as before demonstrated a similar picture. There was a uniform contribution from each of the first four 10 mm layers, and little additional contribution beyond 60 mm depth. Similarly the coherent to Compton scattering ratio remained constant for depths greater than 50 mm depth, though the value is lower than for the previous set-up since the equivalent scattering angle is greater.

Therefore the depth of focus in the phantom does not limit the target volume. Both experimental set-ups demonstrated that the phantom being investigated should be at least 60 mm in depth. The only effect of decreasing the depth of the focus beyond the phantom

surface was to shift the Compton peak to a lower energy. The Compton peak energy was dependent on the thickness of the phantom, indicating that the equivalent scattering angle was also dependent on the phantom thickness. For the set-up with the focus at 20 mm beyond the phantom surface and a phantom thickness of 10 mm, the Compton peak was shifted to 49.1 keV corresponding to a scattering angle of 145°. For a phantom thickness of 50 mm the Compton peak energy fell to 48.95 keV, equivalent to a scattering angle of 150°. Further increases in phantom thickness had little effect on the Compton peak energy. The channel width on the multi-channel analyser for these measurements was 60 eV.

4.4 Discussion

The coherent to Compton scattering ratios for the epoxy-resin phantom have been calculated from the stated composition using the atomic form factors and incoherent scattering function for different scattering angles, and are shown graphically in Figure 4.1. The measured values of coherent to Compton scattering ratio, for the focus at 50 mm beyond the surface of the phantom, are shown in Figure 4.4. The ratios were obtained by summing the counts in the coherent region from 59 to 60 keV, and in the Compton region from 44 to 56 keV. For a phantom thickness of 50 mm the measured values of coherent to Compton scattering ratio were:

11.89×10^{-4} for the focus at 50 mm depth (equivalent scattering angle 134°), and

11.29×10^{-4} for the focus at 20 mm depth (equivalent scattering angle 150°).

The calculated values for these scattering angles are 16.28×10^{-4} (scattering angle 134°) and 13.51×10^{-4} (scattering angle 150°). The measured ratios are less than those calculated, but the measured ratios are sensitive to the energy window selected for the integration of the coherent and Compton peaks. For these measurements, integrating the Compton peak between 44 and 56 keV gives a coherent to Compton scattering ratio five per cent higher than integrating between 40 and 56 keV. The effect of the integration interval on the coherent to Compton scattering ratio is examined further in Chapter 5.

The theory behind the calculated values of coherent to Compton scattering ratio is based on narrow beam geometry, whilst these measurements employ broad beam geometry. The measured data are for a range of scattering angles with a greater contribution from scattering angles of less than 150°. For scatter arising from angles greater than 150°, the path length through the phantom will be greater and thus subject to greater attenuation.

The measured ratio also includes the effect of multiple scattering which will not be present in the narrow beam geometry used for the calculated values of the coherent to Compton scattering ratio.

The results of these investigations on large volume phantoms may be summarised as follows:

- For the experimental set-up described the composition information is the approximate average of the first 50 mm depth of phantom.
- For consistent measurements the phantom or specimen should be at least 60 mm in thickness.
- Also for consistency, the intersection of the radiation beam axis and the detector axis should always be at the same depth in the target material i.e. the source-skin distance should be constant.

Chapter 5 Studies on Water and Ethanol

The aim of the investigations reported in this chapter was to determine whether it would be possible to use the gamma-ray backscattering technique to distinguish between fat and muscle. For the preliminary investigations water was used to represent muscle or lean tissue, and ethanol was used to represent fat. The elemental compositions of these tissues are given below:

Skeletal muscle:	C: 14.3%, H: 10.2%, O: 71%, N: 3.4%, Na: 0.1, S: 0.3, Cl: 0.1, P: 0.2, K: 0.4
Adipose:	C: 59.8%, H: 11.4%, O: 27.8%, N: 0.7, Na: 0.1, S: 0.1, Cl: 0.1
Water:	H: 11%, O: 89%
Ethanol (C_2H_5OH):	C: 52%, H: 13%, O: 35%

The composition of skeletal muscle and adipose is taken from ICRU Report 44, 1989.

Using the experimental apparatus described in Chapter 3, a series of investigations was made with the set-up as shown in Figure 5.1. The 7.4 GBq americium-241 source was collimated with an aperture of 5 mm diameter and the detector was collimated with an aperture of 10 mm diameter. The phantom was positioned so that the intersection of the source and detector axes occurred at 50 mm depth from the front surface of the phantom. Data were acquired from phantoms, which were large polythene containers (surface dimensions 180 mm × 220 mm and depth 120 mm) containing either water or ethanol. These containers with thin non-rigid walls were chosen to represent the patient situation (where the skin surface forms a non-rigid interface) more accurately than a rigid container.

Examples of the spectra obtained from these two materials are shown in Figure 5.2. Several methods of analysis have been investigated to determine the most sensitive method for assessing the fat fraction of a fat/muscle mixture. Investigations were also performed to determine the effect of the size of the phantom. To confirm the validity of using ethanol as a fat substitute, further data were acquired for a block of lard. The same analyses were used on the data and compared with the results for ethanol. The uncertainties arising from the different types of analyses were assessed which included the effects of reproducibility and re-positioning.

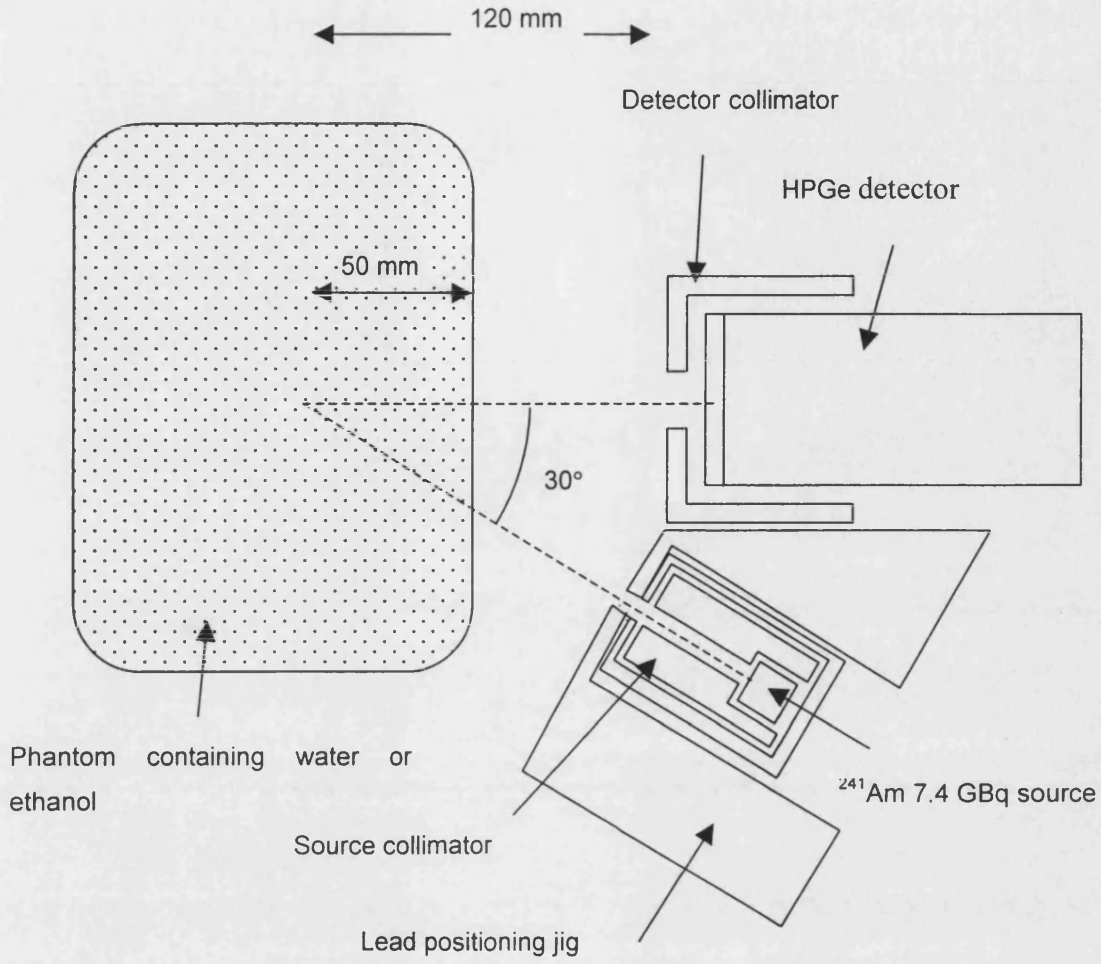

Figure 5.1 Experimental arrangement for water and ethanol investigations

5.1 Coherent to Compton scattering ratio

The data acquired from the phantoms containing water and ethanol were used to determine the coherent to Compton scattering ratio, R. The measured values were compared with calculated values using Equation 2.9 (Chapter 2) for the compositions given above, using values of F(x,Z) and S(x,Z) tabulated by Hubbell *et al* (1975). The calculated values of coherent to Compton scattering ratio for muscle and adipose, and water and ethanol for backscattering angles in the range of interest for an incident energy 59.54 keV are tabulated in Table 5.1 and shown graphically in Figure 5.3.

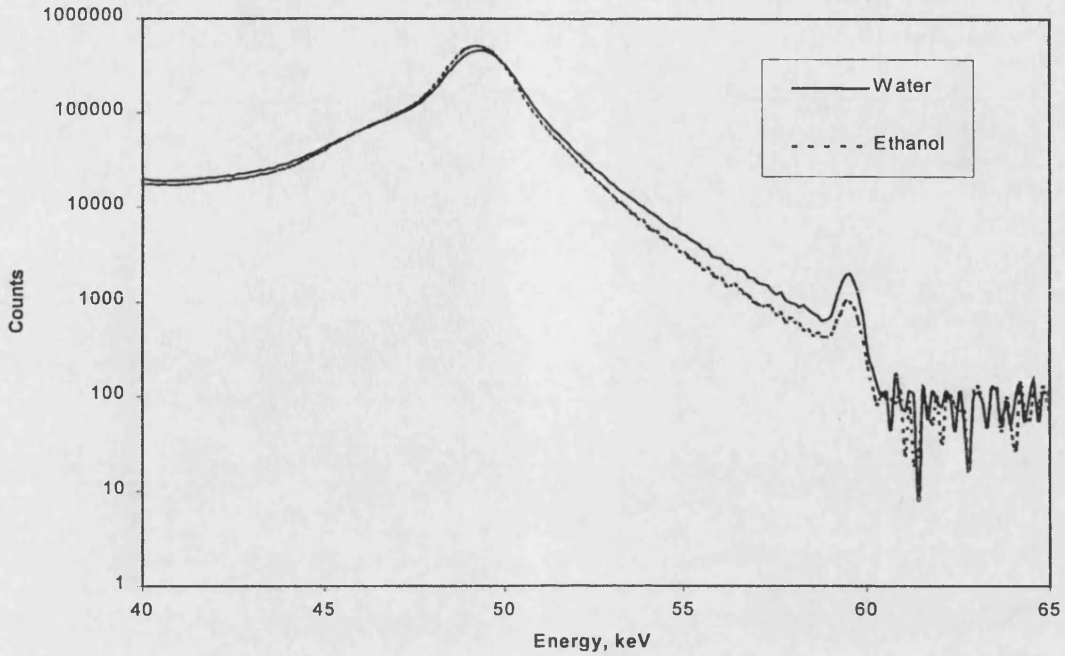

Figure 5.2 **Spectra from large phantom containing water and ethanol; 48-hour acquisitions**

Table 5.1 **Calculated values of coherent to Compton scattering ratios for various scattering angles**

Material	Coherent to Compton scattering ratio R ($\times 10^{-4}$) for various scattering angles			
	110°	130°	150°	160°
Muscle	32.47	21.27	14.82	12.99
Adipose	15.00	9.54	6.52	5.66
Muscle: Adipose	2.16: 1	2.23: 1	2.27: 1	2.30: 1
Water	32.83	20.79	13.88	11.94
Ethanol	15.78	9.92	6.66	5.74
Water: Ethanol	2.08:1	2.10:1	2.08:1	2.08:1

Figure 5.3 demonstrates the suitability of water and ethanol as substitutes for muscle and adipose over the range of scattering angles of interest. For the range of scattering angles considered the probability of Compton scatter remains almost constant whilst the probability of coherent scatter falls by a factor of three as the scattering angle increases. The coherent to Compton scattering ratio for muscle is approximately twice that for

adipose over the range of scattering angles considered (110° to 160°). Similarly, the coherent to Compton ratio for water is approximately twice that for ethanol over the same range of scattering angles. This should allow good discrimination between muscle and adipose and their substitutes.

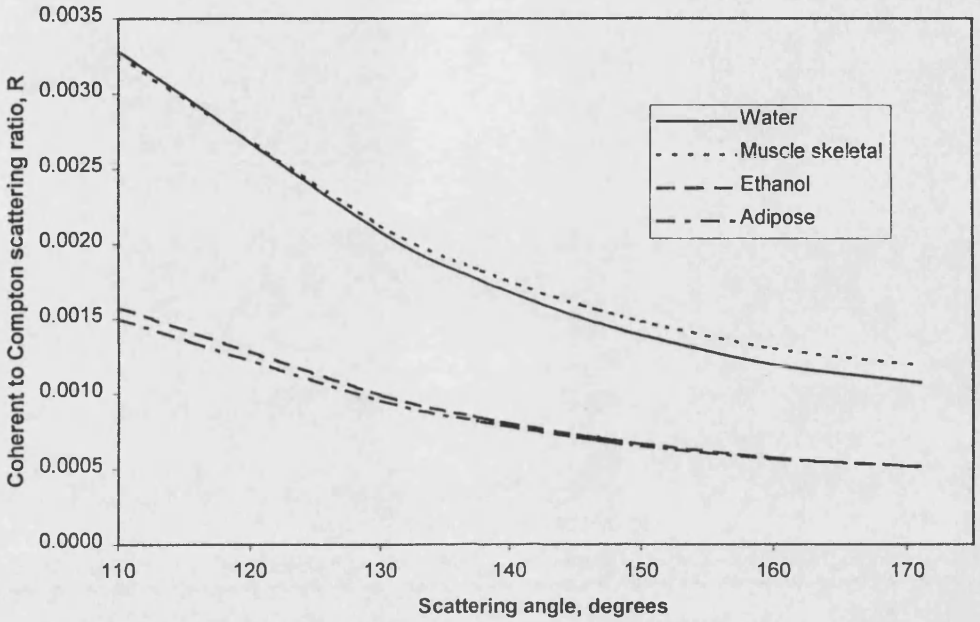

Figure 5.3 Variation of coherent to Compton scattering ratio R with scattering angle for four materials

Tartari *et al* (1991) has used a Monte Carlo code to determine the energy distributions of single and multiple scattered radiation and demonstrated that multiple scatter occurs predominantly at the Compton peak energy and on the low energy side of the Compton peak (Figure 5.4). The detector used was a HPGe detector of the same thickness but smaller area than used in this work. In Figure 5.4 the curves represent the experimental pulse height distribution and two calculated distributions: the Compton distribution profile convoluted with the detector response function only (the narrow profile), and the Compton distribution profile plus multiple scattering component convoluted with the detector response function with a correction also for the collimator geometry. Consequently, restricting the energy interval for Compton integration on the low energy side of the Compton peak (e.g. by not counting beyond the tenth maximum width) reduces the effect of multiple scatter on the measured ratio. Therefore to estimate the coherent to Compton scattering ratio from the measured spectra whilst endeavouring to reduce the contribution

from multiple scatter, the following integration intervals were set. The coherent integration interval was set to include the whole of the coherent peak (58.5 to 60.5 keV) and the Compton interval for integration was taken as the full width tenth maximum (FWTM) values of the Compton peak. For the measurements performed with water and ethanol this corresponds to the interval 45 to 52 keV which is also above the energy range influenced by the detector response correction.

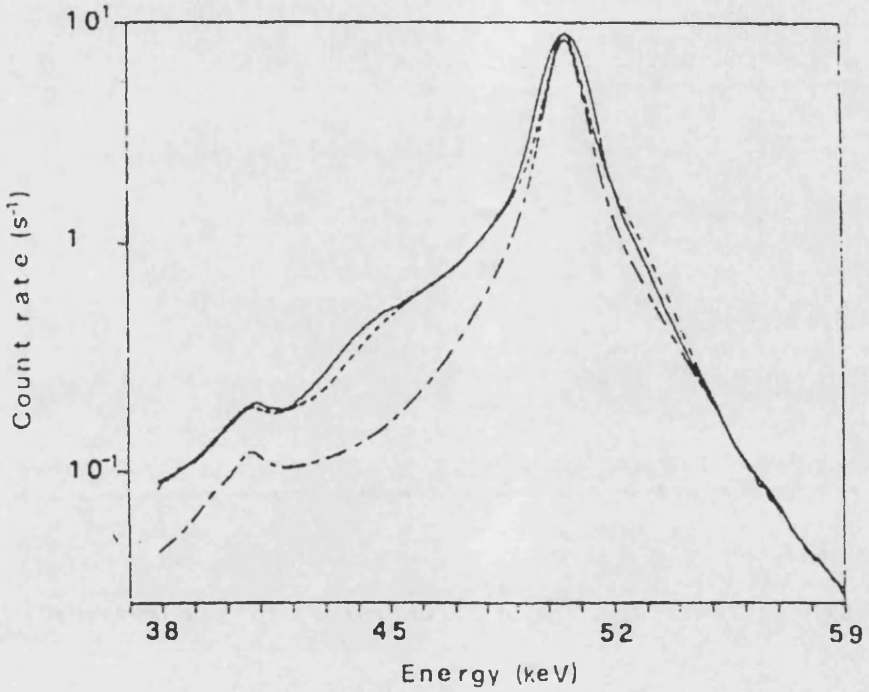

Figure 5.4 **Experimental and calculated pulse height distributions for 59.54 keV incident photons and 120° scattering geometry. ——— experimental; — - — - — - Compton distribution profile convoluted with detector response function only; - - - - - Compton distribution profile plus multiple scattering component convoluted both with resolution and geometrical response functions (Tartari *et al* 1991)**

The measurements were made with the experimental arrangement shown in Figure 5.1. The aperture of the source collimator is 5 mm diameter and the aperture of the detector collimator is 10 mm diameter with an acceptance angle of 16°. The source-detector focus was set to a depth of 50 mm in the phantom. For a 48-hour acquisition time good counting statistics were obtained in both the coherent and Compton regions. The coherent to Compton scattering ratios were determined for the phantoms filled with water or ethanol and are given in Table 5.2. For the experimental set-up employed, the Compton peak occurred at 49.4 keV for water which equates to a scattering angle of 139.6°, whilst for

ethanol the Compton peak occurs at 49.3 keV, which equates to a scattering angle of 141.5°. The calculated values of the coherent to Compton scattering ratio in Table 5.2 have been derived for these two scattering angles. Although there are differences between the calculated and measured values, there is still good discrimination between the measured values of coherent to Compton scattering ratio between water and ethanol.

Table 5.2 Calculated and measured coherent to Compton scattering ratio R

Material	Calculated ratio ($\times 10^{-4}$)	Measured ratio ($\times 10^{-4}$)
Water	16.92	14.1 ± 0.2
Ethanol	7.79	7.9 ± 0.2
Water: Ethanol	2.17: 1	1.79 ± 0.04: 1

The calculated value is based on narrow beam geometry and ignores the presence of multiple scatter. The experimental method uses broad beam geometry that generates multiple scatter which adds to the counts in the Compton peak and hence might be expected to lower the measured value of the coherent to Compton scattering ratio. As mentioned above the Compton interval was reduced to the FWTM of the Compton peak to limit the effect of multiple scatter. However, the measured value of the coherent to Compton scattering ratio is affected by the choice of integration interval for both the coherent and Compton regions. The dependence of the measured value on the integration intervals may be illustrated as follows. Reducing the coherent integration interval from 58.5-60.5 keV to 59-60 keV decreases the measured coherent to Compton scattering ratio value by 15 per cent. Increasing the Compton integration interval from 45-52 keV to 40-56 keV to include the whole Compton peak increases the count rate by 13 per cent and hence reduces the measured coherent to Compton scattering ratio value by the same amount. Thus, the differences between the calculated and measured values may be explained by the uncertainties associated with the presence of multiple scatter and the choice of the energy integration intervals of the coherent and Compton peaks.

In practice the coherent to Compton scattering ratio measured for water is about 1.8 times greater than that for ethanol over a range of Compton integration intervals (range 1.75 to 1.85). The integration intervals investigated extended from ± 1 keV of the Compton peak energy (around 49 keV) to 40-56 keV, which includes the whole of the Compton peak (see Figure 5.2). This demonstrates that the choice of interval for determining the coherent to

Compton scattering ratio is not important in distinguishing between different compositions provided the same energy integration intervals are used for all analyses.

Reducing the aperture of the detector collimator would restrict the range of scattering angles received by the detector and the measured ratio may be expected to approach the calculated value of the coherent to Compton scattering ratio for the scattering angle that equates to the Compton peak energy. Further data acquisitions were made with the detector collimated with an aperture of 5 mm diameter (acceptance angle 8°) instead of the 10 mm diameter used previously, again for counting periods of 48 hours. The calculated and measured values for both set-ups are given in Table 5.3 for comparison. For all data sets the integration limits were 58.5 to 60.5 keV for the coherent scatter and 45 to 52 keV for the Compton scatter. The values in Table 5.3 demonstrate that by reducing the aperture of the detector collimator, the theoretical values of the coherent to Compton scattering ratio for narrow geometry are approached. However, this is at the expense of a severely reduced count rate that greatly increases the standard deviation on the measured values.

Table 5.3 Calculated and measured coherent to Compton scattering ratios for two detector collimator apertures

Detector dia., mm/ Equivalent scattering angle		Phantom material	Coherent to Compton scattering ratio ($\times 10^{-4}$)	
			Calculated	Measured
10 mm dia./	139.6°	Water	16.92	14.1 ± 0.2
	141.5°	Ethanol	7.79	7.9 ± 0.2
		Water: Ethanol	2.17:1	1.79 ± 0.04: 1
5 mm dia./	146.9°	Water	14.67	15.1 ±1.5
	146.9°	Ethanol	7.03	8.1 ±1.3
		Water: Ethanol	2.09:1	1.85 ± 0.36: 1

The coherent to Compton scattering ratio, obtained with the 10 mm diameter collimator aperture, gave a reproducibility of 1.5 per cent (one standard deviation) for the large phantom filled with water, and two per cent for ethanol, for a 48-hour counting period. The smaller coherent scatter signal from ethanol gave rise to the larger standard deviation. When the aperture of the detector collimator was reduced to 5 mm diameter, the standard deviations increased to 10 per cent for water and 16.5 per cent for ethanol for the same counting period.

In order to undertake clinical studies, 30 minutes is the longest reasonable amount of time to expect patient co-operation for a measurement. When measuring the coherent to Compton scattering ratio it is necessary to obtain sufficient counts in the coherent peak to reduce the overall uncertainty of the measurement. The larger collimator aperture of 10 mm diameter on the detector is required to maximise the count rate. If four sources were used, arranged around the detector with each beam axis converging to the same point at a depth in the patient or phantom (i.e. same geometry as Figure 5.1) then a 30-minute measurement period becomes feasible. In this case the standard deviation on the measured coherent to Compton scattering ratios would be expected to increase to approximately 7.5 per cent and 10 per cent for water and ethanol respectively. Since the calculated difference in coherent to Compton scattering ratios between muscle and fat is more than 2:1 (Table 5.1), this technique should allow for the fat fraction in the target volume to be assessed. The uncertainties associated with the determination of fat fraction are discussed in Section 5.6.

In summary:

- The coherent to Compton scattering ratio is a sensitive method of distinguishing between fat and muscle.
- The small coherent signal is the limiting factor on the overall uncertainty on the measurement.

5.2 Compton profile shapes

Compton profile shapes have been investigated as a possible means for assessing body composition. This method has the advantage that there are of the order of 10^3 more counts in the Compton region than in the coherent peak, which should allow the acquisition time to be significantly reduced. For a clinical investigation the acquisition time should not exceed 30 minutes. Using the same experimental set-up, data were collected from polythene containers (surface dimensions 180 mm × 220 mm and depth 120 mm) containing either water (to represent muscle) or ethanol (to represent fat), for 0.5 hours and 48 hours.

The 0.5-hour data acquisitions were made to be representative of the reproducibility achievable in a clinical study with this experimental set-up. For each data acquisition the

phantom was positioned so that its front surface was 50 mm in front of the source-detector focus. Background data were acquired with an empty polythene container in position. The background data were subtracted in each case prior to analysis. (For the 0.5-hour acquisitions an average of five background data sets was subtracted.)

The Compton profile data for the 48-hour acquisitions are shown in Figure 5.5. The peak energy for the two materials is slightly different (approximately 100 eV) and this is thought to be due to the difference in density of the two materials being investigated, which consequently affects the equivalent scattering angle. The density of ethanol is 789 kg m^{-3} compared to water, which has a density of 1000 kg m^{-3}. The full width half maximum (FWHM), full width third maximum (FW1/3M) and full width quarter maximum (FW1/4M) of each Compton peak has been measured.

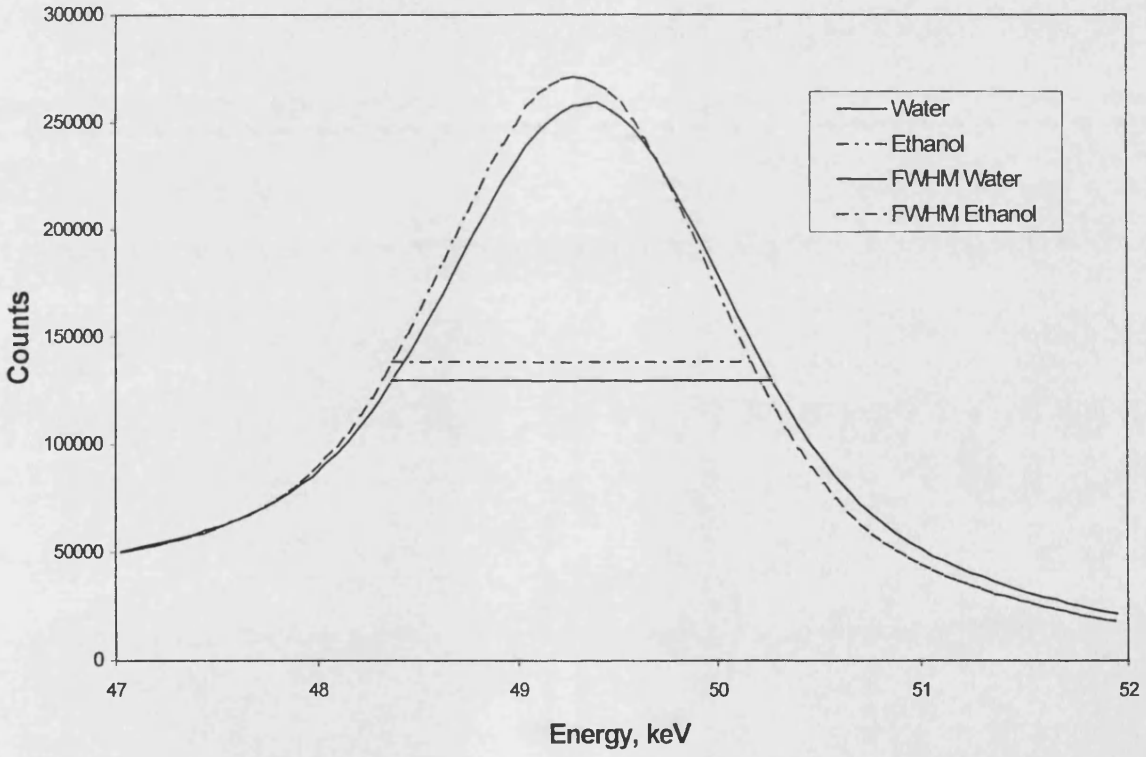

Figure 5.5 Compton profiles for water and ethanol in a large phantom, 48-hour acquisitions

Table 5.4 Compton profile width measurements of water and ethanol

Phantom	Profile width measurement, eV		
	FWHM	FW1/3M	FW1/4M
48-hour acquisition (n=3):			
Water	1910 ± 10	2600 ± 20	3230 ± 30
Ethanol	1820 ± 10	2450 ± 20	2980 ± 30
Water-Ethanol	90 ± 15	150 ± 30	250 ± 40
0.5-hour acquisition (n=5):			
Water	1890 ± 20	2620 ± 30	-
Ethanol	1790 ± 20	2420 ± 30	-
Water-Ethanol	100 ± 30	200 ± 45	-

The Compton profile width measurements for the two series of acquisitions (48-hour and 0.5-hour) are given in Table 5.4. For the 48-hour acquisitions the uncertainties quoted are one standard deviation based on three data sets. The 0.5-hour data acquisitions were smoothed by eye and the average measured value of the five data sets for each material is given with one standard deviation in Table 5.4. Examples of the 0.5-hour acquisitions are shown in Figure 5.6.

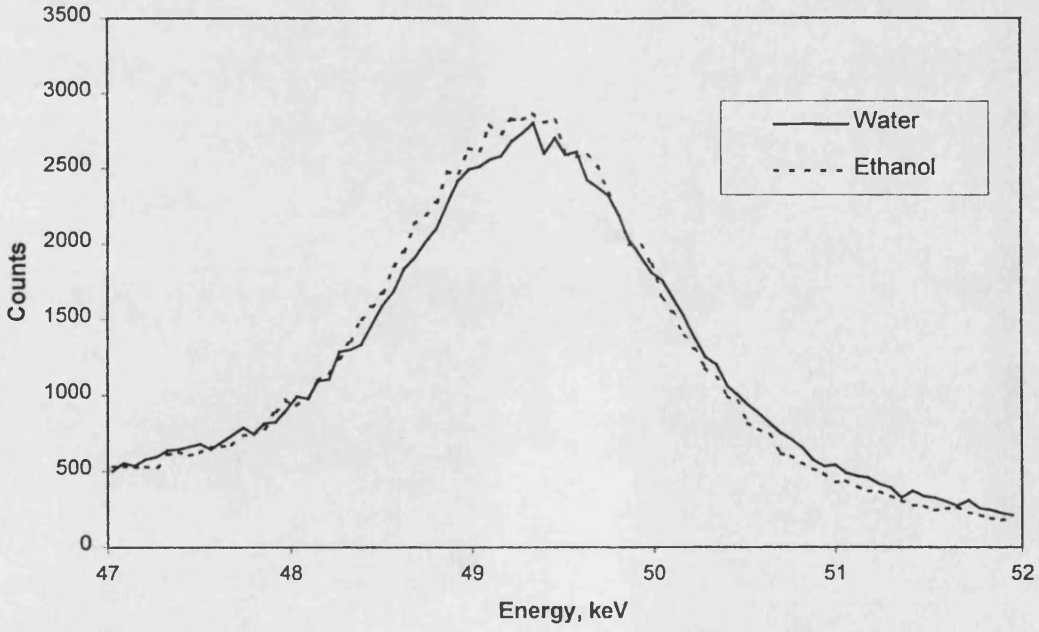

Figure 5.6 Compton profile for water and ethanol in large phantom for 0.5-hour acquisition

For the 0.5-hour data acquisitions the uncertainties on the counting statistics at the level of the FW1/4M were too great to measure the width. Table 5.4 demonstrates a difference in profile width between water and ethanol, which increases with the width of the Compton profile measurement. The more sensitive method of discriminating between water and ethanol may be to determine the full width third maximum (FW1/3M). This measurement would include more of the high energy Compton region in which single scatter predominates (Tartari *et al* 1992) and which represents the atomic binding energy of the core electrons and thus the effective atomic number.

To improve the precision of the FWHM measurement, which depends on assessing both the peak height and the profile width, a curve fitting routine was applied to this data. A Gaussian distribution was used to fit the data (Marquardt 1963) on the 0.5-hour data acquisitions in order to use more of the data in the Compton profile. On the high-energy side of the Compton peak a Gaussian curve was fitted to the measured data to one fifth of the Compton peak height with background subtracted. Tartari *et al* (1992) has demonstrated that the low energy side of the Compton profile is distorted by both the detector response function and multiple scatter as demonstrated by Figure 5.4. Consequently the Gaussian fit on the low energy side was only performed on half the number of channels that were used on the high energy side. The mean and one standard deviation of the FWHM for the five data sets for both water and ethanol were:

Water: 1620 ± 20 eV, Ethanol: 1580 ± 20 eV.

An example of the Gaussian fit to one of the water data sets is shown in Figure 5.7. Although a Gaussian distribution fits the data over the central range indicated in the figure, the measured profile is broader than the Gaussian curve further from the peak. The measured data resemble a Gaussian distribution superimposed on a background level. The FWHMs determined by this method are therefore narrower than those measured directly from the spectral data, as the FWHMs are for the fitted Gaussian distribution only and the difference between the profile widths is much less (40 ± 30 eV).

The same method was used to determine the FWHM of the Gaussian fit based on the full height of the Compton peak. The mean and one standard deviation for the same five data sets of water and ethanol were :

Water : 1850 ± 20 eV, Ethanol: 1760 ± 20 eV

The FWHMs are still narrower than those measured directly from the measured data. On the low energy side of the Compton peak the position of the FWHM occurs outside the

Gaussian fit to the measured data. The measured profile on the low energy side of the Compton peak is much broader than the Gaussian curve. However, there is better discrimination between the two phantom materials using the full height of the Compton peak (90 ± 30 eV), comparable with that measured directly from the data.

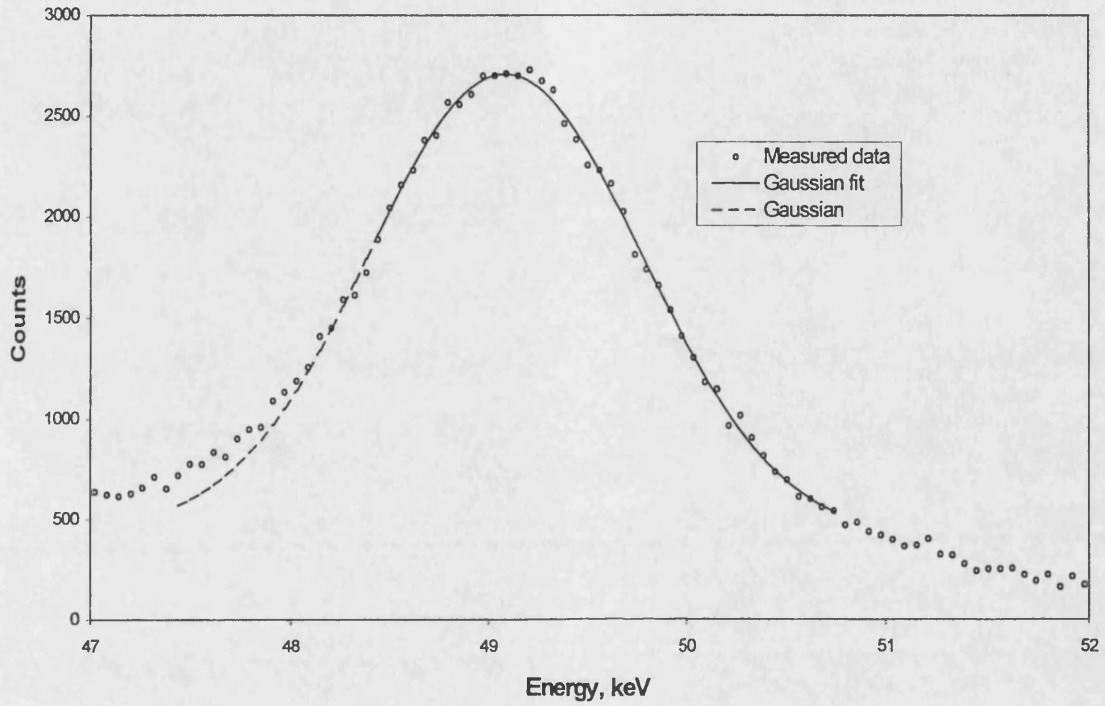

Figure 5.7 Compton profile data for water in large phantom, 0.5-hour acquisition with Gaussian fit (Marquardt 1963)

In conclusion, both the 48-hour and the 0.5-hour data acquisitions clearly show that the Compton profile for water is broader than that for ethanol. However, for the shorter acquisition times necessary for a clinical measurement the uncertainties increase to become a larger proportion of the difference in width and hence reduce the sensitivity of this technique (see Section 5.6).

To determine whether this difference in profile width between water and ethanol was due to Doppler broadening (as discussed in Chapter 2), increased multiple scatter, or scattering angle, further data acquisitions were made using small samples of the materials. For small samples, the multiple scatter would be less and the range of scattering angles small. Plastic tubes of 13 mm diameter were used as containers for the two materials (water and ethanol). With this diameter the probability of a single scattering event is less than 20 per cent and the probability of a photon being re-scattered much less than 20 per cent. (The mean free

path for 60 keV gamma-rays is 49 mm for water and 53 mm for adipose tissue (Hubbell 1982).) The influence of multiple scattering on the Compton profile measured for the 13 mm diameter tube should therefore be small. This was confirmed by Compton profile measurements on a range of different sized narrow diameter tubes filled with water (see Section 5.5).

The 13 mm diameter tubes filled with water or ethanol were placed in turn at the focus of the source-detector arrangement. An empty tube was similarly placed at the focus to acquire background data. The Compton profiles obtained from these small samples for a 48-hour counting period are shown in Figure 5.8. The spectra are narrower than those obtained from the large phantom as the range of scattering angles is much smaller. The FWHM measured for water was 1540 ± 10 eV and for ethanol was 1410 ± 10 eV still demonstrating a difference in FWHM of 130 ± 15 eV, indicating that Doppler broadening is present.

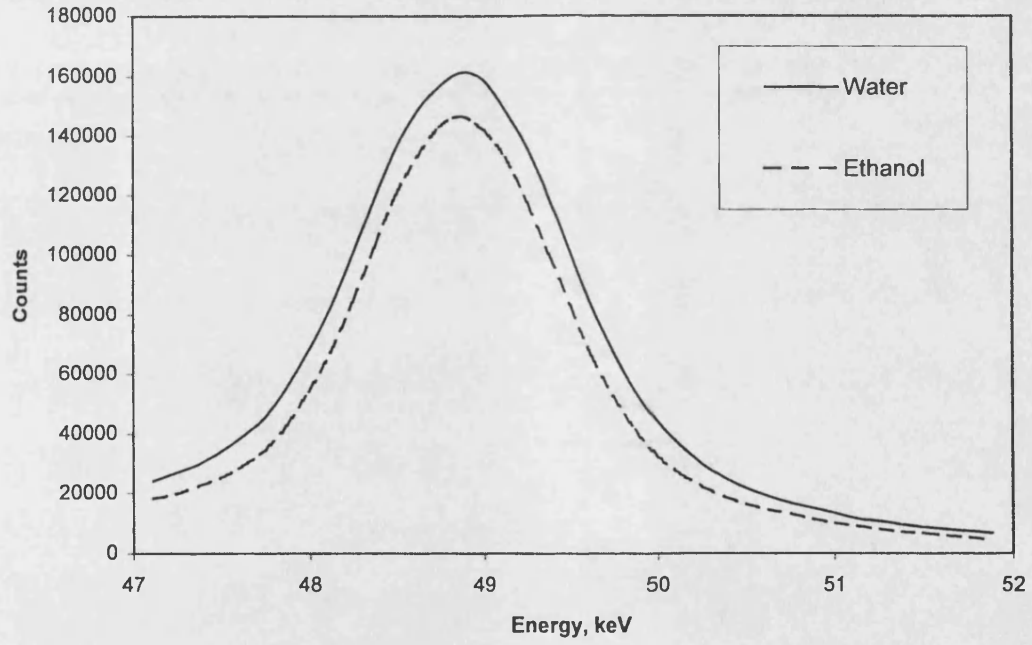

Figure 5.8 Compton profiles for water and ethanol in a 13 mm diameter phantom, 48-hour acquisition

In Chapter 2, Section 2.2.2, an approximate calculation was performed on the expected Doppler broadening of the Compton line resulting from the momentum of the L shell electrons for both carbon and oxygen. This approximate calculation may be extended to water and ethanol, the elemental compositions of which are given in the introduction of this chapter. For both solutions the hydrogen content is similar, between 11 and 13 per

cent. The major differences are in the carbon and oxygen content. For water if the hydrogen contribution is ignored the broadening of the Compton line due to oxygen is estimated as 2.03 keV (from Chapter 2, Section 2.2.2). For ethanol the combined effect of carbon and oxygen yields an estimated broadening of 1.77 keV. This gives an estimated difference in Compton line width for water and ethanol of 260 eV. This is somewhat larger than the measured difference in FWHM of 130 eV but the estimate from the atomic composition is very crude in that it ignores the presence of hydrogen and the effects of molecular orbital electrons. The Compton line widths and differences correspond more closely to the FW1/3M values but the estimated Compton line widths are too approximate for this to be significant.

To use our measurement technique for *in vivo* studies it is necessary to examine a large volume. To see the effect of reducing the range of scattering angles accepted from the large phantom (polythene container) the 48-hour experiment was repeated with the acceptance angle of the detector reduced from 16° to 8° (i.e. detector collimator aperture reduced from 10 mm to 5 mm diameter). The results were compared with those obtained from the 13 mm diameter tube. The smaller acceptance angle gives a nominal target volume diameter at the focus of 21 mm (although it will have a large penumbra). With this set-up the results from the large phantom should approach those obtained with the 13 mm diameter tube since the range of scattering angles accepted by the detector is reduced. The Compton profile width measurements for the different experimental set-ups for water and ethanol phantoms are shown in Table 5.5.

The results in Table 5.5 illustrate that by reducing the acceptance angle of the detector (and hence the range of accepted scattering angles), the profile width measurements obtained from the large phantom are closer to those obtained from the small phantom (13 mm diameter tube). For ethanol the profile width measurements for the large phantom appear to move closer to the narrow tube measured profile width as the detector acceptance angle is reduced than for water. This may be due to the different scattering characteristics of the lower density ethanol. The quoted uncertainties on the measurements are one standard deviation based on independent measurements from three graphical plots of each data set. The differences between water and ethanol for these measurements are tabulated in Table 5.6.

Table 5.5 Compton profile widths of water and ethanol for different phantom sizes and detector collimator aperture diameters

Phantom & size	Detector collimator aperture diameter, mm	Profile width measurement, eV		
		FWHM	FW1/3M	FW1/4M
Water:				
Large	10	1910 ± 10	2600 ± 20	3230 ± 30
Large	5	1830 ± 10	2500 ± 20	3070 ± 30
13 mm dia.	10	1540 ± 10	2040 ± 15	2410 ± 20
Ethanol:				
Large	10	1820 ± 10	2450 ± 20	2980 ± 30
Large	5	1630 ± 10	2220 ± 20	2700 ± 30
13 mm dia.	10	1410 ± 10	1870 ± 20	2160 ± 20

Table 5.6 Difference between water and ethanol in Compton profile width for two phantom sizes and two detector collimator apertures

Phantom size	Detector collimator aperture diameter	Difference in profile width, eV (Water – Ethanol)		
		FWHM	FW1/3M	FW1/4M
Large	10 mm	90 ± 15	150 ± 30	250 ± 40
Large	5 mm	200 ± 15	280 ± 30	370 ± 40
13 mm dia.	10 mm	130 ± 15	170 ± 25	250 ± 30

For each experimental set-up the FW1/3M gave a greater difference in profile width between water and ethanol than the FWHM. However, the greater uncertainty associated with the FW1/3M measurement reduces this advantage (see Sections 5.6 and 5.8).

The FW1/4M measurements of the Compton profiles gave still larger differences between the water and ethanol. However, these data acquisitions were for 48 hours and on a 0.5-hour acquisition (suitable for a clinical measurement) the uncertainties on the counting statistics for the FW1/4M measurement would be too great (see Figure 5.6). The most promising measurement would therefore seem to be that of the FW1/3M Compton profile.

Holt *et al* (1983) used a scattering angle of 171° to analyse small biological specimens *in vitro* and demonstrated a difference in the Compton profile shape due to changes in the

chemical composition of the phantom. By normalising the Compton profiles to equal area for two different materials a difference in height between the two profiles was obtained i.e. the characteristic line shapes were different.

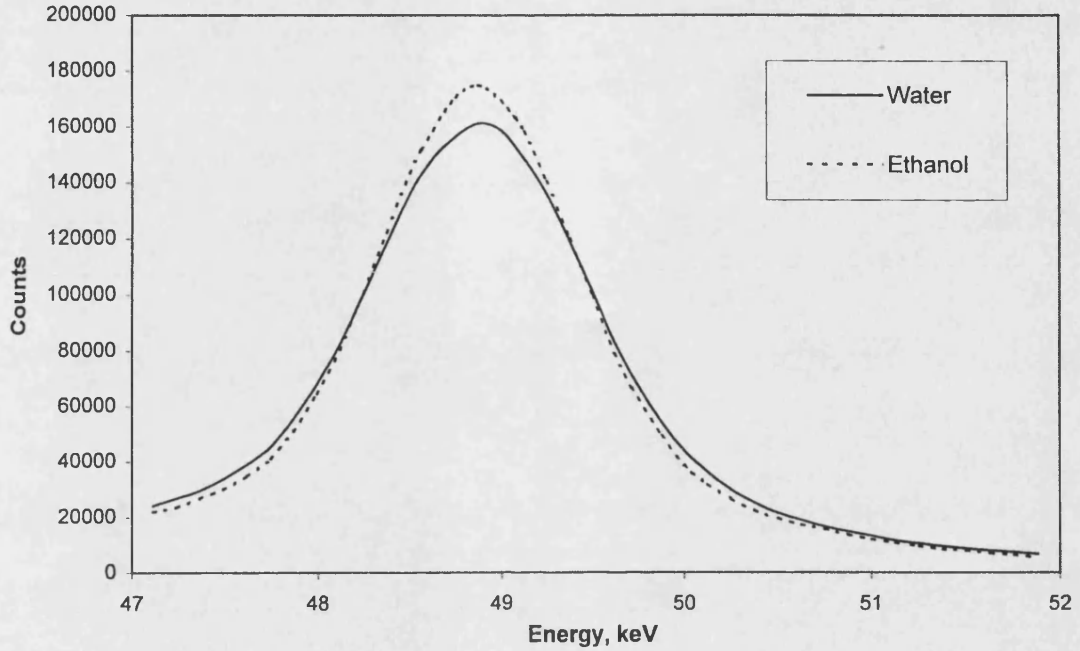

Figure 5.9 Compton profiles for water and ethanol in 13 mm diameter phantom normalised to equal area

This type of analysis was performed on the data collected from the 13 mm diameter tube with the 10 mm diameter detector collimator aperture. The Compton profiles obtained from water and ethanol normalised to equal area are shown in Figure 5.9. This figure demonstrates that the profile obtained from ethanol is narrower than that obtained from water with the same total counts. A difference of eight per cent in profile heights was obtained, with the ethanol having the greatest height. For the small phantom (13 mm diameter tube) the Compton peak occurred at the same energy for both the water and ethanol. The same analysis was performed on data collected from the large phantom with the 10 mm diameter detector collimator aperture. However, although the same geometry was used for each data collection, the energy of the Compton peak measured for ethanol is around 100 eV lower than that measured for water at 49.4 keV (see Figure 5.5). This difference in peak energy indicates a difference in equivalent scattering angle of around 2° for the two materials. This effect is most likely due to the different densities of the two materials being investigated. The height difference between the two profiles is still around eight per cent (the ethanol profile had the greatest height after normalisation), but the difference is due to the non-alignment of the two Compton peaks. These investigations

suggested that the analysis proposed by Holt *et al* (1983), although valid for small samples, was not suitable for use with large phantoms.

The conclusions of these investigations of Compton profile shape as methods for distinguishing between water and ethanol are as follow:

- There is a difference between the Compton profile widths of water and ethanol. Some of the difference is due to Doppler broadening of the spectrum.
- For a large phantom and large detector acceptance angle, the range of scattering angles and multiple scatter accepted by the detector reduces the difference in FWHM of the Compton profiles for water and ethanol. However, even for a clinically acceptable measurement time (say 0.5 hours) there are measurable differences between muscle and fat substitutes.
- The FW1/3M would seem to be the most sensitive of the methods investigated that might be used for the determination of composition differences between water and ethanol.
- Normalising the Compton profiles for total area and then using a subtraction technique (Holt *et al* 1983), although valid as a measure of composition for small samples, is not valid for large volume composition determination.

5.3 Compton profile ratios

In the experimental set-up described here a ratio analysis that did not depend on coherent scattering would be an advantage since in a clinical situation acquisition times should not be more than 30 minutes duration. The ratio analyses suggested by MacKenzie (1990) and Tartari *et al* (1992) reviewed in Chapter 2, Section 2.2.3, which use the high energy tail of the Compton profile, have also been applied to the data acquired from large phantoms containing water and ethanol. MacKenzie (1990) demonstrated that the Compton profile shape was not affected by multiple scatter on the high energy side of the Compton peak but was sensitive to atomic number. Tartari *et al* (1992) have also shown that the high-energy region of the Compton profile is sensitive to the atomic binding energy of the core electrons and hence the atomic number of the phantom material (see Chapter 2, Section 2.2.3).

The results of the analyses proposed by MacKenzie (1990) and Tartari *et al* (1992) for data from large phantoms (180 mm × 220 mm × 120 mm) for two detector acceptance angles are given in Table 5.7. For the ratio HP suggested by MacKenzie (1990), (Chapter 2, Equation 2.10), the numerator is the integrated counts between 52 and 58 keV encompassing the high energy Compton tail, and the denominator is the integrated counts between 40 and 58 keV covering the entire Compton profile.

The analysis suggested by Tartari *et al* (1992) defines the numerator from E_2 (Chapter 2, Equation 2.12) to close to the coherent peak. From Equation 2.3 (Chapter 2), for a scattering angle of 150° the Compton peak energy is 48.91 keV, and from Equation 2.12 (Chapter 2), E_2 is 50.77 keV. For the large detector acceptance angle the Compton peak occurred at 49.4 keV for water (49.3 keV for ethanol), and for the small acceptance angle the Compton peak occurred at 49.0 keV for both water and ethanol. These Compton peak energies equate to scattering angles in the range 139.6° (E=49.4 keV) and 147° (E=49.0 keV) (Chapter 2, Equation 2.3). For these scattering angles, the corresponding values of E_2 (from Chapter 2, Equation 2.12), are 51.66 keV and 51.02 keV respectively. Therefore, when determining the ratio R_k proposed by Tartari *et al* (1992) (Chapter 2, Equation 2.13) the limits of the numerator from 51 to 56 keV and 52 to 56 keV have been compared. The results shown in Table 5.7 are for acquisition times of 48 hours for the two detector collimator apertures. The quoted uncertainties are one standard deviation based on counting statistics.

Table 5.7 Compton profile ratio measurements of water and ethanol for two detector collimator apertures

Ratio	Phantom material		Water:Ethanol
	Water	Ethanol	
Detector collimator aperture 10 mm dia. Acceptance angle: 16°			
$HP \times 10^{-3}$	39.2 ± 0.1	29.5 ± 0.1	1.33 ± 0.01:1
$R_k(\delta\varepsilon=51\text{-}56) \times 10^{-3}$	82.9 ± 0.1	67.6 ± 0.1	1.23 ± 0.01:1
$R_k(\delta\varepsilon=52\text{-}56) \times 10^{-3}$	36.9 ± 0.1	28.0 ± 0.1	1.32 ± 0.01:1
Detector collimator aperture 5 mm dia. Acceptance angle: 8°			
$HP \times 10^{-3}$	38.5 ± 0.3	28.0 ± 0.3	1.37 ± 0.02:1
$R_k(\delta\varepsilon=51\text{-}56) \times 10^{-3}$	80.9 ± 0.4	64.2 ± 0.3	1.26 ± 0.01:1
$R_k(\delta\varepsilon=52\text{-}56) \times 10^{-3}$	36.2 ± 0.3	26.6 ± 0.2	1.36 ± 0.02:1

Table 5.7 demonstrates that the ratios HP (MacKenzie, 1990) and R_k (Tartari *et al* 1992) do not vary significantly when the detector collimator aperture is reduced in diameter suggesting that they are not very sensitive to the effects of increased multiple scatter and range of scattering angles. Hence a large detector acceptance angle could be employed which would increase the count rate and hence improve the statistics for short counting times. For the proposed four-source system and acquisition time of 30 minutes the standard deviation on the ratios HP and R_k would be expected to increase to approximately one per cent for both water and ethanol for the 10 mm diameter detector aperture. However, the discrimination between water and ethanol appears to be slightly reduced when the larger detector collimator aperture is used.

5.4 Ethanol as fat substitute

The ICRU Report 44 (1989) gives a recommended density value for adipose tissue of 950 kg m^{-3}. In the measurements described above ethanol has been used as a substitute for fat as it is a liquid that can be mixed with water to give a range of water/ethanol concentrations. However, although chemically similar to adipose, the density of ethanol is significantly less at 789 kg m^{-3}. In order to test whether ethanol behaves similarly to fat some of the measurements have been repeated using lard as the phantom material. Lard is pure fat with a density of 914 kg m^{-3}, close to that of adipose tissue. The phantom dimensions were such that the incident surface dimensions were 160 mm × 240 mm, with a depth of 115 mm. The americium-241 source collimator had a 5 mm diameter aperture, and the detector collimator also had a 5 mm diameter aperture. Data were acquired for 48 hours. The coherent peak was barely perceptible on this data and therefore comparisons were only made on the Compton profile.

Table 5.8 compares the profile shapes measured from the lard phantom with those measured previously from ethanol and water for the same geometry. The uncertainties are based on the resolution of the measurements from the spectral data plots. The measurements demonstrate good agreement of profile shape between lard and ethanol.

Table 5.8 Compton profile shape measurements

Material	FWHM, eV	FW1/3M, eV	FW1/4M, eV
Lard	1670±10	2255±20	2800±30
Ethanol	1630±10	2220±20	2700±30
Water	1830±10	2500±20	3070±30

The ratios HP suggested by MacKenzie (1990) and R_k suggested by Tartari *et al* (1992) that are tabulated in Table 5.9 show similar agreement between lard and ethanol. The ratios have the same definitions as described in Section 5.3. This demonstrates the validity of using ethanol as a fat substitute.

Table 5.9 Measured Compton profile ratios for lard ethanol and water

Ratio	Lard	Ethanol	Water
HP ($\times 10^{-3}$)	26.7 ± 0.3	28.0 ± 0.3	38.5 ± 0.3
$R_k(\times 10^{-3})(\delta\varepsilon = 51\text{-}56)$	65.1 ± 0.3	64.2 ± 0.3	80.9 ± 0.4
$R_k(\times 10^{-3})(\delta\varepsilon = 52\text{-}56)$	25.7 ± 0.3	26.6 ± 0.2	36.2 ± 0.3

To reduce the uncertainties due to counting statistics (particularly for the coherent peak), a coherent to Compton scattering ratio measurement was made with the aperture on the detector collimator enlarged to 10 mm diameter to improve the count rate. The acquisition time remained the same at 48 hours.

With this experimental set-up the coherent to Compton scattering ratio for the lard was $(6.7 \pm 0.2) \times 10^{-4}$ compared with $(7.9 \pm 0.2) \times 10^{-4}$ for ethanol and $(14.1 \pm 0.2) \times 10^{-4}$ for water, measured previously (Table 5.2). The experimental geometry for this lard measurement gave a Compton peak energy of 49.3 keV that corresponds to a scattering angle of 141.5° (the same Compton peak energy as that measured previously for ethanol). The calculated values for this scattering angle are 7.57×10^{-4} for adipose and 7.79×10^{-4} for ethanol. The higher count rate reduces the uncertainties on the measurement as expected, but the measured value of the coherent to Compton scattering ratio for lard is a little lower than calculated for adipose. The previously measured value for ethanol is in good agreement with the calculated value (Table 5.2). For the lard value the difference may be due to slight differences in chemical composition between lard and adipose according to ICRU Report 44 (1989).

In conclusion, this work has demonstrated that for the measurement techniques investigated, ethanol may be used as a fat substitute, despite the small difference in density, for the following reasons:

- The coherent to Compton scattering ratios measured from lard are close to those measured for ethanol and approximately half the values measured for water.
- Measurements of the Compton profile width for both lard and ethanol are in good agreement.
- The Compton profile ratios proposed by MacKenzie (1990) and Tartari *et al* (1992) have similar values for the two materials.

5.5 Small diameter phantom studies

In earlier work reported in Section 5.2, 13 mm diameter tubes were used as containers for water and ethanol. The smaller size was shown to reduce the effect of multiple scatter and the range of scattering angles detected. These investigations demonstrated that the differences in Compton profile widths between water and ethanol were still present in a small phantom. Doppler broadening of the spectra is the most probable explanation of the measured profile width differences between the water and ethanol obtained from the 13 mm diameter containers. With the 13 mm diameter container a small contribution from multiple scatter was still present. To further investigate the effect of scatter on the measured spectra a range of small diameter water-filled containers were irradiated and the resulting spectra compared.

The experimental set-up employed was the same as described previously (Figure 5.1), but both the source and detector had 5 mm diameter aperture collimators, which restricted the acceptance cone at the source-detector focus to 21 mm diameter. Each phantom was centred at the source-detector focus and acquisition times were 48 hours. The phantom sizes investigated were 8, 13, and 22 mm diameter. Data acquisitions were made for water-filled and empty phantoms. The spectra obtained from the empty phantoms were subtracted from the corresponding data for the water-filled phantom prior to analysis.

The expected transmission and hence probability of single scatter in these phantom dimensions are given in Table 5.10. These values have been derived from the average path length through the cylinders ($=\pi r^2/2r$, where r is the cylinder radius), and the total

attenuation coefficient (μ/ρ) for water of 2.055×10^{-2} m^2 kg^{-1} at 60 keV (Hubbell 1982). The mean free path for 60 keV gamma-rays is 49 mm for water and 53 mm for adipose tissue (Hubbell 1982). The corresponding values for a path length of 50 mm which is the depth of the focus in the large phantom are given for comparison.

Table 5.10 Transmission and probability of scatter for different path lengths in water

Cylinder diameter, mm	Average path length, mm	Transmission	Probability of scatter, %
8	6.3	0.88	12
13	10.2	0.81	19
22	17.3	0.70	30
Large phantom	(50)	0.36	64

From the calculated values of the probability of single scatter, the probability of the scattered photon being re-scattered will increase with phantom size. The profile widths of the Compton peak would also be expected to increase with phantom size due to the effect of increased multiple scatter on the profile shape. The measured Compton profile widths for the different diameter phantoms after background subtraction are given in Table 5.11 and demonstrate that the profile width increases slowly with phantom size. The profile widths obtained from the large phantom (Table 5.5) are repeated in Table 5.11 for ease of comparison.

Table 5.11 FWHM and FW1/3M for different diameter water phantoms

Diameter, mm	FWHM, eV	FW1/3M, eV
8	1490 ± 15	1945 ± 25
13	1520 ± 15	2020 ± 25
22	1530 ± 15	2050 ± 25
Large phantom	1830 ± 10	2500 ± 20

The effect of phantom size on the Compton profile ratios HP (MacKenzie 1990) and R_k (Tartari *et al* 1992) was also considered. The values obtained (Table 5.12) also demonstrate that the ratio values increase slowly with phantom size.

The three small phantoms (8 mm, 13 mm and 22 mm diameter tubes) all have a low probability of multiple scatter and as expected show similar results within experimental

uncertainties. The effect of multiple scatter arising from the large phantom (polythene container) is most marked on the Compton profile ratio measurements.

Table 5.12 Compton profile ratios for different diameter water phantoms

Ratio	Compton profile ratio			
	8 mm dia.	13 mm dia.	22 mm dia.	Large
HP $\times 10^{-3}$	29.8 ± 1.0	31.5 ± 0.6	30.8 ± 0.3	38.5 ± 0.3
$R_k \times 10^{-3}$ ($\delta\varepsilon$= 51-56)	57.1 ± 1.0	58.9 ± 0.6	59.1 ± 0.4	80.9 ± 0.4
$R_k \times 10^{-3}$ ($\delta\varepsilon$= 52-56)	28.4 ± 0.8	29.1 ± 0.5	28.8 ± 0.3	36.2 ± 0.3

In conclusion, with small diameter phantoms the measured differences in the Compton profile shape are most probably due to Doppler broadening as predicted by Dumond (1933). However, for larger phantoms representing human anatomy, the measured differences are due to Doppler broadening, the contribution of multiple scatter, and the range of scattering angles involved.

5.6 Estimation of uncertainties for fat fraction measurements

The measurement of the coherent to Compton scattering ratio gives good discrimination between fat (ethanol) and muscle or lean tissue (water) but with large standard deviations. This will affect the accuracy of any measurement on a mixture of unknown fat content. From the Compton profile shape measurements that of the FW1/3M seemed the most promising. The Compton profile ratios investigated had small standard deviations but not such good discrimination between fat and muscle. The results from these three methods have been analysed theoretically to determine the associated uncertainty in the measurement of different mixtures of fat and muscle.

Let F be the measured calibration ratio for fat and M be the measured calibration ratio for muscle. Then for a fat/muscle mixture with measured ratio C, where x is the fat fraction and y is the muscle fraction:

$$C = xF + yM \qquad \textbf{Equation 5.1}$$

$$1 = x + y \qquad \textbf{Equation 5.2}$$

Substituting for x:

$$C = F(1-y) + yM \qquad \textbf{Equation 5.3}$$

$$y = \frac{(C-F)}{(M-F)} \qquad \textbf{Equation 5.4}$$

Then differentiate with respect to C:

$$\frac{d}{dC}y = \frac{d}{dC}\frac{(C-F)}{(M-F)} \qquad \textbf{Equation 5.5}$$

$$\frac{dy}{dC} = \frac{1}{(M-F)} \qquad \textbf{Equation 5.6}$$

$$\frac{\Delta y}{\Delta C} = \frac{1}{M-F} \qquad \textbf{Equation 5.7}$$

$$\therefore \Delta y = \frac{\Delta C}{|M-F|} \qquad \textbf{Equation 5.8}$$

and similarly, $\Delta x = \dfrac{\Delta C}{|F-M|}$ **Equation 5.9**

This method has been used to estimate the uncertainty in fat fraction measurement for the coherent to Compton scattering ratio R, and the Compton profile ratio methods of analysis HP and R_k, and is similar to the method used by Karellas *et al* (1983) for investigations of bone density. The data were acquired for 48 hours with a single 7.4 GBq americium-241 source and a 10 mm diameter detector collimator aperture. The value ΔC was determined as the average standard deviation on the water and ethanol measurements. For a clinical system using four sources, and an acquisition time of 30 minutes, the uncertainties would be the same as the uncertainties for a two-hour acquisition with a single source. The expected uncertainties in the ratio measurements for fat/muscle mixtures have been determined for the 48-hour acquisition data, and predicted for two-hour acquisitions. The results are given in Table 5.13.

The uncertainties for fat fraction estimation based on the FWHM and FW1/3M Compton profile measurements have been determined from the 30-minute acquisitions, using the same method. The results are given in Table 5.14. The FW1/3M measurement demonstrates a slight improvement in the uncertainty of the measurement over the FWHM measurement.

Table 5.13 Uncertainty (1 standard deviation) in fat fraction measurement with single source for 48-hour and 2-hour acquisitions

Method of analysis	Uncertainty in fat fraction	
	48-hour acquisitions	2-hour acquisitions
R	0.03	0.13
HP	0.006	0.03
R_k ($\delta\varepsilon$=51-56)	0.006	0.03

Table 5.14 Uncertainty (1 standard deviation) in fat fraction measurement with single source for 0.5-hour acquisition

Profile shape measurement	Uncertainty in fat fraction
FWHM	0.21
FW1/3M	0.16

These estimations of expected uncertainty for the different ratio analyses have been based only on counting statistics and for the FWHM and FW1/3M on profile width measurement uncertainties. They do not allow for reproducibility and repositioning. These additional uncertainties are addressed in Section 5.7.

From Tables 5.3 and 5.7 the ratio method giving the greatest discrimination between water and ethanol is the coherent to Compton scattering ratio (water: ethanol = 1.79: 1 for 10 mm diameter aperture in the detector collimator). However, the statistical uncertainties on the coherent to Compton scattering ratio are large due to the low count rate in the coherent region for low atomic number materials. For an unknown mixture of water and ethanol the estimation of fat fraction would have an uncertainty of up to ± 0.13. The Compton profile ratios investigated give less discrimination for the same geometry (water: ethanol = 1.2 - 1.3: 1 for 10 mm diameter aperture in the detector collimator) but the uncertainty in fat fraction estimation from these methods is much less, only ± 0.03 because of the better counting statistics. The Compton profile width measurements have the greatest uncertainties in determining fat fraction. From these results the Compton profile ratio analyses would seem to be the most promising methods for determining the fat fraction of an unknown mixture.

5.7 Reproducibility of measurements

Most of the measurements quoted in earlier sections are based on a single set of data obtained during a 48-hour acquisition. In Section 5.6 the uncertainty of determining the fat fraction on a measurement with a single source for a two-hour acquisition was estimated for each method of analysis. This was to simulate a proposed four-source system with a 0.5-hour acquisition time. To confirm these expected uncertainties a series of experiments was performed with the same single source system for two-hour acquisition periods. In all measurements the source position was fixed at an angle of 30° to the detector as in Figure 5.1. The aperture of the source collimator was 5 mm diameter and the aperture of the detector collimator was 10 mm diameter. The source was the same 7.4 GBq americium-241 bead source. The calibration of the system was checked before, during and at the end of each series of measurements.

To test the reproducibility of the experimental system and the influence of the re-positioning of the phantom the following series of measurements were made. The phantom was the large 4.5 litre polythene container. The water-filled phantom was positioned with the source-detector focus at a depth of 50 mm from the phantom surface and two data acquisitions of two hours each were made. The water-filled phantom was then replaced with an empty phantom and one data acquisition of two hours was made. The ethanol-filled phantom was then positioned in the same way and another two data acquisitions of two hours were made. This procedure was repeated five times. The mean of the five background data sets was subtracted from each of the water and ethanol data sets prior to performing the different types of ratio analysis.

Table 5.15 Percentage uncertainties from repeatability and re-positioning for the three ratios (R, HP and R_k) for phantoms containing water and ethanol

Ratio	Water		Ethanol	
	Average range* (n=5)	std. error, $\sigma_{\bar{x}}$ (n=5)	Average range* (n=5)	std. error, $\sigma_{\bar{x}}$ (n=5)
R	4.8%	4.2%	2.4%	5.5%
HP	0.6%	1.1%	0.6%	1.1%
$R_k(\delta\varepsilon=51\text{-}56)$	0.4%	1.2%	0.6%	1.1%

*Average range is the average of half the difference between each pair of measurements.

Table 5.15 lists the average range of the measured ratios for each for the five pairs of consecutive measurements of both water and ethanol, together with the uncertainty in the mean (standard error, $\sigma_{\bar{x}}$) for the five re-positioning studies.

These results demonstrate that for the coherent to Compton scattering ratio measurements the uncertainties on both the pairs of measurements, and the re-positioning measurements, are consistent with the estimates based upon the 48-hour measurements discussed in Section 5.1. The estimates from the 48-hour measurements, based on counting statistics only, gave uncertainties of 7.5 per cent for water and 10 per cent for ethanol for a two-hour measurement period. The actual uncertainties based on counting statistics for the two-hour measurements were 6.5 per cent for water and 9.5 per cent for ethanol. For the HP and R_k ratios also the uncertainties based on counting statistics are of the order of one per cent, similar to the value of one per cent estimated in Section 5.3 for both water and ethanol. The uncertainties for the Compton profile ratios on repeated measurements after re-positioning are a little larger than those when the phantom is not moved between measurements, indicating that the ratios may be position dependent. However, the uncertainties with all the measured Compton profile ratios are much less than for the coherent to Compton scattering ratio.

The mean values of the ratios measured from the re-positioning studies are shown in Table 5.16. The ratios are a little higher than those in Tables 5.3 and 5.7 for the 10 mm diameter detector collimator aperture. The coherent to Compton scattering ratios are within the standard deviations of the above and previous measurements. However, the Compton profile ratio measurements (HP and R_k) are outside the standard deviations of previous measurements, being consistently about five per cent higher for the current measurements. The time interval between the first measurements and the re-positioning studies was over six months, during which time the equipment was dismantled more than once. This is the most probable explanation for the differences described above. Later in this section it will be shown that the HP (MacKenzie 1990) and R_k (Tartari *et al* 1992) ratio measurements are more dependent on positional accuracy than the measurement of the coherent to Compton scattering ratio, R. It will also be demonstrated that a five per cent change corresponds to a shift in position of approximately 2.5 mm. The significance of positional accuracy in clinical situations is discussed in Section 5.9.

Table 5.16 Means and standard errors of measured ratios for five re-positioning measurements

Ratio	Water	Ethanol	Water: Ethanol
$R \times 10^{-4}$	14.3 ± 0.6	8.5 ± 0.5	1.69 ± 0.13: 1
$HP \times 10^{-3}$	41.3 ± 0.4	30.9 ± 0.3	1.34 ± 0.02: 1
$R_k(\delta\varepsilon=51\text{-}56) \times 10^{-3}$	87.9 ± 1.1	71.2 ± 0.8	1.24 ± 0.02: 1

The FWHM and the FW1/3M were also measured from the Compton profile data once the background had been subtracted, and the mean widths from the five re-positioning measurements are shown in Table 5.17, together with the measurements obtained from the 0.5-hour acquisitions described previously (Table 5.4). The measured profile widths for the two data sets were in agreement.

Table 5.17 Means and standard errors of Compton profile widths for five re-positioning measurements

Phantom material	Compton profile width, eV			
	FWHM		FW1/3M	
	0.5-hour	2-hour	0.5-hour	2-hour
Water	1890 ± 20	1930 ± 15	2620 ± 30	2640 ± 30
Ethanol	1790 ± 20	1820 ± 15	2420 ± 30	2450 ± 30
Water-Ethanol	100 ± 30	110 ± 20	200 ± 45	190 ± 45

This series of re-positioning measurements demonstrated that the Compton profile ratios might be sensitive to the geometry of the experimental set-up. To determine how sensitive the experimental results were to the positioning of the phantom a further set of measurements was performed using a block of lard in place of the filled polythene container. The lard was deliberately positioned with the source-detector focus at different depths from the surface of the lard. A block of lard was used for these measurements as it had a more uniform shape than the flexible polythene container used for the water and ethanol measurements and so could be positioned more accurately. A 10 mm diameter aperture was used on the detector collimator, and a 5 mm diameter aperture on the source collimator.

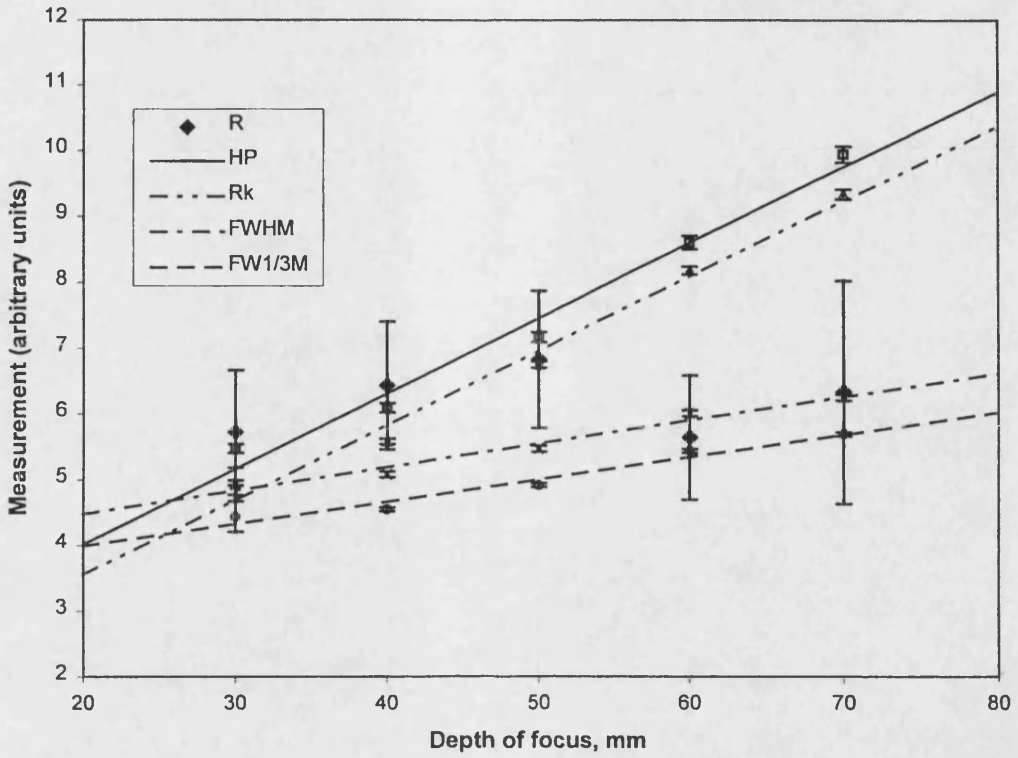

Figure 5.10 Spectrum measurements versus depth of focus in lard

The block of lard was positioned with the source-detector focus at different depths from the surface of the lard over the range 30 mm to 70 mm in 10 mm steps. Two data acquisitions of two hours each were made at each position. The results are shown graphically in Figure 5.10. The coherent to Compton scattering ratios have large uncertainties associated with them due to the low count rate in the coherent peak, but are consistent with their being fairly insensitive to the positioning of the phantom. The HP and R_k values are more position dependent. The uncertainty in these ratios due to positioning is around two per cent per mm. The measures of FWHM and FW1/3M are less sensitive to positioning with uncertainties of around one per cent per mm (equivalent to 15 eV per mm).

The conclusions from this series of experiments are that all the methods of analysis investigated, with the possible exception of the coherent to Compton scattering ratio, are sensitive to the position of the phantom. Referring back to Table 5.15 the additional uncertainties due to re-positioning were up to about one per cent for the Compton profile ratio analyses. The measurements from varying the depth of the source-detector focus in the block of lard indicate that a one per cent uncertainty would correspond to a positioning displacement of 0.5 mm. This uncertainty in re-positioning arises from the flexible walls

of the polythene containers used for the water and ethanol phantoms, which were chosen to be representative of a "flexible" patient. In a clinical investigation it may not be possible to position the patient to an accuracy of better than ± 2 mm. This would generate uncertainties of up to ± 4 per cent for the Compton profile ratios or ± 2 per cent for the profile width measurements.

5.8 Fat fraction determination

The purpose of the reproducibility and re-positioning measurements for two-hour data acquisitions was to determine their impact on the different analyses and hence their effect on the determination of the fat fraction of an unknown fat/muscle mixture. The uncertainties for fat/muscle mixtures have been determined using the same analysis as Section 5.6, using the data from Table 5.16. The results are shown in Table 5.18. The uncertainties of the coherent to Compton scattering ratio measurements are close to the predicted values in Table 5.13. The uncertainties in the Compton profile ratio measurements are a little larger than predicted because of the re-positioning uncertainties. The uncertainties in fat fraction estimation from Compton profile width measurements are similar to the previous estimates (Table 5.14). From these phantom studies the Compton profile ratios HP (MacKenzie 1990) and R_k (Tartari *et al* 1992) would still appear to be the preferred measurements for producing the lowest uncertainty in fat fraction estimation.

Table 5.18 Uncertainty (1 standard deviation) in fat fraction measurement with single source for 2-hour acquisitions

Method of analysis	Uncertainty in fat fraction
R	0.10
HP	0.04
R_k ($\delta\varepsilon$=51-56)	0.06
FWHM	0.14
FW1/3M	0.16

The uncertainties in fat fraction estimation determined from measurements of Compton profile shape are given in Table 5.18. Although the FW1/3M appears to give better discrimination between water and ethanol there is no significant improvement in the uncertainty in fat fraction determination because of the greater measurement uncertainty on the FW1/3M.

All the values in Table 5.18 for the estimated uncertainty in fat fraction determination are derived from measurements on phantoms. Table 5.15 demonstrates that there is only a marginal increase in uncertainty due to re-positioning the phantom when simulating the clinical situation. However, positioning a patient may introduce larger uncertainties. Figure 5.10 shows that the ratios HP (MacKenzie 1990) and R_k (Tartari *et al* 1992) change by two per cent per mm position displacement. Assuming that the patient could be positioned to an accuracy of ± 2 mm, the uncertainty in fat fraction estimation based on Compton profile ratio measurements may be four times greater than the values in Table 5.18. Similarly the profile width measurements are subject to an uncertainty of one per cent per mm position displacement, and for the clinical situation may generate an uncertainty in fat fraction estimation double the value in Table 5.18.

5.9 Summary of Investigations

Several different methods of analysis of spectral data from a backscattering technique have been investigated as methods for the determination of fat fraction in a fat/muscle mixture. Included in the investigation has been the examination of the effect of change in the phantom/patient positioning which might be expected in practice.

The coherent to Compton scattering ratio measurement gives good discrimination between the fat and muscle substitutes (ethanol and water) but has larger uncertainties associated with it than the other methods for a short acquisition time suitable for a clinical investigation (30 minutes). The larger uncertainties are due to the low count rate in the coherent peak. However, this method seems the least sensitive to positioning uncertainties.

The Compton profile width measurements (FWHM and FW1/3M) demonstrated a difference between phantoms containing water and ethanol but larger uncertainties in fat fraction determination than obtained with the coherent to Compton scattering ratio method. The Compton profile width method demonstrated a difference of one per cent per mm in positioning the phantom.

The Compton profile ratios HP (MacKenzie 1990) and R_k (Tartari *et al* 1992) had good counting statistics but gave less discrimination between water and ethanol than the coherent to Compton scattering ratio measurements. The Compton profile ratio

measurements were dependent on the phantom position, with a difference of two per cent per mm change in phantom position.

In conclusion, there does not seem to be a clear advantage of one method over any other for the determination of fat fraction. The uncertainties in the coherent to Compton scattering ratio appear to be the most predictable for determining the fat/muscle content of a mixture. Despite large uncertainties due to poor counting statistics because of the low number of counts in the coherent peak, this method of analysis gives the greatest discrimination between water and ethanol. In a clinical situation where positioning cannot be performed as accurately due to the variable shape of the skin surface, this may be the preferred method and should enable a fat fraction determination with an uncertainty of about 0.1 (one standard deviation).

One application of this technique might be to measure breast tissue density. Boyd *et al* (1995) found statistically significant increases in breast cancer risk associated with increasing mammographic density determined by radiologists and computer assisted methods. Six categories were used to classify breast density from 0 per cent (normal), less than 10 per cent, 10-24 per cent, 25-49 per cent, 50-74 per cent and greater than 75 per cent. All the methods investigated in this report would be useful in assigning the fat fraction of the breast tissue to the categories suggested by Boyd *et al* (1995) in order to determine breast cancer risk.

The technique might also be suitable for monitoring nutritional status (i.e. degree of muscle wasting) by determining the fat fraction in a limb. It might also be applicable as a non-invasive method of determining the fat fraction in the liver as an aid to diagnosis of diffuse liver disease.

Chapter 6 Investigations of Bone Mineral Composition

6.1 Introduction

The studies reported in this chapter investigate the possibility of using a gamma-ray backscattering technique to determine the bone mineral density in the spine. Bone mineral density of the spine is used as an indicator of osteoporosis, as described in Chapter 1. The lumbar spine is the body site most commonly monitored for osteoporosis. The lumbar vertebrae have a high content of trabecular bone (approximately 50 per cent), and it is the trabecular bone that is more susceptible to osteoporotic changes. Trabecular bone has a more rapid turnover than cortical bone and so is more susceptible to metabolic variations. Most adults reach their peak bone mass at the age of 35 years. Osteoporosis usually starts in the central skeleton and later affects peripheral sites. Therefore in order to early detect osteoporotic changes it is better to measure the bone mineral density in the central skeleton. A phantom has been used to investigate the feasibility of using a gamma-ray backscattering technique to determine bone mineral density in the lumbar spine.

Dual energy x-ray absorptiometry (DEXA) and quantitative computed tomography (QCT) are usually used to measure the bone mineral density in the spine or hip, but these are both expensive techniques. In contrast, gamma-ray backscattering methods are relatively inexpensive. The advantages of both DEXA and QCT are that they also yield images of the spine. A backscattering technique might prove useful as a screening tool for osteoporosis prior to using more expensive techniques to investigate the patient further. To be useful in this way, the backscattering technique must yield similar precision to the DEXA and QCT measurements. Estimates of the precision of bone mineral density measurements in the spine using these methods are between one and two per cent. An upper limit for the precision of an inexpensive screening tool is proposed as five per cent of the difference in density between lean tissue (water) and healthy trabecular or spongiosa bone for a clinically realistic situation. Spongiosa bone is defined in ICRU Report 44 (1989) as 33 per cent cortical bone and 67 per cent marrow. As the difference in density between spongiosa bone and lean tissue is about 180 kg m^{-3}, the upper limit of precision is about 9 kg m^{-3}, i.e. just less than one per cent of the actual density measurement. In the work that follows the precision achievable with a bone phantom at various depths in a

tissue phantom is explored with a view to assessing whether the backscattering technique can be made sufficiently precise for clinical use.

To examine the possibility of using the gamma-ray backscattering technique for peripheral sites other phantoms have been constructed. These are discussed in Chapters 7 and 8. Phantoms have been constructed to simulate the heel bone (calcaneus) and the jawbone (mandible), which may be other areas of interest for this type of skeletal status monitoring. A measurement of the bone density at a peripheral site can still be useful in demonstrating a decrease in bone mass even if the bone has not become osteoporotic and may determine whether or not a patient should be referred for a bone mineral density measurement of the spine.

6.2 Description of the lumbar spine

The lumbar spine forms part of the vertebral column as shown in Figure 6.1, and consists of five vertebrae, which support the lower back. The lumbar vertebrae are the largest and strongest vertebrae in the column and their various projections are short and thick.

A superior view of a lumbar vertebra is shown in Figure 6.2. The body is the thick disc shaped anterior portion that is the weight bearing part of the vertebra. Its superior and inferior surfaces are roughened for the attachment of intervertebral discs. The vertebral arch extends posteriorly from the body and with the body it surrounds the spinal cord. The arch is formed by two short thick pedicles, which project posteriorly from the vertebral body to unite with the laminae. The laminae are the flat parts, which join to form the posterior portion of the vertebral arch. The space between the vertebral arch and the body is called the vertebral foramen. The vertebral foramens of all vertebrae together are known as the spinal canal. Seven processes arise from the vertebral arch. The two transverse processes and two spinous processes are for muscle attachment, whilst the two superior and two inferior processes articulate with the vertebrae superior and inferior to them. The articulating surfaces are known as facets.

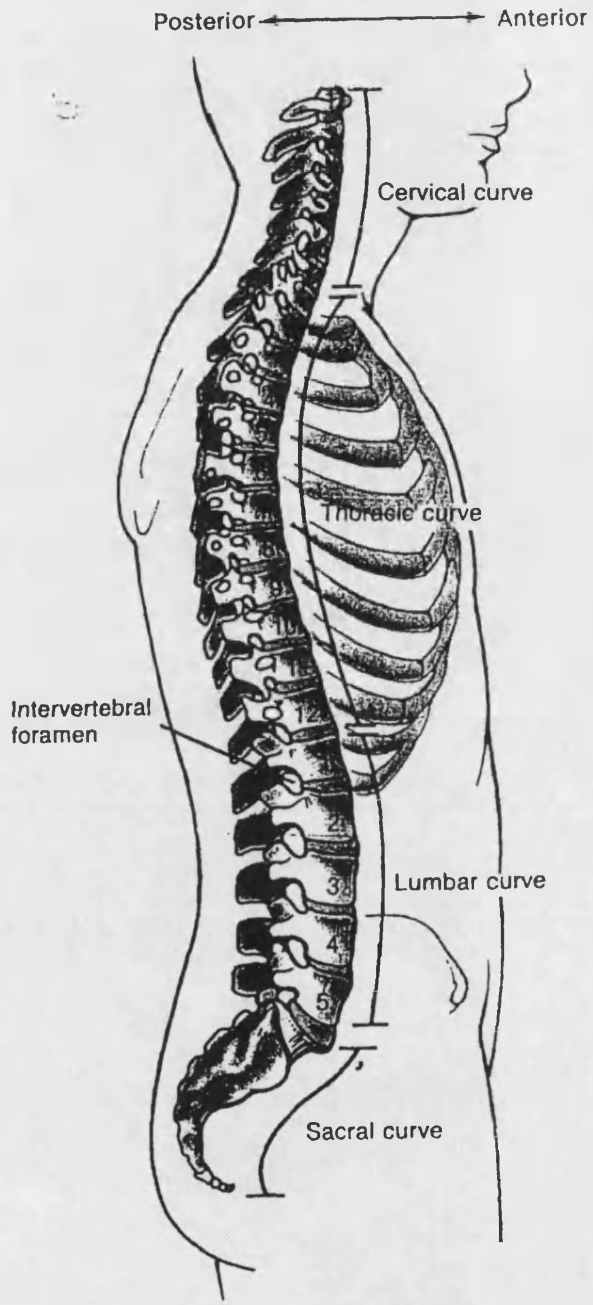

Figure 6.1 Diagram to show position of lumbar spine within vertebral column (Tortora and Anagnostakos 1987)

In the adult skeleton the bodies of the lumbar vertebrae are of the order of 40 mm diameter and 25 mm thick. Measurements from CT scans demonstrate that the lumbar vertebral bodies lie at depths of 80-90 mm beneath the posterior skin surface in the adult.

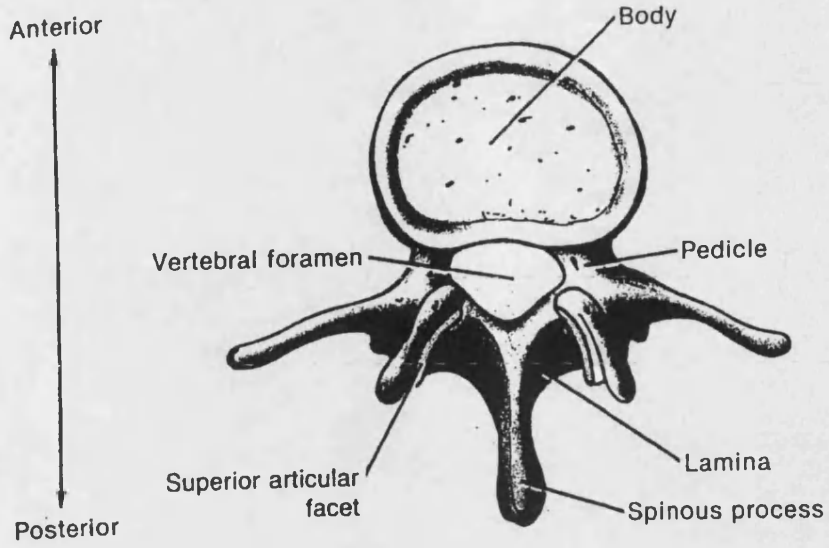

Figure 6.2 Superior view of lumbar vertebra (Tortora and Anagnostakos 1987)

6.3 Experimental arrangement

To simulate the lumbar vertebrae bodies, polythene containers 38 mm diameter and 65 mm in height were filled with different concentration solutions of potassium hydrogen phosphate (K_2HPO_4). Solutions of K_2HPO_4 of different concentrations have been used to mimic trabecular bone and also cortical bone. This compound is easily soluble in water and can be made up into solutions having a similar effective atomic number, Z, to trabecular bone (approximate range $8<Z<11$). Solutions of K_2HPO_4 have been widely used in radiological measurements for the simulation of bone (Ling *et al* 1982, Stalp and Mazess 1980 and Karellas *et al* 1983). Different solutions varying in concentration between 0 g and 90 g per 100 ml of distilled water corresponding to densities of 995 kg m^{-3} for distilled water up to 1493 kg m^{-3} for the most concentrated solution were prepared. The most concentrated solution had a density comparable to that expected in the lumbar vertebrae, which are composed of around 50 per cent each of trabecular and cortical bone of density 1180 kg m^{-3} and 1920 kg m^{-3} respectively (ICRU 44 1989). The densities of the different concentration solutions of K_2HPO_4 were determined by weighing measured volumes of each solution:

Concentration (g/100 ml):	0	9	30	60	90
Density (± 2 kg m^{-3}):	995	1067	1192	1369	1493

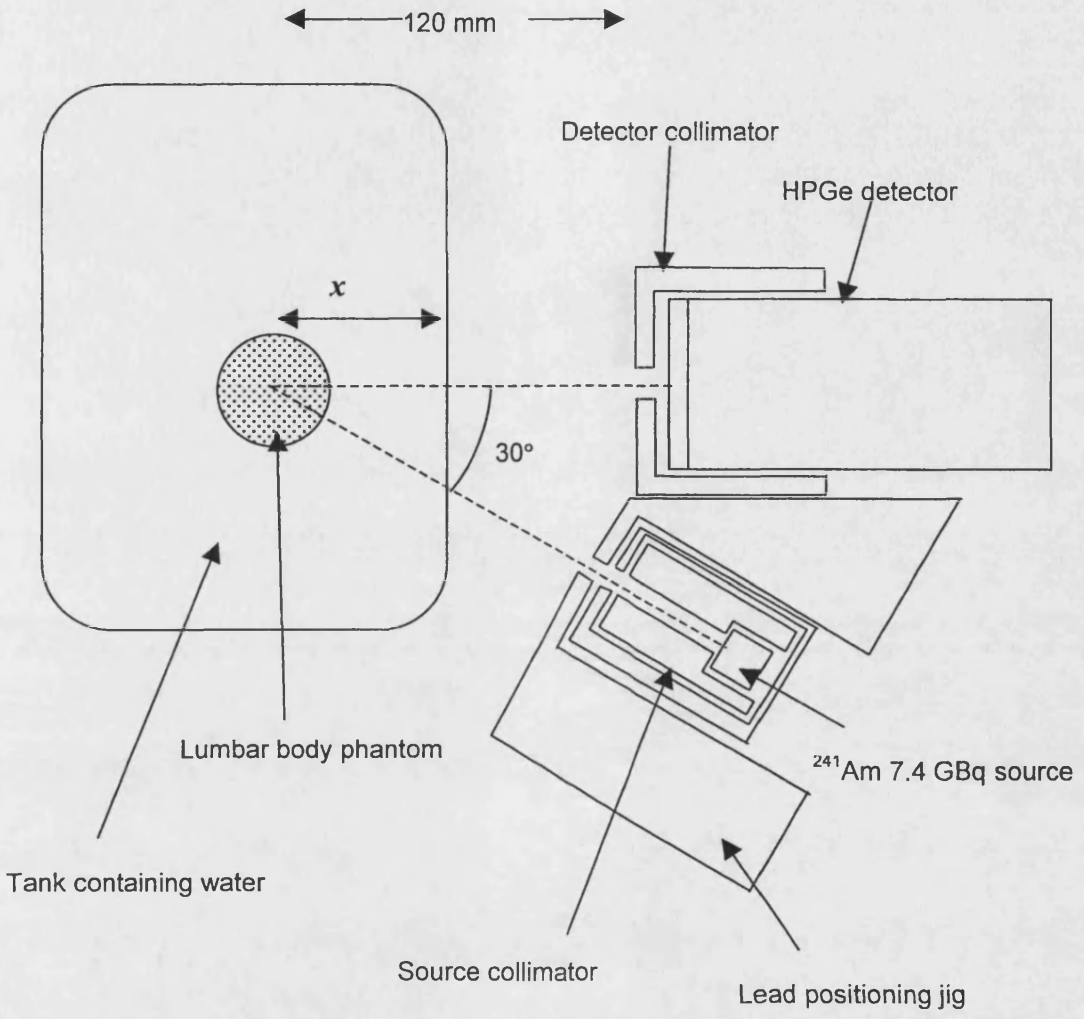

Figure 6.3 Experimental arrangement for lumbar spine investigations. The lumbar body phantom is in air or at a depth *x* in the water tank.

The experimental arrangement is shown in Figure 6.3. For the first set of measurements the 38 mm diameter polythene containers were placed in air (i.e. without the large water container present) and filled with either water or a different concentration of K_2HPO_4. The centre of the container was positioned at the focus of the source-detector arrangement. For all the investigations the 7.4 GBq americium-241 bead source was collimated with an aperture of 5 mm diameter. The detector was collimated with a 5 mm diameter aperture, which allowed a nominal acceptance cone of 21 mm diameter at the intersection of the source and detector axes. Acquisition times were 24 hours. These measurements were

made to determine whether the technique was sensitive to the different concentrations of the bone mimic. Examples of the spectra obtained from this set-up are shown in Figure 6.4.

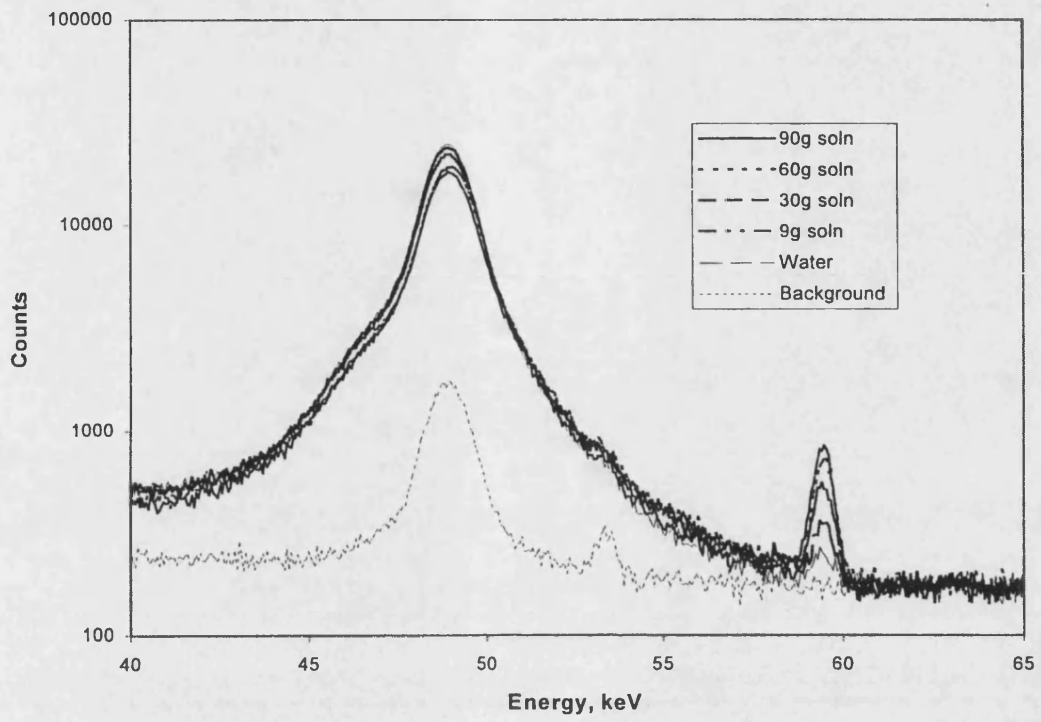

Figure 6.4 Spectra acquired in 24 hours from lumbar body phantom in air containing water and different concentration solutions of K_2HPO_4

For the second set of measurements, the 38 mm diameter polythene containers were again positioned at the focus of the source-detector arrangement, but immersed in a water tank to mimic the *in vivo* situation. The depth of water between the incident surface and the container was varied so that the distance from the incident surface to the centre of the bone phantom was between 35 mm and 60 mm. Data were again acquired for 24 hours for each set-up.

The spectra obtained from these measurements (with the background subtracted) were examined to determine the coherent to Compton scattering ratios (Section 6.4), the Compton profile shapes (Section 6.5) and the Compton profile ratios (Section 6.6). A background spectrum was obtained with an empty 38 mm diameter polythene container placed at the focus.

The measurements for the lumbar spine phantom in air were then repeated with a 40 mm diameter aperture on the detector collimator so that the whole of the detector face was exposed. The data acquisition time was one hour. These measurements were to determine whether or not it would be possible to increase the count rate sufficiently whilst reducing the acquisition time, in order to assess the feasibility of a clinical application. The results of these one-hour investigations are reported in Section 6.9.

6.4 Coherent to Compton scattering ratios

The spectra acquired for 24 hours from different concentrations of bone solution in air shown in Figure 6.4 demonstrate that the coherent signal is much stronger than that seen in double the acquisition time from samples of water and ethanol (Chapter 5, Figure 5.2). As expected the coherent peak shows a marked increase in size with increasing concentration of K_2HPO_4 solutions and hence increasing atomic number. In contrast the Compton spectra are not influenced significantly by the increasing concentration of the K_2HPO_4 solutions. The acquired spectra for the in-air studies were used to determine the coherent to Compton scattering ratio for the different concentrations of the K_2HPO_4 solutions. The calculated values have also been determined for a scattering angle of 150° and incident energy of 59.54 keV. The two sets of values are tabulated in Table 6.1. The coherent peak, which was well defined for these data acquisitions, was integrated over the range 58.5 keV to 60.5 keV, and the Compton region was integrated over the range 45 keV to 52 keV, equivalent to the full width tenth maximum, as for the water and ethanol studies. The uncertainties in Table 6.1 are one standard deviation due to counting statistics.

Table 6.1 Calculated and measured values of coherent to Compton scattering ratio for different concentrations of K_2HPO_4 (24 hours)

Concentration: g per 100 ml water	Coherent to Compton scattering ratio, R ($\times 10^{-4}$)	
	Calculated	Measured
0	13.88	14.6 ± 1.4
9	29.46	28.6 ± 1.5
30	59.25	62.2 ± 1.7
60	89.75	99.0 ± 2.1
90	110.81	122.3 ± 2.3

The calculated and measured values of the coherent to Compton scattering ratio in Table 6.1 show similar trends. There is an increase in ratio value of eight-fold over this range of concentration of the K_2HPO_4 solution. This should give good sensitivity for discrimination between different concentrations. However, at low concentrations the uncertainties from counting statistics are large. In the coherent region the background count was around 6000 with an additional 1200 counts for water and 7500 counts from the 1493 kg m^{-3} density solution. These low counts gave rise to uncertainties on the measured ratios of around 10 per cent for water and two per cent for the most concentrated solution of K_2HPO_4 of 90 g per 100 ml distilled water (density 1493 kg m^{-3}). These uncertainties are for a 24-hour data collection period. As discussed earlier (Chapter 5, Section 5.1), for a clinical application the acquisition time should be no longer than 30 minutes. Since the coherent signal for bone solutions is almost double that for the water and ethanol studies (Chapter 5, Figure 5.2), it should be possible to use a clinical acquisition time of only 15 minutes for bone studies. If a four-source system were to be used for a 15-minute acquisition period the expected uncertainties would be 50 per cent for the water measurement and 10 per cent for the densest solution.

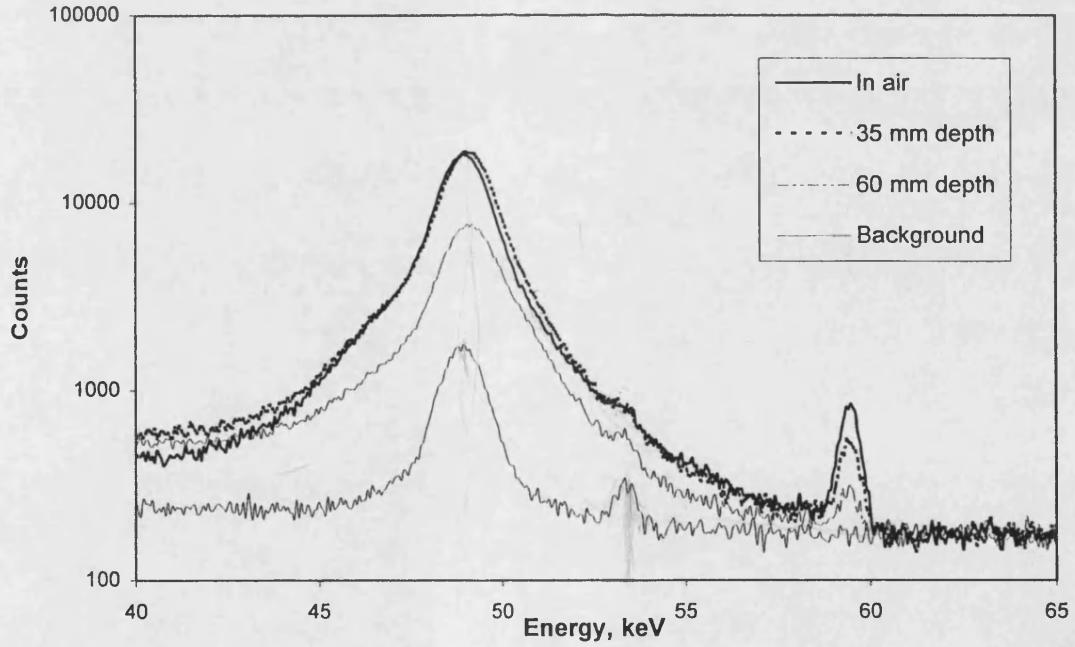

Figure 6.5 Spectra from lumbar body phantom containing K_2HPO_4 density 1493 kg m^{-3}, in air and at a different depths in a water tank; 24-hour acquisitions

When the bone phantom is placed in the water tank to simulate the *in vivo* situation the water attenuates both the incident beam and the scattered radiation. In addition the water

surrounding the bone phantom also acts as a scatterer. The attenuation of the coherent peak with depth is clearly shown in Figure 6.5. In this figure the measured spectra from a lumbar body phantom containing K_2HPO_4 solution of density 1493 kg m^{-3} are plotted for the phantom in air and at depths of 35 mm and 60 mm in the water tank. Compared with the in-air measurement, the number of counts in the coherent peak for the 35 mm depth measurement is 60 per cent, and for the depth of 60 mm the number of counts is 22 per cent. These values correspond closely with the values expected for the attenuation of 59.54 keV photons in water (52 per cent and 17 per cent respectively). Depths greater than 60 mm were not investigated as the coherent peak at low concentrations of K_2HPO_4 solution at 60 mm depth became close to the background level with a consequent large increase in uncertainties.

To ascertain whether a measurement of the coherent to Compton scattering ratio can distinguish between different bone densities when surrounded by water (simulating soft tissue), data were acquired for different concentration K_2HPO_4 solutions in the lumbar body phantom at different depths in a water tank. The lumbar body phantom was placed at depths of 35 mm and 60 mm

Table 6.2 tabulates the measured values of coherent to Compton scattering ratio obtained for the lumbar body phantom in air and at different depths from the outer wall of a water tank which simulated the *in vivo* conditions. The different concentrations of K_2HPO_4 used for these investigations and their densities are given in the table.

Table 6.2 Measured coherent to Compton scattering ratio with one standard deviation, for lumbar body phantom in air and at depth in water tank

Concentration, g/100ml	Density, ± 2 kg m^{-3}	Coherent to Compton scattering ratio, R($\times 10^{-4}$)		
		In air	35 mm	60 mm
0	995	14.6 ± 1.4	13.4 ± 1.4	19.5 ± 3.6
30	1192	62.2 ± 1.7	36.2 ± 1.6	39.2 ± 3.9
60	1369	99.0 ± 2.1	55.8 ± 1.8	52.8 ± 4.2
90	1493	122.3 ± 2.3	68.7 ± 2.0	59.9 ± 4.3

For the water-filled phantom the measured ratios in air and at a depth of 35 mm in a water tank are within the standard deviations of each other. At a depth of 60 mm the measured ratio is slightly larger but so is the uncertainty on the measurement.

For the lumbar body phantom in-air measurements, the measured value of coherent to Compton scattering ratio increases with density and is close to the value predicted from calculation. This increase in ratio with density is evident at the depths of 35 mm and 60 mm in the water tank. However, the increase in measured ratio for the increasing density of the solutions is reduced as the amount of overlying water is increased and the proportion of Compton scattering increases.

When the lumbar body phantom is placed in the water tank the overlying water contributes to the detected scatter spectrum in addition to the irradiated bone phantom. This is clear from Figure 6.5 where the Compton scatter spectrum is not attenuated as rapidly as the coherent scatter spectrum for the 1493 kg m^{-3} density K_2HPO_4 solution.

For the coherent to Compton scattering ratio to be of value as a measurement technique to determine the density of bone at a depth in tissue it must be able to differentiate between different densities at a known depth in tissue. This assumes that the depth can be assessed with sufficient precision. Figure 6.6 plots the variation of the coherent to Compton scattering ratio normalised to water against the concentration of K_2HPO_4 in the lumbar body phantom. The variation is shown for the lumbar body phantom in air and at depths of 35 mm and 60 mm in the water tank. For both the in-air and calculated values there is an eight-fold increase in value over the range of densities investigated. This increase in ratio value drops to a three-fold difference when the lumbar body phantom is at a depth of 60 mm in the water tank. At 60 mm depth the number of counts in the spectrum are reduced due to the attenuation by the water and consequently the uncertainties on the measured values are greater.

The uncertainty in the estimated bone density is related to the uncertainty in the measured coherent to Compton scattering ratio by the following expression:

$$\Delta D = (1/S) \times \Delta(R/R_w) \qquad \textbf{Equation 6.1}$$

where ΔD is the uncertainty in the density,

S is the slope of the curve of R against D, and

$\Delta(R/R_w)$ is determined by the counting statistics and is the uncertainty in the measured coherent to Compton scattering ratio normalised to the measured water ratio (R/R_w).

In Figure 6.6, a least squares method has been used to fit the data. Close to the density of trabecular bone (1192 kg m^{-3}), the uncertainties on the measured ratio values (normalised to water) are 0.12, 0.12 and 0.20, for measurements made in air and at 35 mm and 60 mm depth respectively. The corresponding values of S are 0.015, 0.008 and 0.004 m^3 kg^{-1}, giving uncertainties in density of ± 8 kg m^{-3} (0.6%), ± 15 kg m^{-3} (1.3%), and ± 50 kg m^{-3} (4.2%).

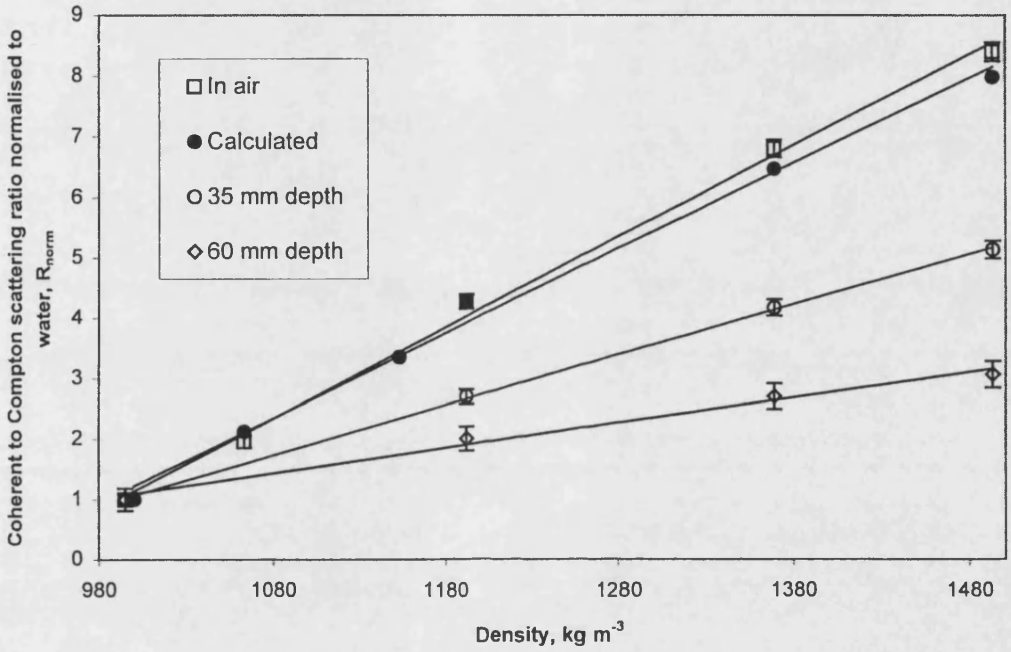

Figure 6.6 Calculated and measured coherent to Compton scattering ratios for lumbar body phantom in air and at different depths in a water tank

The proposed precision target of one per cent of the density measurement is met for the measurement in air but just exceeded for the measurement at 35 mm depth. At 60 mm depth the precision target is exceeded and therefore this technique would not be suitable for measuring bone density in the lumbar spine as the vertebral bodies lie at a depth of more than 60 mm in tissue.

In order to increase the count rate to obtain acceptable counting statistics in one hour the collimator aperture on the detector would need to be increased. This in turn would lead to an increase in the proportion of Compton scatter and a consequent reduction in the value of the coherent to Compton scattering ratio R.

To summarise:

- The density estimation of a solution of K_2HPO_4 with a density close to that expected for trabecular bone has a precision of up to 1.3 per cent at depths up to 35 mm in water. However at greater depths such as those of the lumbar spine the uncertainties become too large for a useful measurement of bone density.

- The contribution to the Compton scatter from overlying water reduces the measured value of the coherent to Compton scattering ratio and consequently makes the slope of R against density very dependent on depth, even at shallow depths for more superficial bones. Therefore to use the technique for the measurement of bone density of superficial bones would require a careful estimation of the depth of tissue overlying the bone.

6.5 Compton profiles

The Compton profile shape was determined from the lumbar body phantom in-air data acquisitions for the phantom filled with water and the most concentrated bone substitute solution (density 1493 kg m^{-3}) in order to assess the maximum difference that might be observed. The full width half maximum (FWHM), the full width third maximum (FW1/3M) and the full width quarter maximum (FW1/4M) of the Compton profiles were measured. The Compton profiles are shown graphically in Figure 6.7 and the measured profile widths are tabulated in Table 6.3.

The differences in profile widths between the measurements for the two solutions are comparable to the differences between water and ethanol in a 13 mm diameter phantom (Tables 5.5 and 5.6). The most concentrated solution of K_2HPO_4 was equivalent to a density of 1493 kg m^{-3}, compared with a cortical bone density of 1920 kg m^{-3} and spongiosa bone density of 1180 kg m^{-3}.

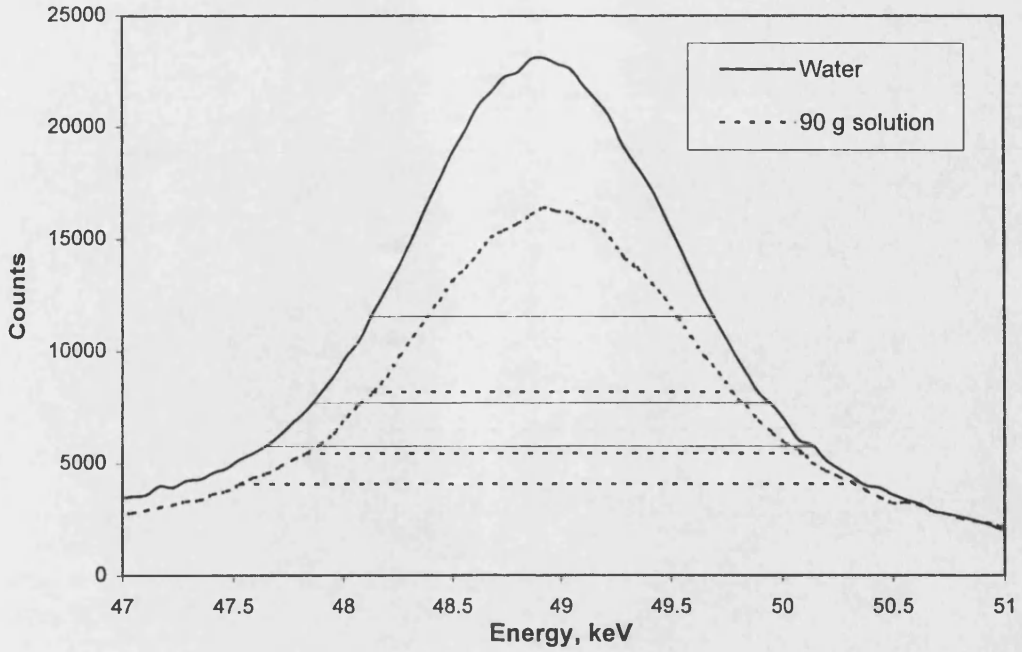

Figure 6.7 Compton profiles from lumbar body phantom in air for 24-hour acquisitions, for water and 90 g K_2HPO_4 per 100 ml water. The positions of the FWHM, FW1/3M and FW1/4M are indicated.

Table 6.3 Compton profile width measurements from spectra acquired from lumbar body phantom in air

Phantom content	FWHM, eV	FW1/3M, eV	FW1/4M, eV
Water	1580 ±10	2100 ± 20	2520 ± 30
K_2HPO_4 soln.*	1650 ±10	2285 ± 20	2810 ± 30
Difference	70 ± 15 (21%)	185 ± 30 (16%)	290 ± 40 (14%)

*90g K_2HPO_4 per 100 ml water (density 1493 kg m^{-3})

In conclusion, it would appear that even for the 24-hour counting times the differences in the width of the Compton profiles are not sufficiently large to determine change in bone density at intermediate densities more characteristic of spongiosa bone. The greatest difference in Compton profile width between water and the 90 g solution of K_2HPO_4 is the measure of FW1/4M. Even at this density the standard deviation is 14 per cent which is outside the target precision of five per cent of the difference in density between bone and water. For acquisition times suitable for a clinical investigation (a maximum of 30 minutes rather than 24 hours) the uncertainties for the width measurement due to low counts in this region would be even greater.

6.6 Compton profile ratios

The ratio HP proposed by MacKenzie (1990) and the ratio R_k proposed by Tartari *et al* (1992) have also been investigated. These ratios (reviewed in Chapter 2) use the high energy tail of the Compton profile. For the ratio HP (MacKenzie 1990), the numerator is the integrated counts between 52 keV and 58 keV, and the denominator is the integrated counts between 40 keV and 58 keV to include the whole of the Compton profile. For R_k (Tartari *et al* 1992) the limits were chosen as 51 keV to 56 keV in the numerator and 40 keV to 56 keV in the denominator, as described in Chapter 5, Section 5.3. Previously, a second limit of 52 keV to 56 keV in the numerator was also investigated (Chapter 5, Section 5.3). These limits were found to give very similar values to the ratio HP and so have not been investigated further.

Table 6.4 Measured Compton profile ratios from lumbar body phantom in air containing different density solutions of K_2HPO_4

Density, ± 2 kg m^{-3}	HP ($\times 10^{-3}$)	R_k ($\times 10^{-3}$)
995	28.3 ± 0.3	56.1 ± 0.4
1063	31.6 ± 0.3	60.6 ± 0.4
1192	38.5 ± 0.3	70.1 ± 0.4
1369	46.2 ± 0.4	83.2 ± 0.5
1493	48.5 ± 0.4	85.0 ± 0.5

The Compton profile ratios were determined from the spectra acquired from the lumbar body phantom in air containing both water and different concentrations of K_2HPO_4 solution. The results are tabulated in Table 6.4. The HP ratio shows a 1.7-fold increase and the R_k ratio demonstrates a 1.5-fold increase for the most concentrated solution investigated compared with water. This compares with an eight-fold increase for the coherent to Compton scattering ratio. However, the uncertainties due to counting statistics are much less and are similar for water and the different concentration K_2HPO_4 solutions. The greatest relative uncertainty is for the water measurement. This amounts to an uncertainty of one per cent for HP and 0.6 per cent for R_k, compared with 10 per cent for the coherent to Compton scattering ratio, R (Table 6.2).

The Compton profile ratios were similarly determined from the spectra obtained with the lumbar body phantom at different depths in the water tank. They are tabulated in Tables 6.5 and 6.6.

Table 6.5 Compton profile ratio HP for lumbar body phantom containing different density solutions of K_2HPO_4 in air and at depth in water tank

Density, ± 2 kg m^{-3}	HP ($\times 10^{-3}$)		
	In air	35 mm depth	60 mm depth
995	28.3 ± 0.3	32.1± 0.3	43.8 ± 0.7
1192	38.5 ± 0.3	36.4 ± 0.3	47.8 ± 0.7
1369	46.2 ± 0.4	42.5 ± 0.4	52.2 ± 0.8
1493	48.5 ± 0.4	44.1 ± 0.4	53.8 ± 0.8

Table 6.6 Compton profile ratio R_k for lumbar body phantom containing different density solutions of K_2HPO_4 in air and at depth in water tank

Density, ± 2 kg m^{-3}	R_k ($\times 10^{-3}$)		
	In air	35 mm depth	60 mm depth
995	56.1 ± 0.4	65.2 ± 0.4	95.1 ± 0.8
1192	70.1 ± 0.4	72.8 ± 0.4	102.2 ± 0.8
1369	83.2 ± 0.5	81.6 ± 0.4	108.1 ± 0.9
1493	85.0 ± 0.5	84.9 ± 0.5	109.4 ± 0.9

The measured ratios for both HP (MacKenzie 1990) and R_k (Tartari *et al* 1992) increase with increasing density in the lumbar body phantom. The measured ratios of HP and R_k are plotted in Figures 6.8 and 6.9 respectively. A straight line has been fitted to each data set using a least squares method. The figures show that the slopes of the lines reduce with increasing depth due to the increasing proportion of the water signal and the change in geometry. The uncertainty in the estimation of bone density can similarly be determined from Equation 6.1 using the ratio uncertainties in Tables 6.5 and 6.6 normalised to water, and the gradients of the lines in Figures 6.8 and 6.9. For the ratio HP, the uncertainties in the ratio measurements for a solution with density 1192 kg m^{-3} (closest to trabecular bone) are 0.012, 0.010 and 0.016, for measurements in air and depths of 35 mm and 60 mm respectively. The corresponding values of S are 0.0014, 0.0008 and 0.0005 m^3 kg^{-1}, which give uncertainties in density determination of ± 9 kg m^{-3} (0.7 %) in air, ± 13 kg m^{-3} (1.1%) at a depth of 35 mm and ± 32 kg m^{-3} (2.7%) at a depth of 60 mm. The corresponding

values for the uncertainty in ratio measurement R_k are 0.007, 0.0006 and 0.0009 with S values of 0.0011, 0.0006 and 0.0003 $m^3\ kg^{-1}$. These values give uncertainties in density determination of ± 7 kg m^{-3} (0.5%) in air, ± 10 kg m^{-3} (0.8%) at 35 mm depth and ± 30 kg m^{-3} (2.5%) at 60 mm depth respectively. The slightly improved uncertainty figures for the R_k ratio arise from the energy band in the numerator being closer to the Compton peak of the spectrum and therefore having a higher count. For both ratios HP and R_k the measurements in air and at 35 mm depth are within or close to the target precision of one per cent. As with the results of the coherent to Compton scattering ratio measurements the indication is that this method of bone density measurement is becoming too imprecise at the depths required for measurement of the lumbar spine density. A practical instrument would require a detector with a larger aperture collimator in order to increase the count rate sufficiently to allow the acquisition time to be reduced for a clinical application.

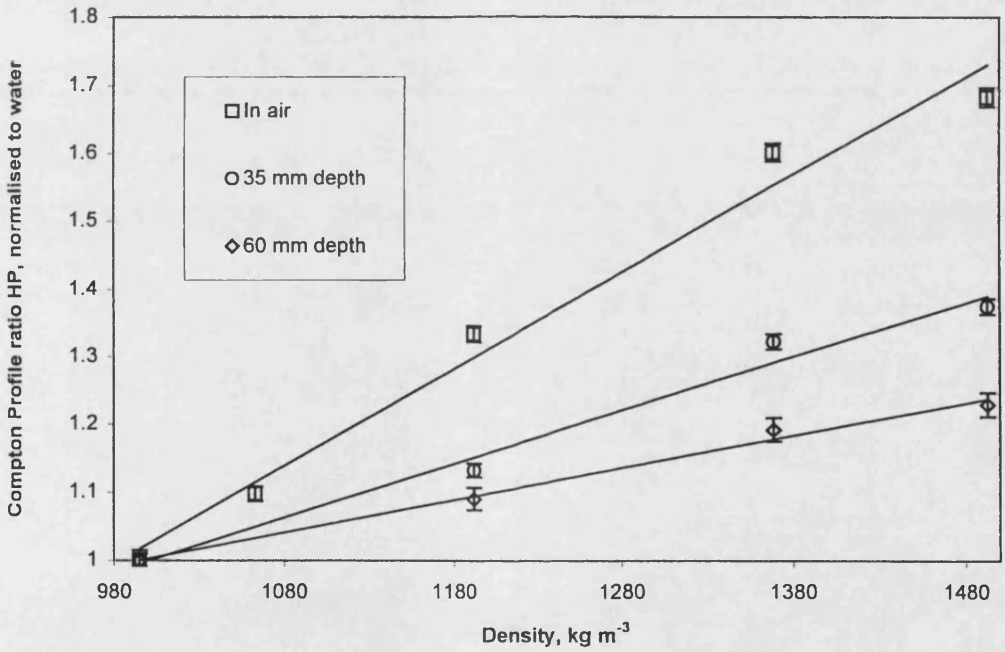

Figure 6.8 Measured HP ratio values normalised to water for lumbar body phantom in air and at different depths in water tank

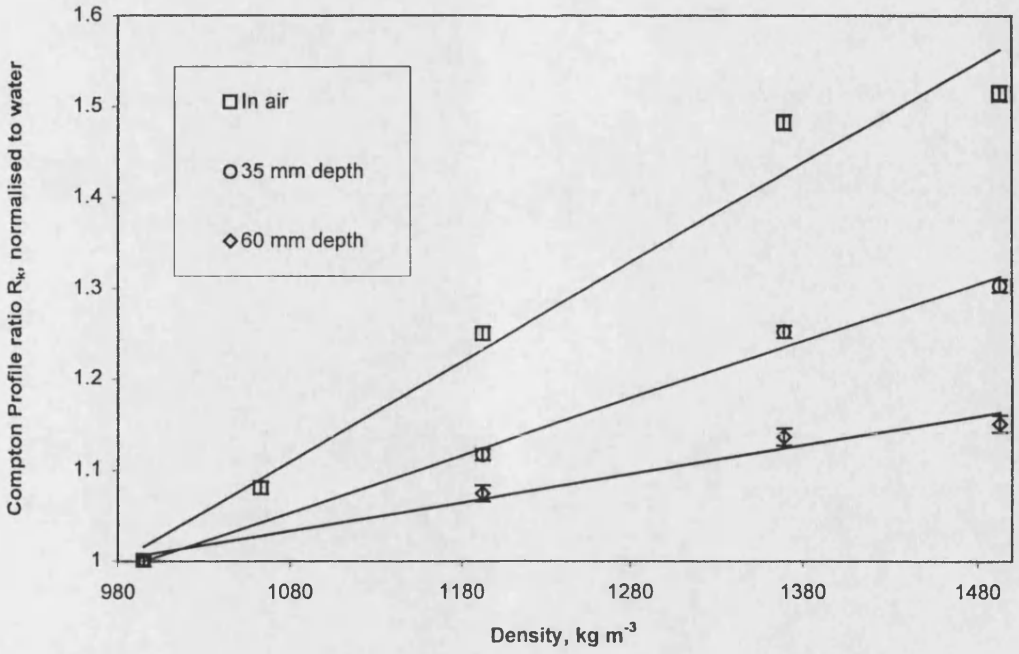

Figure 6.9 Measured R_k ratio values normalised to water for lumbar body phantom in air and at different depths in water tank

Even with the relatively confined geometry employed, the shape of the Compton profile is changing with depth as can be seen from the results of the experiment with the lumbar body phantom at 60 mm depth. Tables 6.5 and 6.6 show that the HP and R_k ratios apparently increase at this depth compared with the values when the lumbar body phantom is at 35 mm depth. However the reason for this is clear from Figure 6.10 where the spectra obtained from the lumbar body phantom in air and at 60 mm depth in water are plotted for the phantom filled with the densest solution of K_2HPO_4 (1493 kg m^{-3}). The spectrum from the lumbar body phantom at a depth has been normalised to the peak count rate obtained for the phantom in air. The Compton peak energy has increased by around 0.2 keV on the spectrum acquired with the phantom at a depth of 60 mm. The spectrum obtained from the lumbar body phantom in the water tank is also much broader than that obtained in air due to the increase in multiple scatter arising from the extra depth of water and the increased range of scattering angles viewed by the detector.

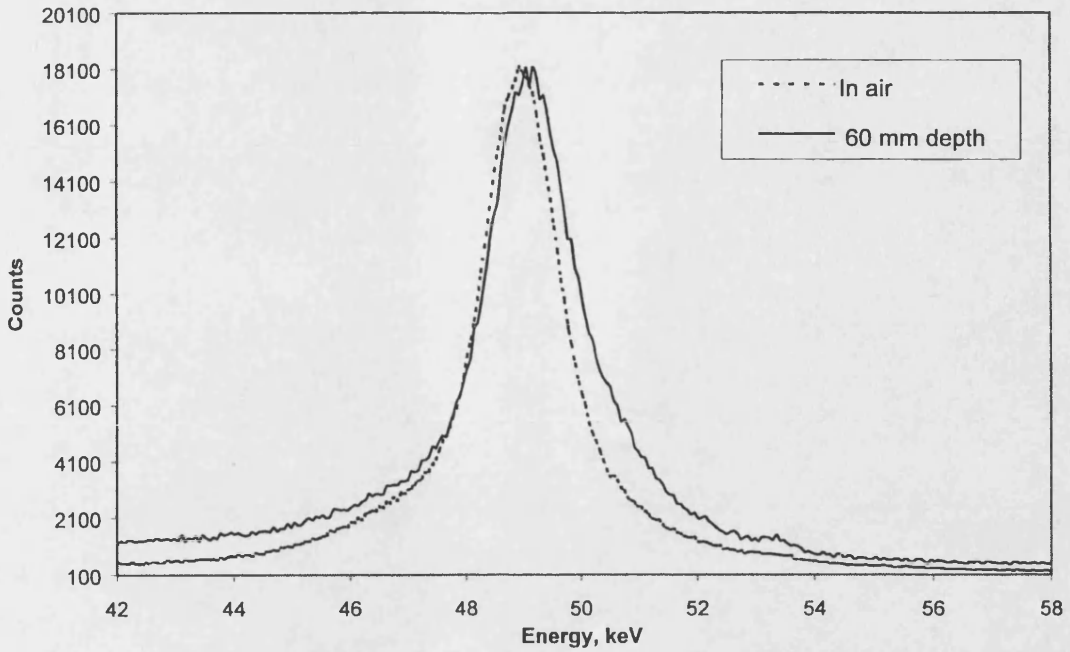

Figure 6.10 Spectra for lumbar body phantom filled with K_2HPO_4 density 1493 kg m^{-3} in air and at depth 60 mm normalised to Compton peak count rate in air

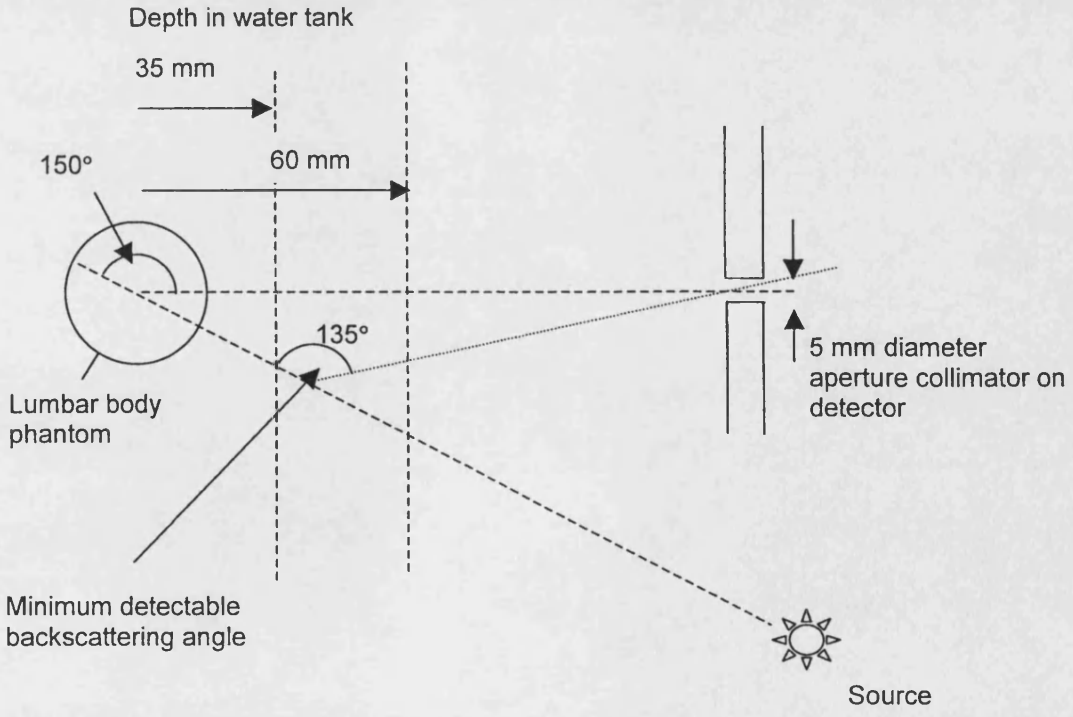

Figure 6.11 Schematic diagram to demonstrate minimum detectable backscattering angle in presence of overlying water

The shift in peak energy is equivalent to a reduction in average scattering angle of 4°, from around 149° to 145°. Figure 6.11 demonstrates how the range of scattering angles detected increases as the depth of water overlying the lumbar body phantom is increased. With the geometry used and a 5 mm diameter aperture on the detector collimator, the minimum detectable single scattering angle is 135° which occurs at a depth of 40 mm.

6.7 Comparison with the results of other workers

Both Karellas *et al* (1983) and Gigante and Sciuti (1985) have investigated a backscattering technique for the determination of bone mineral content. In their work, bone phantoms were irradiated in air without being surrounded by a soft tissue phantom. Their experimental arrangement may therefore be compared with the in-air measurements reported here. The dimensions of the phantom used by Karellas *et al* (1983) were $30 \times 30 \times 30$ mm^3 and Gigante and Sciuti (1985) used a cylindrical box 32 mm diameter and 35 mm in height. The bone phantom used for the work reported here was a cylinder 38 mm diameter filled to a height of 65 mm. Karellas *et al* (1983) used a line of six americium-241 bead sources with total activity of 44.4 GBq collimated to produce a fan beam, and explored scattering angles in the range 37° up to a maximum of 98°. Gigante and Sciuti (1985) used a single 7.4 GBq americium-241 source and performed similar investigations but with scattering angles up to 135°. This latter geometry is more similar to the present work, which uses the same activity point source and a scattering angle of 150°.

In the system employed by Karellas *et al* (1983) a 15-minute irradiation resulted in an estimated density uncertainty (one standard deviation) of 0.19 per cent for the data acquired with a backscattering geometry of 98°. Gigante and Sciuti (1985) quote a 1.1 per cent uncertainty in weight fraction in a 400-second acquisition with a backscattering geometry of 135°. However Karellas *et al* (1983) used six americium-241 bead sources for a longer irradiation time than Gigante and Sciuti (1985). If for comparison a one-hour irradiation time is assumed for both systems and a single 7.4 GBq americium-241 bead source is employed the uncertainties would become 0.23 per cent and 0.37 per cent for the systems of Karellas *et al* (1983) and Gigante and Sciuti (1985) respectively. These values are much closer to each other than the published values, even though the comparisons are crude since the precise geometries are not given in the publications.

The uncertainties above of standard deviations less than 0.4 per cent in density determination are much smaller than the value obtained in Section 6.4 for the current work. For the most concentrated solution (density 1493 kg m^{-3}) the uncertainty in the density determination (one standard deviation) is 0.7 per cent for a 24-hour exposure which is equivalent to 3.4 per cent for a one-hour exposure.

The probable reason for the increased uncertainty in this work is the low count rate achieved. In order to reduce the contribution from tissue scatter surrounding the bone phantom at different depths narrow collimation was used on both the source and detector. Both collimators had 5 mm diameter apertures. To achieve a higher count rate the in-air experiment was repeated with the detector collimator aperture increased to 40 mm diameter. This enabled the whole of the detector face to be exposed (32 mm diameter). In addition to using more of the detector area this geometry gave an acceptance cone of 76 mm diameter at the focus compared with 21 mm diameter for the 5 mm diameter aperture. Therefore the detector viewed the whole of the bone phantom. Acquisitions were made for one hour, with water and the different density solutions of K_2HPO_4 in the 38 mm diameter phantom in air. (An acquisition time of one hour with one source will give the same uncertainties as the proposed system with four sources and a 15-minute acquisition period.) The results for the phantom in air with the two detector collimators and acquisition times are given in Table 6.7. The quoted uncertainties are one standard deviation from counting statistics.

Table 6.7 Measured coherent to Compton scattering ratio R, for lumbar spine phantom in air, for two aperture diameters in detector collimator

	Coherent to Compton scattering ratio, R ($\times 10^{-4}$)	
Density, ± 2 kg m^{-3}	5 mm dia. aperture 24-hour acquisition	40 mm dia. aperture 1-hour acquisition
995	14.6 ± 1.4	11.6 ± 0.4
1192	62.2 ± 1.7	53.8 ± 0.7
1369	99.0 ± 2.1	89.4 ± 1.0
1493	122.3 ± 2.3	116.7 ± 1.2

The measured values of coherent to Compton scattering ratio obtained from the one-hour acquisitions with the larger detector aperture are slightly lower than those obtained from the 24-hour acquisitions, but more multiple scatter in the Compton region will be detected with the large aperture collimator. The uncertainties due to counting statistics have been

reduced by using the large diameter aperture on the detector. For the solution with a density of 1192 kg m^{-3} the uncertainties on the measured coherent to Compton scattering ratio due to counting statistics were 2.8 per cent for the 24-hour acquisition with a 5 mm diameter aperture. This uncertainty reduced to 1.4 per cent for the one-hour acquisition with the 40 mm diameter aperture. This latter value compares with the uncertainty in counting statistics obtained by Karellas *et al* (1983) which was equivalent to 2.1 per cent for the same source activity and one-hour acquisition. When each series of the measured ratios are normalised to the water value they demonstrate good agreement. The normalised values for these two sets of measurements are plotted in Figure 6.12. A least squares method has been applied to both data sets in order to determine the uncertainty in density determination as described by Equation 6.1. The results are given in Table 6.8.

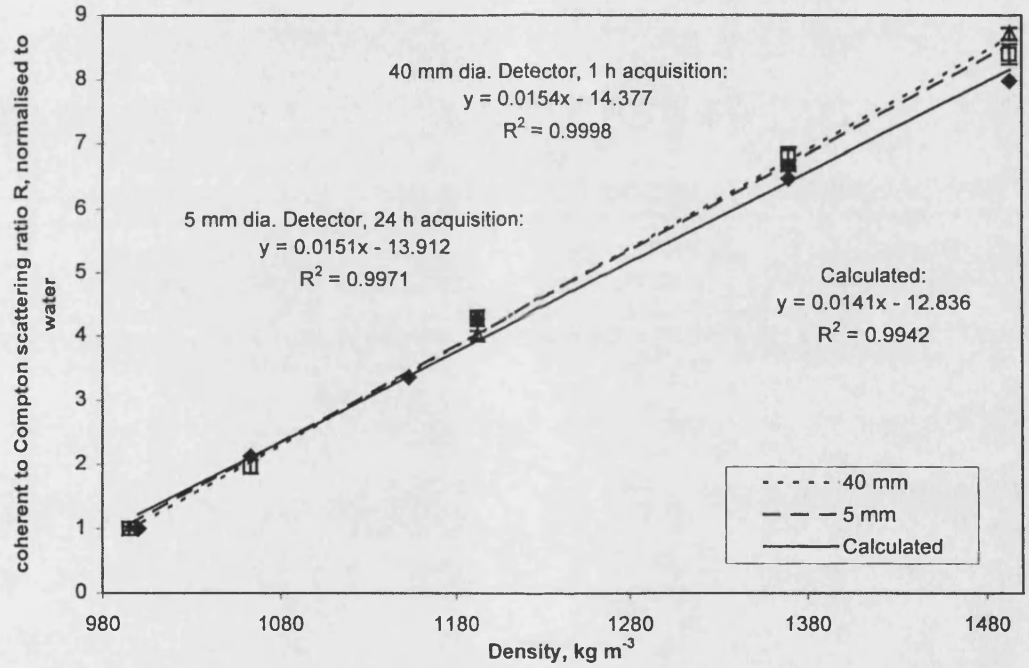

Figure 6.12 Coherent to Compton scattering ratios normalised to water, calculated and measured with two different detector apertures; 5 mm aperture for 24-hour acquisition and 40 mm aperture for 1-hour acquisition

From Table 6.8, for the coherent to Compton scattering ratio R the uncertainty in the density determination for a density similar to that of normal spongiosa bone (density 1180 kg m^{-3}) is reduced to 0.34 per cent. This is achieved by increasing the aperture diameter of the detector collimator from 5 mm to 40 mm and reducing the acquisition time to one hour. This value is much closer to those obtained by Karellas *et al* (1983) and Gigante and Sciuti (1985) which are equivalent to 0.23 per cent and 0.37 per cent respectively for a one-hour acquisition and the same source activity of 7.4 GBq.

Table 6.8 Slope and uncertainties of measured ratios (R, HP and R_k) and uncertainty in density determination for two experimental methods

Experiment details	Ratio	Slope, $m^3 kg^{-1}$	$\Delta\left(R/R_w\right)$	ΔD, kg m^{-3}
24 hours,	R	0.015	0.12	8
5 mm diameter	HP	0.0014	0.012	9
aperture	R_k	0.0011	0.007	7
1 hour,	R	0.015	0.06	4
40 mm diameter	HP	0.0015	0.007	5
aperture	R_k	0.0011	0.005	5

Table 6.8 also gives the uncertainties in density determination for the Compton profile ratios. With the 40 mm detector aperture, the uncertainties on the Compton profile ratios HP (MacKenzie 1990) and R_k (Tartari *et al* 1992) were similarly reduced. This slightly improved the uncertainty on the density determination for the bone phantom in air to just below 0.5 per cent for these two ratios.

6.8 Conclusions

In order to examine the feasibility of using a gamma-ray backscattering technique to make useful measurements of lumbar spine bone density, three parameters have been investigated with a bone phantom at different depths in a water tank. The three parameters were: the coherent to Compton scattering ratio, the Compton profile width and the two Compton profile ratios HP and R_k in which part of the high energy profile of the Compton peak is compared with the total. The Compton profile width did not prove to be sensitive enough to distinguish between the different simulated bone densities. The ratio measurements were more promising.

The coherent to Compton scattering ratio R and the ratios HP proposed by MacKenzie (1990) and R_k by Tartari *et al* (1992) all increase with increasing concentration of K_2HPO_4. R increases linearly with density, but HP and R_k fit a constant slope less well.

All the three ratio methods gave acceptable precision based on counting statistics, at depths up to 35 mm. However at 60 mm depth the uncertainties in the estimated bone densities

rise above the one per cent target. In addition, for R, the coherent peak becomes difficult to resolve from background because of the attenuation of the coherent signal by the surrounding water. This technique would therefore not be suitable for bone density measurements on the lumbar spine, which is usually at a depth of around 80 mm to 90 mm in tissue.

For the two Compton profile ratios the Compton peak energy shifts to higher energies as the depth of overlying water is increased due to a reduction in the average scattering angle. This change considerably alters the expected ratio and emphasises the importance of allowing for overlying tissue even at shallow depths where the technique has most potential.

All the above results were obtained with counting times of 24 hours and narrow beam geometry. When these results are compared with those of other workers using similar geometry (Karellas *et al* 1983 and Gigante and Sciuti 1985) the precision is less for similar activities and counting times.

In order to achieve similar precision in a measurement in a clinical situation it has been demonstrated (Section 6.9) that it is necessary to open up the collimator aperture on the detector to increase the count rate and hence reduce the uncertainties on the counting statistics.

By opening the aperture on the detector the target precision of one per cent on the density determination has been achieved for an in-air measurement with a one-hour counting time for all three ratio methods investigated. This precision should be achievable in a clinical situation for a fifteen-minute acquisition time and a four-source system on superficial bones. However, as reducing the collimation increased the scatter detected the technique would not be suitable for measuring bone mineral density in the lumbar spine. The lumbar spine typically lies at depths around 85 mm below the skin surface and the scatter from bone will be masked by the scatter from the water with the wider collimation even more than with the narrow collimation.

The main conclusion from the work reported in this chapter is that the gamma-ray backscattering technique is promising for bone density determination on bone at shallow depths where good bone density precision can be achieved. However, the technique is not

suitable for the determination of bone density in the lumbar spine, which lies at too great a depth below the skin surface. The potential of the technique for measuring bone density at sites where the bone is near the skin surface is explored in the next two chapters.

Chapter 7 Studies on Heel Phantom

7.1 Introduction

The previous chapter examining the potential of using gamma-ray backscattering for lumbar spine measurements indicated that the technique may be more useful for measuring bone density at peripheral sites. In this chapter the investigations made to examine the possibility of using the gamma-ray backscattering technique to predict the bone density in the heel bone (calcaneum) are reported.

It is recognised that bone density measurements of the heel bone (calcaneum) can be used as a predictor of osteoporosis and also for long term monitoring to determine the effect of treatment. Vogel *et al* (1988) reviewed bone mineral content measurements and their relationship to various factors. They concluded that calcaneal bone mineral content related as well as spinal bone mineral content to osteoporotic fracture risk. Their findings indicated that osteoporosis is a systemic disease and that trabecular bone losses are reflected in the calcaneum as well as in the spine. More recently, Kang and Speller (1999) concluded that the calcaneum was a precise, sensitive and simple measurement site suitable for assessment of osteoporosis, especially in the elderly where degenerative changes in the spine and hip can complicate bone mineral density assessment.

The sensitivity of the backscattering technique for the determination of bone density in air and at various depths in a water phantom was assessed in the previous chapter. This chapter investigates the effect of the thickness of overlying tissue and the dependence on the accuracy of positioning. Although this method has been suggested or used by a number of workers (Stalp and Mazess 1980, Karellas *et al* 1983, Gigante and Sciuti 1985 and Shukla *et al* 1986), the effects of overlying tissue and reproducibility due to re-positioning have been largely ignored.

The World Health Organisation (1994) has published recommendations for defining osteoporosis from DEXA measurements of the hip, spine and forearm in women, and classifies patients into four groups:

- Normal: The bone mineral density is up to one standard deviation below young adult mean and this indicates that the skeleton is as strong as that of a normal young individual.
- Osteopaenia: The bone mineral density is between one and 2.5 standard deviations below the mean.
- Osteoporosis: The bone mineral density is more than 2.5 standard deviations below the mean.
- Established osteoporosis: The bone mineral density is more than 2.5 standard deviations below the mean in the presence of fractures.

There is little agreement on what the absolute values should be and these are defined for a particular type of instrument and centre performing the measurements. Cann (1999) suggested that a peripheral bone mineral density test could demonstrate a decrease in bone mass. He said that following a bone densitometry test a woman would receive one of four diagnoses:

- Normal: The skeletal system is as strong as that of a normal young individual.
- Osteopaenia: This correlates with the skeletal bone mineral density being 10 to 25 per cent below peak mass and the person is at risk of developing osteoporosis.
- Osteoporosis: The skeletal bone mineral density is 25 per cent or more below normal.
- Established osteoporosis: The skeletal bone mineral density is 25 per cent or more below normal, and the patient has had an inappropriate fracture, typically in the spine, hip or forearm.

The bone mineral density of bone from cadavers has been determined by ashing the bone and then dividing the mass of the ashed sample by the previously determined volume of the original intact bone. Using calibration phantoms of ashed bone, Shukla *et al* (1986) measured bone mineral density in the heel bone of healthy volunteer subjects with a coherent to Compton scattering ratio method and obtained values of up to 357 mg/ml in men and 321 mg/ml in women. This was much higher than values of 185 mg/ml in men and 173 mg/ml in females measured by Weaver and Chalmers (1966) from cadaver samples.

The investigations reported here have measured bone density (which includes the bone marrow) as opposed to bone mineral density. For the backscattering technique to be useful

clinically it must be able to distinguish between the different disease states. This means that the uncertainties in the density determination relative to soft tissue must be less than five per cent. Since soft tissue has a density of around 1000 kg m^{-3} and trabecular bone has a density of 1180 kg m^{-3} (ICRU 44 1989) the total difference is of the order of 180 kg m^{-3}. Five per cent of this difference is 9 kg m^{-3}, which corresponds to an uncertainty in density determination of better than one per cent on a trabecular bone density measurement.

7.2 Description of the calcaneum (heel bone)

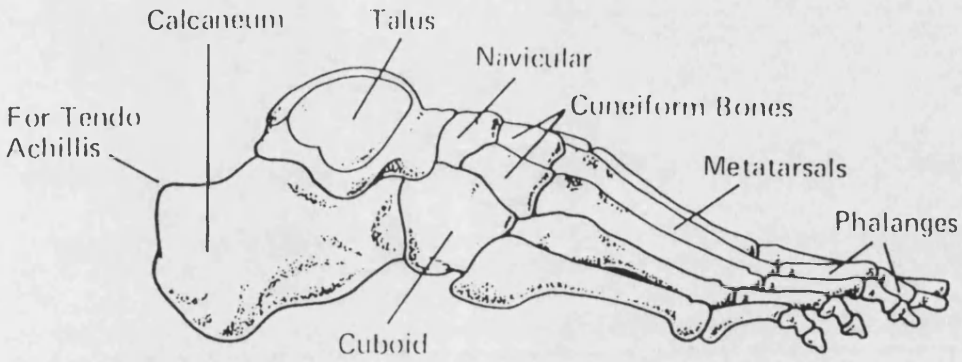

Figure 7.1 Bones of the right foot (Sears and Winwood 1976)

The framework of the foot demonstrating the position of the calcaneum is shown in Figure 7.1. The framework consists of the tarsus, the metatarsals and the phalanges. The tarsus comprises the talus, navicular, three cuneiform bones, calcaneum and cuboid. The calcaneum is the largest and strongest of the tarsal bones. It is irregularly cuboidal in form. It is situated at the lower and back part of the foot, and serves to transmit the weight of the body to the ground and forms a strong lever for the calf muscles. The calcaneum is situated below the talus. The Achilles tendon (*Tendo Achillis*) is attached to its posterior margin and at the front it articulates with the cuboid. In the adult, the calcaneum is of the order of 65 mm in length, 35 mm in width and 40 mm in depth. The calcaneum is primarily trabecular bone; greater than 90 per cent trabecular by volume. However, since it is an irregular bone with significant inhomogeneity, proper re-positioning will be important for accurate and reproducible measurements (Vogel *et al* 1988). A survey of seven colleagues indicated that the lateral separation of the heel ranged from 46 mm to 61 mm. It is likely that the separation of the calcaneum also has a range of values. It is therefore reasonable to assume that the calcaneum might have a lateral separation of 35 ± 5 mm and the overlying thickness might be 10 ± 3 mm.

7.3 Experimental arrangement

The detection system is as described in Chapter 2 and the experimental arrangement is as shown in Figure 7.2. The heel was represented by a phantom, which comprised two concentric containers. The inner container represented the calcaneum (heel bone) and this was filled with either water or solutions of K_2HPO_4 of different concentration. The inner container was 35 mm diameter and 50 mm in height. The outer container was filled with water to represent overlying lean tissue. To determine the effect of different thicknesses of overlying tissue, the outer container was either 55 mm or 75 mm diameter, to represent 10 mm or 20 mm overlying tissue respectively. A further series of experiments was made with the outer container absent to see the effect of no overlying tissue. These dimensions covered the range of lateral separations measured from a small group of colleagues.

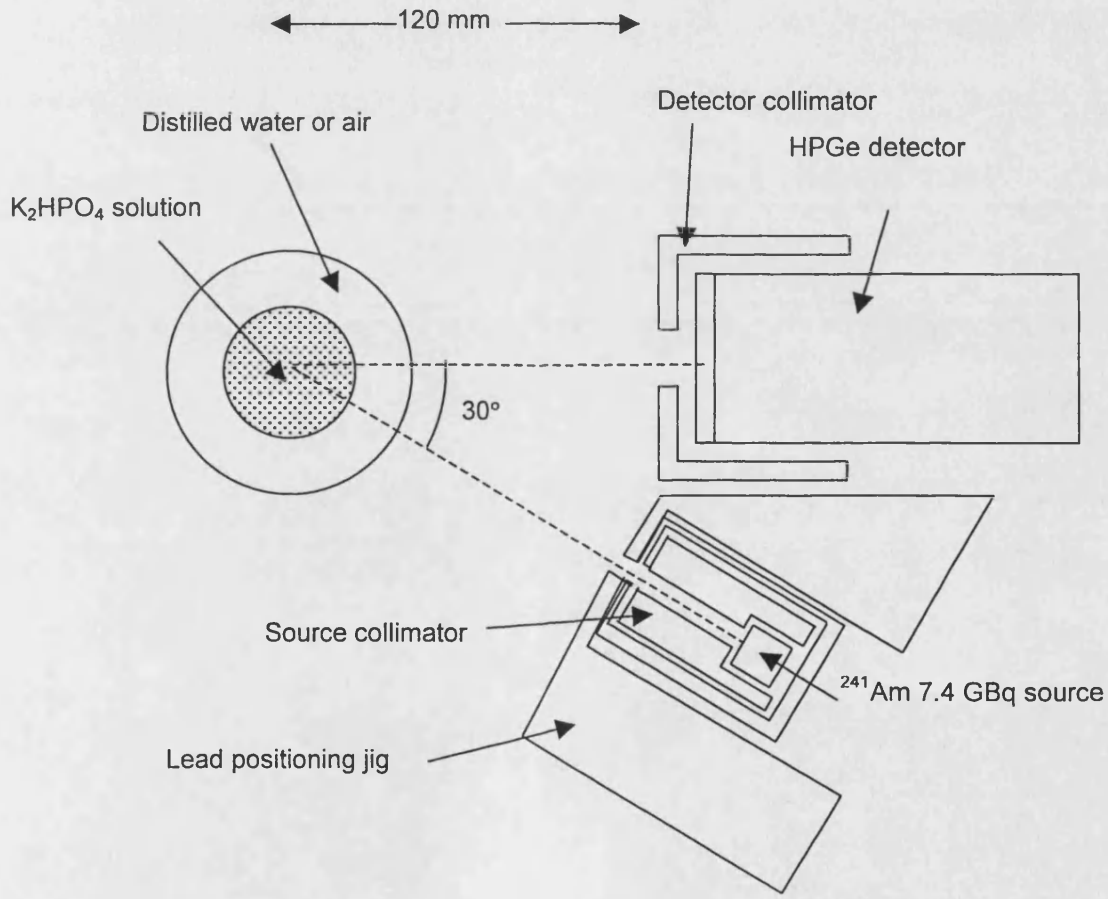

Figure 7.2 Schematic diagram to show measuring set-up for measurements on heel bone phantom.

The different concentration solutions of K_2HPO_4 made for the previously described investigations on the lumbar body phantom were used again. An additional solution of

20 g of K_2HPO_4 dissolved in 100 ml of distilled water was made. This approximated more closely the density of spongiosa bone at 1180 kg m^{-3} (ICRU 44 1989) and the lower of the reported values of bone mineral density by Weaver and Chalmers (1966) of around 180 mg/ml. The densities of the solutions and the distilled water were then determined by weighing a measured volume of each solution:

Concentration (g/100 ml):	0	20	60	90
Density (± 2 kg m^{-3}):	995	1153	1379	1507

The measured density of distilled water compares with 998 kg m^{-3} for pure air-free water at 20°C under one atmosphere (Kaye and Laby 1978). The previously used solutions with concentrations of 60 g and 90 g of K_2HPO_4 per 100 ml distilled water had increased in density by around eight per cent due to evaporation.

For all experiments the phantom was positioned such that the focus of the source-detector system was at the centre of the heel phantom. Background data acquisitions were obtained with the empty container(s) positioned at the focus. The detector was collimated with an aperture of either 5 mm (cylindrical) or 40 mm (divergent) diameter. The detector collimator with either aperture shielded the detector from direct irradiation by the source from the side. The 5 mm diameter aperture in the detector collimator enabled the 'sampling volume' to be confined within the bone of the phantom (a volume of the order of 4000 mm^3). The 40 mm diameter aperture allowed both bone and overlying water to be in the sampling volume (a volume of 5800 mm^3 or 7900 mm^3 depending on phantom size) (see Chapter 3, Table 3.3). The 40 mm diameter aperture served to expose the whole of the detector face. The 7.4 GBq americium-241 source was used in a lead collimator with an aperture of 5 mm diameter, which limited the irradiated area to about 17 mm diameter at the focus (ignoring the penumbra due to source size). Data were acquired for 24 hours with the narrow detector collimator and one hour with the open detector. The one-hour acquisition time was chosen to be representative of a four-source system with a 15-minute acquisition time, which would be suitable in a clinical setting (Chapter 6, Section 6.4). The ratios investigated were the coherent to Compton scattering ratio R, and the ratios HP and R_k, proposed by Mackenzie (1990) and Tartari *et al* (1992) respectively. The Compton profile width was also measured. Each measurement with the 40 mm diameter aperture on the detector was repeated three times. Examples of the spectra acquired from the heel

phantom with 10 mm of overlying water and distilled water or different concentrations of K_2HPO_4 in the inner container for the one-hour acquisitions are shown in Figure 7.3.

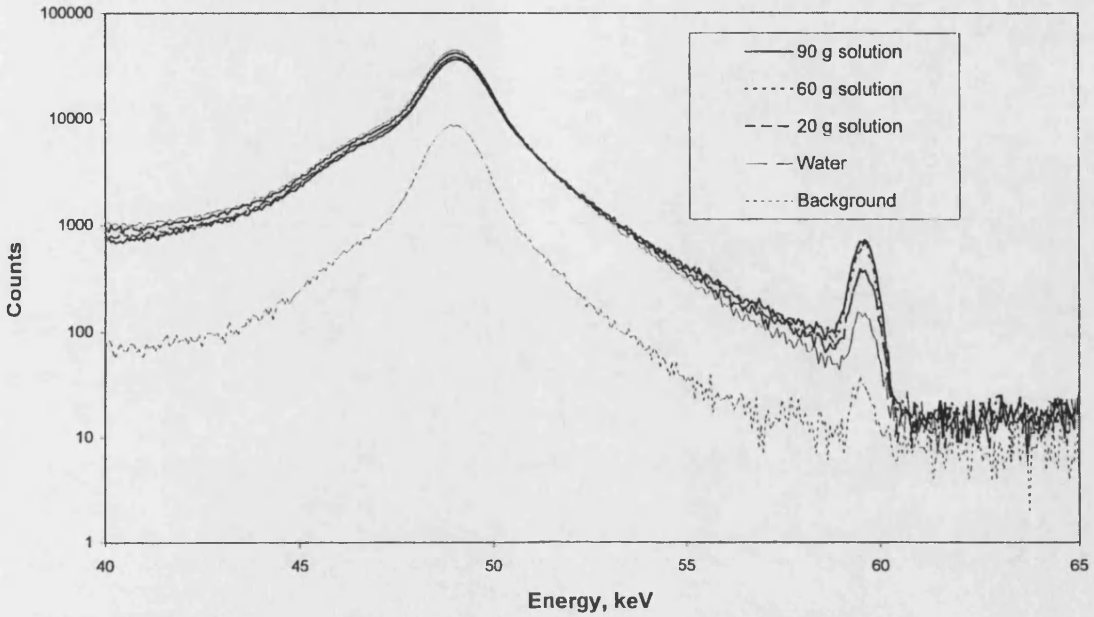

Figure 7.3 Spectra for heel phantom containing different solutions of K_2HPO_4, with 10 mm overlying water

7.4 Feasibility study and comparison of results with other workers

Other workers (Karellas *et al* 1983, and Gigante and Sciuti 1985) have investigated a backscattering technique for the determination of bone mineral content in the heel. In the previous chapter it was noted that the measurement technique employed for the investigations reported here using a 5 mm diameter aperture on the detector collimator gave much greater uncertainties than those determined by Karellas *et al* (1983) and Gigante and Sciuti (1985). The method under investigation in these previous studies (Chapter 6) needed a higher count rate in order to reduce the uncertainties due to counting statistics. This could be achieved either by increasing the activity of the americium-241 source or by increasing the aperture of the collimator on the detector. For a clinical application it is proposed to use a four-source system and a counting time of 15 minutes instead of one source for a counting time of one hour. Enlarging the aperture of the collimator on the detector would further increase the count rate.

A feasibility study was therefore performed to determine whether increasing the diameter of the aperture on the detector collimator would give a count rate that was sufficiently high to generate acceptable uncertainties in counting statistics. Measurements were made with the heel bone phantom. The inner container (35 mm diameter) was filled with either water or a solution of K_2HPO_4 (20 g per 100 ml water) with a density of 1153 kg m^{-3}, which would simulate spongiosa bone. The outer container of 55 mm diameter was filled with distilled water. First the detector was collimated with an aperture of 5 mm diameter as for previous experiments and acquisitions were made for 24 hours. The collimator aperture on the detector was then increased to 40 mm diameter so that the whole of the detector face was exposed and acquisitions were made for one hour. (The detector face is 32 mm in diameter.) The coherent to Compton scattering ratios and the uncertainties (one standard deviation) due to counting statistics were determined and are given in Table 7.1.

Table 7.1 Coherent to Compton scattering ratios, for two detector collimator apertures and acquisition times and two solutions in inner container (outer container 10 mm layer of distilled water)

Aperture diameter, mm	Acquisition time, h	Coherent to Compton scattering ratio R ($\times 10^{-4}$)	
		Water, inner	20 g soln K_2HPO_4, (density 1153 kg m^{-3}) inner
5	24	11.1 ± 1.5 (13.5%)	42.4 ± 1.8 (4.3%)
40	1	11.7 ± 0.4 (3.6%)	30.3 ± 0.5 (1.8%)

From the results in Table 7.1, the 5 mm diameter collimator aperture gives a statistical uncertainty of 4.3 per cent (20 g per 100 ml concentration of K_2HPO_4) for a 24-hour acquisition. This uncertainty on the coherent to Compton scattering ratio arises from the large background count in the coherent interval, which is twice the magnitude of the signal count. Despite the shielding around the sides of the detector and the americium-241 source, 30 per cent of this background signal is due to the background count in the room and the remainder is due to the americium-241 source. For this set-up and an acquisition period reduced to one hour the uncertainty on the measured coherent to Compton scattering ratio would be expected to increase to 20 per cent, which would be unacceptable.

Increasing the exposed area of the detector from 5 mm diameter to 32 mm diameter should increase the count rate by a factor of about 41 ($=32^2/5^2$). Reducing the acquisition period from 24 hours to one hour should therefore give a net increase in total counts by a factor of 1.7. This compares with a measured increase in signal count of around 1.9 in the Compton

intervals for the inner container filled with both water and K_2HPO_4 solution (1153 kg m^{-3}). For the coherent interval the signal count increased by a factor of 1.9 when the inner container was filled with water and increased by a factor of 1.4 when the inner container was filled with the bone solution. Based on these assumptions the expected uncertainty on a coherent to Compton scattering ratio measurement with the large detector aperture and a one-hour acquisition would be around three per cent. In practice the measured uncertainty with this experimental set-up was 1.8 per cent. The improvement in the uncertainty is due to the small background count in the coherent interval. With the large detector aperture the background count is only 12 per cent of the net signal in the coherent interval compared with double the coherent signal for the 5 mm diameter aperture.

The slopes of the curves for both the 5 mm and 40 mm diameter collimator apertures, based on two measurement points (water and K_2HPO_4 with a density of 1153 kg m^{-3} in the inner container) were determined. For all measurements the outer container was filled with water. The uncertainty in density was determined from the slope and uncertainty $\Delta(R/R_w)$ (Equation 6.1, Chapter 6). The results are summarised in Table 7.2. With the small diameter collimator aperture the slope of the line is 1.8 times greater than that with the larger diameter aperture, giving greater discrimination between the water and the solution of K_2HPO_4 (density 1153 kg m^{-3}). This is because the signal from the K_2HPO_4 solution is diluted by the signal from the water as the detector aperture is increased. However, the small diameter aperture on the detector reduces the count rate, which leads to large uncertainties due to counting statistics and hence gives much larger uncertainties in the density determination. The $\Delta(R/R_w)$ value and the percentage density uncertainty (ΔD) quoted in Table 7.2 is for a density of 1153 kg m^{-3}.

Table 7.2 Slope and uncertainty in density determination for the two aperture diameters on the detector collimator

Collimator aperture diameter	Slope, m^3 kg^{-1}	$\Delta(R/R_w)$	ΔD, kg m^{-3}
5 mm (24 h)	0.018	0.16	9 (0.8%)
40 mm (1 h)	0.010	0.05	5 (0.4%)

As described in the previous chapter, in order to compare the results of Karellas *et al* (1983) and Gigante and Sciuti (1984) with the results described here it is necessary to consider similar counting times and source activities. Karellas *et al* (1983) quoted statistical uncertainties of 1.68 per cent and uncertainties in density determination of

0.19 per cent using a counting period of 15 minutes and source activity of 44.4 GBq at a scattering angle of 98°. For a one-hour counting period and 7.4 GBq this corresponds to a statistical uncertainty of 2.1 per cent and an uncertainty in density determination of 0.23 per cent. Similarly, Gigante and Sciuti (1985) quoted weight fraction uncertainties of 1.1 per cent using a counting period of 400 seconds and 7.4 GBq activity at a scattering angle of 135°. This corresponds to an uncertainty of 0.37 per cent in weight fraction for a one-hour counting period with the same activity. From the results in Tables 7.1 and 7.2 above, it is evident that in order to match the uncertainties of Karellas *et al* (1983) and Gigante and Sciuti (1985) it is necessary to use the large diameter aperture on the detector collimator to increase the count rate and reduce the uncertainties due to counting statistics in the ratio measurements.

The results obtained from this feasibility study give comparable uncertainties to those quoted by Karellas *et al* (1983) and Gigante and Sciuti (1985). However, in these feasibility measurements a realistic 10 mm of overlying tissue was included over the bone phantom whilst in the results quoted by Karellas *et al* (1983) and Gigante and Sciuti (1985) there was no overlying tissue. As noted in Chapter 6, Section 6.7, these comparisons are only approximate since the experimental arrangements have different geometries.

Since the calcaneus is an irregular bone with significant non-homogeneity it may be difficult to achieve good reproducibility if only a small volume of the bone is investigated. It may therefore be an advantage to have a large detector aperture in order to investigate a large volume of the bone. Kang and Speller (1999) used dual energy x-ray absorptiometry measurements and found differences of 20 per cent in bone mineral density between the anterior region and the mid and posterior parts of the calcaneus.

The conclusions of these investigations are:

- The narrow collimation on the detector gives better discrimination between different densities at the expense of a low count rate, which gives rise to large uncertainties in counting statistics and hence large uncertainties in density determination.
- The open collimation reduces the discrimination of the system by a factor of 1.8 (slope of the ratio against density curve), but the higher count rate leads to smaller uncertainties in counting statistics and hence reduces the uncertainty in density determination.

- In a period of one hour the 40 mm diameter aperture on the detector yielded an estimated uncertainty in density determination of 0.4 per cent, within the limit of one per cent required for bone density monitoring. With the narrow 5 mm diameter aperture collimator the uncertainty in density determination would rise to around four per cent in a one-hour measurement period and would not therefore meet the required precision.

Since the objective is a clinical application with an acquisition time of 15 minutes it is necessary to have a higher count rate than that obtained with the 5 mm diameter collimator aperture on the detector. A high count rate is necessary to achieve acceptable uncertainties in the density determination. Consequently, all the following analyses were made on data acquired with the large diameter aperture of 40 mm on the detector collimator and acquisition times of one hour.

7.5 Coherent to Compton scattering ratio

Using the experimental arrangement shown in Figure 7.2, a series of data acquisitions were made to investigate the sensitivity of the coherent to Compton scattering ratio as a method for determining bone density in the heel bone. The experiment was first performed with the outer container absent, in order to compare measured values for water and different density solutions of K_2HPO_4 with the calculated values.

Table 7.3 shows the calculated values for 150° scattering angle and the nominal weight of K_2HPO_4 used to make the different concentration solutions, together with the measured values. The measured values of coherent to Compton scattering ratios have been determined from an integration range of 58.5 to 60.5 keV for the coherent scatter, and 45 to 52 keV for the Compton scatter. The latter range represents the full width tenth maximum (FWTM) of the Compton profile for the 150° measurement geometry. The results are given in Table 7.3. The measured values quoted in the table are the means of three independent data acquisitions with one standard deviation based on counting statistics. The uncertainties due to counting statistics were 3.5 per cent for water, falling to one per cent for the densest solution of K_2HPO_4. The uncertainties due to reproducibility were ± 2 per cent but are not included in these results. The backscattering geometry employed, i.e. scattering angle of 150°, should yield a Compton peak of around 48.9 keV.

The Compton peak was around 49.0 ± 0.06 keV, which corresponds to an equivalent scattering angle of 148°. This difference in peak energy corresponds to about one channel on the multi-channel analyser.

Table 7.3 Calculated and measured coherent to Compton scattering ratios for water and different density solutions of K_2HPO_4 (35 mm diameter phantom)

Concentration of K_2HPO_4, g/100 ml distilled water	Calculated ($\times 10^{-4}$)	Density, ± 2 kg m^{-3}	Measured ($\times 10^{-4}$)
0	13.88	995	12.3 ± 0.4
20	46.59	1153	46.7 ± 0.8
60	89.75	1379	94.2 ± 1.1
90	110.81	1507	123.2 ± 1.3

The calculated values assume narrow beam geometry, whilst the experimental method uses broad beam geometry. The calculated and measured values demonstrate similar increases in the coherent to Compton scattering ratio R with increasing concentration and density of K_2HPO_4 solutions.

The K_2HPO_4 solution with a density of 1153 kg m^{-3} was chosen to be representative of the trabecular bone density of the calcaneum (spongiosa bone density 1180 kg m^{-3}, ICRU 44 1989). The measured coherent to Compton scattering ratio for this solution was almost four times the measured value for water (lean tissue). This should give good discrimination for the measurement of bone mineral density.

The same calculated and measured coherent to Compton scattering ratios have been normalised to the value for water and are shown graphically in Figure 7.4. A straight line has been fitted to the data, using a least squares fit method. For the calculated data the straight line has a coefficient of determination R^2 of 0.998 and for the measured data R^2 is 0.9999, demonstrating a linear relationship for both calculated and measured values of coherent to Compton scattering ratio and density.

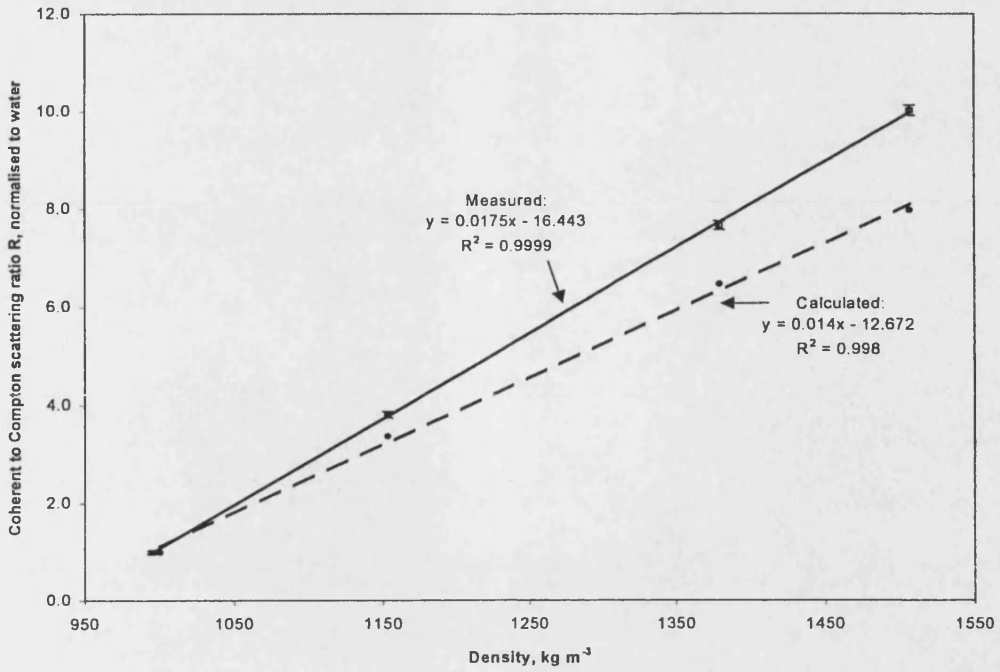

Figure 7.4 Variation of coherent to Compton scattering ratios with density measured for heel bone phantom in air and calculated (normalised to water)

To ascertain the effects of overlying tissue, which would be present for *in vivo* investigations, the measurements were repeated with the outer container present and filled with water. Two different diameters of outer container (55 mm and 75 mm) were used to simulate 10 mm overlying tissue and 20 mm overlying tissue respectively.

Table 7.4 Measured coherent to Compton scattering ratios for water and different concentration solutions of K_2HPO_4 with different amounts of overlying water

Density of inner solution, ± 2 kg m^{-3}	Coherent to Compton scattering ratio R ($\times 10^{-4}$)		
	In air	+ 10 mm water	+ 20 mm water
995	12.3 ± 0.4	12.6 ± 0.4	12.7 ± 0.3
1153	46.7 ± 0.8	32.1 ± 0.6	24.3 ± 0.4
1379	94.2 ± 1.1	60.2 ± 0.8	40.0 ± 0.6
1507	123.2 ± 1.3	75.4 ± 0.9	47.4 ± 0.6

The results are given in Table 7.4. The measured ratios are the means of three measurements and the uncertainty is one standard deviation, based on the counting statistics. For the all-water phantoms, the measured values of the coherent to Compton scattering ratio are within the standard deviations of the counting statistics. As the density

of the K_2HPO_4 solution in the inner container is increased, the coherent to Compton ratio increases for all the phantoms. However for the densest solution, the increase in value falls from ten times the value for water with the sample in air, to only four times the value for water when it is surrounded by 20 mm of water. For the different concentration solutions of K_2HPO_4, the measured value of the coherent to Compton scattering ratio R is reduced by around three per cent per mm depth of overlying water. The measured ratio values for each of the three phantoms have been normalised to the ratio value obtained for the water only phantom and are shown graphically in Figure 7.5.

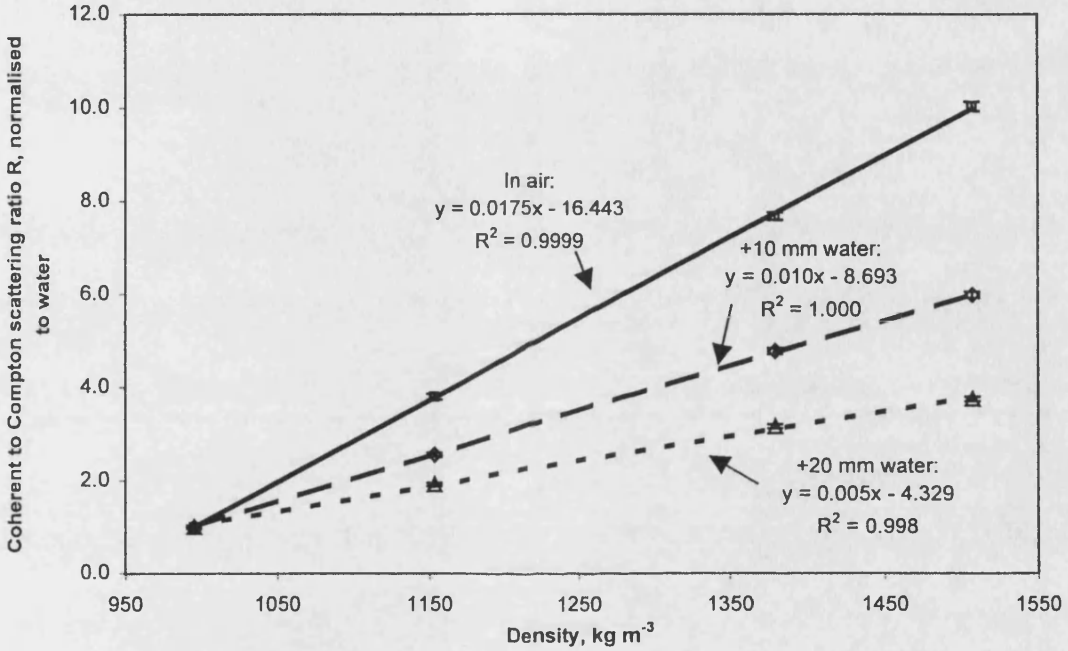

Figure 7.5 Variation of coherent to Compton scattering ratios (normalised to water) with density for the three heel bone phantoms

These measurements indicate that for a clinical situation it would be important to know the thickness of the overlying tissue on the calcaneum in order to determine the bone mineral density. It may also be necessary to determine the volume of the calcaneum and the heel that has been irradiated.

The ratio values measured for the phantom with 10 mm of overlying water quoted in Table 7.4 are a little higher than the values in Table 7.1 for the same measurement set-up. The difference is probably due to re-positioning (see Section 7.8). However, the relative difference between the values for water and the K_2HPO_4 solution of density 1153 kg m^{-3} in the inner phantom is the same.

To ascertain whether the overlying tissue would have less of an effect at smaller scattering angles, further measurements were made with the source at an angle of 90° to the detector axis. The 35 mm diameter phantom was placed at the focus and one-hour data acquisitions were obtained with the phantom filled with water, and then with the densest K_2HPO_4 solution. These measurements were then repeated with the two concentric containers placed at the focus. The inner container (35 mm diameter) was again filled with either water or the densest K_2HPO_4 solution. The outer container (75 mm diameter) was filled with water for both measurements, giving 20 mm of overlying water. The calculated and measured ratio values are given in Table 7.5. The Compton peak was summed from 50 keV to 56 keV, which corresponded to the full width tenth maximum (FWTM) for the 90° geometry. The coherent peak was summed from 58.5 keV to 60.5 keV as before.

Table 7.5 Calculated and measured coherent to Compton scattering ratios for 90° scattering angle geometry

Inner solution density, ± 2 kg m^{-3}	Coherent to Compton scattering ratio R ($\times 10^{-4}$)		
	Calculated for 90°	In air	+ 20 mm water
995	61.77	74.9 ± 1.3	93.2 ± 1.4
1507	232.8	322.6 ± 3.4	209.2 ± 2.4

Because coherent scatter increases as the scattering angle decreases, the coherent to Compton scattering ratios are much larger with the 90° geometry. However the dependence on atomic number also decreases with the scattering angle. Table 7.5 demonstrates that for the calculated ratio value and the measured value for the phantom containing water to the densest solution with no overlying water, there is an increase in coherent to Compton scattering ratio of around four-fold. This compares with eight times calculated and ten times measured for the 150° geometry (Table 7.3). When the inner phantom is surrounded by 20 mm water, the increase in coherent to Compton scattering ratio is only a factor of two compared with a factor of four for the 150° geometry (Table 7.4). For the K_2HPO_4 solution the effect of the overlying water is to reduce the measured value of the coherent to Compton scattering ratio by around two per cent per mm due to the contribution to the Compton scatter from the water. This compares with a reduction of the coherent to Compton scattering ratio by three per cent per mm at 150° geometry.

The different geometries with the surrounding water present or not, and the different densities of solution in the inner container, all have an effect on the mean Compton scattering angle. This effect is illustrated in Figure 7.6. As the geometry of the set-up approaches 180° backscatter the dependence of the scattering angle on the average depth of scatter will reduce.

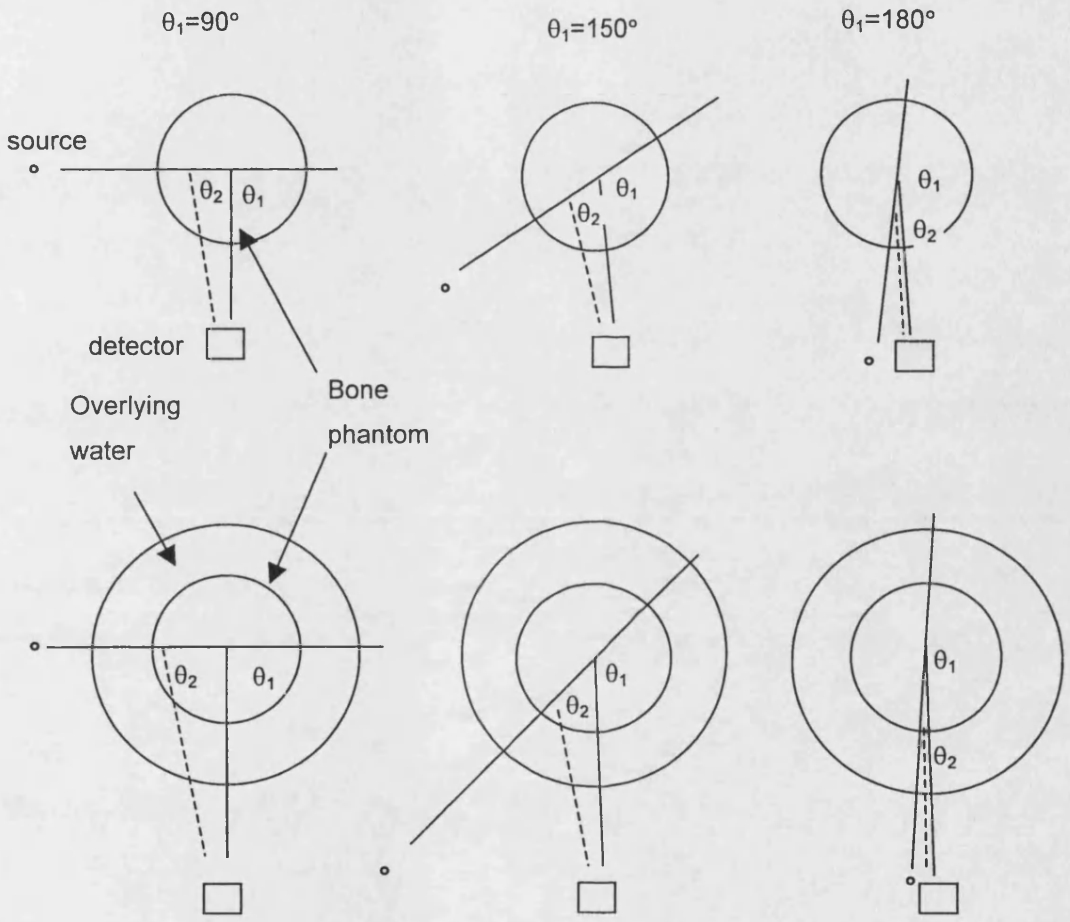

Figure 7.6 **Illustration of effect of overlying tissue on scattering angle. θ_1 is the nominal scattering angle and θ_2 is the average scattering angle. θ_2 reduces as the depth of overlying water increases, but the reduction is less marked as θ_1 approaches 180°.**

For the 90° geometry set-up the Compton peak energy was 53.4 keV for the water phantom in air and 54.0 keV for the phantom surrounded by 20 mm water. For each set-up, the difference in Compton peak energy between the inner container filled with water and filled with the densest solution of K_2HPO_4 was three channels on the multi-channel analyser, corresponding to 180 eV. In each case, the lower energy Compton

peak was for the inner container filled with water, which corresponded to a larger scattering angle.

The water filled phantom in air gave a Compton peak energy that equated to a scattering angle of 89.2°. When surrounded by an extra 20 mm of water the Compton peak energy equated to a scattering angle of 83.5°. For water these different scattering angles correspond to calculated coherent to Compton scattering ratios that differ by 44 per cent:

$$83.5°: R = 93.38 \times 10^{-4}$$

$$89.2°: R = 65.26 \times 10^{-4}$$

The measured value of coherent to Compton scattering ratio shows a 25 per cent increase with the change in diameter of the phantom from 35 mm to 75 mm (i.e. from in-air to 20 mm overlying water), for an angle of 90° between the source and detector (Table 7.5). For the 150° backscattering geometry, there was no significant increase in the coherent to Compton scattering ratio for the different diameter water phantoms (Table 7.4). This is consistent with the mean scattering angle being less dependent on the average depth of scatter as the geometry of the set-up approaches 180° backscatter.

A similar analysis can be performed for the densest solution of K_2HPO_4. For the phantom in air the Compton peak energy equated to a scattering angle of 87.2°. When the phantom was surrounded by 20 mm of water the scattering angle reduced to 81.1°, because the average scatter depth was nearer the incident surface for the denser solution. For these scattering angles the calculated coherent to Compton scattering ratios for the 90 g concentration solution of K_2HPO_4 differ by only 17 per cent:

$$81.1°: R = 279.39 \times 10^{-4}$$

$$87.2°: R = 238.08 \times 10^{-4}$$

For both the 90° and 150° scattering geometries the "bone" signal is diluted with the signal from the overlying water as the depth of overlying water is increased. For the 90° geometry, 20 mm of overlying water reduces the measured ratio to around 65 per cent of the in-air value (Table 7.5). This compares with a reduction to 38 per cent of the in-air value with a scattering geometry of 150° (Table 7.4). For the 90° geometry, the reduction in mean scattering angle with the overlying water present has the effect of increasing the coherent to Compton scattering ratio. The reduction in scattering angle with overlying water appears to reduce the effect of overlying water depth on the measured ratio.

The uncertainty in density that might be expected for a density of the order of 1153 kg m^{-3} for the two scattering geometries of 90° and 150° have been determined from the slope and uncertainty in measurement $\Delta(R/R_w)$ (Equation 6.1, Chapter 6). The results are summarised in Table 7.6. Based on these limited measurements there is no advantage of the 90° scattering geometry over that of 150°. The main advantage of the 150° scatter geometry is the comparative ease of set-up for a clinical application.

Table 7.6 Slope and uncertainty in density determination for 90° and 150° scattering geometry

Phantom	Geometry	Slope, m^3 kg^{-1}	ΔD, kg m^{-3}
In air	90°	0.006	6 (0.5%)
	150°	0.018	4 (0.3%)
+ 20 mm water	90°	0.001	17 (1.5%)
	150°	0.005	6 (0.6%)

The conclusions of these investigations are as follows:

- The backscattering technique with 150° geometry gives good discrimination between a solution of K_2HPO_4 with a density representative of trabecular bone (1153kg m^{-3}) and water. However, the discrimination is reduced by the presence of overlying water (three per cent per mm).
- The 90° geometry shows a slight advantage over the 150° geometry, with the effect of overlying water being reduced from three to two per cent per mm. The discrimination between different densities is also reduced with the 90° geometry and the net effect is to give no advantage over the 150° geometry with regard to determining the uncertainty on a density determination.
- For the 90° geometry the mean scattering angle as determined from the Compton peak energy is dependent on the amount of overlying water which affects the average depth of scatter. This effect reduces as the backscatter geometry approaches 180°. For the 150° geometry there was no measurable difference in Compton peak energy with different amounts of water overlying the bone phantom.

7.6 Compton profile ratios

The data collected for the determination of the coherent to Compton scattering ratios were also analysed to determine the Compton profile ratios HP (MacKenzie 1990) and R_k (Tartari *et al* 1992). The integration intervals were as for previous measurements. For the ratio HP the numerator counts were integrated from 52 to 58 keV, and the denominator from 40 to 58 keV. For R_k, the numerator counts were integrated from 51 to 56 keV and the denominator from 40 to 56 keV. The data collected for the inner phantom filled with water or different concentrations of K_2HPO_4 with no overlying water gave the ratios in Table 7.7. The measured values in the table are the means of three independent set-ups with one standard deviation due to the uncertainties in counting statistics. The uncertainties due to reproducibility for both ratio methods are of the order of two per cent. The value of the ratio increases with the concentration of the K_2HPO_4 solution, although this increase is not as great as for the coherent to Compton scattering ratio. For the density of 1153 kg m^{-3}, comparable to that of trabecular bone, the ratio value increases by 25 per cent for HP and just under 20 per cent for R_k. For comparison, the coherent to Compton scattering ratio increased by a factor of four over the same density range (Table 7.4).

Table 7.7 Compton profile ratios for water and different densities (concentrations) of K_2HPO_4

Density, ± 2 kg m^{-3}	HP ($\times 10^{-3}$)	R_k ($\times 10^{-3}$)
995	28.9 ± 0.2	56.0 ± 0.2
1153	36.2 ± 0.2	66.7 ± 0.3
1379	45.5 ± 0.3	80.6 ± 0.3
1507	51.1 ± 0.3	87.9 ± 0.4

The analysis was also performed on the data collected with different diameter outer containers filled with water. Table 7.8 gives the measured ratio values HP, which are the means of three independent measurement set-ups with one standard deviation due to counting statistics. The value of the Compton profile ratio HP for water increases slightly with the diameter of the phantom. As the concentration of the K_2HPO_4 solution in the inner container is increased the ratio HP increases. However, the magnitude of the increase in HP ratio is reduced as the depth of water overlying the inner container is increased. This reduction is around one per cent per mm of added water depth. The HP ratios have been normalised to water and are shown graphically in Figure 7.7. A least

squares fit has been determined for each set of data with different overlying water depth. The different slopes of these lines demonstrate that the overlying water reduces the discrimination between the different density solutions in the inner container. For the measurements made with 20 mm of overlying water the discrimination is a factor of three less than for the in-air measurements.

Table 7.8 Measured Compton profile ratio HP for water and different densities (concentrations) of K_2HPO_4, with different amounts of overlying water

Density of inner solution, ± 2 kg m^{-3}	Compton profile ratio HP ($\times 10^{-3}$)		
	In air	+ 10 mm water	+ 20 mm water
995	28.9± 0.2	30.1 ± 0.2	31.7 ± 0.2
1153	36.2 ± 0.2	34.5 ± 0.2	34.9 ± 0.2
1379	45.5 ± 0.3	40.6 ± 0.2	38.8 ± 0.2
1507	51.1 ± 0.3	44.1 ± 0.2	40.3 ± 0.2

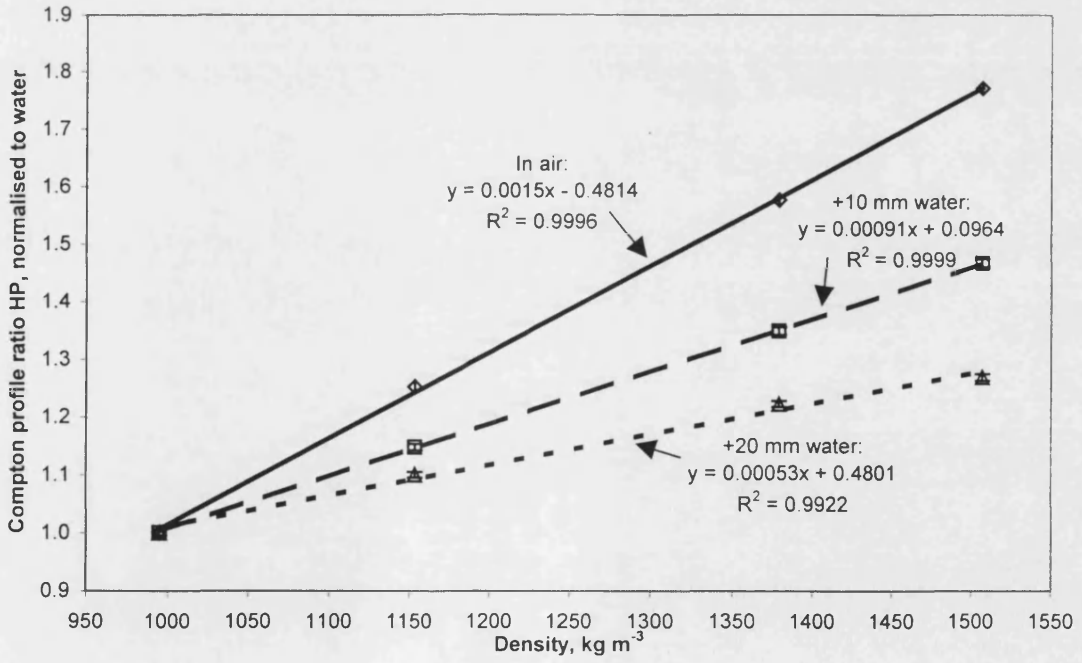

Figure 7.1 Variation of Compton profile ratio HP (normalised to water) with density for the three heel bone phantoms with different amounts of overlying water

Similar results were obtained for the ratio R_k and these are given in Table 7.9. The ratio values are again the means of three independent measurement set-ups with one standard deviation based on counting statistics. It can be seen from the data in Table 7.9 that R_k for water increases with the diameter of the phantom in a similar way to HP. For the increasing concentration solutions of K_2HPO_4 in the inner container, the ratio R_k also increases. The magnitude of the increase is reduced by the presence of overlying water for the first 10 mm of added water by around one per cent per mm, and somewhat less for a further 10 mm of added water.

Table 7.9 Measured Compton profile ratio R_k for water and different densities (concentrations) of K_2HPO_4, with different amounts of overlying water

Density of inner solution, ± 2 kg m^{-3}	Compton profile ratio R_k ($\times 10^{-3}$)		
	In air	+ 10 mm water	+ 20 mm water
995	56.0 ± 0.2	59.2 ± 0.2	63.4 ± 0.2
1153	66.7 ± 0.3	65.4 ± 0.2	68.3 ± 0.2
1379	80.6 ± 0.3	74.6 ± 0.3	74.4 ± 0.2
1507	87.9 ± 0.4	79.7 ± 0.3	76.3 ± 0.3

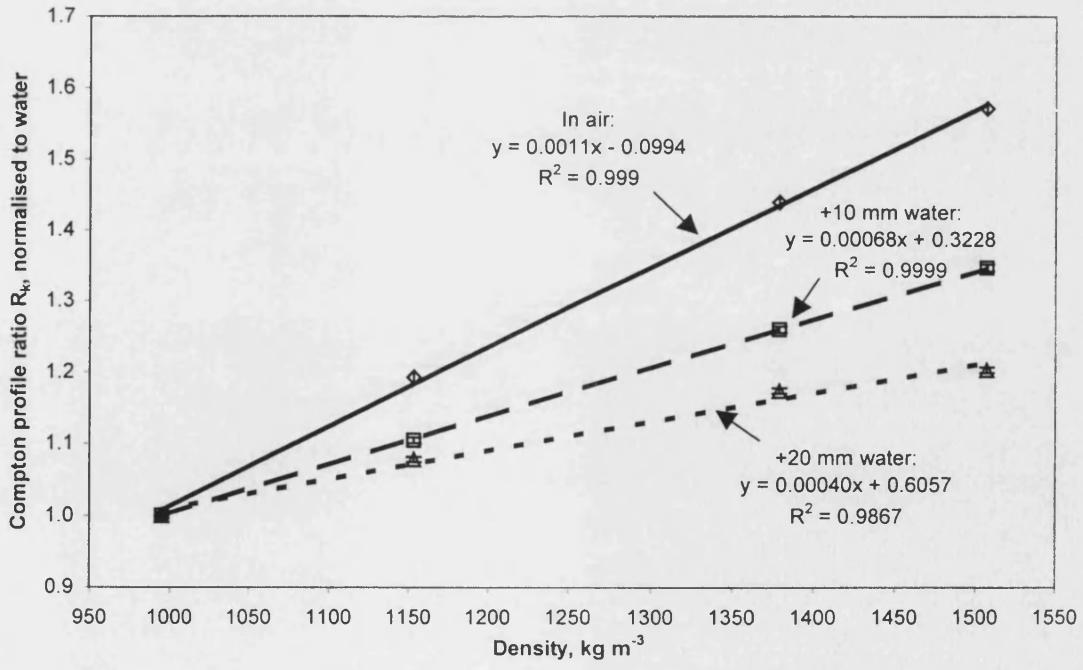

Figure 7.2 Variation of Compton profile ratio R_k (normalised to water) with density for the three heel bone phantoms with different amounts of overlying water

The measured ratio values for R_k in Table 7.9 have also been normalised to water and are shown graphically in Figure 7.8. A least squares fit for each data set has again been determined. The slopes of these lines demonstrate that the overlying water reduces the discrimination between the different densities in the inner container. For the ratio R_k, the discrimination of the measurement with 20 mm overlying water is about a factor of three less than that of the measurement in air.

7.7 Compton profile width

The same data acquisitions have also been used to determine the Compton profile widths. The full width half maximum (FWHM), full width third maximum (FW1/3M) and full width quarter maximum (FW1/4M) have been measured for one series of data for the measurements in air, and with 10 mm and 20 mm of overlying water.

Table 7.10 Full width half maximums (FWHM) of the Compton profile for water and different concentrations of K_2HPO_4 with different amounts of overlying water

Density,	FWHM, eV		
± 2 kg m^{-3}	In air	+ 10 mm water	+ 20 mm water
995	1695 ± 15	1760 ± 15	1780 ± 15
1153	1705 ± 15	1755 ± 15	1770 ± 15
1379	1780 ± 15	1775 ± 15	1790 ± 15
1507	1820 ± 15	1775 ± 15	1780 ± 15

Table 7.10 gives the FWHMs for the different concentrations of K_2HPO_4 solutions in the inner container and with different amounts of overlying water. The widths show a similar trend to all the ratio methods investigated above, in as much as the FWHM increases with concentration for the inner phantom in air. There is an increase in profile width of 125 eV between water and the densest solution of K_2HPO_4 investigated (density 1507 kg m^{-3}). However, this difference is lost when the bone phantom is surrounded by water. There is an increase in count rate of 50 per cent in the Compton region with 20 mm of overlying water compared with the bone phantom in air. This increase in count rate may be accounted for by an increase in both the scatter contribution and the range of scattering angles with the surrounding water, which probably masks the in-air difference.

Table 7.11 gives the FW1/3Ms of the Compton profiles. For the in-air situation, there is a difference of 145 eV between water and the most concentrated solution of K_2HPO_4 investigated, compared with 125 eV for the FWHM. Again, for the different concentration solutions of K_2HPO_4 with overlying water there is no distinguishable difference between the Compton profile widths.

Table 7.11 Full width third maximums (FW1/3M) of the Compton profile for water and different concentrations of K_2HPO_4 with different amounts of overlying water

Density, ± 2 kg m^{-3}	FW1/3M, eV		
	In air	+ 10 mm water	+ 20 mm water
995	2320 ± 15	2400 ± 15	2460 ± 15
1153	2380 ± 15	2455 ± 15	2450 ± 15
1379	2450 ± 15	2440 ± 15	2440 ± 15
1507	2465 ± 15	2455 ± 15	2450 ± 15

The FW1/4Ms have also been determined from the same data (Table 7.12). These width measurements give the greatest discrimination over the range of densities investigated for the in-air measurements, a difference of 360 eV in profile width. There is also a greater increase in profile width (320 eV) with increasing diameter of the phantom (35 mm to 75 mm) when it only contains water. However the uncertainties are larger due to the shallow slope of the profile at this height together with the lower count rate. When there is overlying water the differences in profile width are once again indistinguishable.

Table 7.12 Full width quarter maximums (FW1/4M) of the Compton profile for water and different concentrations of K_2HPO_4 with different amounts of overlying water

Density, ± 2 kg m^{-3}	FW1/4M, eV		
	In air	+ 10 mm water	+ 20 mm water
995	2800 ± 30	3055 ± 30	3120 ± 30
1153	2960 ± 30	3055 ± 30	3075 ± 30
1379	3050 ± 30	3070 ± 30	3140 ± 30
1507	3160 ± 30	3090 ± 30	3130 ± 30

In conclusion, the method of Compton profile width measurement of FWHM, FW1/3M and FW1/4M does not appear to be sufficiently sensitive as a method for bone density

determination when overlying tissue is present. This is a similar conclusion to that obtained from work with the lumbar body phantom reported in the previous chapter.

7.8 Effect of phantom position

For all the heel phantom measurements described so far the phantoms were positioned so that they were centred at the intersection of the radiation beam axis and the longitudinal axis of the detector. The phantom was re-positioned for each data collection and three data collections were made for each combination of water or K_2HPO_4 solution density in the inner container and the different amounts of overlying water to ascertain the reproducibility of the set-up. The results of these re-positioning studies were that for all ratio measurements one standard deviation amounted to two per cent of the measured ratio. This value is well within the statistical uncertainties of the measured coherent to Compton scattering ratio R, but greater than the statistical uncertainties on the Compton profile ratios HP and R_k. Patient re-positioning is more difficult than re-positioning a phantom. To test what might happen in practice, further experiments were performed where the phantom was deliberately positioned off-centre. For these measurements the inner container was filled with the K_2HPO_4 solution with a density of 1379 kg m^{-3} and the outer container was absent. One acquisition was made with the phantom centred as described previously. Two further sets of data were then collected: one with the phantom moved 3 mm closer to the detector, and one with the phantom moved 3 mm further from the detector relative to the reference position. A background data acquisition was made with the inner container empty at the reference position. The background was subtracted from the data prior to analysis. The ratios for the coherent to Compton scattering ratio R, and the Compton profile ratios HP and R_k, normalised to the value at the reference position are tabulated in Table 7.13. The uncertainties in this table allow for reproducibility.

Table 7.13 Measured ratios normalised to the reference position for two off-sets

Ratio	Measured ratio (normalised)		
	3 mm closer to detector	Reference	3 mm further from detector
R	1.01 ± 0.02	1.00 ± 0.02	0.99 ± 0.02
HP	1.03 ± 0.02	1.00 ± 0.02	0.98 ± 0.02
R_k	1.03 ± 0.02	1.00 ± 0.02	0.97 ± 0.02

These measurements indicate positioning uncertainties of around 0.5 per cent per mm for the coherent to Compton scattering ratio R, whilst for the Compton profile ratios the uncertainties are slightly greater at around one per cent per mm. The reason for this is that the Compton profile ratio measurements are more sensitive to changes in the mean scattering angle, which affects the shape of the Compton profile on the high-energy side of the Compton peak. These results are consistent with previous measurements, which gave reproducibility of the order of two per cent. For a clinical set-up re-positioning to ± 2 mm may be the best that can be achieved. This will give rise to uncertainties of greater than two per cent.

7.9 Uncertainties in density determinations

The plots of the different ratios against density have been fitted using a least squares method to determine the slopes of the curves. The uncertainty in density determination of the solution with density closest to that of trabecular bone (1153 kg m^{-3}) has been calculated using Equation 6.1 (Chapter 6). The uncertainty depends on the slope of the least squares fit line to the measurement points (Figures 7.5, 7.7 and 7.8) and the uncertainty in $\Delta(\text{Ratio}/\text{Ratio}_w)$ based on statistical uncertainty. The results are shown in Table 7.14.

Table 7.14 Slope, uncertainty in ratio measurement and in density determination for the three ratio methods R, HP and R_k

Ratio	Overlying tissue, mm	Slope, S $m^3\ kg^{-1}$	$\Delta(\text{Ratio}/\text{Ratio}_w)$	ΔD, kg m^{-3}
R	0	0.018	0.065	4 (0.3%)
	10	0.010	0.044	4 (0.3%)
	20	0.0054	0.035	6 (0.5%)
HP	0	0.0015	0.0073	5 (0.4%)
	10	0.00091	0.0057	6 (0.5%)
	20	0.00053	0.0050	10 (0.9%)
R_k	0	0.0011	0.0052	5 (0.4%)
	10	0.00068	0.0041	6 (0.5%)
	20	0.00040	0.0036	9 (0.8%)

The uncertainties in density determination are similar for all three ratio methods when based on the statistical uncertainties of the measured ratios. Although the coherent to Compton scattering ratio has poorer statistics because of the low number of counts in the coherent peak, the steeper gradient of the plot of ratio against density compensates for this. For all three ratio methods, a density measurement on normal spongiosa bone with a density of 1180 kg m^{-3} would have an uncertainty on the measurement due to statistical uncertainties of the order of one per cent or less.

In addition to the statistical uncertainties on the ratio measurements, there is also the uncertainty resulting from the re-positioning of the phantom and the water depth overlying the bone phantom. The reproducibility of the phantom positioning measurements has been demonstrated to be two per cent for all three ratio methods. In a clinical situation, for each millimetre uncertainty in the measurement of soft tissue depth over the bone, an additional uncertainty of three per cent will be introduced to the coherent to Compton scattering ratio, (Table 7.4). For the ratios HP and R_k (Tables 7.8 and 7.9 respectively), the uncertainty introduced by ± 1 mm of overlying soft tissue is one per cent. Combining these uncertainties (reproducibility and for ± 1 mm overlying tissue) by summing in quadrature approximately doubles the uncertainty in density determination for coherent to Compton scattering ratio measurements. For the coherent to Compton scattering ratio the overall uncertainty in density determination is up to one per cent. For the Compton profile ratios HP and R_k the overall uncertainty is around two per cent for no overlying water, rising to three per cent for overlying water depths of 10 mm. For an overlying water depth of 20 mm, the overall uncertainty in density from a determination of the ratio HP becomes around four per cent, while that for R_k becomes just over five per cent.

7.10 Conclusions

The investigations reported in this chapter were to determine whether the backscattering technique would be a suitable method for determining the density of trabecular (spongiosa) bone at shallow depths below the skin. The site studied was the calcaneum or heel bone as it has been shown to be a good indicator of the onset of osteoporosis (Vogel *et al* 1988, Kang and Speller 1999).

As discussed in Section 7.1, in approximate terms the density of normal spongiosa bone has a density of 1180 kg m^{-3} (ICRU 44 1989), around 18 per cent higher than soft tissue.

Osteoporotic spongiosa bone has a bone mineral density of 25 per cent or less than normal bone and a density of around 1135 kg m^{-3}. This is around 14 per cent (or less) denser than soft tissue. Therefore to be useful the technique must discriminate well between the two states. This requires a measurement uncertainty of better than two per cent and ideally nearer one per cent.

Initial investigations and comparison with published work (Karellas *et al* 1983, and Gigante and Sciuti 1985) demonstrated that in order to reduce the uncertainties arising from counting statistics to an acceptable level it would be necessary to increase the count rate at the detector. To achieve an increased count rate a larger aperture on the detector collimator was used. The consequence of this was to increase the volume of interest, which would no longer be confined within the "bone", but would include more of the overlying tissue. Consequently, the effect of differing amounts of overlying tissue (none, 10 mm and 20 mm) was investigated.

Four types of analysis were performed on the acquired data: coherent to Compton scattering ratio R, Compton profile ratios HP (MacKenzie 1990) and R_k (Tartari *et al* 1992), and Compton profile shape.

The coherent to Compton scattering ratio R gave good discrimination (10-fold) between phantoms with densities representing trabecular bone and soft tissue although the discrimination was reduced in the presence of overlying water (tissue) by three per cent per mm. The uncertainties due to counting statistics on these measurements were of the order of two per cent.

The Compton profile ratios (HP and R_k) were not as sensitive at discriminating between phantoms with densities representing trabecular bone and soft tissue (only 1.8 and 1.6-fold respectively). This sensitivity was further reduced by overlying water but by only one per cent per mm. The uncertainties due to counting statistics on both the Compton profile ratios were less than one per cent.

For the Compton profile shape measurements there was no distinguishable difference between phantoms representing trabecular bone and soft tissue when overlying water was present. This method was therefore unsuitable for density determination of the calcaneum.

When all sources of uncertainty are taken into account, i.e. reproducibility (re-positioning and counting statistics) and depth of overlying tissue (± 1 mm), the coherent to Compton scattering ratio method gave the smallest uncertainty in density determination of up to one per cent. For the same conditions, the Compton profile ratios gave an uncertainty in density determination of up to three per cent for an overlying tissue depth of 10 ± 1 mm.

In conclusion, of the methods reported here the coherent to Compton scattering ratio is the best method for determining bone density in the calcaneum. This is despite the small count rate in the coherent peak and consequent counting uncertainties. The measurement uncertainty of up to one per cent makes it a viable method for monitoring the state of osteoporosis in the heel bone.

Chapter 8 Studies on Jaw Phantom

8.1 Introduction

This chapter describes the investigations performed to assess the use of the backscattering technique in the determination of bone density in the jawbone (mandible). There has been considerable interest in the measurement of bone density in the jawbone for two reasons: either to determine the relationship between mandibular and skeletal bone mineral density (BMD) as an indicator of osteoporosis or to study bone resorption following tooth loss.

In order to use the measurement of mandibular BMD as a predictor of osteoporosis it is necessary to establish whether or not there is a significant correlation between mandibular BMD and that of skeletal sites. Quantitative computed tomography (QCT), dual photon absorptiometry (DPA), dual x-ray absorptiometry (DEXA) and radiographic films have been used to study this relationship. Several workers have investigated the correlation between bone mineral density in the jawbone and the lumbar vertebrae with a view to using dental radiographs as a simple method of predicting and monitoring osteoporosis with conflicting results (Henrikson *et al* 1974, Kribbs *et al* 1983, 1989, 1990, Kribbs 1990, Horner and Devlin 1992, Mohajery and Brooks 1992). More significant correlations have been made between mandibular bone mineral density and skeletal bone density using quantitative computed tomography (QCT) and dual energy x-ray absorptiometry (DEXA) (Klemetti *et al* 1993, 1994, Horner *et al* 1996). Horner *et al* (1996) concluded "the evidence from the literature in favour of the mandible being a useful indicator of the general skeletal bone status is mixed. It appears that significant correlations are obtained when more sophisticated analysis of the mandible such as QCT is used." Horner *et al* (1996) found that mandibular bone density measurements with DEXA reflected that in other skeletal sites. A subsequent study by Pluskiewicz *et al* (2000) using the methodology proposed by Horner *et al* (1996) also found significant correlation between mandibular bone mineral density and other skeletal sites.

The other area of interest is in assessing the strength of the jawbone prior to performing dental implants. These often fail if the jawbone is not sufficiently strong due to a deficit of bone mineral (Klemetti *et al* 1993, Clift *et al* 1995).

The effect of the thickness of overlying tissue has been determined as for the previous studies on the heel bone phantom. In addition the affect of air and tissue on the far side of the 'bone' has been investigated.

8.2 Description of the Jawbone

The jawbone is the largest and strongest bone of the face and serves as a receptor for the lower teeth. Its structure is shown in Figure 8.1. It consists of a curved horizontal portion, the body and two perpendicular portions, the rami, which join the back part of the body almost at right angles.

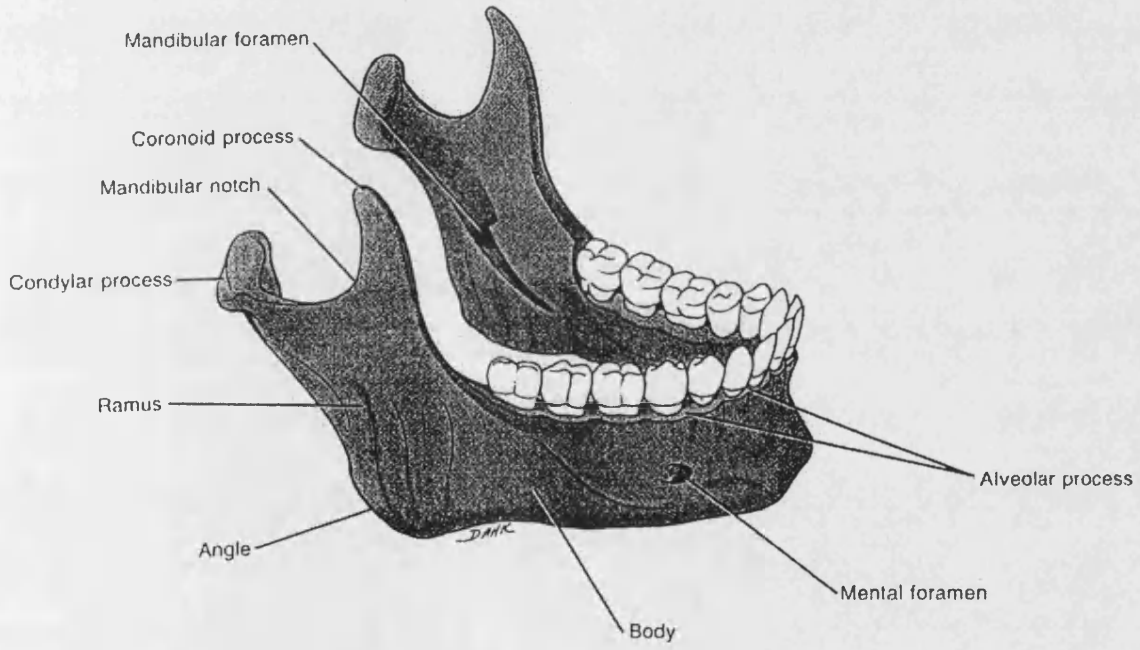

Figure 8.1 Jawbone - right lateral view (Tortora and Anagnostakos 1987)

The body is convex in outline and shaped like a horseshoe with two surfaces, external and internal. The external surface forms the chin in front and its central point is called the symphysis. The upper border of the body has sixteen cavities in which teeth sit. They are of variable size and depth depending on the teeth that they contain. In old age, with the loss of teeth the alveolar process (upper margin) is absorbed, and only the basilar process or lower margin remains resulting in a narrowing in depth of the body of the mandible. In the adult the maximum lateral separation (at the angle of the jaw) is of the order of 100 mm. The body of the jaw is of the order of 25 mm deep and 10 to 15 mm thick.

The rami are of a quadrilateral form. Each ramus presents two surfaces. The external surface is flat with ridges and gives attachment to the Masseter muscle over almost the whole of its extent. The lower border of the ramus is thick, straight and continuous with the body of the bone. The posterior border (angle of the jaw) is also thick, smooth and rounded whilst the anterior and upper borders are both thin. The rami each terminate with two processes, the coronoid and condylye, which articulate with the temporal bone to form the temporomandibular joint. In old age the rami are no longer vertical but make an obtuse angle with the body.

8.3 Experimental Arrangement

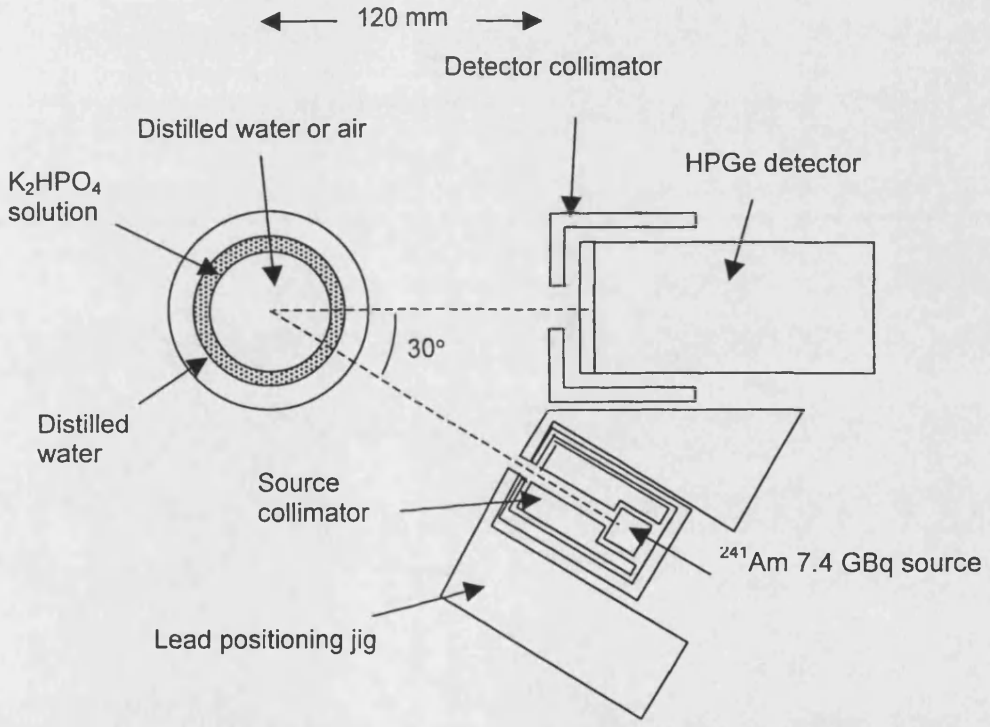

Figure 8.2 Experimental arrangement for jawbone phantom

The backscattering technique has been used to explore the potential of measuring bone density in the jawbone. The experimental arrangement with a phantom to simulate the jaw is shown in Figure 8.2, using the detection system described in Chapter 3. The jaw phantom comprised three concentric cylindrical containers. The innermost container had an internal diameter of 54 mm. The second cylinder had an internal diameter of 74 mm creating a layer to represent the jawbone, which was 10 mm thick. The outermost cylinder

had an internal diameter of 90 mm or 96 mm, creating an external layer of 8 mm or 11 mm thickness respectively. The wall thickness of each container was 1 mm. This configuration gave a reasonable approximation to the horseshoe shape of the body of the jawbone. The different layers of the phantom were filled to a height of 45 mm.

The innermost container was either filled with distilled water or empty, in order to ascertain the effect of the mouth cavity being occupied by the tongue or empty. The outermost layer was filled with distilled water to represent the soft tissue overlying the jawbone. The constant thickness layer of 10 mm representing the jawbone was filled with distilled water or different concentration solutions of K_2HPO_4. The same stock solutions of K_2HPO_4 that were used in Chapters 6 and 7 were used for these investigations. The densities were re-measured and were found to be slightly denser than before as some evaporation had occurred. The measured density of the distilled water remained as 995 kg m^{-3} at room temperature, as expected.

Concentration (g/100 ml):	0	9	20	30
Density (± 2 kg m^{-3}):	995	1068	1172	1206

For each experiment the jawbone phantom was placed with its centre at the focus of the source–detector system. The 7.4 GBq americium-241 bead source was contained in a lead shield with an aperture of 5 mm diameter and length 55 mm. This gave the irradiated area a nominal diameter of 12 mm at the focus. The detector was shielded with a steel collimator 10 mm thick. This had an aperture of 40 mm which allowed the whole of the detector face to be exposed (32 mm diameter), and extended around the sides of the detector. The angle between the axes of the source and detector was maintained at 30°, to detect backscatter through a nominal 150°. The distance from the front face of the detector steel collimator to the focus was 120 mm.

Data were acquired for one hour. This time was chosen to be representative of a four-source system with a fifteen minute acquisition time, which would be suitable for use in a clinical setting. Examples of the spectra acquired from the jawbone phantom in one hour are shown in Figure 8.3. The spectra shown are for the phantom filled only with water, and with the jawbone layer filled with the densest solution of K_2HPO_4 investigated (1206 kg m^{-3}). Two spectra of background data are also shown in the figure; one is with the empty phantom present and one with no phantom present (see Section 8.4). For all

other measurements in this series background data were collected with the same experimental set-up but with the phantom absent as the containers are considered to be part of the jaw simulation. One set of data was acquired for each concentration of K_2HPO_4 solution; the phantom was re-positioned for each measurement. Each series of investigations was made during a 24-hour period and usually within an eight-hour period.

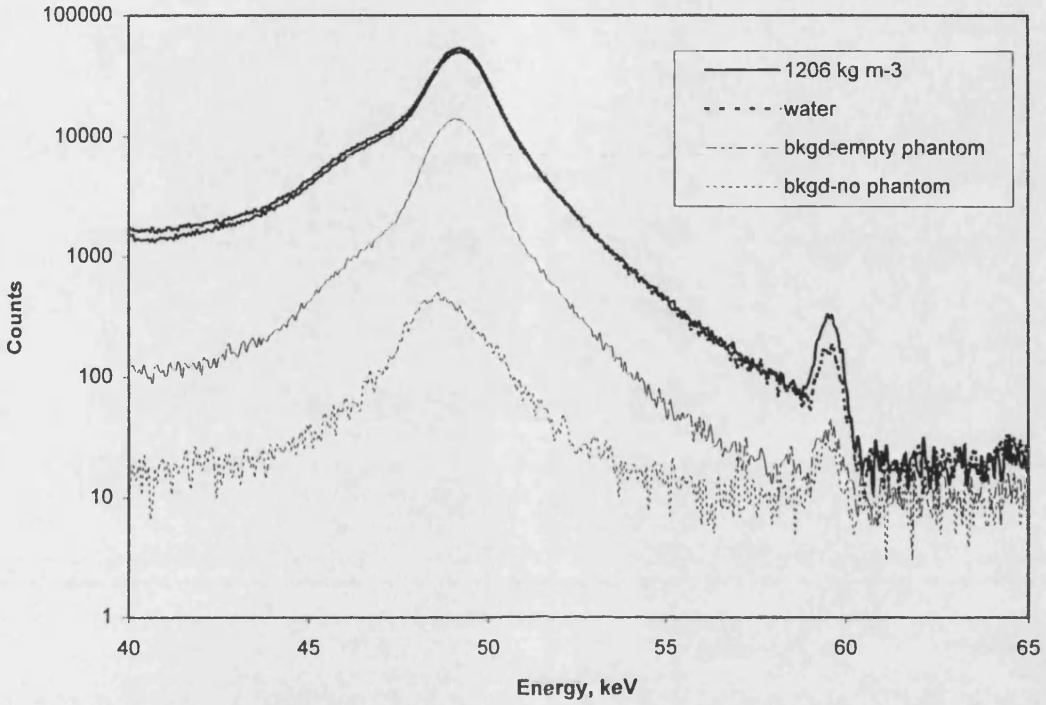

Figure 8.3 Spectra from jawbone phantom for water and the densest solution of K_2HPO_4 in the jawbone layer and two different background measurements, with and without the empty phantom.

The acquired spectra were used to investigate the sensitivity of the different ratio methods, discussed in previous chapters, for the determination of bone mineral density. The three ratios were the coherent to Compton scattering ratio R, and the ratios HP and R_k proposed by MacKenzie (1990) and Tartari *et al* (1992). The use of the Compton profile width was not investigated since the studies in the previous chapter using a simplified heel bone phantom had demonstrated that it was not a sufficiently sensitive technique.

8.4 Coherent to Compton scattering ratio

Data analysis was performed on spectra acquired with the innermost and outermost containers filled with distilled water to represent soft tissue, whilst the layer in between

was filled with distilled water or different concentration solutions of K_2HPO_4 to represent trabecular bone. Analysis was also performed on a similar set of spectra obtained with the innermost container empty or 'air filled' to give an indication of the effect of air gaps in the mouth. To determine the coherent to Compton scattering ratio, the coherent scatter was integrated from 58.5 to 60.5 keV, and the Compton scatter was integrated from 45 to 52 keV. The range 45-52 keV represents the full width tenth maximum (FWTM) of the Compton profile. Background data over the same interval ranges were subtracted prior to determining the ratios. The results are given in Table 8.1. The uncertainties on the measured values are due to counting statistics and are of the order of 2.5 per cent. Although the geometry employed should yield a Compton peak of around 48.9 keV (for 150° scattering angle), the measured Compton peak was 49.19 ± 0.06 keV, which equates to a scattering angle of 143°. This value is very similar to the Compton peak energy of 49.0 ± 0.06 keV obtained for the heel phantom (Chapter 7, Section 7.5). The difference between the calculated and measured Compton peak energies is because the calculated values assume narrow beam geometry, whilst the experimental method uses broad beam geometry. This difference is equivalent to four or five channels on the multi-channel analyser (one channel is approximately 60 eV).

Table 8.1 Measured coherent to Compton scattering ratios from jawbone phantom (8 mm thick outer water layer) with innermost container filled with distilled water or empty

Density, ± 2 kg m^{-3} of 10 mm jawbone layer	Coherent to Compton scattering ratio R ($\times 10^{-4}$)	
	Inner container -Distilled water	Inner container -Empty
995	11.3 ± 0.3	10.5 ± 0.4
1068	13.8 ± 0.3	16.5 ± 0.4
1172	19.3 ± 0.3	23.7 ± 0.5
1206	21.0 ± 0.4	26.5 ± 0.5

The results in Table 8.1 demonstrate that when the innermost container is filled with water the coherent to Compton ratio method is sensitive to the increase in density of the jawbone layer, with an increase of almost 100 per cent over the range investigated. However, the ratio R increases further when the innermost container is empty, compared with being filled with water, by up to 25 per cent for the most dense solution of K_2HPO_4 investigated. Scattered photons from the inner container (when filled with water), bone layer and outer

water layer are detected. When the inner container is empty the proportion of scatter from the bone layer is greater than when the inner container is filled with water and so the coherent to Compton scattering ratio is greater. The implication of this is that for a clinical investigation it would be necessary to maintain the position of the tongue in the mouth during the measurement period to avoid any changes to air gaps in the mouth. The lower measured value of the coherent to Compton scattering ratio for water with the innermost container empty compared to being filled with water is most likely due to the different scatter geometries although the two values are only just outside the standard deviation.

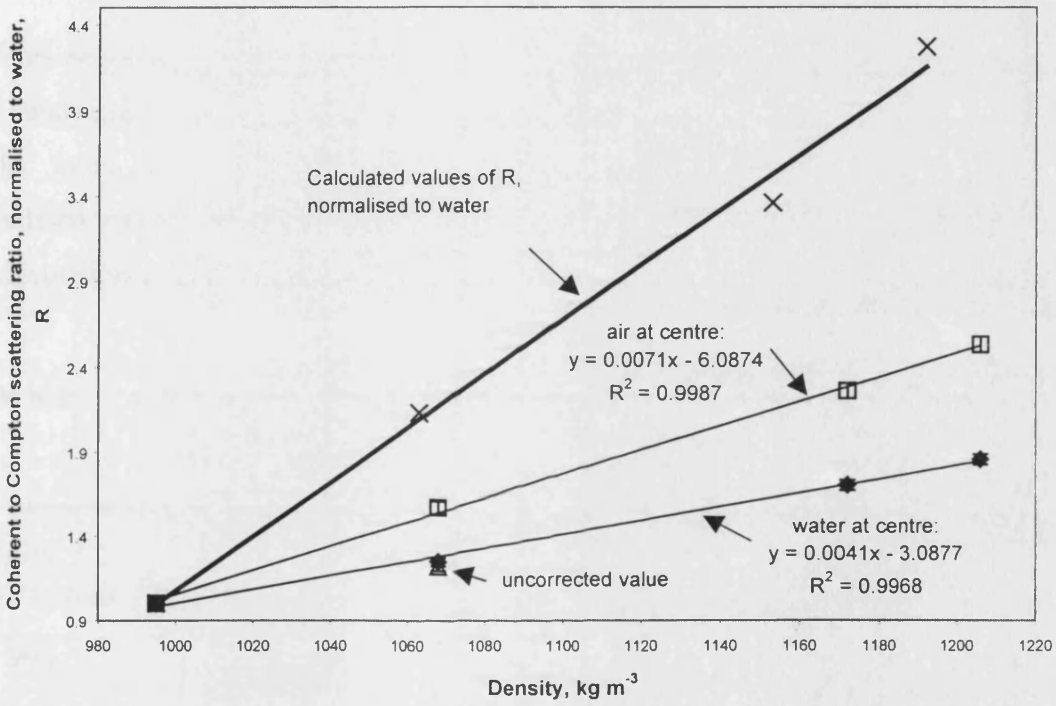

Figure 8.1 Variation of coherent to Compton scattering ratio (normalised to water) with density. Calculated values and measured values from jawbone phantom with 8 mm outer water layer, different density solutions of K_2HPO_4 in jawbone layer and innermost container empty or filled with water.

These results are also shown graphically in Figure 8.4 where the ratios have been normalised to the value obtained when the jawbone layer is filled with distilled water. The calculated values of coherent to Compton scattering ratio for the different concentrations of K_2HPO_4 normalised to water are also given for comparison. These calculated values have been plotted against the densities, which were determined when the solutions were freshly made. A linear relationship is demonstrated between the normalised coherent to Compton scattering ratio R, and the density of the jawbone layer. The series of data obtained with the innermost container filled with distilled water has one ratio measurement, which is just

outside one standard deviation from the least squares fit line (density 1068 kg m^{-3}). On further investigation it was found that for this particular set of data the coherent peak occurred at a lower energy, almost one channel different, than the other spectra in this series. After adjusting the integration limits by one channel to allow for this apparent change in the system calibration, the value of R increased by 2.2 per cent, which gave a better fit to the line (the coefficient of determination R^2 increased from 0.992 to 0.997), although the slope of the line was unchanged. (Both values are plotted.) The error bars on the measured values are one standard deviation based on uncertainties from counting statistics.

The data acquired with the greater thickness of water (11 mm) overlying the jawbone layer were analysed using the same method. The results are tabulated in Table 8.2 and show a similar trend to those obtained with an 8 mm thick outer water layer. The values normalised to water are plotted in Figure 8.5. There is a slight reduction in the discrimination with increasing density of the solution of K_2HPO_4 in the jawbone layer.

Table 8.2 Measured coherent to Compton scattering ratios from large jawbone phantom (11 mm thick outer water layer) with innermost container filled with distilled water or empty

Density, ± 2 kg m^{-3} of 10 mm jawbone layer	Coherent to Compton scattering ratio R ($\times 10^{-4}$)	
	Inner container -Distilled water	Inner container -Empty
995	12.0 ± 0.3	12.2 ± 0.3
1068	14.8 ± 0.3	16.7 ± 0.4
1172	19.6 ± 0.3	23.9 ± 0.4
1206	20.7 ± 0.4	25.3 ± 0.5

The effect of increasing the width of the outer layer of water by 3 mm is to slightly increase the ratio value except for the densest solution of K_2HPO_4. However, for each density of jawbone layer, the ratios obtained for the two different thicknesses of outer layer are within the uncertainties of one standard deviation due to counting statistics. For clarity, the data obtained from the two phantoms with the innermost container filled with water are tabulated in Table 8.3. These results have been normalised to water and are plotted in Figure 8.6. The implications of these results are considered in Section 8.6.

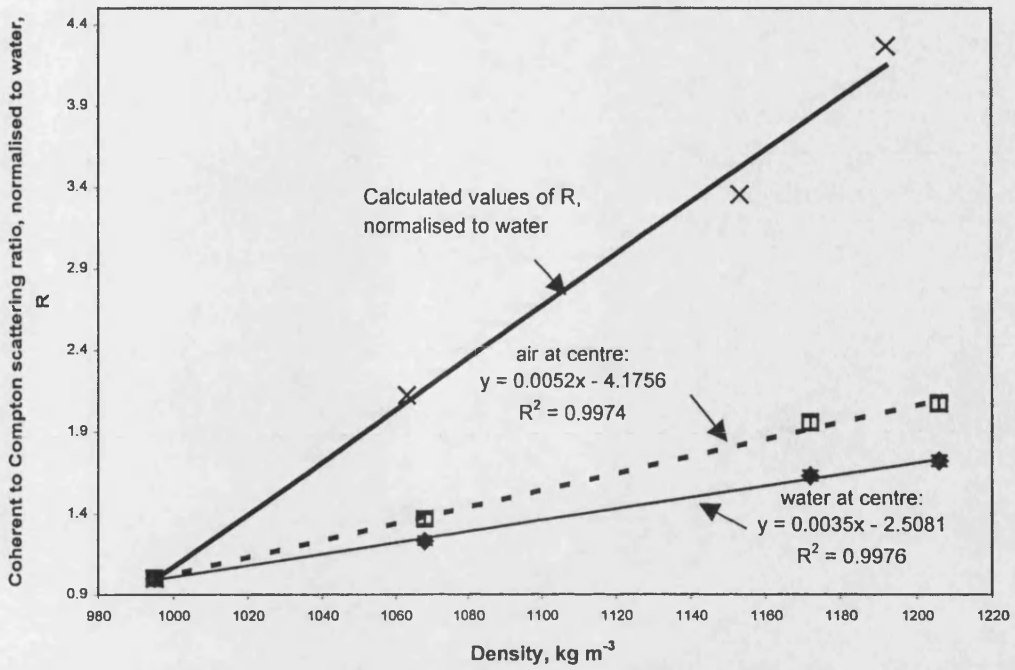

Figure 8.5 **Variation of coherent to Compton scattering ratio (normalised to water) with density. Calculated values and measured values from jawbone phantom with 11 mm outer water layer, different density solutions of K_2HPO_4 in jawbone layer and innermost container filled with water or empty.**

Table 8.3 **Measured coherent to Compton scattering ratios from jawbone phantoms for two thicknesses of outer water layer, with innermost container filled with distilled water**

Density, ± 2 kg m^{-3} of 10 mm jawbone layer	Coherent to Compton scattering ratio R ($\times 10^{-4}$)	
	Outer layer 8 mm thick	Outer layer 11 mm thick
995	11.3 ± 0.3	12.0 ± 0.3
1068	14.1 ± 0.3*	14.8 ± 0.3
1172	19.3 ± 0.3	19.6 ± 0.3
1206	21.0 ± 0.4	20.7 ± 0.4

*This value is corrected for the shift in coherent peak as mentioned in the text.

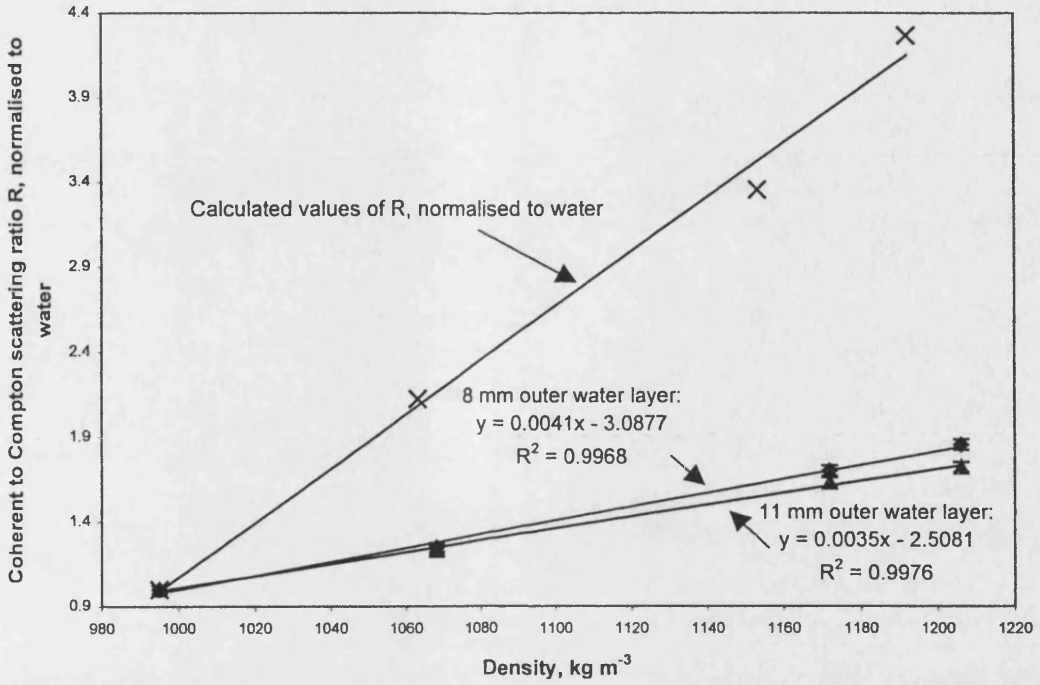

Figure 8.6 Variation of coherent to Compton scattering ratio (normalised to water) with density. Calculated values and measured values from jawbone phantom with 8 mm and 11 mm outer water layer, different density solutions of K_2HPO_4 in jawbone layer and innermost container filled with water.

8.5 Compton profile ratios

The ratios proposed by MacKenzie (1990) and Tartari *et al* (1992) have also been investigated in order to assess their usefulness in determining the bone density of the jawbone. The ratios have been determined from the same sets of phantom data described in Section 8.4. The same integration intervals as described in previous chapters have been used. For HP (MacKenzie 1990) the numerator was integrated from 52 to 58 keV and the denominator from 40 to 58 keV, whilst for R_k (Tartari *et al* 1992) the numerator was integrated from 51 to 56 keV and the denominator from 40 to 56 keV.

The jawbone phantom with both the 8 mm outer layer and inner cylinder containing water generated the ratio values tabulated in Table 8.4. The values of both ratios increase with the increasing density of the jawbone layer but only by 11 per cent for HP and 7.5 per cent for R_k over the range of densities investigated. This compares with a doubling in value for

the coherent to Compton scattering ratio, for the same range of densities in the jawbone layer.

Table 8.4 Compton profile ratios for water and different densities of K_2HPO_4 in jawbone layer, and 8 mm outer water layer, innermost container filled with water

Density, ± 2 kg m^{-3} of 10 mm jawbone layer	HP ($\times 10^{-3}$)	R_k ($\times 10^{-3}$)
995	32.8 ± 0.1	65.3 ± 0.2
1068	33.6 ± 0.1	66.6 ± 0.2
1172	35.3 ± 0.1	68.6 ± 0.2
1206	35.7 ± 0.1	69.1 ± 0.2

The jawbone phantom with the 8 mm outer water layer and the inner cylinder empty generated the values in Table 8.5. As with the coherent to Compton scattering ratios, when the inner container is empty the Compton profile ratio values are slightly greater than when the inner container is filled with water because of the increased proportion of bone phantom in the scattering volume. This result emphasises the need to minimise or be able to correct for any empty gaps in the mouth.

Table 8.5 Compton profile ratios for water and different densities of K_2HPO_4 in jawbone layer, and 8 mm outer water layer, innermost container empty

Density, ± 2 kg m^{-3} of 10 mm jawbone layer	HP ($\times 10^{-3}$)	R_k ($\times 10^{-3}$)
995	33.0 ± 0.2	66.4 ± 0.2
1068	34.6 ± 0.2	69.1 ± 0.2
1172	36.0 ± 0.2	71.2 ± 0.2
1206	37.2 ± 0.2	72.6 ± 0.2

The results tabulated in Table 8.4 and 8.5 have all been normalised to the value with water in the jawbone layer and are shown graphically in Figures 8.7 and 8.8. Figure 8.7 plots the normalised HP ratios and Figure 8.8 the normalised R_k ratios. The error bars in the figures are one standard deviation and are the uncertainties due to counting statistics and are all less than 0.5 per cent.

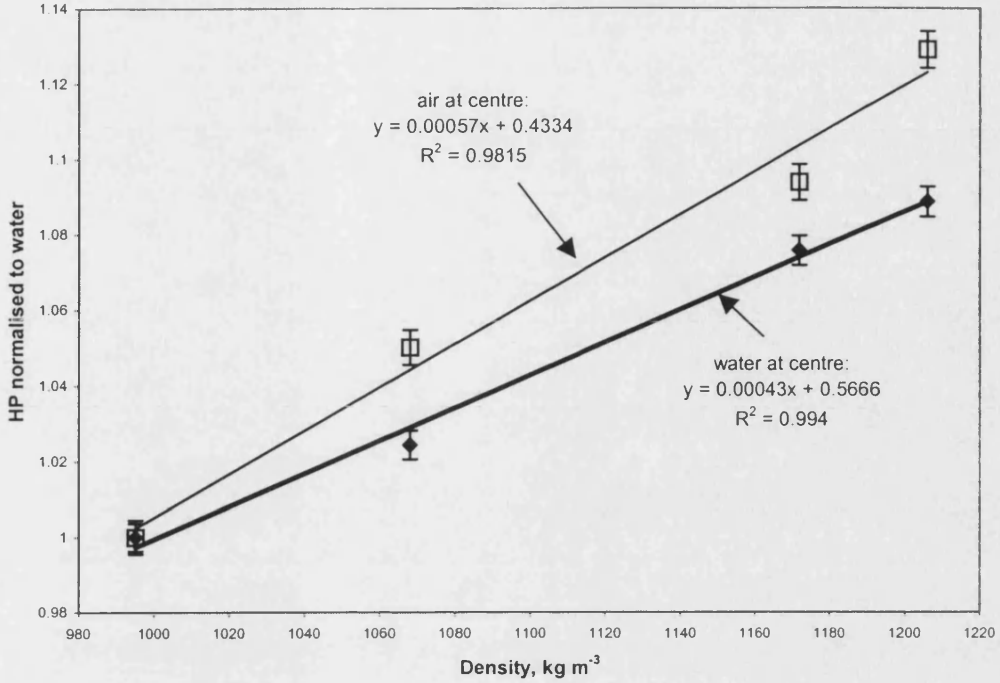

Figure 8.7 **Variation of measured Compton profile ratio HP (normalised to water) with density. Jawbone phantom with 8 mm outer water layer, different density solutions of K_2HPO_4 in jawbone layer and inner container filled with water or empty.**

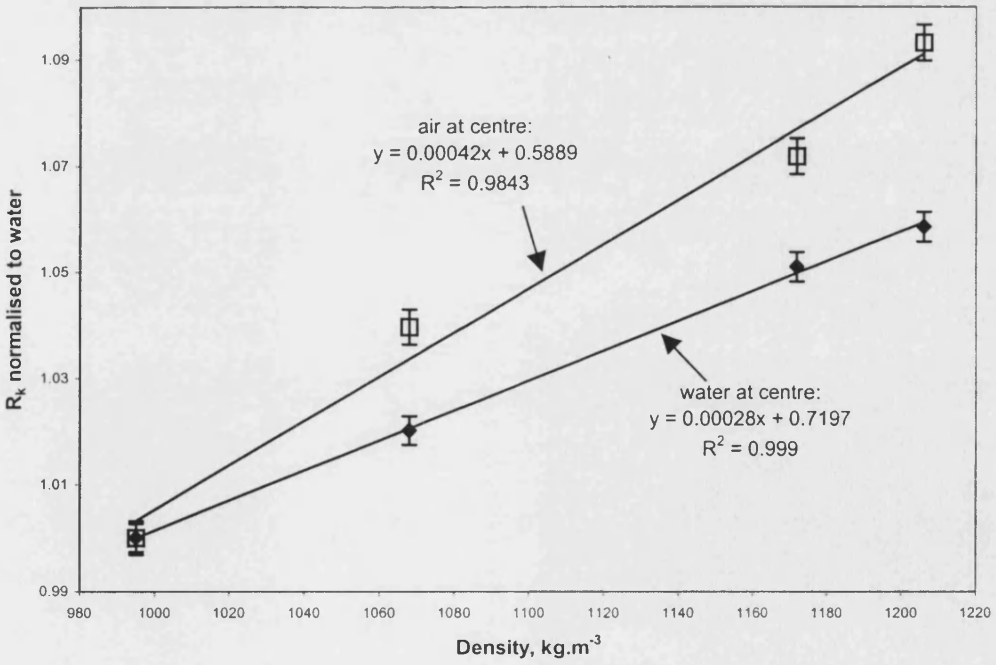

Figure 8.8 **Variation of measured Compton profile ratio R_k (normalised to water) with density in jawbone layer. Jawbone phantom with 8 mm outer water layer, different density solutions of K_2HPO_4 in jawbone layer and inner container filled with water or empty.**

A straight line has been fitted to each series of data using a least-squares method. The slopes of the lines fitted to the Compton profile ratio values are an order of magnitude less than that fitted to the coherent to Compton scattering ratios. However, the uncertainties on the Compton profile ratios are less than on the coherent to Compton scattering ratios due to better counting statistics.

When the outer layer water width of the jawbone phantom is increased to 11 mm the Compton profile ratios for the different densities demonstrate a similar trend to those measured with the 8 mm outer water layer (Tables 8.6 and 8.7). The Compton profile ratios increase with increasing density in the jawbone layer as expected. When the inner container is empty, compared with it being filled with water, the ratio values are slightly higher for the same density in the jawbone layer.

Table 8.6 Compton profile ratios HP for water and different densities of K_2HPO_4 in jawbone layer, 11 mm outer water layer and innermost container filled with water or empty

Density, ± 2 kg m^{-3} of 10 mm jawbone layer	HP ($\times 10^{-3}$)	
	Inner container water-filled	Inner container empty
995	35.0 ± 0.1	35.4 ± 0.1
1068	36.2 ± 0.1	37.2 ± 0.1
1172	37.7 ± 0.1	38.6 ± 0.2
1206	38.1 ± 0.1	39.3 ± 0.2

Table 8.7 Compton profile ratios R_k for water and different densities of K_2HPO_4 in jawbone layer, 11 mm outer water layer and innermost container filled with water or empty

Density, ± 2 kg m^{-3} of 10 mm jawbone layer	R_k ($\times 10^{-3}$)	
	Inner container water-filled	Inner container empty
995	70.1 ± 0.2	71.7 ± 0.2
1068	72.0 ± 0.2	74.5 ± 0.2
1172	74.3 ± 0.2	76.5 ± 0.2
1206	75.0 ± 0.2	77.3 ± 0.2

The effect of increasing the thickness of the outer water layer is to slightly increase the value of the Compton profile ratios. Increasing the phantom size alters the geometry

slightly and the amount of Compton scatter. The increase in ratio for an increase in phantom size of 3 mm in radius (8 mm to 11 mm) equates to an average of 2.3 per cent per mm for the ratio HP and 2.7 per cent per mm for the ratio R_k. These results are shown in Table 8.8 and 8.9. This is in contrast with the results of Section 8.4, where the coherent to Compton scattering ratios for the two different thicknesses were within the uncertainties of one standard deviation. However, when normalised to water all the ratios for the different thicknesses of overlying tissue lie within one per cent of each other for the same densities. This is shown graphically in Figures 8.9 and 8.10 for the ratios HP and R_k respectively.

Table 8.8 Compton profile ratios HP for water and different densities of K_2HPO_4 in jawbone layer, with two thicknesses of outer water layer (innermost container filled with water)

Density, ± 2 kg m^{-3} of 10 mm jawbone layer	HP ($\times 10^{-3}$)		Percentage difference per mm
	Outer layer 8 mm	Outer layer 11 mm	
995	32.8 ± 0.1	35.0 ± 0.1	2.2
1068	33.6 ± 0.1	36.2 ± 0.1	2.6
1172	35.3 ± 0.1	37.7 ± 0.1	2.3
1206	35.7 ± 0.1	38.1 ± 0.1	2.2

Table 8.9 Compton profile ratios R_k for water and different densities of K_2HPO_4 in jawbone layer, with two thicknesses of outer water layer (innermost container filled with water)

Density, ± 2 kg m^{-3} of 10 mm jawbone layer	R_k ($\times 10^{-3}$)		Percentage difference per mm
	Outer layer 8 mm	Outer layer 11 mm	
995	65.3 ± 0.2	70.1 ± 0.2	2.5
1068	66.6 ± 0.2	72.0 ± 0.2	2.7
1172	68.6 ± 0.2	74.3 ± 0.2	2.8
1206	69.1 ± 0.2	75.0 ± 0.2	2.8

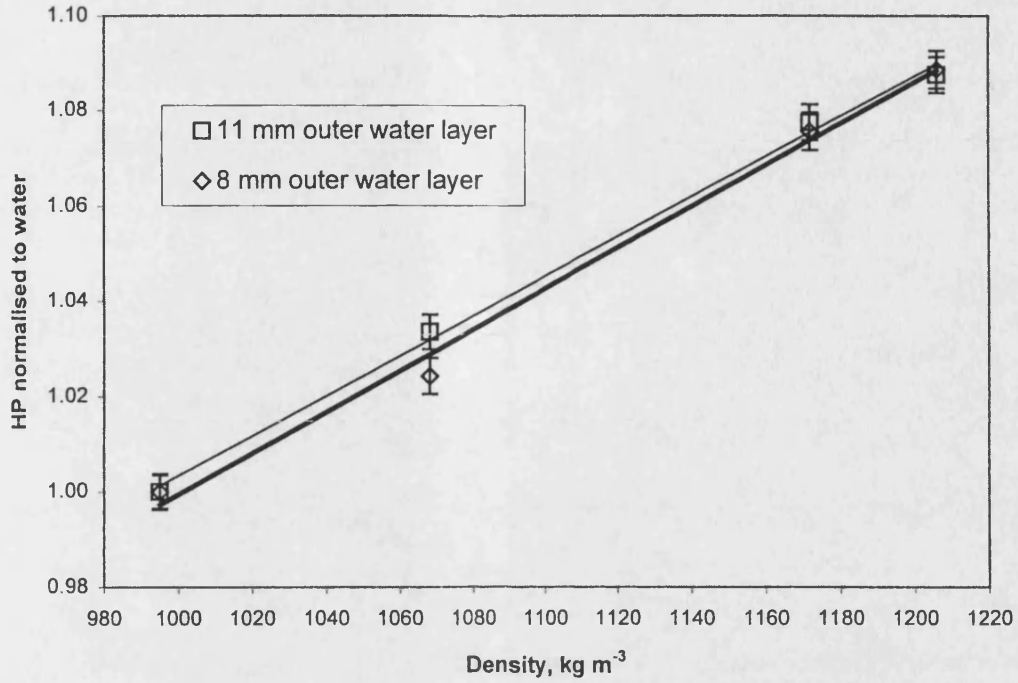

Figure 8.9 **Variation of Compton profile ratio HP (normalised to water) with density for two thicknesses of outer water layers (innermost container filled with water)**

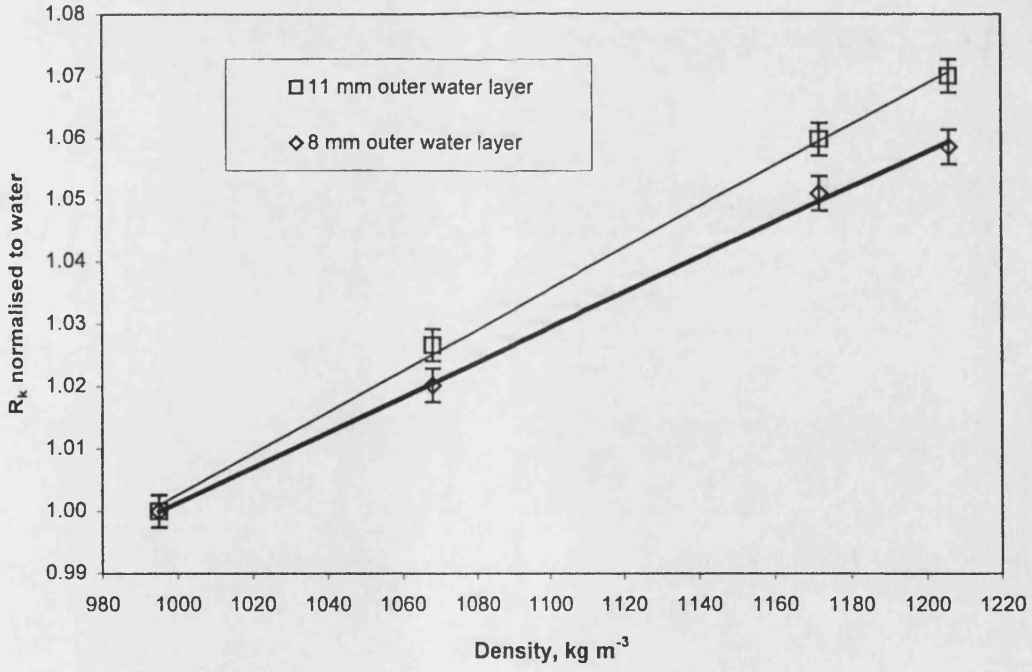

Figure 8.10 **Variation of Compton profile ratio R_k (normalised to water) with density for two thicknesses of outer water layer (innermost container filled with water)**

8.6 Uncertainties in density determination

For all the investigations with the jawbone phantoms the quoted uncertainties on the measured ratios are one standard deviation arising from counting statistics. The uncertainties are around 1.5 per cent for the coherent to Compton scattering ratios and mostly 0.3 per cent for the Compton profile ratios. The reproducibility investigations performed with the heel phantom indicated that the combined uncertainties arising from re-positioning and counting statistics were around two per cent for all ratio methods. For the coherent to Compton scattering ratio R, the positioning uncertainty was less than 0.5 per cent per mm, whilst for the Compton profile ratios the re-positioning uncertainty was around one per cent per mm for both HP and R_k. It can be assumed that these uncertainties would be of a similar magnitude for the jaw phantom. However, for the jaw phantom the main areas of uncertainty that will affect the density determination are the thickness of water overlying the jawbone layer, and whether the innermost container is filled with water or empty. In a clinical setting this translates to the amount of soft tissue overlying the jawbone, and the position of the tongue within the oral cavity. These issues are addressed in Section 8.7.

The slope of each data set, with all values normalised to that of water, has been determined using the method of least squares. The uncertainty in density determination of the solution with density closest to that of trabecular bone has been determined from Equation 6.1 (Chapter 6) and uses the slope of the least-squares-fit line to the measured ratio values and the mean uncertainty in $\Delta(\text{Ratio}/\text{Ratio}_w)$ based on statistical uncertainty.

In Table 8.10 the effect of the different thicknesses of outer water layer in the jawbone phantom on the uncertainty on the density determination is demonstrated. The slope of the coherent to Compton scattering ratio against density is a factor of ten greater than the slopes for the Compton profile ratios HP and R_k. The greatest effect on the slope from the two thicknesses of outer water layer on the plot of ratio normalised to water against density is obtained for the coherent to Compton scattering ratio R. The uncertainties in the ratio measurement normalised to water are similar for the three ratio methods. For the coherent to Compton scattering ratio R, the uncertainty in density determination is of the order of 0.7 per cent of trabecular bone density (1180 kg m^{-3}) for the two thicknesses of water layer. For the two Compton profile ratios HP and R_k the uncertainty in density determination is slightly greater, up to 0.8 per cent of trabecular bone density.

Table 8.10 **Slope and uncertainties for two thicknesses of water overlying the jawbone layer for the three different ratio methods (innermost container filled with water)**

Ratio	Overlying water, mm	Slope, S $m^3\ kg^{-1}$	$\Delta\left(Ratio/Ratio_w\right)$	ΔD, kg m^{-3}
R	8	0.0041	0.030	7
	11	0.0035	0.029	8
HP	8	0.00043	0.0039	9
	11	0.00042	0.0038	9
R_k	8	0.00028	0.0028	10
	11	0.00033	0.0027	8

Table 8.11 **Slope and uncertainties for two thicknesses of water overlying the jawbone layer for the three different ratio methods (innermost container empty)**

Ratio	Overlying water, mm	Slope, S $m^3\ kg^{-1}$	$\Delta\left(Ratio/Ratio_w\right)$	ΔD, kg m^{-3}
R	8	0.0071	0.044	6
	11	0.0052	0.036	7
HP	8	0.00057	0.0048	8
	11	0.00050	0.0044	9
R_k	8	0.00042	0.0033	8
	11	0.00036	0.0031	9

Table 8.11 shows the slope and uncertainties for the innermost container being empty (air-filled) for the two thicknesses of outer water layer. The same trends as for the innermost container filled with water are apparent. The slope of the coherent to Compton scattering ratio R against density is most affected by the thickness of the outer water layer, and these slopes are both a factor of ten greater than all the slopes obtained for the Compton profile ratios HP and R_k.

For this series of measurements, the uncertainty in density determination for the coherent to Compton scattering ratio R is of the order of 0.5 per cent of trabecular bone density (1180 kg m^{-3}) for the two thicknesses of outer water layer. For the two Compton profile

ratios HP and R_k the uncertainty in density determination is slightly greater, around 0.7 per cent of trabecular bone density. These uncertainties are slightly less than those obtained with the innermost container filled with water, but are very similar.

Therefore, provided the thickness of tissue overlying the jawbone is known, all the three ratio methods investigated will give similar uncertainties in density determination. The density uncertainties due to the coherent to Compton scattering ratios are marginally less than the density uncertainties on both the Compton profile ratios.

The effect of the innermost container being filled with water or empty also needs to be considered. In a clinical investigation this will correspond to the position of the tongue within the oral cavity during the measurement. For clarity the results of these two situations for the 8 mm outer water layer are tabulated in Table 8.12. For the three ratio methods, the slope of normalised ratio against density is greater when the innermost container is empty, and this corresponds to a reduced uncertainty in the density determination, even though the uncertainty in the normalised ratio is greater when the innermost container is empty. The uncertainty in density determination is less than one per cent for all cases, but in a clinical situation it would be difficult to determine the volume of the oral cavity. It would therefore be important to exclude air by filling the cavity with a bolus material.

Table 8.12 Slope and uncertainties for 8 mm thickness of water overlying the jawbone layer for the three different ratio methods (innermost container filled with water or empty)

Ratio	Innermost container content	Slope, S $m^3 kg^{-1}$	$\Delta\left(Ratio/Ratio_w\right)$	ΔD, kg m^{-3}
R	water	0.0041	0.030	7
	air	0.0071	0.044	6
HP	water	0.00043	0.0039	9
	air	0.00057	0.0048	8
R_k	water	0.00028	0.0028	10
	air	0.00042	0.0033	8

8.7 Discussion

The uncertainties in density determination for the three ratio methods investigated are all less than one per cent and would therefore be suitable as methods for determining the jawbone density in a clinical situation. However, in a clinical situation the thickness of tissue overlying the jawbone will vary, the proportion of air in the oral cavity will be an unknown factor and there will be a variation in positional accuracy.

The investigations performed on the jawbone phantom have demonstrated that the thickness of tissue overlying the jawbone will affect the value of the ratio measurement. The measured values of coherent to Compton scattering ratio for the two outer water thicknesses are plotted in Figure 8.11. The slopes of the least-squares-fit line are similar and the values for the same density solution in the jawbone layer are within three standard deviations of each other. This suggests that a difference of up to 3 mm in the overlying tissue thickness may not be an important factor in determining the bone mineral density of the jawbone using the measurement of coherent to Compton scattering ratio. Consequently if the thickness of overlying tissue could be determined to ± 1.5 mm, this would be sufficient for an acceptable clinical measurement.

The measured values of the Compton profile ratios HP (MacKenzie 1990) and R_k (Tartari *et al* 1992) for the two outer water thicknesses are plotted in Figures 8.12 and 8.13 respectively. In both cases the slopes of the lines for the two thicknesses of overlying water are similar but the measured values demonstrate differences of around 2.5 per cent per mm of overlying tissue. This implies the need for a calibration curve for each thickness of overlying tissue to ensure that the uncertainty in the density determination remains near to one per cent.

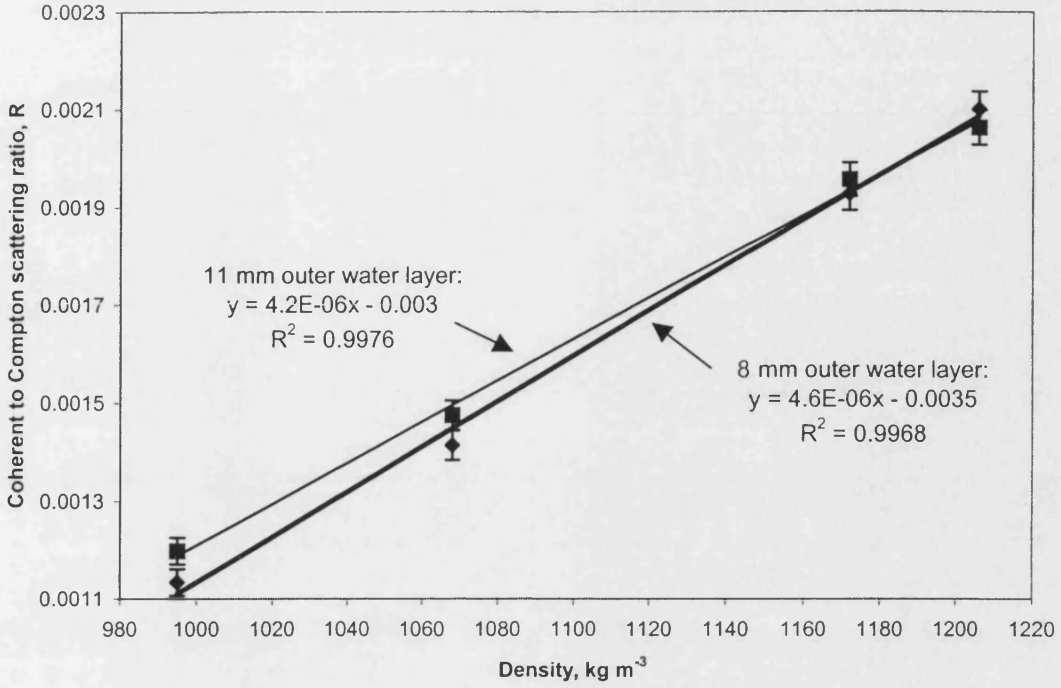

Figure 8.11 **Variation of coherent to Compton scattering ratio R with density for two thicknesses of outer water layer (innermost container filled with water)**

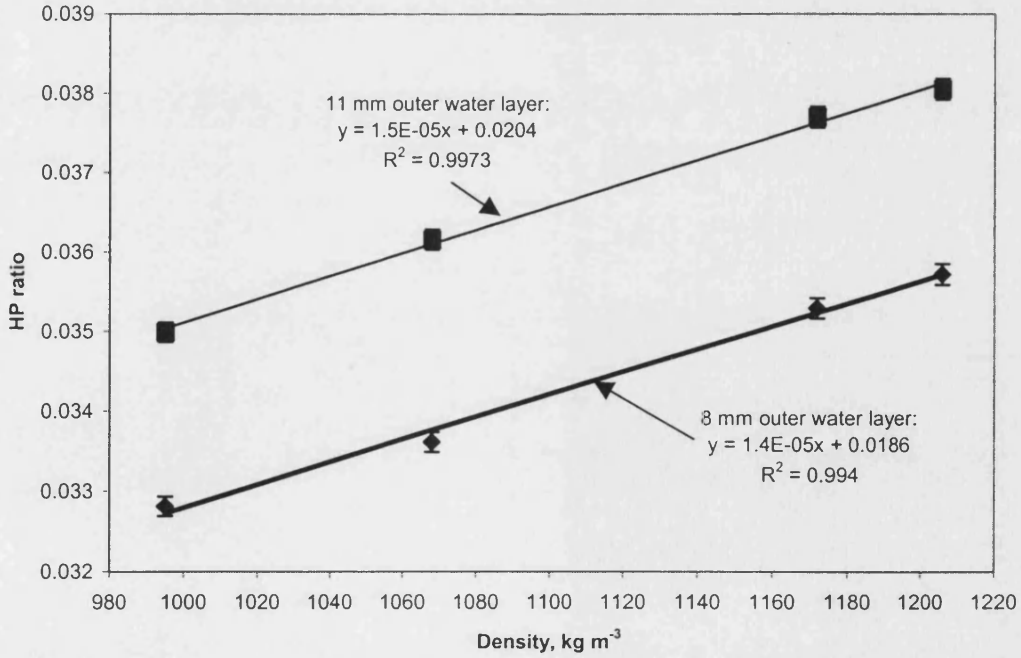

Figure 8.12 **Variation of Compton profile ratio HP with density for two thicknesses of outer water layer (innermost container filled with water)**

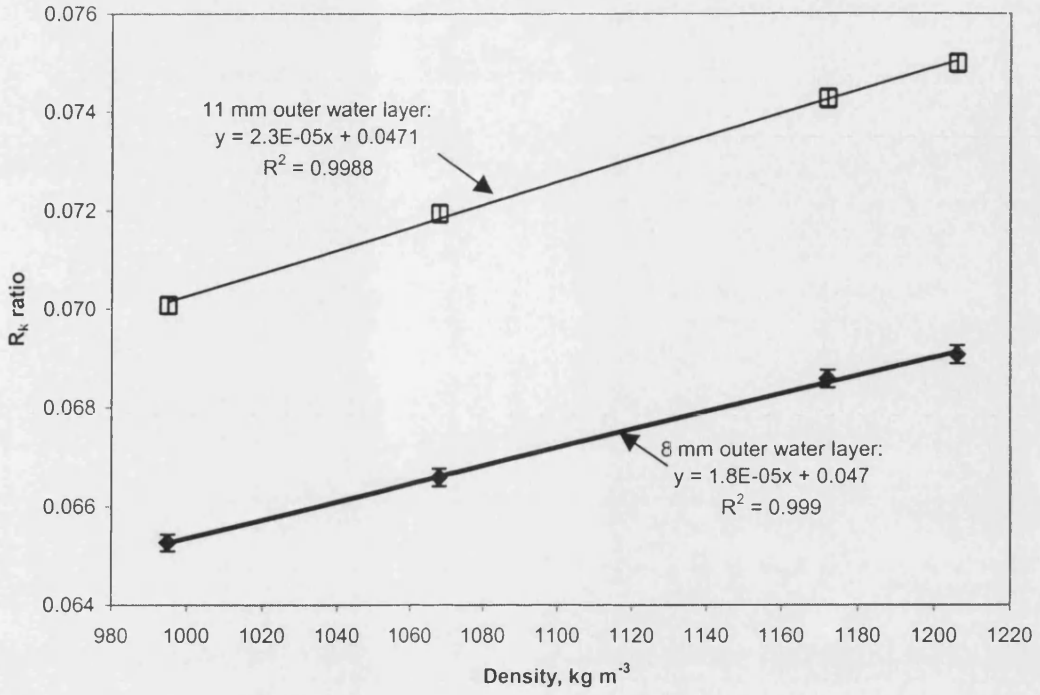

Figure 8.13 Variation of Compton profile ratio R_k with density for two thicknesses of outer water layer (innermost container filled with water)

Re-positioning measurements with the heel bone phantom discussed in the previous chapter demonstrated an uncertainty of two per cent for all ratio measurement methods. Since the experimental set-up for the jaw phantom is very similar it is reasonable to assume that the same uncertainty in re-positioning would be achieved for this phantom. If the uncertainties for ± 1 mm of overlying tissue and for re-positioning are summed in quadrature, then the total uncertainty in density determination for a density around that of trabecular bone becomes about one per cent for the coherent to Compton scattering ratio method. For the Compton profile ratios the uncertainty is much greater; around six per cent for the ratio HP and 10 per cent for the ratio R_k. The magnitude of the Compton profile uncertainties in density determination makes these methods unacceptable for jaw bone density measurements.

A much larger effect on the ratio is caused when the innermost container is empty rather than filled with water. The measured values of coherent to Compton scattering ratio for these two cases are plotted in Figure 8.14. For example a measured coherent to Compton scattering ratio of around 0.002 indicates a density of 1180 kg m^{-3} (normal trabecular bone) when the innermost container is full of water, and the lower density of 1115 kg m^{-3} when

the innermost container is empty (Figure 8.14). As the empty innermost container is meant to represent the oral cavity, the coherent to Compton scattering ratio measurement could overestimate the jawbone density by up to 65 kg m^{-3} if the cavity was not taken into account.

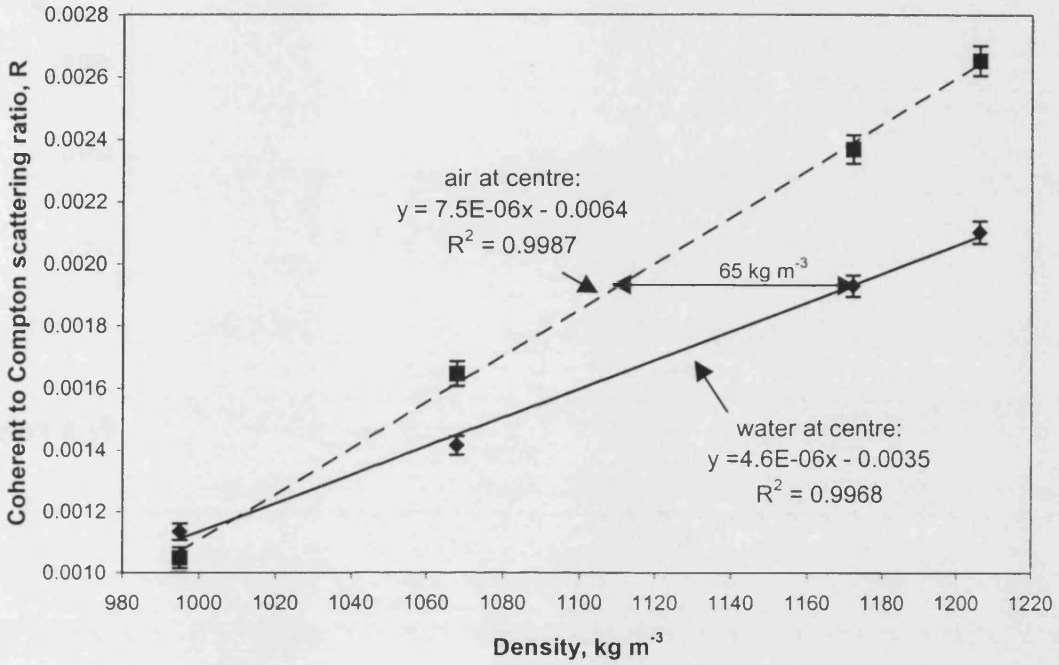

Figure 8.14 Variation of coherent to Compton scattering ratio R with density for phantom with 8 mm thick outer water layer and innermost container filled with water or empty

The measured values of the Compton profile ratios HP and R_k (MacKenzie 1990 and Tartari *et al* 1992) with the innermost container filled with water or empty are shown in Figures 8.15 and 8.16 for the 8 mm thick outer layer. Like the coherent to Compton scattering ratio method, measurements using the Compton profile ratios HP and R_k could overestimate the jawbone density (by up to 60 kg m^{-3} and 100 kg m^{-3} respectively) if the cavity was not taken into account.

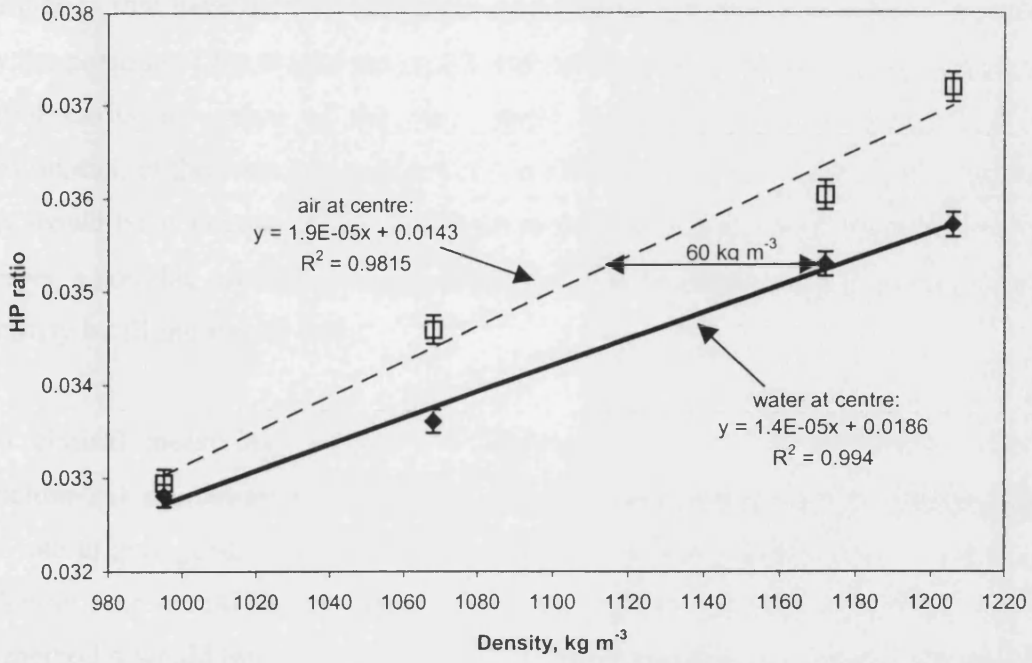

Figure 8.15 **Variation of Compton profile ratio HP with density for phantom with 8 mm thick outer water layer and innermost container filled with water or empty**

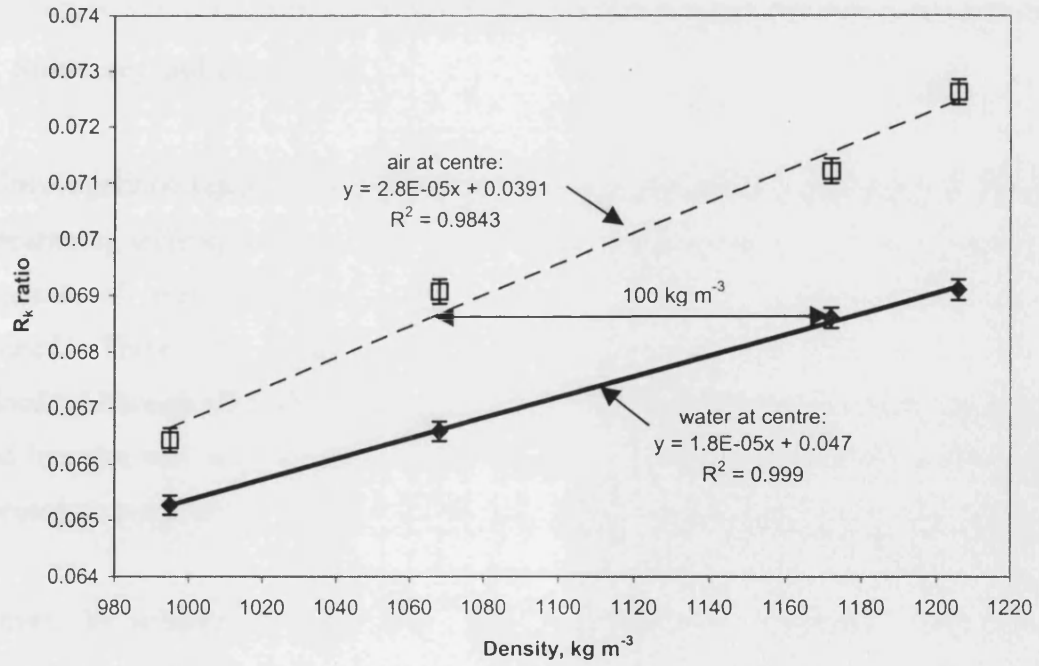

Figure 8.16 **Variation of Compton profile ratio R_k with density for phantom with 8 mm thick outer water layer and innermost container filled with water or empty**

The uncertainties due to air gaps in the oral cavity are the greatest of the potential uncertainties that have been investigated. In a clinical situation it would be important to know the position of the tongue within the oral cavity because if there were any air gaps in the oral cavity the value of the ratio would be greater and this would lead to an overestimation of the bone mineral density. In a clinical situation it is unlikely that the oral cavity would be as large as in the jaw phantom so these uncertainties would be much less. However, a possible solution to this problem would be to ensure air was excluded from the oral cavity by filling it with bolus.

For a clinical measuring system it is proposed to have a single detector with four americium-241 sources arranged in a ring around it. This would enable a sufficiently high count rate to give good counting statistics in a 15-minute acquisition time. This length of acquisition time should be acceptable to patients. For the coherent to Compton scattering ratio method it would improve accuracy of density measurement to determine the thickness of the tissue overlying the jawbone to ± 1.5 mm. It should be possible to measure this thickness by means of a diagnostic ultrasound beam. The uncertainties in density determinations from the Compton profile measurements would be too large even with this thickness information.

8.8 Summary and conclusions

The investigations reported in this chapter have examined the possibility of using the backscattering technique for density determination of the jawbone. The effect of different thicknesses of overlying tissue on the jawbone and air in the oral cavity has been examined. Three ratio methods have been considered for analysing the spectral data obtained. Although all methods look promising, in a clinical application the uncertainties would increase and only the coherent to Compton scattering ratio method would achieve the necessary precision of one per cent on bone density determination of the jawbone.

However, to achieve this precision with a coherent to Compton scattering ratio measurement it would be important to be able to determine the thickness of tissue overlying the jawbone to ± 1.5 mm. It would also be necessary to fill the oral cavity with a bolus material to exclude air and to be able to have a reproducible set-up. In practice, from

the work reported in Chapter 7, patient positioning uncertainties of about ± 2 mm might be expected to double the measurement precision to two per cent.

A backscattering technique for mandibular measurements is unlikely to achieve the precision of such techniques as QCT or DEXA. Precision of DEXA measurements of the spine range from 0.5 to one per cent, and for the femoral neck the range is two to five per cent, although poorer precision was realised for mandibular measurements (Horner *et al* 1996). However, both QCT and DEXA are expensive and would not be cost effective as a screening tool. For this reason some researchers (Henrikson *et al* 1974, Kribbs *et al* 1983, 1989, 1990, Kribbs 1990, Horner and Devlin 1992, Mohajery and Brooks 1992) have considered whether dental x-rays could be used to detect osteoporosis. This backscattering method might be more useful than using dental radiographs as it would give a more precise density measurement which would be expected to correlate with skeletal bone status more closely.

Chapter 9 Dosimetry

A clinical investigation involving a radiation dose must have a net benefit to the patient. For a clinical application of the gamma-ray backscattering technique described in this report it would be necessary for the radiation dose to be well within the range of doses delivered by accepted diagnostic procedures. The diagnostic reference level for a chest x-ray is a surface dose of 0.2 mGy (NRPB 1996). The recommended limit of mean glandular dose for a single view mammogram is 2 mGy (NHSBSP 1993). A survey by Young *et al* (1995) demonstrated a mean glandular dose of 1.4 mGy and a mean surface dose of 6.3 mGy for a single view mammogram. The effective dose equivalent often quoted for a dual energy x-ray absorptiometry (DEXA) scan is between 1 and 3 μSv. However, the more recent generation fan beam DEXA devices give higher doses. On one unit the dose was 59 μSv for a lumbar spine scan and 75 μSv from a total body scan (Steel *et al* 1998). A typical quantitative computed tomography (QCT) scan delivers a dose of 60 μSv (Gugliemi *et al* 1997). This chapter discusses the measured and calculated doses from the gamma-ray backscattering technique.

9.1 Measured Surface Dose Rates

An approximate measurement was first made with a calibrated portable dose rate meter. A measurement was then made using thermoluminescence dosimetry (TLD). The TLD was exposed at a distance of 70 mm with full backscatter. The 70 mm distance was representative of the surface distance used for the fat fraction investigations and the bone density investigations.

An indication of the likely dose rate was obtained from measurements with a calibrated portable dose rate meter (Mini-Rad, Mini-Instruments). The dose rate measured at one metre from the uncollimated 7.4 GBq americium-241source was 12 μSv h^{-1} ± 10%, but this was reduced to 10.4 μSv h^{-1} ± 10% when the source was collimated with the cylindrical lead collimator. The dose rate was further reduced to 3 μSv h^{-1} ± 10% when the source with the lead collimator was placed in the positioning jig. This reduction in dose rate was because of the shielding effect of the collimation. The expected dose rate at 70 mm is

therefore of the order of 0.6 mSv h^{-1} ± 10% with the collimated source in the experimental set-up.

To determine the likely skin dose from an investigation of this type, thermoluminescence dosimetry (TLD) was used. Epoxy-resin water substitute material was used as the phantom material on which to measure the surface dose. The phantom was positioned with its entrance surface at 70 mm from the americium-241 source. A phantom thickness of 110 mm was used to provide full backscatter. The 7.4 GBq americium-241 source was positioned in its lead collimator with 5 mm diameter aperture in the lead positioning block. An envelope-wrapped diagnostic x-ray film was placed against the entrance surface of the phantom and its position marked. The film was exposed for 24 hours. After processing the film was measured on a scanning densitometer to determine the size and exact location of the radiation beam entry point. The 50 per cent isodensity contour was an ellipse with axes dimensions of 12 mm × 10 mm and the 90 per cent isodensity contour was approximately 5 mm diameter. This information was used to position the thermoluminescence dosimeters. High sensitivity thermoluminescence dosimeters of type TLD-100H were used for these measurements. The size of these dosimeters is 3.2 mm × 3.2 mm and 0.9 mm thick so it was only possible to irradiate one dosimeter at a time within the 90 per cent isodensity contour. To improve the precision a total of three dosimeters were irradiated consecutively. During each irradiation another dosimeter was positioned approximately one metre behind the radiation source to measure the background radiation level in the room. Each dosimeter was exposed for 72 hours. Further dosimeters were exposed to measured doses of x-rays at 100 kVp for calibration. The measured surface dose rate with this method was 0.39 ± 0.03 mGy h^{-1} for a 7.4 GBq americium-241 bead source at a distance of 70 mm. For a multi-source arrangement the surface dose rate would be the same, but the total area irradiated would be increased according to the number of sources employed.

9.2 Calculated Surface Dose Rates

The dose rate $(dK_{air}/dt)_{\delta}$ at a distance l from a source of activity A, may be determined from the air kerma rate constant Γ_{δ}:

$$(dK_{air}/dt)_{\delta} = \Gamma_{\delta} \times A / l^2 \qquad \textbf{Equation 9.1}$$

The tabulated value of Γ_{δ} for 60 keV is 8.40 × 10^{-3} μGy h^{-1} MBq^{-1} m^2 (Johns and Cunningham 1978). For americium-241 the main photon emission is at 59.54 keV with a line efficiency of 35.7% (Lederer and Shirley 1978). The other photons emitted are of low energy or have a low line efficiency. There is self-absorption of the photons within the source, and there is attenuation of the photons by the stainless steel encapsulation. The low energy emissions are almost completely attenuated by either the bead or the source encapsulation. For the 7.4 GBq americium-241 source there will be attenuation within the 5 mm diameter active element. The elements in the active material are silicon, aluminium and oxygen. From Table 9.1, for an average distance travelled within the active element of 2.5 mm, a transmission factor of 0.83 is expected for both silicon and aluminium. There will also be further attenuation by the stainless steel encapsulation which is quoted as being between 0.25 mm and 0.3 mm thick (Amersham AMC 26). From the values in Table 9.1 a transmission factor of 0.75 for the 59.54 keV emission through the stainless steel would be expected. This reduces the efficiency of the source from 35.7 per cent to 22 per cent. Substituting in Equation 9.1 for a 7.4 GBq source with efficiency of 22 per cent the expected dose rate at one metre will be 13.7 μSv h^{-1}. This calculated value of 13.7 μSv h^{-1} is in good agreement with the 12 μSv h^{-1} ± 10% measured at one metre for the uncollimated source.

Table 9.1 Mass attenuation coefficients for 60 keV (Hubbell 1982) and densities (Kaye and Laby 1978) of materials used in source construction

Material	Mass attenuation coefficient μ/ρ, m^2 kg	Density, ρ kg m^{-3}
aluminium	2.763 × 10^{-2}	2700
silicon	3.186 × 10^{-2}	2320
stainless steel	1.197 × 10^{-1} (iron)	7800

9.3 Discussion

From measurements with the survey meter, the dose rate for the uncollimated source at one metre is 12 μSv h^{-1} ± 10% and this value is in agreement with the calculated dose rate at one metre of 13.7 μSv h^{-1}. For the experimental set-up, the measured dose rate at one

metre is 3 μSv h^{-1} ± 10%, which would give a dose rate of 0.6 mSv h^{-1} ± 10% at a distance of 70 mm. This is in good agreement with the TLD measurement of surface dose rate of 0.39 ± 0.03 mGy h^{-1} at a distance of 70 mm.

For a four-source system with a maximum acquisition time of 30 minutes, the skin dose would be 0.2 mGy based on the TLD measurement. For most applications where there are no significant organs in the radiation beam path the effective dose would be of the order of 2 μSv (using a tissue weighting factor w_T of 0.01 (ICRP 1990)). This dose is similar to that received from a DEXA scan and an order of magnitude less than the dose received from a chest x-ray or a single view mammogram. For breast tissue the nominal probability of fatal cancer is 2×10^{-3} Sv^{-1} and for bone surface the probability is 5×10^{-4} Sv^{-1} (ICRP 1990). For a measurement time of 30 minutes delivering a surface dose of 0.2 mGy the risk per investigation will be less than 0.4×10^{-6} for breast tissue and less than 1×10^{-7} for bone. Thus the gamma-ray backscattering technique represents a low dose investigation with a very small radiation risk.

Chapter 10 Conclusions

10.1 Summary of work to date

The work reported here has examined the possibility of using a gamma-ray backscattering technique to determine fat fraction and bone mineral density in certain anatomical sites. Other researchers have previously investigated Compton techniques but have aimed to detect scatter through small scattering angles in order to obtain high coherent counting rates (Stalp and Mazess 1980, Ling *et al* 1981, Karellas *et al* 1983, Gigante and Sciuti 1984, Leichter *et al* 1985 and Shukla *et al* 1986). The advantage of a backscattering technique such as that investigated here is a compact detection system, which would be suitable for a clinical set-up with good reproducibility.

A backscattering technique has the advantage of a simpler set-up for patient investigations but suffers from a low coherent count rate that decreases as the scattering angle increases. With this in mind various methods of analysis were used on the backscattered spectra to discover whether it would be possible to use an analysis which did not depend on the coherent count rate. The analyses investigated in addition to the coherent to Compton scattering ratio were the Compton profile shape and Compton profile ratios.

For the technique to be useful for diagnostic measurements it should be able to determine a fat fraction with an uncertainty of about 0.1 (one standard deviation) and a bone density measurement with an uncertainty of one per cent. It should also have a low radiation dose compared with other simple diagnostic techniques.

10.1.1 Fat fraction investigations

The measurement of fat fraction has been shown to be useful as an indicator for breast cancer risk and as a diagnostic tool in liver disease as well as in nutritional studies. The investigations performed with water to represent lean (muscle) tissue and ethanol to represent fat demonstrated that the measurement of the coherent to Compton scattering ratio gave good discrimination between the two solutions (a factor of two). However, the low coherent count rate is a disadvantage when determining acquisition times and the collimation of the detector.

An analysis that did not use the coherent signal would therefore be beneficial. With this aim the Compton profile shape was examined and the full width half maximum (FWHM), the full width third maximum (FW1/3M) and the full width quarter maximum (FW1/4M) were measured from the data. FWHMs were also determined from the Gaussian fit of the Compton profile data. These methods demonstrated a clear difference between water and ethanol with the measurement of the FW1/3M being the most promising method. However for an acquisition period suitable for a clinical measurement the uncertainties on the measurements reduce the sensitivity of the technique.

The Compton profile ratios suggested by McKenzie (1990) and Tartari *et al* (1992), which compare the count rate on the high energy side of the Compton peak to the total number of counts in the Compton peak, are also measures of profile shape. These ratios gave small uncertainties due to counting statistics but the discrimination between water and ethanol was much less than for the coherent to Compton scattering ratio.

Investigations into the effect of phantom size tended to show that for small phantoms there was evidence of Doppler broadening as suggested by Dumond (1933). As the phantom size increased this effect was accompanied by multiple scatter within the phantom and an increase in the range of scattering angles detected. These two effects masked the difference in Doppler broadening between water and ethanol from that seen in small phantoms. In a clinical application large volumes would be investigated, and the accompanying multiple scatter and range of scattering angles detected will probably mask differences due to Doppler broadening.

Investigations into the reproducibility of the measurements allowing for re-positioning of the phantoms demonstrated that there was only a marginal increase in the uncertainty of the measurements. As the coherent to Compton scattering ratio measurement is the least sensitive to re-positioning this is advantageous in this respect.

The conclusions from this work using ethanol and water as fat and muscle substitutes are:

- Both the coherent to Compton scattering ratio and the Compton profile ratio measurements are suitable for estimating fat fraction in extended tissue samples such as determination of breast tissue density or measurement of status of the liver.

- It would be useful to increase the count rate to improve the counting statistics.

10.1.2 Bone mineral composition investigations

The same methods of analysis used to determine fat fraction have been used to measure bone density. Bone mineral density measurements are important as a screening tool to identify those at risk from osteoporosis and also as a means of monitoring the efficacy of treatment to control the condition. Dual energy x-ray absorptiometry (DEXA) and quantitative computed tomography (QCT) are the commonly used techniques for these measurements but unfortunately they are expensive. There are several studies (Vogel *et al* 1988, Horner *et al* 1996 and Pluskiewicz *et al* 2000) that have demonstrated good correlation between measurements at different sites of the skeleton. The investigations reported here have examined the possibilities of using a low cost backscattering technique at three different anatomical sites. The main difference between these investigations and those to determine fat fraction were that the fat fraction measurements were based on a large volume of fairly uniform density material whilst the bone composition investigations had well defined target "bones". When examining bone composition the effect of overlying tissue needs to be considered.

Phantoms were used to represent three anatomical sites: the lumbar spine, the heel and the jaw. Dual energy x-ray absorptiometry (DEXA) is commonly used to measure central skeleton bone mineral density in the lumbar spine. Broad band ultrasound attenuation (BUA) and DEXA have been used to determine bone mineral density in the calcaneus (heel bone) (Kang and Speller 1998, 1999). The jaw has been examined by DEXA, quantitative ultrasound (which measures the speed of sound) and radiographic methods for determining bone mineral density (Horner *et al* 1996, Pluskiewicz *et al* 2000). The strength of the jawbone prior to dental implants is also of interest (Klemetti *et al* 1993, Clift *et al* 1995).

Investigations with the lumbar spine phantom demonstrated that the backscattering technique was suitable for assessing the bone composition of superficial bones but not for deep bony structures. The water overlying the bone attenuated the coherent signal from the bone and also increased the multiple scatter. These two effects decrease the sensitivity of the measurement. It would therefore be necessary to know the depth of tissue overlying the lumbar spine before the result could be interpreted. The Compton profile shape measurements demonstrated only small differences in profile width between water (lean tissue) and the most dense bone solution (equivalent to roughly the average of spongiosa and cortical bone densities). The Compton profile width measurements were without any

overlying water and so even smaller differences would be expected for measurements on the lumbar spine, which occurs at depths of around 85 mm. Similarly for the Compton profile ratios the sensitivity decreased with increasing depth of overlying water.

The above investigations demonstrated that the backscattering technique would not be suitable for measurements of the lumbar spine composition. However, it did prove suitable for determining the composition of more superficial bones such as the heel bone and the jawbone. Investigations with the heel bone phantom demonstrated that by increasing the aperture on the detector the count rate could be increased sufficiently to reduce the uncertainties due to counting statistics to an acceptable level for the coherent to Compton scattering ratio. However, this was at the expense of a reduction in discrimination over the range of concentrations of bone solutions investigated. The discrimination between the different concentrations was further reduced by the presence of overlying water (or tissue). The Compton profile ratios are similarly affected by the presence of overlying water. All the ratio methods gave results that produced an uncertainty in density measurement of better than one per cent, based on counting statistics. The uncertainties introduced by re-positioning were also examined and the coherent to Compton scattering ratio gave the smallest uncertainty. Overall the technique that gave the smallest uncertainties, within the one per cent limit, was the coherent to Compton scattering ratio measurement.

Similar conclusions were also drawn from the investigations on the jawbone phantom where the depth of overlying tissue again had an effect on the discrimination between different bone densities with all of the methods investigated. However, the effect was least for the coherent to Compton scattering ratio. For the measurements on the jawbone the oral cavity beyond the jawbone also affected the measured ratios (i.e. whether the oral cavity is filled with air or tissue). For a clinical application it would be necessary to fill the oral cavity with a bolus material to exclude any air in order to improve reproducibility.
The conclusions from the work with bone phantoms are:

- For superficial bones such as the heel and jaw bones the coherent to Compton scattering ratio and the Compton profile ratio measurements can give useful clinical results.
- The coherent to Compton scattering ratio was shown to be the preferred method of analysis.

10.2 Proposal for a clinical system

The investigations to date have demonstrated that the backscattering technique would be suitable for assessing fat fraction and bone composition in superficial bones such as the heel bone and the jawbone. It would be less suitable for measurements on the lumbar spine. All the analysis methods investigated would be suitable for the measurement of fat fraction but for bone composition measurements the coherent to Compton scattering ratio would be the method of choice.

For all the investigations long counting times were required to reduce the uncertainties arising from counting statistics because the measurements were made with only one 7.4 GBq americium-241 source. This activity is the highest currently available as a single source. In order to make the measurements within a suitable period for patient tolerance (less than half an hour) a system using four sources is proposed for a clinical instrument.

Such a four-source system is shown in Figure 10.1. It would need to be mounted on a suitable stand to be able to position the instrument close to the patient and directed at the patient anatomy under investigation. The work reported in this thesis indicates that such a system could form a useful clinical diagnostic tool for both fat fraction and bone density measurement.

For each anatomical site to be examined it would be necessary to have calibration phantoms to cover the range of expected densities. For measurements of bone density the calibration phantoms would also need to have different depths of overlying water to reflect the normal range of tissue depths.

The proposed system would be suitable for providing a relatively low cost screening tool for the assessment of fat fraction or bone density with a low radiation dose to the patient.

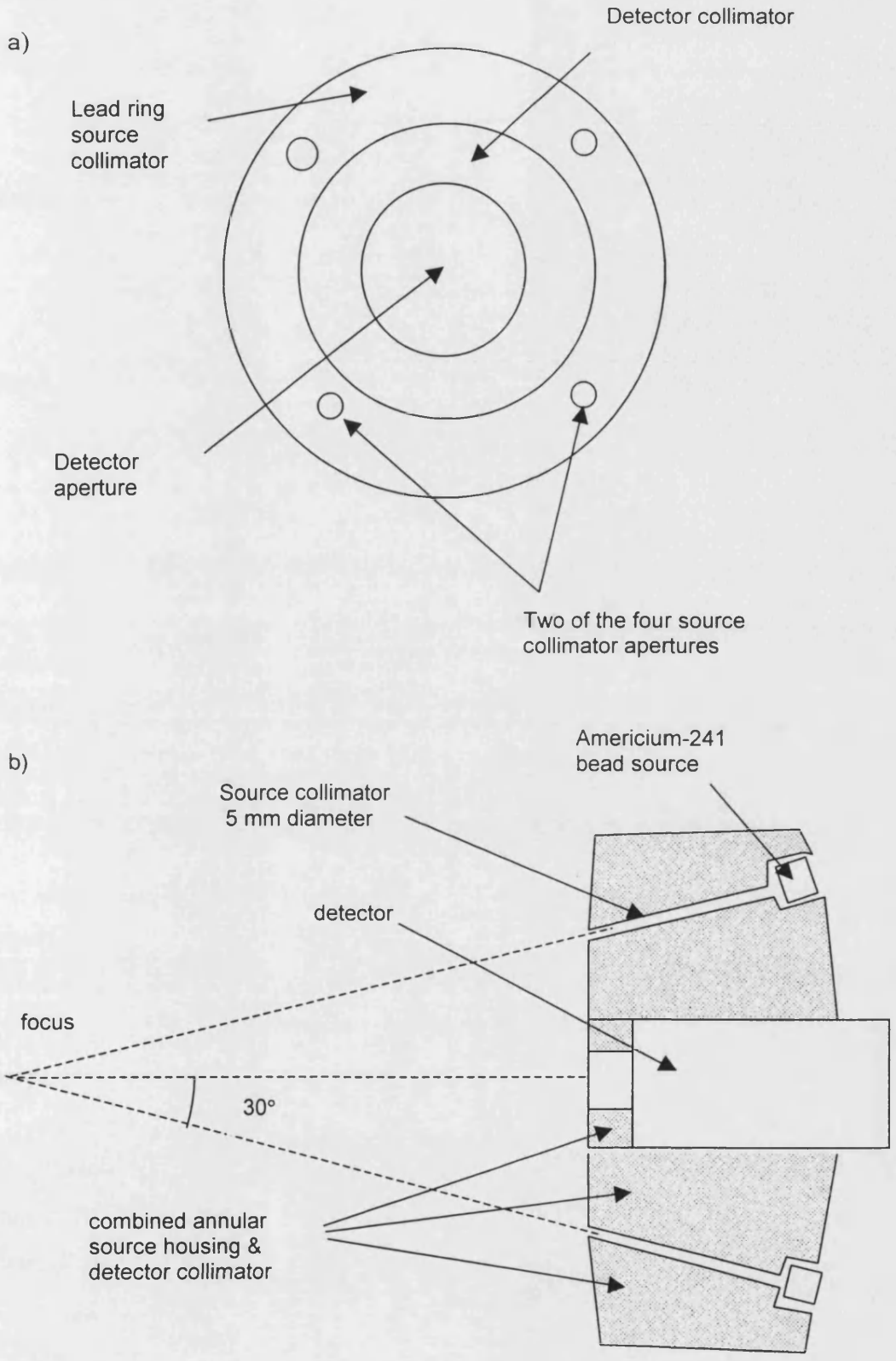

Figure 10.1 Schematic to show proposed four-source measurement system a) Plan and b) Section.

List of references

Allen J R, Humphries I R J, McCauley J C, Waters D L, Allen B J, Baur L A, Roberts D C K and Gaskin K J 1998. Assessment of body composition of children with cystic fibrosis. *Appl. Radiat. Isot.* **49** 591-592.

Areberg J, Bramnert M, Linden M, Manheim P, Ahlgren L and Mattsson S 1998. Only a temporary increase in the amount of body protein during long-term treatment with growth-hormone (GH) of adults with GH-deficiency (GHD). *Appl. Radiat. Isot.* **49** 667-669.

Boyd N F, Byng J W, Jong R A, Fishell E K, Little L E, Miller A B, Lockwood G A, Tritchler D L and Yaffe M J 1995. Quantitative classification of mammographic densities and breast cancer risk: results from the Canadian National Breast Screening Study. *Ntl. Cancer. Inst.* **87** 670-675.

Calman K 1995. Local provision for osteoporosis. Essential requirements for a hospital-based clinical service in the health district. National Osteoporosis Society.

Cann C E 1999. RSNA 1998 meeting report. *Rad Magazine* Jan 1999 39.

Christianson C 1993. Consensus development conference: Diagnosis, prophylaxis and treatment of osteoporosis. *Am. J. Med.* **94** 646-650.

Clift S E, Fisher J and Edwards B N 1995. Comparative analysis of bone stresses and strains in the Intoss dental implant with and without a flexible internal post. *Proc. Instn. Mech. Engrs.* **209** 139-147.

Department of Health 1995. Advisory Group on Osteoporosis (England: HMSO).

Dumond J W M 1933. The linear momenta of electrons in atoms and in solid bodies as revealed by x-ray scattering. *Rev. Mod. Phys.* **5** 1-33.

European Commission 1998. Building strong bones and preventing fractures. Summary report on osteoporosis in the European Community - Action for prevention. European Communities European Foundation for Osteoporosis, Germany.

Evans R D 1958. Handbuch der Physik **34** 218.

Fowler P A, Fuller M F, Glasbey G G and Foster M A 1992. Validation of the *in vivo* measurement of adipose tissue by magnetic resonance imaging of lean and obese pigs. *Am. J. Clin. Nutr.* **56** 7-13.

Gigante G E and Sciuti S 1985. A large angle coherent/Compton scattering method for measurement *in vitro* of trabecular bone mineral concentration. *Med. Phys.* **12** 321-326.

Gugliemi G, Schneider P, Lang T F, Giannatemp G M and Genant H K 1997. Quantitative computed tomography at the axial and peripheral skeleton. *European Radiology* **7** S33-S42.

Harding G, Neeton M and Koseanetzky J 1990. Energy dispersive X-ray diffraction tomography. *Phys. Med. Biol.* **35** 33-42.

Henrikson P A, Wallenius K and Astrand K 1974. The mandible and osteoporosis (2). Methods for deteremining mineraal content of mandible and radius. *J. Oral. Rehabil.* **1** 75-84.

Holt R S, Kouris K, Cooper M J, and Jackson D F 1983. Assessment of gamma-ray scattering for the characterisation of biological material. *Phys. Med. Biol.* **28** 1435-1440.

Holt R S, Kouris K, Cooper M J, and Jackson D F 1984. Gamma-ray scattering techniques for non-destructive testing and imaging. *Nucl. Instr. and Meth.* **221** 98-104.

Horner K and Devlin H 1992. Clinical bone densitometric study of mandibular atrophy using dental panoramic tomography. *J. Dent.* **20** 33-37.

Horner K, Devlin H, Alsop C W, Hodgkinson I M and Adams J E 1996. Mandibular bone mineral density as a predictor of skeletal osteoporosis. *Brit. J. Radiol.* **69** 1019-1025.

Hubbell J H 1982. Photon mass attenuation and energy absorption coefficients from 1 keV to 20 MeV. *Int. J. Appl. Radiat. Isot.* **33** 1269-1290.

Hubbell J H, Veigle Wm J, Briggs E A, Brown R T, Cromer D T, and Howerton R J 1975. Atomic form factors, incoherent scattering functions, and photon scattering cross sections. *J. Phys. Chem. Ref. Data* **4** 475-538.

Hussaini S H, Soo S, Stewart S P, Oldroyd B, Roman F, Smith M A, O'Grady J G, and Losowsky M S 1998. Risk factors for loss of lean body mass after liver transplantation. *Appl. Radiat. Isot.* **49** 663-664.

ICRP 1974. Report of the task group on reference man. Task Group Report 23. The International Commission on Radiological Protection (Oxford: Pergamon Press).

ICRP 1990. Recommendations of the International Commission on Radiological Protection. ICRP Publication 60 (Pergamon Press: Oxford).

ICRU 1989. Tissue substitutes in radiation dosimetry and measurement. ICRU Report 44 (Maryland, USA: ICRU publications).

Johansson A C, Haraldson B, and Attman P O 1998. Body composition in renal failure and the effect of dialysis. *Appl. Radiat. Isot.* **49** 665-666.

Johns H E and Cunningham J R 1978. The Physics of Radiology (Illinois, USA: Charles C Thomas).

Kang C and Speller R 1998. Comparison of ultrasound and dual energy x-ray absorptiometry measurements in the calcaneus. *Brit. J Radiol.* **71** 861-867.

Kang C and Speller R 1999. The effect of region of interest selection on dual energy x-ray absorptiometry measurements of the calcaneus in 55 post-menopausal women. *Brit. J Radiol.* **72** 864-871.

Karellas A, Leichter I, Craven J D, and Greenfield M A 1983. Characterization of tissue via coherent to Compton scattering ratio: Sensitivity considerations. *Med. Phys.* **10** 605-609.

Kaye G W C and Laby T H 1978. Tables of Physical and Chemical Constants (London: Longman).

Kelly T L, Berger N and Richardson T L 1998. DXA Body composition: Theory and practice. *Appl. Radiat. Isot.* **49** 511-513.

Kerr S A, Kouris K, Webber C E and Kennett T J 1980. Coherent scattering and the assessment of mineral concentration in trabecular bone. *Phys. Med. Biol.* **25** 1037-1047.

Kleerekoper M, Villanueva A R, Stanciu J, Rao D S, Parfitt A M 1985. The role of three dimensional trabecular microstucture in the pathogenesis of vertebral compression fractures. *Calcified Tissue International* **37** 594-597.

Klemetti E, Vainio P, Lassila V and Alhava E 1993. Cortical bone mineral density in the mandible and osteoporosis status in post-menopausal women. *Scand. J. Dent. Res.* **101** 219-223.

Knoll G F 1979. Radiation Detection and Measurement (USA: John Wiley and Sons).

Kribbs P J, Smith D E and Chesnut C H 1983. Oral findings in osteoporosis. Part II: Relationship between residual ridge and alveolar bone resorption and generalized skeletal osteopenia. *J. Prosthet. Dent.* **50** 719-724.

Kribbs P J, Chesnut C H, Ott S M and Kilcoyne R F 1989. Relationships between mandibular and skeletal bone in an osteoporotic population. *J. Prosthet. Dent.* **62** 703-707.

Kribbs P J, Chesnut C H, Ott S M and Kilcoyne R F 1990. Relationships between mandibular and skeletal bone in a population of normal women. *J. Prosthet. Dent.* **63** 86-89.

Kribbs P J 1990. Comparison of mandibular bone in normal and osteoporotic women. *J. Prosthet. Dent.* **63** 218-222.

Lederer C M and Shirley V S 1978. Table of Isotopes 7th Edition (New York, USA: John Wiley and Sons).

Leichter I, Karellas A, Craven J D, and Greenfield M A 1984. The effect of momentum transfer on the sensitivity of a photon scattering method for the characterization of tissues. *Med. Phys.* **11** 31-36.

Leichter I, Karellas A, Shukla S S, Looper J L, Craven J D, and Greenfield M A 1985. Quantitative assessment of bone mineral by photon scattering: Calibration considerations. *Med. Phys.* **12** 466-468.

Ling S S, Rustgi S, Karellas A, Craven J D, Whiting J S, Greenfield M A and Stern R 1982. The measurement of trabecular bone mineral density using coherent and Compton scattered photons *in vitro*. *Med. Phys.* **9** 208-215.

MacKenzie I K 1990. An axially symmetric gamma ray backscatter system for Dumond spectroscopy. *Nuclear Instruments and Methods in Physics Research* **A299** 377-381.

Marquardt D W 1963. An algorithm for least-squares estimation of non-linear parameters. *Journal of the Society of Industrial and Applied Mathematics* **11**(2) 431-444.

Mohajery M and Brooks S L 1992. Oral radiographs in the detection of early signs of osteoporosis. *Oral Surg. Oral Med. Oral Pathol.* **73** 112-117.

Ndlovu A M, Farrell T J, and Webber C E 1991. Coherent scattering and bone mineral measurement: The dependence of sensitivity on angle and energy. *Med. Phys.* **18** 985-989.

Nord R H 1998. Body composition stability in Lunar DPX. *Appl. Radiat. Isot.* **49** 519-520.

Nord R H and Payne R K 1990. Standards for body composition calibration in DEXA. *Current research in osteoporosis and bone mineral measurement* Ed: Ring E F J (London: British Institute of Radiology)

NHSBSP 1993. Objectives for the breast screening programme (NHS Breast screening programme).

NRPB 1996. Doses to patients from medical x-ray examinations in the UK – 1995 Review. NRPB R289 (National Radiological Protection Board).

Oldroyd B, Milner R, Smith A H and Smith M A 1998. A total body phantom for use with lunar dual energy x-ray absorptiometers. *Appl. Radiat. Isot.* **49** 525-526.

Pierson R N Jnr, Wang J, Thornton J C, Kotler D P, Heymsfield S B, Weber D A and Ma R M 1995. Bone mineral and body fat measurements by two absorptiometry systems: Comparisons with neutron activation analysis. *Calc. Tissue Int.* **56** 93-98.

Pluskiewicz W, Tarnawska B and Drozdzowska B 2000. Mandibular bone mineral density measured using dual energy x-ray absorptiometry: relationship to hip bone mineral density and quantitative ultrasound at calcaneus and hand phalanges. *Brit. J Radiol* **73** 288-292.

Putney R J 1996. Private communication.

Puumalainen P, Olkkonen H and Sikanen P 1977. Assessment of fat content of liver by a photon scattering technique. *Int. J. App. Radiat Isot.* **28** 785-787.

Puumalainen P, Uimarihuhta A and Olkkonen H 1982. A coherent/Compton scattering method employing an X-ray tube for measurement of trabecular bone mineral content. *Phys. Med. Biol.* **27** 425-429.

Richtmyer F K, Kennard E H and Lauritsen T 1955. Introduction to Modern Physics (New York: McGraw-Hill).

Royle G J and Speller R D 1991. Low angle x-ray scattering for bone analysis. *Phys. Med. Biol.* **36** 383-390.

Ryde S J S, Eston R, Laskey M A, Evans C J and Hancock D A 1998. Changes in body fat: Measurements by neutron activation, densitometry and dual energy x-ray absorptiometry. *Appl. Radiat. Isot.* **49** 507-509.

Sears W G and Winwood R S 1976. Anatomy and physiology for nurses (London: Edward Arnold).

Shypailo R J, Posada J K J and Ellis K J 1998. Whole-body phantoms with anthropomorphic-shaped skeletons for evaluation of dual-energy x-ray absorptiometry measurements. *Appl. Radiat. Isot.* **49** 503-505.

Shukla S S, Karellas A, Leichter I, Craven J D and Greenfield M A 1985. Quantitative assessment of bone mineral by photon scattering: accuracy and precision considerations. *Med. Phys.* **12** 4447-448.

Shukla S S, Leichter I, Karellas A, Craven J D and Greenfield M A 1986. Trabecular bone mineral density measurement *in vivo*: use of the ratio of coherent to Compton-scattered photons in the calcaneus. *Radiology* **158** 695-697.

Singh B, Tartari A, Baraldi C and Casnati E 1997. Tissue characterisation by Compton scattering profile measurements using low resolution detectors. *Physica Medica* **13** Supp. 1 354-355.

Soo S, Hussaini S H, Oldroyd B, Steewart S P, O'Grady J G, Smith M A and Losowsky M S 1998. Fat-free mass, muscle bulk and strength in liver disease. *Appl. Radiat. Isot.* **49** 661-662.

Stalp J T and Mazess R B 1980. Determination of bone density by coherent-Compton scattering. *Med. Phys.* 7 723-726.

Steel S A, Baker A J and Saunderson J R 1998. An assessment of the radiation dose to patients and staff from a Lunar Expert-XL fan beam densitometer. *Current research in osteoporosis and bone mineral measurement V* Ed: Ring E F J, Elvins D M and Bhalla A K (London: British Institute of Radiology).

Tartari A 1996. Private communication.

Tartari A, Baraldi C, Felsteiner J and Casnati E 1991. Compton scattering profile for *in vivo* XRF techniques. *Phys. Med. Biol.* **36** 567-578.

Tartari A, Casnati E, Felsteiner J, Baraldi C and Singh B 1992. Feasibility of *in vivo* tissue characterisation by Compton scattering profile measurements. *Nuclear Instruments and Methods in Physics Research* **B71** 209-213.

Tartari A, Casnati E, Fernandez J E, Felsteiner J and Baraldi C 1994. Photon backscattering tissue characterisation by energy dispersive spectroscopy evaluations. *Phys. Med. Biol.* **39** 219-230.

Tortora G J and Anagnostakos N P 1987. Principles of anatomy and physiology (Toronto: Harper and Row).

Tothill P, Avenell A, Love J and Reid D M 1994. Comparisons between Hologic, Lunar and Norland dual-energy x-ray absorptiometers and other techniques used for whole body soft tissue measurements. *Eur. J. Clin. Nutr.* **48** 781-794.

Tothill P, Han T S, Avenell A, McNeill G and Reid D M 1998. Comparisons between fat measurements by dual-energy x-ray absorptiometry, magnetic resonance imaging and under water weighing. *Appl. Radiat. Isot.* **49** 457-459.

Vogel J M 1987. Application principles and technical considerations in SPA. *Osteoporosis update 1987.* 219-231. Ed: Genant H K (Berkeley: University Press).

Vogel J M, Wasnich R D and Ross P D 1988. The clinical relevance of calcaneus bone mineral measurements: a review. *Bone and Mineral* **5** 35-58.

Weaver J and Chalmers J 1966. Cancellous bone: its strength and changes with ageing and an evaluation of some methods for measuring its mineral content. *J. Bone Joint Surg.* **48a** 289-299

Webster D J and Lillicrap S C 1985. Coherent/Compton scattering for the assessment of bone mineral content using heavily filtered x-ray beams. *Phys. Med. Biol.* **30** 531-539.

Westmacott C, Oldroyd B, Truscott J, O'Kane M, Wales J and Smith M A 1998. A pilot study to measure changes in body composition in very obese women on hypocaloric diets. *Appl. Radiat. Isot.* **49** 627-628.

White D R, Martin R J and Darlison R 1977. Epoxy-resin based substitutes. *Brit. J. Radiol.* **50** 814-821.

Williams B G (Ed.) 1977. Compton Scattering (London: McGraw Hill).

World Health Organisation 1994. Assessment of fracture risk and its application to screening for post-menopausal osteoporosis. WHO technical report 1994, series 843 (Geneva).

Young K C, Ramsdale M L and Rust A 1995. Mammographic dose and image quality in the UK Breast Screening Programme. NHSBSP Publication No 35.

Appendix

Published work

Some of the work reported in this thesis has been peer reviewed and published. The three papers and one letter are listed below and are appended to this thesis.

Gamma-ray backscatter for body composition measurement

Morgan H M, Shakeshaft J T and Lillicrap S C
Appl. Radiat. Isot. **49** 555-557, 1998.

Gamma-ray scattering for mandibular bone density measurement

Morgan H M, Shakeshaft J T and Lillicrap S C
Brit. J. Radiol. **72** 1069-1072, 1999.

Gamma-ray scattering for fat fraction measurement

Shakeshaft J, Morgan H M and Lillicrap S C
Phys. Med. Biol. **42** 1403-1413, 1997.

Bone density measurement by gamma-ray scattering – influence of overlying soft tissue
(Letter to the Editor)

Shakeshaft J T, Morgan H M and Lillicrap S C
Physica Medica **14** 175-177, 1998.

Pergamon

PII: S0969-8043(97)00186-3

Appl. Radiat. Isot. Vol. 49, No. 5/6, pp. 555–557, 1998

Printed in Great Britain
0969-8043/98 $19.00 + 0.00

Gamma-ray Backscatter for Body Composition Measurement

H. M. MORGAN*, J. T. SHAKESHAFT and S. C. LILLICRAP

Medical Physics Department, Royal United Hospital, Combe Park, Bath BA1 3NG, U.K.

The purpose of this study was to examine the potential of using backscatter information to assess regional body composition at selected sites. Two measurement techniques are examined: the measurement of the ratio of coherent to Compton scatter, and the measurement of the Compton scatter profile. Two possible applications are considered: the measurement of trabecular bone mineral density, and the measurement of the average fat/muscle ratio in a tissue volume. The results presented indicate that the analysis of coherent and Compton backscattered γ-ray spectra from an ^{241}Am source has the potential for measuring both trabecular bone mineral density and average fat/muscle ratio in a tissue volume, with a low absorbed dose to the subject. © 1998 Elsevier Science Ltd. All rights reserved

Introduction

The purpose of this study was to examine the potential of using backscatter information to assess regional body composition at selected sites. Two measurement techniques are examined: the measurement of the ratio of coherent to Compton scatter, and the measurement of the Compton scatter profile. Most of the previous work on coherent/Compton scattering (Ling *et al.*, 1982; Puumalainen *et al.*, 1982; Karellas *et al.*, 1983) has employed smaller scattering angles. The Compton scatterer profile is sensitive to the chemical composition of the scatterer as a result of Doppler broadening due to the momentum distribution of the target electrons (Williams, 1977). Multiple scatter also influences the profile (MacKenzie, 1990; Tartari *et al.*, 1992). Two possible applications are considered: the measurement of trabecular bone mineral density, and the measurement of the average fat/muscle ratio in a tissue volume. The results presented indicate that the analysis of coherent and Compton backscattered γ-ray spectra from an ^{241}Am source has the potential for measuring both trabecular bone mineral density and average fat/muscle ratio in a tissue volume, with a low absorbed dose to the subject.

Experimental Arrangement

The experimental arrangement for backscatter measurement is shown in Fig. 1. The radiation source is a collimated 7.4 GBq ^{241}Am point source. A 32 mm diameter 10 mm depth hyperpure germanium detector recorded the scattered photon spectrum. A backscatter measurement geometry has clear advantages in a clinical setting as it allows for a simple measurement set up and positioning relative to the patient. Various phantom materials were used to simulate different tissues. Aqueous solutions of K_2HPO_4 in the concentration range 0–90 g per 100 ml were used to simulate the density range of trabecular bone. The solutions were contained in thin-walled polythene bottles, 38 mm in diameter and 60 mm in height. Ethanol and water were used, respectively, as fat and muscle substitutes, and these were contained in a large polythene tank.

Bone Mineral Measurement

Results

To explore the potential of the technique for measurement of trabecular bone density at different depths in soft tissue, measurements were made with the bone phantom bottles placed first in air and then at different depths (35–60 mm to centre of bottle) in a water tank. Figure 2 shows how the measured coherent/Compton scatter ratio R varies with the concentration of K_2HPO_4 for the bone phantom in air and at different depths in water. Measured Compton profiles show differences of up to 70 eV in FWHM values with different K_2HPO_4 concentrations for the above phantom in air. However, the differences reduce to below a significant level when the bone phantom is measured in the water tank.

Conclusions

Over the range of expected trabecular bone mineral density the coherent/Compton scattering ratio R is a sensitive indicator of bone mineral density for peripheral bone locations. The technique is less

*To whom all correspondence should be addressed.

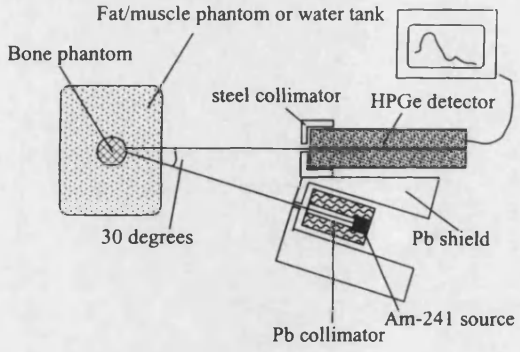

Fig. 1. The experimental arrangement used for gamma-ray backscattering measurements. The Am-241 source has a 5 mm diameter lead collimator for all measurements. The hyperpure germanium detector was used with a 5 mm diameter collimator for the studies with bone mineral investigations, and a 10 mm diameter collimator for the studies of fat/muscle ratios.

sensitive for bone lying at depths beyond 50 mm due to the overlying scatter components in the measured spectrum.

Fat/Muscle Ratio

Results

In order to explore whether the technique could distinguish clearly between muscle and fat, phantoms of water, ethanol (both in a polythene tank) and epoxy resin blocks were used as tissue substitutes. Figure 3 shows the dependence of the coherent scatter and Compton scatter on phantom thickness. The major contribution to both spectra is from material lying within 50 mm of the surface. Thus the technique would be useful for investigating the composition of tissue within 50 mm of the body surface, since 90% of the counts arise from this region. The measured

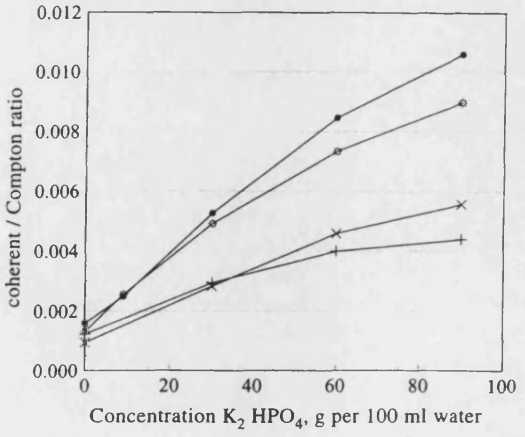

Fig. 2. Variation of coherent/Compton ratio with solutions of K_2HPO_4 in water of different concentrations, calculated values (○), in air (●), and at two depths in a water tank, 35 mm (×) and 60 mm (+).

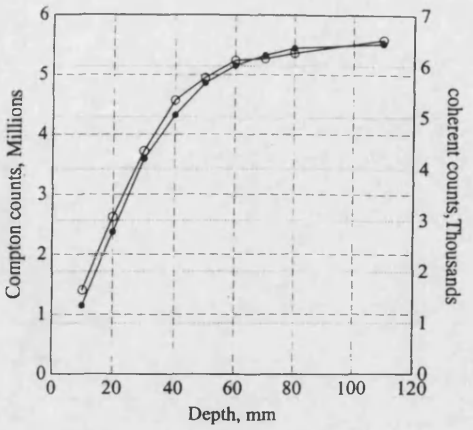

Fig. 3. Variation of backscatter with depth. Slabs of epoxy-resin phantom (300 mm × 300 mm) were used to increase the depth. The front surface of the phantom remained at a constant distance from the detector, 50 mm in front of the source–detector focus. Counts in the Compton region are denoted by (●), and in the coherent region by (○).

values of the coherent/Compton scatter ratio for depths more than 50 mm represent an approximate average of the ratios in the first 50 mm. Water (H: 11%, O: 89%) has a similar elemental composition to muscle (C: 14%, H: 10%, O: 71%, N: 3.4%) and ethanol – C_2H_5OH (C: 52%, H: 13%, O: 35%) has a similar elemental composition to fat (C: 60%, H: 11%, O: 28%) (ICRU, 1989).

For depths greater than 50 mm the measured coherent/Compton ratio R for water is 10.5×10^{-4} and for ethanol 5.7×10^{-4}, a difference of 85%. Differences were also detected in the Compton profiles. For 30 min acquisitions, the FWHM of the Compton profile for water is 2.02 ± 0.005 keV, and for ethanol is 1.92 ± 0.005 keV, a difference of 0.10 ± 0.007 keV.

Conclusions

Both the coherent/Compton scatter ratio and the Compton profile shape are sensitive to the composition differences between ethanol and water, and might be explored as a means of monitoring the proportion of fat in a tissue volume.

Summary

The results presented indicate that the analysis of coherent and Compton backscattered γ-ray spectra from an ^{241}Am source has the potential for measuring both trabecular bone mineral density and average fat/muscle ratio in a tissue volume, with a low absorbed dose to the subject. This work has been performed using tissue substitute materials. The next step is to construct a multi-source instrument suitable for clinical use. It will be tested first using animal tissues.

Acknowledgement—J. T. Shakeshaft acknowledges support from the Wellcome Trust.

References

ICRU (1989) Tissue substitutes in radiation dosimetry and measurement. Report 44, ICRU, Bethesda, MD.

Karellas, A., Leichter, I., Cravan, J. D. and Greenfield. M. A. (1983) Characterization of tissue via coherent to Compton scattering ratio: sensitivity considerations. *Medical Physics* **10,** 605.

Ling, S.-S., Rustgi, S., Karellas, A., Craven, J. D., Whiting, J. S. and Greenfield, M. A. (1982) The measurement of trabecular bone mineral density using coherent and Compton scattered photons *in vitro*. *Medical Physics* **9,** 208.

MacKenzie, I. K. (1990) An axially symmetric gamma ray backscatter system for Dumond spectroscopy. *Nuclear Instruments and Methods* **A299,** 377.

Puumalainen, P., Uimarihuhta, A. and Olkkonen, H. (1982) A coherent/Compton scattering method employing an X-ray tube for measurement of trabecular bone mineral content. *Physics in Medicine and Biology* **27,** 425.

Tartari, A., Casnati, E., Felsteiner, J., Baraldi, C. and Singh, B. (1992) Feasibility of *in vivo* tissue characterisation by Compton scattering profile measurements. *Nuclear Instruments and Methods* **B71,** 209.

Williams, B. G. (Ed.) (1977) *Compton Scattering*. McGraw–Hill, London.

The British Journal of Radiology, 72 (1999), 1069–1072

Gamma-ray scattering for mandibular bone density measurement

H M MORGAN, J T SHAKESHAFT and S C LILLICRAP

Medical Physics Department, Royal United Hospital, Combe Park, Bath BA1 3NG, UK

Abstract. There has been considerable interest in the measurement of bone density in the mandible, either to study bone resorption following tooth loss or to determine the relationship between mandibular and skeletal bone mineral density. Measurements mostly have been made on dental radiographs but more significant correlations between mandibular and skeletal bone density have been obtained when more sophisticated techniques have been used, such as quantitative CT and dual energy X-ray absorptiometry. The present work investigates the feasibility of using gamma-ray scattering measurements to estimate mandibular bone density. Using a phantom to simulate the jaw, an ^{241}Am source and a hyperpure germanium detector it is shown that bone density may be measured with a precision of about 1%.

The bone mineral density (BMD) of the mandible has been reported by a number of authors investigating both bone resorption following tooth loss and the relationship between mandibular BMD and skeletal BMD as an indicator of osteoporosis [1–12].

For the measurement of mandibular BMD to be considered as a predictor of osteoporosis, it is first necessary to establish whether there is a significant correlation between the mandibular BMD and that of skeletal sites. Quantitative CT (QCT), dual photon absorptiometry (DPA) and dual energy X-ray absorptiometry (DXA) as well as radiographic film have been used to study this relationship. In a review of published data, Horner et al [12] concluded that "the evidence from the literature in favour of the mandible being a useful indicator of the general skeletal bone status is mixed. It appears that significant correlations are obtained when more sophisticated analysis of the mandible, such as QCT, is used". Their own results where DXA was used to measure both mandibular and skeletal BMD also showed good correlation between the two sites.

The aim of the work reported here was to investigate the feasibility of using a gamma-ray scattering technique to give a measure of mandibular bone density. Both measurement precision and linearity *vs* density have been assessed. Potentially, such a technique offers a low dose, compact and relatively inexpensive means of indicating mandibular bone density compared with DXA and QCT. Gamma-ray scattering techniques have been previously used or investigated for the measurement of BMD in the heel as a predictor of skeletal osteoporosis [13–17].

Received 2 February 1999 and in final form 25 June 1999, accepted 8 July 1999.

Scattering parameters

A number of workers [13–17] have proposed or used the measurement of the ratio of coherent to Compton scattered photons from irradiated bone or other tissues to determine information on the composition of that tissue. Because coherent scatter is very dependent on the atomic number of the scatterer, the ratio of coherent to Compton scatter is also dependent on the atomic number of the scatterer, varying approximately as Z^2 [18]. Similarly the coherent/Compton scattering ratio of a composite material, such as bone, containing many elements, is dependent on the atomic numbers of its component elements and their proportion in the material.

More recently, the sensitivity of the Compton scattering profile to the chemical composition of the scatterer has been suggested as an alternative method of characterizing bone tissue [19, 20]. These latter authors have compared the high energy tail of the Compton distribution with the region dominated by singly scattered Compton gamma-rays. The ratio measured is shown to be dependent on the concentration of K_2HPO_4 used to simulate varying BMDs.

This paper examines the potential of both of the above methods to give a measure of mandibular bone density for either bone resorption studies or as a predictor of osteoporosis.

Experimental arrangement

The experimental arrangement is shown schematically in Figure 1. A backscatter geometry was

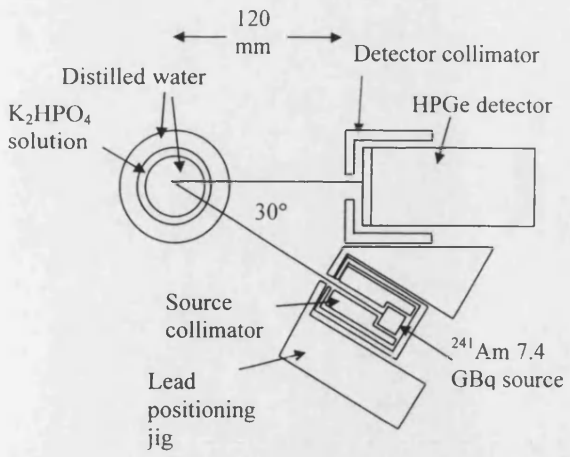

Figure 1. The experimental arrangement showing the ^{241}Am source, the jaw phantom and the HPGe detector.

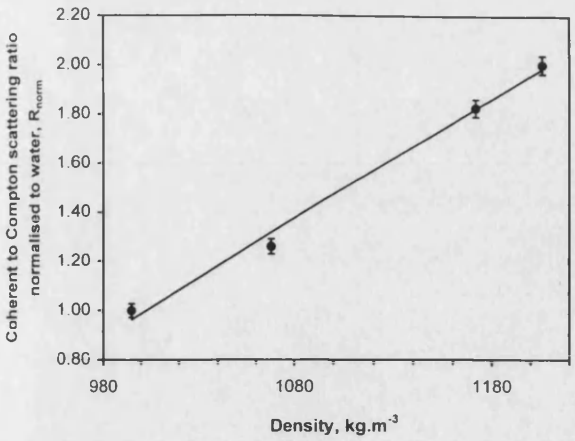

Figure 2. The variation in coherent/Compton scattering ratio with increasing density of the K_2HPO_4 solutions.

chosen for compactness and ease of set-up. A 7.4 GBq ^{241}Am source (5 mm diameter sphere) was collimated using a 5 mm diameter lead cylinder. A 32 mm diameter, 10 mm depth hyperpure germanium detector recorded the scattered photon spectrum. A 10 mm thick steel sleeve was fitted over the detector housing with a central 40 mm diameter hole exposing the detector.

To simulate the mandible a phantom was constructed of concentric thin-walled polypropylene cylinders as shown in Figure 1. The inner diameters of the cylinders were 54 mm, 74 mm and 90 mm, creating two concentric layers of 10 mm and 8 mm thickness surrounding the inner 54 mm diameter cylinder. The outer 8 mm layer was filled with water as a soft tissue substitute to a depth of 45 mm. Solutions of K_2HPO_4 were used as bone substitutes in the inner 10 mm layer to simulate the mandibular bone. The inner cylinder also contained water as a soft tissue substitute.

The phantom was irradiated with the inner 10 mm layer containing varying concentrations of K_2HPO_4 to a depth of 45 mm in the range 0–30 g K_2HPO_4 per 100 ml water simulating bone in the density range 1000–1200 kg m^{-3}. In this feasibility study the irradiation time was set at 1 h as in a practical instrument many sources could be arranged around the detector in the configuration shown in Figure 1, reducing the irradiation time proportionately. The measurement system focus was positioned at the phantom axis rather than at the "bone" layer to increase the count rate.

Results and discussion

Coherent/Compton scattering ratio

Figure 2 plots the variation of the measured coherent/Compton scattering ratio, R, against the density of the K_2HPO_4 solutions. The ratios are normalized to the value for water and the error bars show the standard deviation for each measurement. The line is the least-squares fit. If S is the slope of the plot then an uncertainty of ΔR on the measured ratio translates to a density uncertainty (ΔD) of $\Delta R/S$.

The average uncertainty in coherent/Compton ratio over the density range 1000–1200 kg m^{-3} is 2.5%. The measured slope is 0.005 m^3 kg^{-1} which results in a density uncertainty of about 1% when derived from a ratio measurement.

Compton profile ratios

Both MacKenzie [19] and Tartari et al [20] have suggested, as an alternative to the coherent/Compton scattering ratio, comparing the high energy tail of the Compton profile with the region dominated by singly scattered Compton gamma-rays. These authors have suggested slightly different energy limits for these ratios. MacKenzie [19] defined a ratio HP where the numerator is the integrated counts between 52 keV and 58 keV encompassing the high energy Compton tail, and the denominator is the integrated counts between 40 keV and 58 keV. Tartari et al [20] define a ratio R_k which results in summing over a slightly narrower portion of the high energy Compton tail.

Both parameters, HP and R_k are plotted in Figure 3 *vs* density of the K_2HPO_4 solutions. Again the ratios are normalized to that for water. A similar analysis to the above for the coherent/Compton scattering ratios gives an average density uncertainty of about 1% when derived from either the HP or R_k ratio parameter. This is similar to the uncertainty obtained for the coherent/Compton scattering ratio. Although the slopes of the plot are much less for the Compton profile ratio measurements, the statistical uncertainty is much less because of the increased counts in the Compton tail compared with the coherent peak.

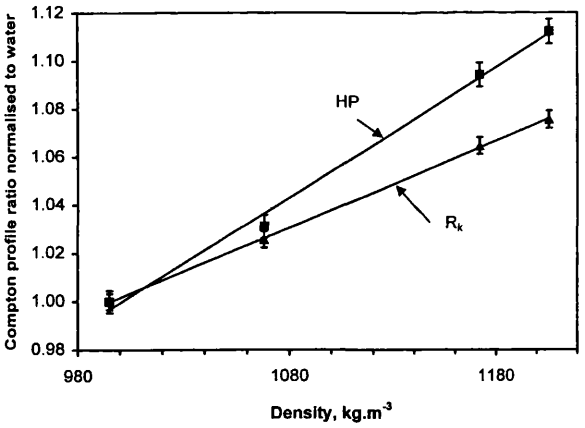

Figure 3. The variation of the parameters HP and R_k (see text) with increasing density of the K_2HPO_4 solutions.

Dose measurements

The absorbed dose at the surface of the phantom was measured using lithium fluoride (LiF) thermoluminescent dosemeters (Harshaw TLD 100) calibrated using a 100 kVp diagnostic X-ray beam. The dose at the phantom surface was 0.4 mGy per measurement which is similar to the skin dose received during dental radiography.

Conclusions

There has been considerable interest, reported in the last two decades [1–12], in the measurement of mandibular bone density either following tooth loss in bone resorption studies, or as an indicator of skeletal bone density. It has been shown that both coherent/Compton scatter ratio measurements and Compton profile measurements are sensitive to the density of K_2HPO_4 solutions in a jaw phantom giving a measurement precision of about 1% at densities near 1200 kg m^{-3}, typical of trabecular bone. In practice, patient positioning and anatomical variations would be expected to increase the measurement precision to nearer 3%. This is not as good as that achievable with QCT and DXA of between 1% and 2%, but is better than can be obtained from dental radiographs. Such scatter measurements might therefore offer low dose inexpensive alternatives to the use of dental radiographs in studies of mandibular bone density. As referred to in the introduction, because the technique gives a more precise density measurement than a dental radiograph, the results of such measurements would be expected to correlate more closely with skeletal bone status.

The aim of this work was to investigate the feasibility of using gamma-ray scattering measurements to estimate mandibular bone density. It is recognized that further work is required to provide information on other factors such as ease of use and costs of a complete system.

References

1. Henrikson PA, Wallenius K, Astrand K. The mandible and osteoporosis (2). Methods for determining mineral content of mandible and radius. J Oral Rehabil 1974;1:75–84.
2. Von Wowern N, Hjorting-Hansen E, Stoltze K. Changes in bone mass in rat mandibles after tooth extractions. Int J Oral Surg 1979;8:229–33.
3. Kribbs PJ, Smith DE, Chesnut CH. Oral findings in osteoporosis. Part II: Relationship between residual ridge and alveolar bone resorption and generalized skeletal osteopenia. J Prosthet Dent 1983;50:719–24.
4. Kribbs PJ, Chesnut CH, Ott SM, Kilcoyne RF. Relationships between mandibular and skeletal bone in an osteoporotic population. J Prosthet Dent 1989;62:703–7.
5. Kribbs PJ, Chesnut CH, Ott SM, Kilcoyne RF. Relationships between mandibular and skeletal bone in a population of normal women. J Prosthet Dent 1990;63:86–9.
6. Kribbs PJ. Comparison of mandibular bone in normal and osteoporotic women. J Prosthet Dent 1990;63:218–22.
7. Mohajery M, Brooks SL. Oral radiographs in the detection of early signs of osteoporosis. Oral Surg Oral Med Oral Pathol 1992;73:112–7.
8. Horner K, Devlin H. Clinical bone densitometric study of mandibular atrophy using dental panoramic tomography. J Dent 1992;20:33–7.
9. Klemetti E, Vainio P. Effect of bone mineral density in skeleton and mandible on extraction of teeth and clinical alveolar height. J Prosthet Dent 1993; 70:21–5.
10. Klemetti E, Vainio P, Lassila V, Alhava E. Cortical bone mineral density in the mandible and osteoporosis status in postmenopausal women. Scand J Dent Res 1993;101:219–23.
11. Klemetti E, Kolmakov S, Kroger H. Pantomography in assessment of the osteoporosis risk group. Scand J Dent Res 1994;102:68–72.
12. Horner K, Devlin H, Alsop CW, Hodgkinson IM. Mandibular bone mineral density as a predictor of skeletal osteoporosis. Br J Radiol 1996;69:1019–25.
13. Kerr SA, Kouris K, Webber CE, Kennett TJ. Coherent scattering and the assessment of mineral concentration in trabecular bone. Phys Med Biol 1980;25:1037–47.
14. Puumalainen P, Uimarihuhta A, Olkkonen H. A coherent–Compton scattering method employing an X-ray tube for measurement of trabecular bone mineral content. Phys Med Biol 1982;27:425–9.
15. Webster DJ, Lillicrap SC. Coherent–Compton scattering for the assessment of bone mineral content using heavily filtered X-ray beams. Phys Med Biol 1985;30:531–9.
16. Gigante GE, Sciuti S. A large angle coherent–Compton scattering method for measurement *in vivo* of trabecular bone mineral concentration. Med Phys 1985;12:321–6.
17. Shukla SS, Leichter I, Karellas A, Craven JD, Greenfield MA. Trabecular bone mineral density measurement *in vivo*: use of the ratio of coherent to Compton-scattered photons in the calcaneus. Radiology 1986;158:695–7.
18. Holt RS, Kouris K, Cooper MJ, Jackson DF. Assessment of gamma ray scattering for the characterisation of biological material. Phys Med Biol 1983;28:1435–40.

19. MacKenzie IK. An axially symmetric gamma-ray backscatter system for Du Mond spectrometry. Nucl Instr Meth 1990;A299:377–81.

20. Tartari A, Casnati E, Felsteiner J, Baraldi C, Singh B. Feasibility of *in vivo* tissue characterisation by Compton scattering profile measurements. Nucl Instr Meth 1992;B71:209–13.

Phys. Med. Biol. 42 (1997) 1403–1413. Printed in the UK PII: S0031-9155(97)78994-2

Gamma-ray scattering for fat fraction measurement

J Shakeshaft, H M Morgan and S C Lillicrap
Medical Physics Department, Royal United Hospital, Combe Park, Bath BA1 3NG, UK

Received 17 October 1996, in final form 24 February 1997

Abstract. The work reported examines the potential of using gamma-ray photon backscatter information to measure *in vivo* the percentage of fat in specific tissue volumes. ^{241}Am gamma rays are used as the source and the backscatter detected with a hyperpure germanium detector, with ethanol (approximately 80% fat, 20% muscle) and water (muscle) being used as tissue substitutes. Two measurement techniques are examined; the measurement of the ratio of coherent scatter to Compton scatter and the measurement of the Compton scatter profile. Both are shown to be sensitive to the composition difference between ethanol and water. For the coherent–Compton scatter ratio, the measured difference between water and ethanol is 1.85:1, close to the value calculated (about 2:1). A similar difference in the coherent–Compton ratios between muscle and fat is calculated (2.2:1). The FWHM of the Compton profile has also been shown to vary with tissue composition with a difference of 0.10 keV (5%) between the ethanol and water profile widths.

1. Introduction

X-ray and gamma-ray sources have been used in medical diagnostic applications both to image and to analyse various tissues of the body. The main applications have been transmission imaging with x-ray sources and organ imaging with gamma-ray emitting radiopharmaceuticals in nuclear medicine studies. Both of these applications are based on the measurement of the residual unscattered x-ray or gamma-ray photons. Steps are taken during measurement to suppress interference by the scattered photons.

Measurement techniques which use the information provided by scattered radiation have not found a widespread application. A number of authors (whose work has been reviewed by Holt *et al* 1984) have investigated the use of Compton scattered x-rays and gamma rays for both imaging and densitometry. Coherent scatter in x-ray diffraction studies is well established. More recently low-angle x-ray scattering using broad-spectrum x-ray sources has been used for tissue characterization (Harding *et al* 1990, Royle and Speller 1991).

A number of workers (Kerr *et al* 1980, Puumalainen *et al* 1982, Webster and Lillicrap 1985, Gigante and Sciuti 1985) have also proposed or used the measurement of the ratio of coherent to Compton scattered photons from irradiated bone and other tissues to determine information on the composition of the tissue. Because the probability of coherent scatter reduces rapidly with increasing angle of scatter, much work has been done using scattering angles of 90° or less. However, Holt *et al* (1983) using small biological specimens detected clear coherent scatter peaks in the scatter spectrum with a scattering angle approaching 180°. They also showed differences in the Compton scatter profile due to changes in the chemical composition of the scatter.

A backscatter measurement geometry has clear advantages in a clinical setting as it allows for a simpler measurement set-up and positioning. The purpose of the work reported

is to examine the potential of using gamma-ray photon backscatter information to assess regional body composition *in vivo* at selected sites. Two measurement techniques are examined; the measurement of the ratio of coherent scatter to Compton scatter, considered in more detail below, and the measurement of the Compton scatter profile. The Compton profile shape is sensitive to the chemical composition of the scatterer as the scattered radiation is effectively Doppler broadened because of the momenta of the target electrons (Williams 1977, Holt *et al* 1983). A possible application considered is the measurement of percentage fat at specific tissue sites. The measurement of bone mineral density is another possible application but is not considered in this work.

There are areas where the measurement of percentage fat might give useful information. Boyd *et al* (1995) have shown that breast tissue density, as assessed by mammography, is a strong risk factor for breast cancer. The radiographic appearance of the breast varies among individuals according to the relative amounts of fat which is responsible for the denser areas on the mammograms. Also, a number of diseases, including cancer and liver disease, result in weight loss and differential loss of protein and fat. The treatment of the disease can improve the patient's nutritional status and a number of groups have used a variety of methods to monitor these changes (Ellis and Eastman 1993, Taylor 1997).

In the work reported tissue substitutes are used to simulate different tissue composition. It is possible to use small-volume samples for *in vitro* studies as in the work of Holt *et al* (1983). However, this is not possible for *in vivo* patient studies. The effect of the poorer geometry and the effect of multiple scatter present in *in vivo* studies (MacKenzie 1990, Tartari *et al* 1992), both leading to the degradation of the coherent and Compton scatter spectra, are examined. Despite these effects, the results presented indicate the potential of the method as an *in vivo* measurement technique.

2. Coherent–Compton scattering ratio

The ratio of coherent to Compton scattering is derived from the Klein–Nishina formula for Compton interactions and the Rayleigh scattering formula. The ratio R is

$$R = P(k,\theta)\frac{(F(x,Z))^2}{S(x,Z)} \tag{1}$$

where

$$P(k,\theta) = \frac{[1+k(1-\cos\theta)]^2(1+\cos^2\theta)}{1+\cos^2\theta+[k^2(1-\cos\theta)^2]/[1+k(1-\cos\theta)]}$$

and where $F(x,Z)$ is the atomic form factor which allows for the whole atom to be acting as a scatterer rather than an individual electron, $S(x,Z)$ is the incoherent scattering function to allow for electron binding effects, k is the incident energy in units of electron rest mass and x is the momentum transfer which is a function of θ and k. For a given incident energy and scattering angle, $P(k,\theta)$ is a constant.

Values of R obtained from equation (1) are only valid for pure elements, i.e. integral values of atomic number Z. For a composite material of known composition an approximation to the value of R may be calculated by averaging the coherent to Compton scattering contributions from component elements, weighted for fractional atomic abundance:

$$R = P(k,\theta)\frac{\sum_i (F(x,Z_i))^2 a_i}{\sum_i S(x,Z_i)a_i} \tag{2}$$

where a_i is the atomic fraction of element i in the composite.

Because coherent scatter is very dependent on the atomic number of the scatterer the ratio, R, is also dependent on the atomic number of the scatterer, varying approximately as Z^2 (Holt *et al* 1983). The ratio, R, for a composite material is similarly dependent on the atomic numbers of its component elements and their proportion in the composite. In a mixture of two composite materials, even with small component differences, e.g. muscle and fat, the measured coherent–Compton scatter ratio may be sensitive enough to indicate their proportions in the mixture.

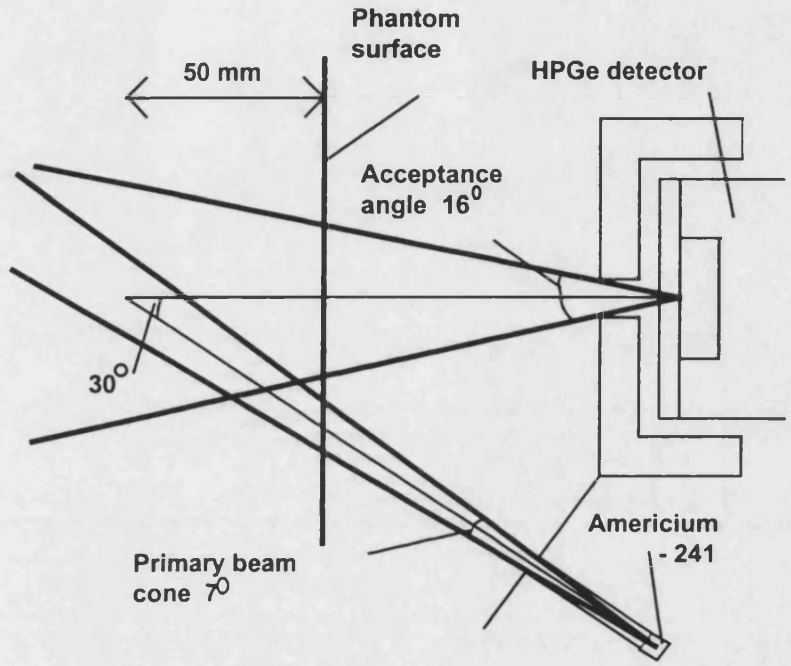

Figure 1. The experimental arrangement showing the target volume defined by the intersection of the primary beam cone and the acceptance angle of the HPGe detector.

3. Experimental arrangement

The experimental arrangement is shown schematically in figure 1. A 7.4 GBq ^{241}Am source (5 mm diameter sphere) was collimated using a lead cylinder to produce an angle of acceptance of 7°. A 32 mm diameter 10 mm depth hyperpure germanium detector recorded the scattered photon spectrum. The detector was calibrated for linearity with an ^{241}Am variable-energy x-ray source (Amersham 3832 LA) and at each measurement the position of the 59.54 keV coherent peak was checked. A 10 mm steel sleeve was fitted over the detector with a 10 mm diameter central collimating hole limiting the acceptance angle to the centre of the detector to 16°. For measurements of the depth dependence 300 mm square slabs of epoxy resin phantom of varying thickness were used. For other measurements a polythene walled tank was used (180 mm × 140 mm × 150 mm). The phantoms were placed at a set distance of 70 mm from the detector collimator. The angle between the two collimator axes (source and detector) was 30° (150° scatter angle).

Three phantom materials were used: epoxy resin slabs (Royal London Hospital formulation: H, 8.32%; C, 68.1%; N, 2.38%; O, 19.11%; Cl, 0.14%; Ca, 1.92%), water (H, 11%; O, 89%) and ethanol. The elemental composition of ethanol, C_2H_5OH (C, 52%; H, 13%; O, 35%) is approximately equivalent to 20% muscle (C, 14%; H, 10%; O, 71%; N,

3.4%) and 80% fat (C, 60%; H, 11%; O, 28%) (ICRU 1989). The elemental composition of the epoxy resin slabs is fairly close to that of fat. However, the presence of calcium and chlorine produces a higher effective atomic number than for fat.

4. Results and discussion

4.1. Target volume

In order to keep the counting rate to an acceptably high level, fairly large collimator acceptance angles were employed. The detector received primary scattered gamma rays from along much of the length of the primary beam cone (see figure 1) and secondary scatter from all parts of the phantom viewed by the detector collimator. The 'target volume' of the phantom contributing to the recorded scattered spectrum is therefore quite large and lies mostly in the primary beam cone extending from near the phantom surface to the intersection of the beam and detector collimator axes.

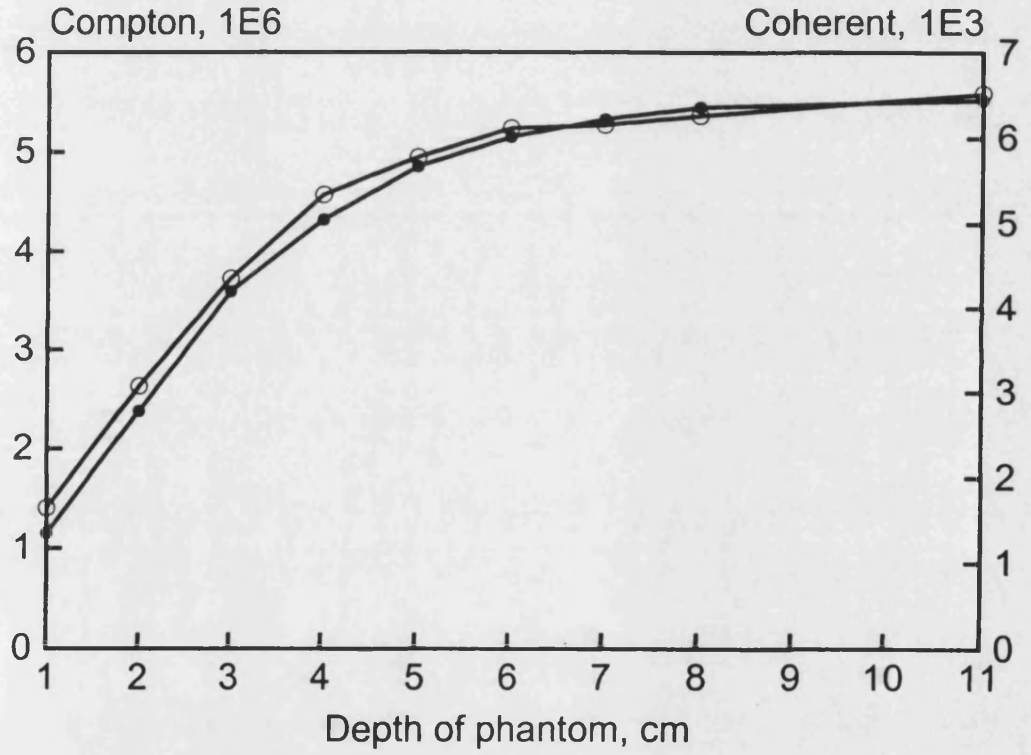

Figure 2. The Compton (●) and coherent (○) counts arising from an increasing thickness of epoxy resin phantom for a scattering angle of 150°. The position of the focus remains constant at 5 cm beyond the phantom surface.

In order to assess the effect of different tissue depths on the scatter spectrum and intensity, measurements were repeated with increasing depths of the epoxy resin phantom. For these measurements the detector-to-phantom distance was kept constant as the phantom depth was increased. The intersection of the source and detector collimator axes was 5 cm beyond the phantom surface. Figure 2 shows the variation of the integrated count rates in both the Compton scatter peak and the coherent scatter peak with phantom thickness. The coherent peak was summed between 58.9 and 60.1 keV, and the Compton peak between 40.0 and 56.0 keV (similar measured spectra are shown in figure 4). It can be seen that

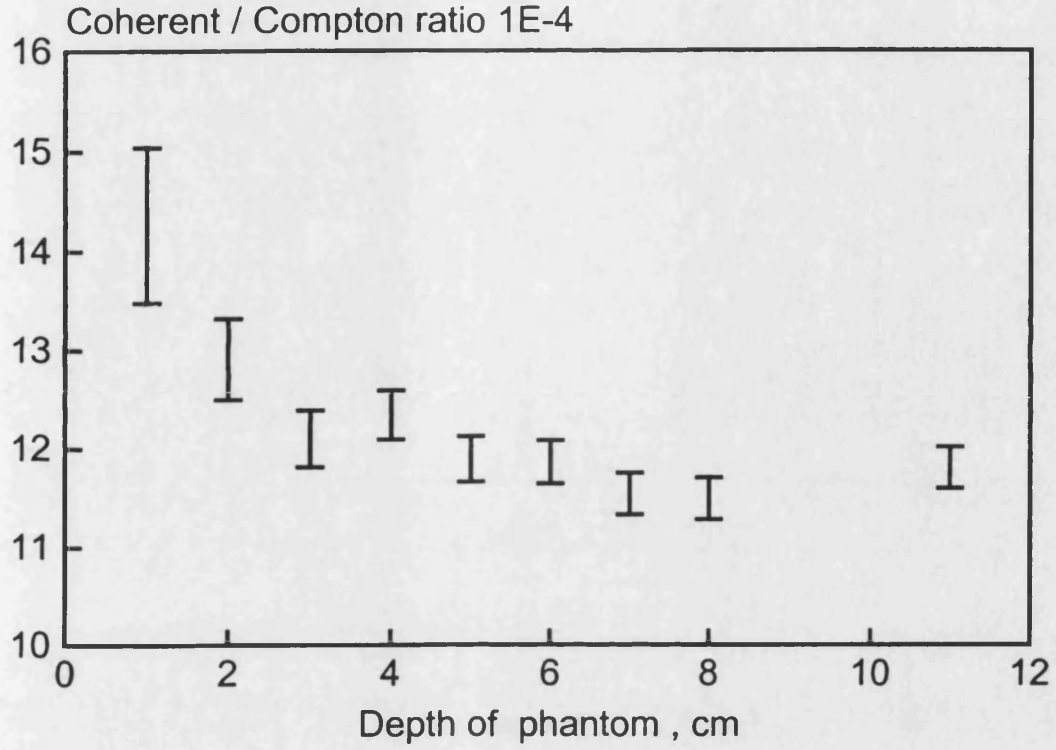

Figure 3. The variation in coherent–Compton ratio with increasing thickness of an epoxy resin phantom. The error bars show the mean ± one standard deviation. The position of the focus remains constant at 5 cm beyond the phantom surface.

the major contribution to both peaks is from material lying within 5 cm of the surface with a fairly uniform contribution from each of the first four 1 cm layers and little additional contribution beyond 6 cm depth. Thus, providing that the tissue is at least 5 cm in depth over 90% of both the coherent and Compton scatter counts arise from the first 5 cm depth with the experimental geometry used. Clearly however the angle of scatter will vary with depth. Near the phantom surface the angle of scatter is close to 130°, increasing to 150° at 5 cm depth. This change of scattering angle will influence the measured coherent–Compton ratio and Compton scatter profile and this is addressed in the following sections.

4.2. Coherent–Compton scattering ratio

The spectral measurements obtained with increasing depths of the epoxy resin phantom material described above were used to investigate the effect of phantom depth on the measured coherent–Compton scatter ratio. Figure 3 shows the variation of the measured ratio with the depth of the phantom. As would be expected from the results in figure 2, which shows that 90% of the scattered counts arise from the first 5 cm depth, the measured coherent–Compton scatter ratio remains constant with increasing depth beyond 5 cm. The higher values for 1 and 2 cm depths of phantom result from the smaller angle of scatter at these depths, because the coherent scatter increases more rapidly than Compton scatter as the scattering angle reduces. The measured values of the coherent–Compton scatter ratio for depths of 5 cm or more represents an approximate average of the ratios in the first 5 cm depth of tissue.

Using equation (2) and with the formulation provided by the Royal London Hospital, the calculated value for the coherent–Compton scattering ratio at 130° scattering angle is

15.7×10^{-4}; this falls to 13.0×10^{-4} at 150°. Both of these values are a little higher than the measured ratios, but the measured ratios are sensitive to the energy window selected for the Compton peak integration which can alter the ratio by ±10%. Also the effect of multiple scattering on the measured ratio is ignored in the calculation.

In order to assess whether the technique is able to distinguish between muscle and fat, scattered spectra were measured using the polythene tank described earlier filled either with water or ethanol to simulate muscle or a fat–muscle mixture respectively. Figure 4 shows the spectra obtained with water and with ethanol. Again the intersection of the source and detector collimator axes was positioned 5 cm beyond the phantom surface. The coherent–Compton scatter ratio measured for water was $10.52 \pm 0.15 \times 10^{-4}$ and that for ethanol was $5.67 \pm 0.14 \times 10^{-4}$. The uncertainties were due to both repositioning of the tank and counting statistics. To reduce the standard deviation in this feasibility study a long counting period of 48 h was used. The implications for a practical system where counting times of 30 min or less are required are discussed below. Table 1 shows the coherent–Compton scatter ratios for the ethanol and water phantoms and for the epoxy resin phantom (thicknesses over 5 cm).

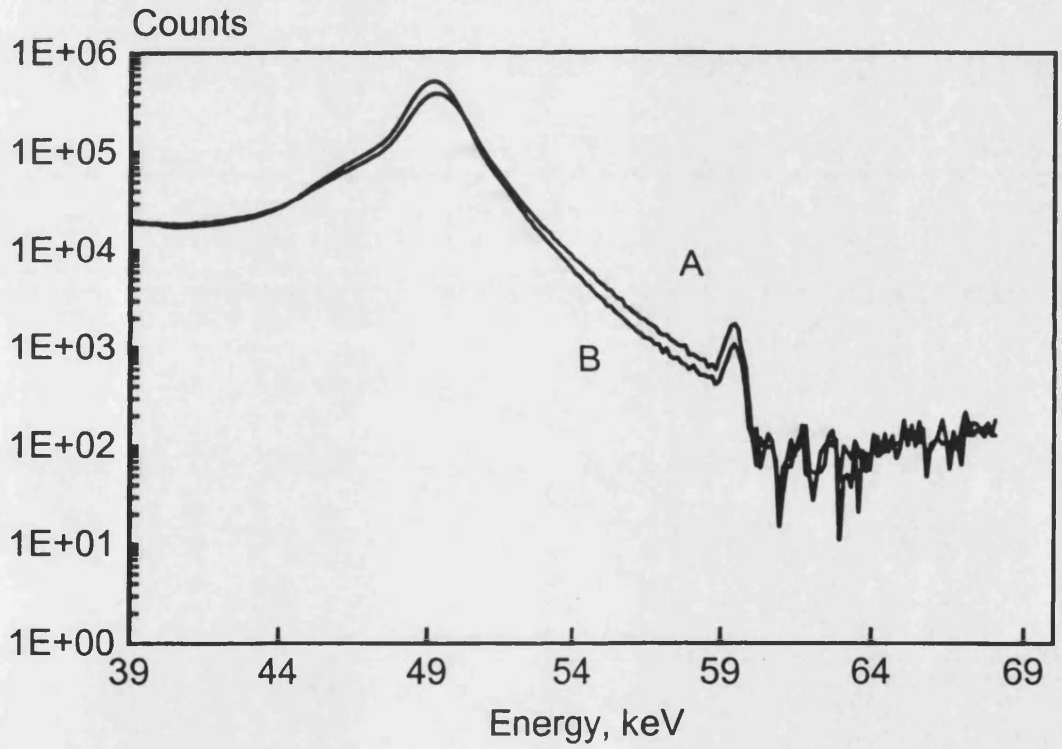

Figure 4. Spectra measured from a large phantom for water (A) and ethanol (B). The Compton peak is summed between 40.0 and 56.0 keV and the coherent peak is summed between 58.9 and 60.1 keV.

Using equation (2) the calculated value for the coherent–Compton scatter ratio for a 150° scattering angle for water is 13.0×10^{-4} and that for ethanol is 6.3×10^{-4}. The expected difference in the ratios is therefore about 2:1. The difference in the measured ratios is a little less (1.85:1) but sufficient to give good differentiation between the two tissue substitutes. As with the measurements with the epoxy resin phantom the calculated values of the coherent–Compton ratios are somewhat larger than measured. Using equation (2) and the *ICRU Report* 44 (1989) composition data, the calculated value for the coherent–

Compton ratio for a 150° scattering angle for muscle is 13.6×10^{-4} and that for fat is 6.1×10^{-4}, a difference in the ratios of 2.2:1. This is somewhat larger but still fairly close to the water–ethanol ratio difference.

Table 1. Measured coherent–Compton scatter ratios for the ethanol and water phantoms and for the epoxy resin phantoms for thicknesses greater than 5 cm.

	Ethanol	Water	Epoxy resin
Coherent–Compton ratio ($\times 10^{-4}$)	5.67 ± 0.14	10.52 ± 0.15	11.71 ± 0.15

As mentioned above, in order to undertake patient studies, 30 min is the longest reasonable time for a measurement. When measuring the coherent–Compton scatter ratio, it is necessary to obtain sufficient counts in the coherent peak to reduce the overall uncertainty of the measurement. In a practical system a number of sources could be placed around the detector with each beam axis converging to the same point at a depth in the patient/phantom, i.e. each source having the same source geometry as shown in figure 1.

With the single-source measurement of the coherent–Compton scatter ratio the water phantom gave a reproducibility of 1.5% (standard deviation) and the ethanol 2.5% (standard deviation) over a 48 h counting period. The smaller coherent scatter signal from ethanol gave rise to the larger standard deviation. If four sources were used for a 30 min measurement period, the standard deviations would be expected to increase to approximately 7.5 and 12.5% for water and ethanol respectively. As the calculated difference in the coherent–Compton scatter ratios between muscle and fat is more than 2:1 (measured water–ethanol ratio difference 1.85:1) this technique should allow for the average fat–muscle ratio in the target volume to be assessed with a standard deviation of approximately 0.1.

4.3. Compton profile

The Compton scatter profile is sensitive to the chemical composition of the scatterer. The inelastically scattered gamma radiation is effectively Doppler broadened because of the momentum of target electrons (Williams 1977, Holt *et al* 1983). However multiple scatter in the sample will also influence the spectral shape (MacKenzie 1990, Tartari *et al* 1992).

In order first to determine whether a difference in Compton profile can be measured, a narrow (13 mm diameter) glass cylinder filled with either water or ethanol was positioned at the intersection of the collimator axes and the Compton scatter spectra measured. With this diameter the probability of a single scattering event is less than 20% and the probability of the scattered photon being re-scattered much less. The influence of multiple scattering on the Compton profile should therefore be small.

Figure 5(a) shows the Compton spectrum profiles for both water and ethanol obtained using the cylindrical container. Background spectra, obtained with an empty container, have been subtracted. The water spectrum is broader than the ethanol spectrum. The full width at half maximum (FWHM) for the water spectrum is 1.54 keV, and that for the ethanol spectrum is 1.42 keV, a difference of 0.12 keV.

Obtaining good counting statistics is not a problem when measuring Compton scattering (compared with coherent scattering). It would be possible, therefore, to design a practical system with well collimated source and detector, designed to view a volume of cross section similar to that of the cylindrical phantom used to obtain figure 5(a). However, to see first whether the same experimental system as used to obtain the coherent–Compton scatter ratios

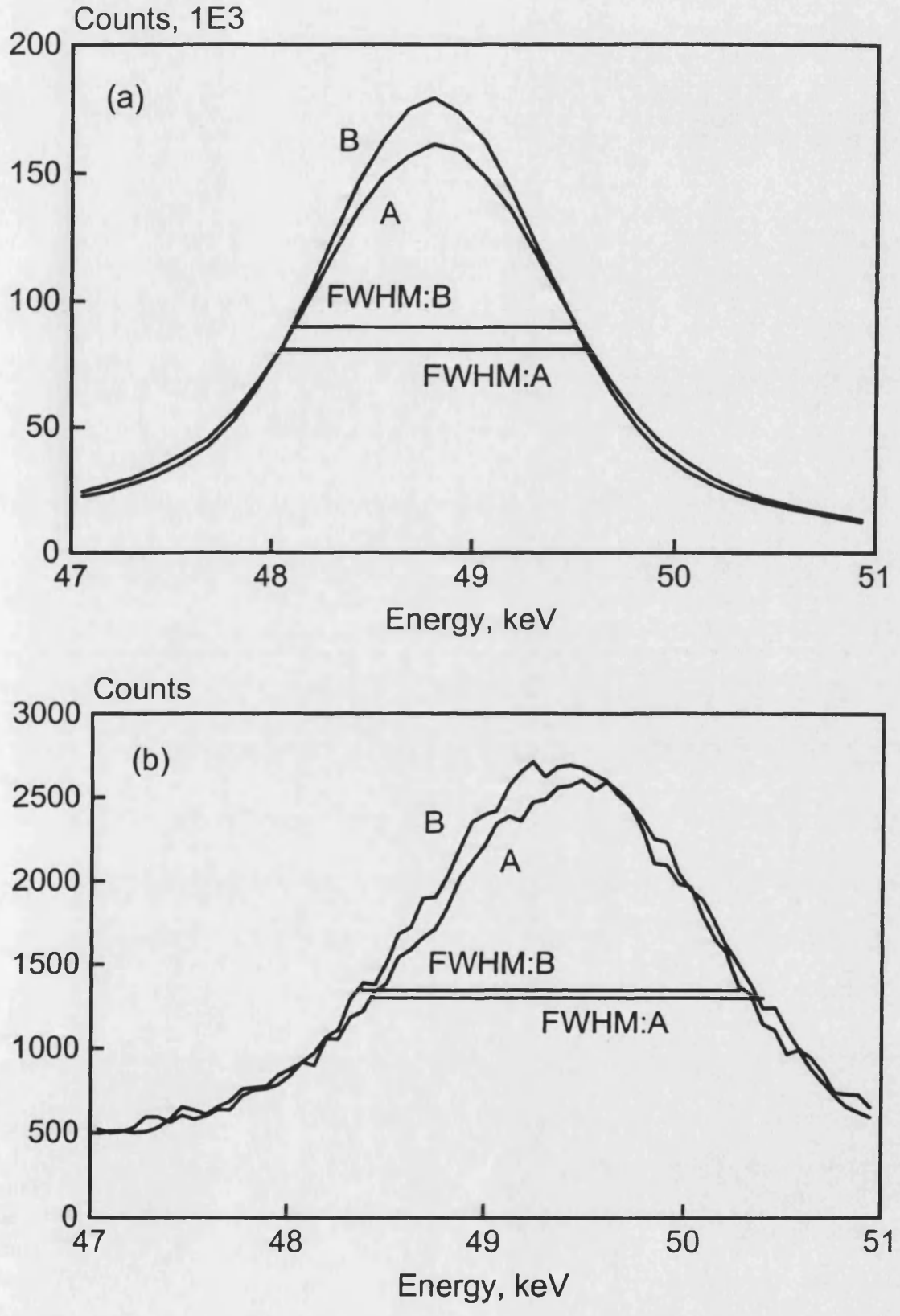

Figure 5. Compton profiles for water (A) and ethanol (B) obtained from (a) a small cylindrical phantom, 13 mm diameter, 48 h acquisition time (the spectra have been normalized for the same total count in the Compton region) and (b) a large phantom with surface 150 mm×180 mm and thickness 140 mm, 30 min acquisition time. The FWHMs are indicated in both cases.

(figure 1) could be used for Compton profile measurements, the influence of phantom depth on the profile shape was examined. Figure 6 plots the FWHM of the Compton spectra of photons scattered from the epoxy resin phantom as a function of phantom thickness using the experimental measurements made for the results plotted in figures 2 and 3. As with the coherent–Compton scatter ratio, the width of the Compton profile changes with depth and stabilizes with depths over 5 cm. Again, as with the scatter ratio, the Compton profile measurement for depths of 5 cm or more represents an approximate average of the profiles in the first 5 cm depth of material.

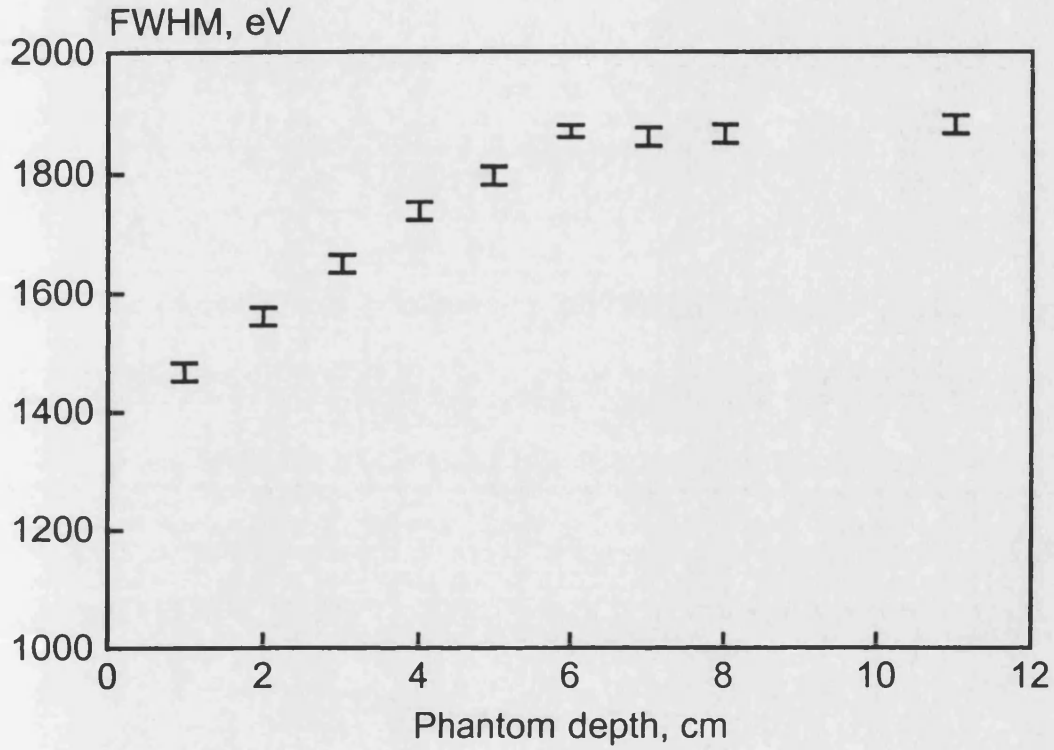

Figure 6. FWHM of Compton profiles for increasing thickness of epoxy resin phantom.

In order to assess whether a measurement of the Compton profile in 30 min is sufficient to be able to distinguish between the muscle and fat phantoms in a larger volume typical for patient studies, repeated Compton spectra profiles were obtained using the polythene tank container filled with either water or ethanol and measured for their FWHM values. Again the intersection of the source and detector collimator axes was positioned 5 cm beyond the phantom surface. These 30 min Compton spectra profiles for water and ethanol are replotted in figure 5(b) to compare with the results obtained with the 13 mm diameter cylindrical container. The increase in size of the phantom leads to a broadening of the Compton profile due to the range of scattering angles involved and the increased presence of multiple scatter (Tartari *et al* 1992). However, the difference between the widths of the ethanol and water spectra remains. It is not clear though whether any differences due to Doppler broadening have been masked by the influence of scattering angle differences or of increased multiple scatter in the two materials. The FWHM for water is $2.02 \pm 0.00(5)$ keV and for ethanol $1.92 \pm 0.00(5)$ keV, a difference of $0.10 \pm 0.00(7)$ keV, where the uncertainties are the standard deviations from five repeated measurements, a smaller difference than obtained with the 13 mm diameter cylinder but sufficient to give good differentiation between the water and ethanol profiles. Thus, provided that the depth of tissue to be measured is greater

than 5 cm the width of the spectral profile may be related to the fat–muscle ratio in the first 5 cm depth of the irradiated volume. It is assumed that with similar elemental composition ethanol and fat have similar Compton profiles and that the water and muscle profiles are also similar. This assumption, however, needs to be tested by measurements on real tissues.

4.4. Dose measurements

The absorbed dose at the surface of the phantom was measured using Li F thermoluminescence dosimeters (Harshaw TLD100H) calibrated using a 100 kV_p diagnostic x-ray beam. The dosimeter chips were irradiated for 72 h. The phantom surface dose rate was 0.4 mGy h^{-1}. At the surface the beam shape is approximately elliptical with axis dimensions of 12 mm×10 mm. For a half-hour measurement this is equivalent to the mean entrance surface dose for a chest x-ray (NRPB 1996) but delivered to a much smaller area and is about 5% of the mean entrance surface dose for a single-view mammogram.

5. Conclusions

Both coherent–Compton scatter ratio measurements and Compton profile measurements are sensitive to the composition difference between ethanol and water and are being explored further for clinical uses in the monitoring of the percentage fat at specific tissue sites as outlined in section 1. The experimental arrangement used will give a result characteristic of the fat–muscle ratio over the first 5 cm depth of tissue. The work described to explore the potential of using gamma-ray photon backscatter information to assess regional body composition has been performed using tissue substitute materials. It is planned now to construct two multi-source instruments for separate coherent–Compton scatter and Compton profile studies to reduce measurement times to be acceptable for clinical use and to improve counting statistics. They will be tested first using animal tissues.

References

Boyd N F, Byng J W, Jong R A, Fishell E K, Little L E, Miller A B, Lockwood G A, Tritchler D L and Yaffe M J 1995 Quantitative classification of mammographic densities and breast cancer risk: results from the Canadian National Breast Screening Study *J. Natl Cancer Inst.* **87** 670–5

Ellis K J and Eastman J D 1993 *Human Body Composition, Proc. Int. Symp. on In Vivo Body Composition Studies* (New York: Plenum)

Gigante G E and Sciuti S 1985 A large angle coherent–Compton scattering method for measurement in vitro of trabecular bone mineral concentration *Med. Phys.* **12** 321–6

Harding G, Newton M and Kosanetzky J 1990 Energy-dispersive x-ray diffraction tomography *Phys. Med. Biol.* **35** 33–42

Holt R S, Cooper M J, and Jackson D F 1984 Gamma- ray scattering techniques for non-destructive testing and imaging *Nucl. Instrum. Methods* **221** 98–104

Holt R S, Kouris K, Cooper M J and Jackson D F 1983 Assessment of gamma ray scattering for the characterisation of biological material *Phys. Med. Biol.* **28** 1435–40

International Commission on Radiation Units and Measurements (ICRU) 1989 Tissue substitutes in radiation dosimetry and measurement *ICRU Report* 44

Kerr S A, Kouris K, Webber C E and Kennett T J 1980 Coherent scattering and the assessment of mineral concentration in trabecular bone *Phys. Med. Biol.* **25** 1037–47

MacKenzie I K 1990 An axially symmetric gamma ray backscatter system for DuMond spectrometry *Nucl. Instrum. Methods* A **299** 377–81

National Radiological Protection Board (NRPB) 1996 Doses to patients from medical X-ray examinations in the UK—1995 review *NRPB Report* R289

Puumalainen P, Uimarihuhta A and Olkkonen H 1982 A coherent–Compton scattering method employing an x-ray tube for measurement of trabecular bone mineral content *Phys. Med. Biol.* **27** 425–9

Royle G J and Speller R D 1991 Low angle x-ray scattering for bone analysis *Phys. Med. Biol.* **36** 383–90

Tartari A, Casnati E, Felsteiner J, Baraldi C and Singh B 1992 Feasibility of in vivo tissue characterisation by Compton scattering profile measurements *Nucl. Instrum. Methods* B **71** 209–13

Taylor D M 1997 *Proc. Int. Symp. on Body Composition Studies; Appl. Radiat. Isot. Suppl.* at press

Webster D J and Lillicrap S C 1985 Coherent–Compton scattering for the assessment of bone mineral content using heavily filtered x-ray beams *Phys. Med. Biol.* **30** 531–9

Williams B G (ed) 1977 *Compton Scattering* (New York: McGraw-Hill)

Physica Medica - Vol. XIV, N. 4, October-December 1998

Bone Density Measurement by Gamma Ray Scattering – Influence of Overlying Soft Tissue

J.T. Shakeshaft, H.M. Morgan and S.C. Lillicrap

Medical Physics Department, Royal United Hospital, Combe Park, Bath BA1 3NG (UK)

Manuscript received: August 21, 1998; revised: October 22, 1998.

Accepted for publication: October 27, 1998.

Abstract

Spectral measurements of scattered gamma rays from suitable radionuclide sources have been proposed and used to determine tissue characteristics, notably bone density. A complicating factor for bone density measurements is the presence of overlying soft tissue, and this paper examines the influence of scatter from soft tissue in the situation where the density of the heel bone is being assessed. The influence of soft tissue scatter in a backscatter geometry is demonstrated for a Compton profile measurement technique suggested by Singh et al [1] and for a coherent/Compton ratio measurement technique.

KEY WORDS: Compton scattering, tissue characterisation, backscatter geometry.

1. Introduction

A number of groups, e.g. [1-4], have proposed or used the measurement of the ratio of coherent to Compton scattered X-rays and gamma rays from irradiated bone to determine information on its composition. More recently the sensitivity of the Compton scatter profile to the chemical composition of the scatterer has been suggested as an alternative method of characterising bone mineral content [5, 6]. In their recent paper Singh et al [7] have described a technique to characterise bone mineral content, based on the measurement of the Compton scatter profile using an ^{241}Am source as the irradiator and a NaI scintillation detector placed to receive backscattered radiation. The technique compares the high-energy tail of the Compton distribution with the region dominated by singly Compton scattered gamma rays. The ratio measured is shown to be dependent on the concentration of K_2HPO_4 used to simulate varying bone mineral densities. The technique has obvious applications in measuring the bone mineral density in the heel bone, which may be a predictor for spinal bone mineral density. The work reported below explores the proposed technique with a phantom simulating the heel, where the bone is surrounded by a soft tissue layer. The effect of the soft tissue thickness on the resulting ratio is measured and indicates the importance of applying a thickness correction to the ratio measurement. The effect of the thickness of the soft tissue layer on the measured coherent/Compton scattering ratio is also measured and compared with the Compton profile ratio.

2. Experimental

The experimental arrangement for backscatter measurement is shown in Figure 1. The radiation source is a collimated 7.4 GBq ^{241}Am point source. A 32 mm diameter 10 mm depth hyperpure Germanium detector recorded the scattered gamma ray spectrum. The heel bone phantom was a 35 mm diameter, 35 mm height thin-walled polypropylene cylinder filled with solutions of K_2HPO_4 in the concentration range 0-90 g/100ml (density range 1.0-1.5 g/cm^3). To simulate surrounding soft tissue, the bone phantom cylinder was placed concentrically within cylinders of diameter either 55mm or 75mm, and the gap between them either

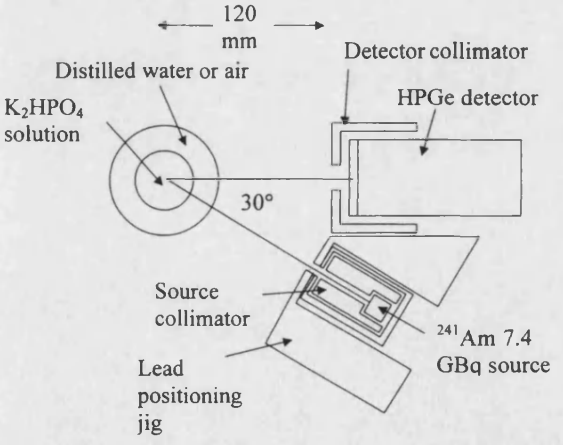

Fig. 1 – Schematic diagram of the experimental arrangement showing the ^{241}Am source, Germanium detector and heel phantom.

left empty (for in air measurement) or filled with water to produce surrounding water envelopes of 10 mm or 20 mm thickness. Because the cylindrical phantom does not reproduce the more complex structure and geometry of the human heel, the results obtained with it will not apply exactly to the heel, but it does serve to indicate the effect of soft tissue overlying bone.

For scatter measurements, the centre of the central cylinder was always placed at the intersection of the source and detector axes. The focus was at 120 mm from the front face of the detector collimator as illustrated in Figure 1. The angle between the detector and source collimator axes was 30° to detect backscatter through 150°.

3. Results and Discussion

Tartari et al [6] defined a ratio $R_k = I_k/I_c$ where I_k is the area under the high-energy Compton tail and I_c is the area in the energy region of the singly scattered Compton distribution. For this work, the energy limits for I_k were 51 keV to 56 keV and for I_c were 40 keV to 56 keV. Figure 2 shows the values of R_k for these energy

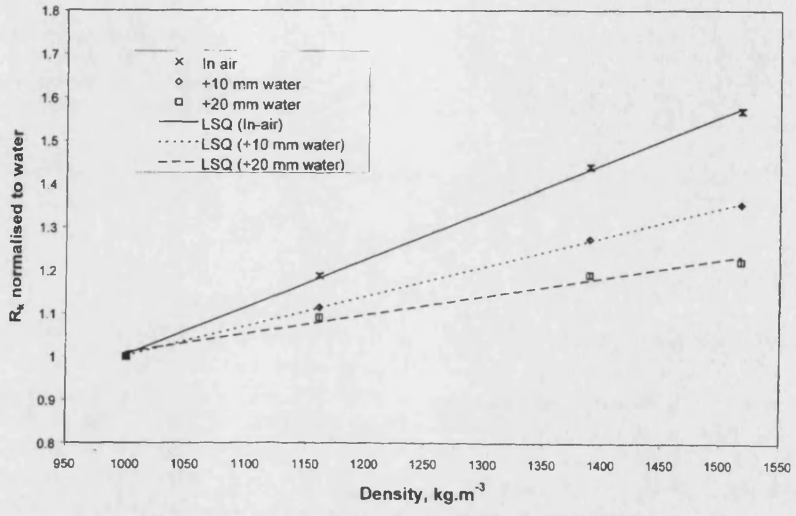

Fig. 2 – Plot of the Compton profile ratio R_k, normalised to water versus density (kg m^{-3}) for different thicknesses of surrounding water layer. A linear least squares fit (LSQ) has been applied to each set of data.

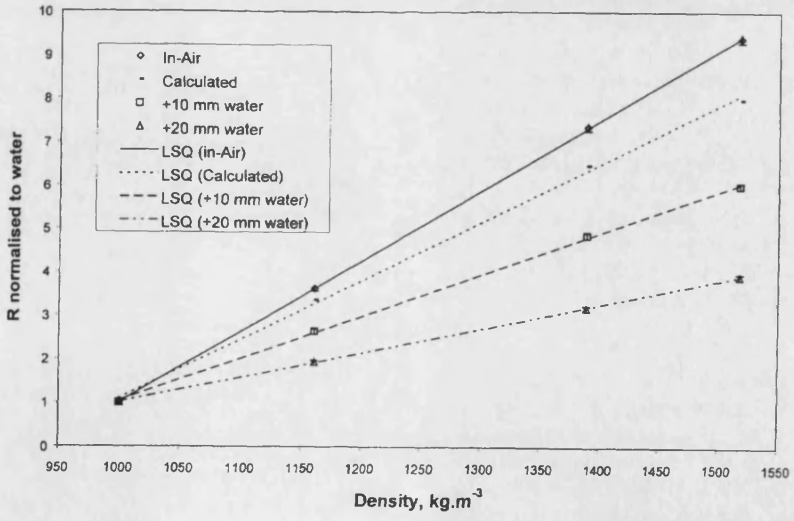

Fig. 3 – Plot of the coherent to Compton scattering ratio R, normalised to water versus density (kg m^{-3}) for different thicknesses of surrounding water layer, and calculated in air. A linear least squares fit (LSQ) has been applied to each set of data.

limits as a function of K_2HPO_4 concentration for different thicknesses of surrounding water layer (0 mm, 10 mm and 20 mm).

With the source detector geometry used and for the bone phantom alone, the R_k ratio value varies sufficiently to allow good discrimination between samples with different bone densities. However, the addition of a water layer reduces the R_k versus density slope as the detector receives also scattered radiation from the surrounding water.

A similar effect is seen with the measurement of the coherent/Compton ratio which is shown in Figure 3, together with the calculated in air values for 150° scattering angle. The slope of the coherent/Compton ratio versus density plot is steeper than with the R_k slope. However, the uncertainties in the coherent/Compton ratio values are larger because of the lower number of counts in the coherent peak.

The results shown in Figures 2 and 3 illustrate that for either of the above ratio measurements to be used for the assessment of bone density, it will be necessary to have an accurate measurement of the overlying soft tissue thickness, in order to apply an appropriate correction. Other corrections may also be needed if the experimental geometry varies. Using an axially symmetric backscatter system for heel bone measurement, MacKenzie [5] noted that the reproducibility of the readings was much poorer than anticipated from counting statistics and some of the worsening may have been due to differences in overlying tissue thicknesses between repositionings.

In a backscatter geometry it is not possible to avoid recording scatter from both bone and overlying soft tissue. In earlier work, Shukla et al [8] used a 71° angle between the source and detector axis, where the influence of overlying tissue on the result will be less, as collimation can be arranged to limit irradiation and detector viewing volumes.

REFERENCES

[1] Kerr SA, Kouris K, Webber CE and Kennett TJ. Coherent scattering and the assessment of mineral concentration in trabecular bone. Phys Med Biol 1980: 25; 1037-47.

[2] Puumalainen P, Uimarihuhta A and Olkkonen H. A coherent-Compton scattering method employing an X-ray tube for measurement of trabecular bone mineral content. Phys Med Biol 1982: 27; 425-429.

[3] Webster DJ and Lillicrap SC. Coherent-Compton scattering for the assessment of bone mineral content using heavily filtered X-ray beams. Phys Med Biol 1985: 30; 531-539.

[4] Gigante GE and Sciuti S. A large angle coherent-Compton scattering method for measurement in vivo of trabecular bone mineral concentration. Med Phys 1985: 12; 321-326.

[5] MacKenzie I K. An axially symmetric gamma-ray backscatter system for Du Mond spectrometry. Nucl Instr and Meth 1990: A299; 377-381.

[6] Tartari A, Casnati E, Felsteiner J, Baraldi C and Singh B. Feasibility of in vivo tissue characterisation by Compton scattering profile measurements. Nucl Instr and Meth 1992: B71; 209-213.

[7] Singh B, Tartari A, Baraldi C and Casnati E. Tissue characterisation by Compton scattering profile measurements using low resolution detectors. Physica Medica 1997: Suppl 1; 354-355.

[8] Shukla S S, Leichter I, Karellas A, Craven J D and Greenfield M A. Trabecular bone mineral density measurement in vivo: use of the ratio of coherent to Compton-scattered photons in the calcaneus. Radiology 1986: 158; 695-697.